Delivery of Targeted Nanoparticles Across the Blood-Brain Barrier Using a Detachable Targeting Ligand

Thesis by

Andrew James Clark

In Partial Fulfillment of the Requirements for

the degree of

Doctor of Philosophy

CALIFORNIA INSTITUTE OF TECHNOLOGY

Pasadena, California

2016

(Defended 26 April 2016)

Andrew James Clark
ORCID: 0000-0003-4240-7119

ACKNOWLEDGEMENTS

First, I would like to thank my soon-to-be wife Abby Uhrinak for being a constant source of support during my MD/PhD training. Her unwavering love has been my foundation for the past eight years and I could not thank her more.

I would also like to thank Dr. Mark Davis for giving me the opportunity to train in his lab. It has been a privilege to work with and learn from such a talented scientist. The breadth and depth of science I have been exposed to while working with him at Caltech has been enormous and given me a wonderful foundation on which to build. I especially appreciate the opportunity he offered me to work with patients on a clinical trial where true translational medicine was occurring. I hope to enter similar partnerships as I continue on in my career.

Other students in the Davis group have had a tremendous impact on this work and deserve recognition. Devin Wiley, a previous graduate student who started this project in earnest, was fundamental in training me and helping me become a proficient experimentalist. He was extraordinarily generous with his time and a wonderful mentor. Emily Wyatt was an all-around delight with which to work, constantly offering helpful suggestions and engaging in insightful discussions during our time together. She also synthesized and donated the MAP polymer I used in my final experiments, which would have been impossible to complete without her efforts. I have no doubt this project will continue to flourish with her taking the lead. Dorothy Pan, my fellow MD/PhD trainee, was also an outstanding coworker and helped me synthesize the nPBA-PEG used in my final experiments along with innumerable other tasks she assisted me with during my PhD training.

I'd also like to thank the members of my PhD committee, Jim Heath, Mikhail Shapiro, and Jesse Beauchamp, who have served as wonderful guides and challenged me to grow as a scientist and critical thinker.

I would also like to thank several members of the broader Caltech community who helped me during my time here. Mona Shahgholi assisted with mass spectrometry measurements and Nathan Dalleska helped me make ICP-MS measurements. Alasdair McDowall and Paul Webster helped me with electron microscopy studies while also teaching me how to understand and interpret images. Gwen Williams and Melissa McPherson were

tremendously helpful in training me to conduct animal experiments safely and skillfully. Martha Hepworth and Agnes Tong have been great sources for administrative help and support. I appreciate Bill Bing giving me the opportunity to drum in the jazz improv band to help take my mind off science for a little while.

I'd also like to acknowledge my collaborators at City of Hope, Joseph Chao, James Lin, Yafan Wang, Eloise Luevanos, and Yun Yen, as well as Jon Zuckerman at UCLA, who are all incredibly kind and were essential to completing the nanoparticle clinical trial.

Several members of the USC MD/PhD program have been a great help during my time training. Roland Rapanot is an outstanding administrator and helpful in any situation. Steve Mittleman has been a wonderful director of the MD/PhD program and I have every belief the program will continue to grow and excel under his leadership. I also want to thank the previous program co-directors, Bob Chow and Paul Patterson, for giving me the opportunity to train as an MD/PhD in this outstanding program.

I would also like to thank the community at Pepperdine University who first got me interested in research and gave me the tools I needed to pursue an MD/PhD. Jane Ganske was an outstanding research mentor alongside being one of the kindest individuals I have had the pleasure of knowing. The other professors who I had the chance to learn from were similarly outstanding and compassionate teachers.

Many friends have helped encourage me during my training. In particular, I'd like to thank Tommy Kimmerle, Neal Tambe, Jon Tucci, and Matt Webb for their friendship, laughs, and support. My bandmates were also generous to share their talent with me and let me express myself creatively in a different way. I'd also like to thank the many friends with whom I began medical school in 2010. Though many of them are dispersed throughout the country training as physicians now, they often provide me strong words of encouragement that I greatly appreciate.

I would not have come close to achieving anything in life if it were not for my family. They have shaped the person I have become and I can never repay them for their love and dedication. My father has constantly encouraged me to pursue my dreams and given me every opportunity to succeed. My grandmother has always nurtured my intellectual side and

been a constant source of love. Even my sister still offers her annoying little brother love and support.

Finally, I'd like to dedicate this work to two people very important to me who I lost during my time training as an MD/PhD. To my grandfather, who taught me to invest in my mind. And to my mother, who was an incomparable source of joy and the best teacher I ever had.

ABSTRACT

Chronic diseases of the central nervous system are poorly treated due to the inability of most therapeutics to cross the blood-brain barrier. The blood-brain barrier is an anatomical and physiological barrier that severely restricts solute influx, including most drugs, from the blood to the brain. One promising method to overcome this obstacle is to use endogenous solute influx systems at the blood-brain barrier to transport drugs. Therapeutics designed to enter the brain through transcytosis by binding the transferrin receptor, however, are restricted within endothelial cells. The focus of this work was to develop a method to increase uptake of transferrin-containing nanoparticles into the brain by overcoming these restrictive processes.

To accomplish this goal, nanoparticles were prepared with surface transferrin molecules bound through various liable chemical bonds. These nanoparticles were designed to shed the targeting molecule during transcytosis to allow increased accumulation of nanoparticles within the brain.

Transferrin was added to the surface of nanoparticles through either redox or pH sensitive chemistry. First, nanoparticles with transferrin bound through disulfide bonds were prepared. These nanoparticles showed decreased avidity for the transferrin receptor after exposure to reducing agents and increased ability to enter the brain in vivo compared to those lacking the disulfide link.

Next, transferrin was attached through a chemical bond that cleaves at mildly acidic pH. Nanoparticles containing a cleavable link between transferrin and gold nanoparticle cores were found to both cross an in vitro model of the blood-brain barrier and accumulate within the brain in significantly higher numbers than similar nanoparticles lacking the cleavable bond. Also, this increased accumulation was not seen when using this same strategy with an antibody to transferrin receptor, indicating that behavior of nanoparticles at the blood-brain barrier varies depending on what type of targeting ligand is used.

Finally, polymeric nanoparticles loaded with dopamine and utilizing a superior acid-cleavable targeting chemistry were investigated as a potential treatment for Parkinson's disease. These nanoparticles were capable of increasing dopamine quantities in the brains of

healthy mice, highlighting the therapeutic potential of this design. Overall, this work describes a novel method to increase targeted nanoparticle accumulation in the brain.

PUBLISHED CONTENT AND CONTRIBUTIONS

1. Clark, A. J., Davis, M. E. (2015). Increased brain uptake of targeted nanoparticles by adding an acid-cleavable linkage between transferrin and the nanoparticle core. *Proceedings of the National Academy of Sciences*, *112*(40), 12486–12491. [http://doi.org/10.1073/pnas.1517048112]

A.J.C. designed and performed research, analyzed data, and wrote the manuscript.

2. Clark, A. J., Wiley, D. T., Zuckerman, J. E., Webster, P., Chao, J., Lin, J., et al. (2016). CRLX101 nanoparticles localize in human tumors and not in adjacent, nonneoplastic tissue after intravenous dosing. *Proceedings of the National Academy of Sciences*, *113*(14), 3850-3854. [http://doi.org/10.1073/pnas.1603018113]

A.J.C. designed and performed research, analyzed data, and wrote the manuscript.

TABLE OF CONTENTS

DETAILED TABLE OF CONTENTS

LIST OF FIGURES

Chapter I *Page*

Chapter II

Chapter III

Chapter IV

Appendix A

LIST OF TABLES

ABBREVIATIONS

Ab-C. Nanoparticle formulation containing anti-transferrin receptor antibody bound through acid-cleavable link

Ab-N. Nanoparticle formulation containing anti-transferrin receptor antibody bound through non-cleavable link

ABC. ATP binding-cassette

ACh. Acetylcholine

ACN. Acetonitrile

AD. Alzheimer's disease

ADC. Antibody-drug conjugate

AMT. Adsorptive-mediated transcytosis

ApoE. Apolipoprotein E

AuNP. Gold nanoparticle

BA. Boronic acid

BBB. Blood-brain barrier

BME. 2-mercaptoethanol

BSA. Bovine serum albumin

CED. Convection enhanced diffusion

CNS. Central nervous system

CPT. Camptothecin

CSF. Cerebrospinal fluid

Cys. L-cysteine

DA. Dopamine

DAK. Diamino ketal, 2,2-bis(aminoethoxy)propane

DCM. Dichloromethane

DLS. Dynamic light scattering

DMF. Dimethylformamide

DMSO. Dimethylsulfoxide

DTT. Dithiothreitol

Fc. Fragment crystallizable

FcRN. Neonatal Fc receptor

FMT. Fluid phase transcytosis

FR. Folate receptor

FRET. Fluorescence resonance energy transfer

FUS. Focused ultrasound

GBM. Glioblastoma multiforme

GSH. Reduced glutathione

GSSG. Oxidized glutathione

H_2O_2. Hydrogen peroxide

HOS. Hyperosmotic shrinkage

ICI. Intracerebral implantation

ICP-MS. Inductively coupled plasma mass spectrometry

ICV. Intracerebroventricular infusion

L-DOPA. Levadopa

LID. Levodopa-induced dyskinesia

LRP1. Lipoprotein receptor-related protein 1

mAb. Monoclonal antibody

MALDI-TOF. Matrix-assisted laser desorption/ionization time-of-flight mass spectrometry

MAP-DA. Dopamine-loaded mucic acid polymer nanoparticles

MAP. Mucic acid polymer

mPEG. Methoxy-terminated polyethylene glycol

MTfR. Melanotransferrin receptor

NMDA. N-methyl-D-aspartate

NP. Nanoparticle

nPBA. Nitro phenyl boronic acid

PBS. Phosphate buffered saline

PD. Parkinson's disease

PDI. Protein disulfide isomerase

PEG. Polyethylene glycol

PLGA-AF488. PLGA polymer conjugated to an Alexa-Fluor 488 fluorescent tag

PLGA-mPEG. Block co-polymer between PLGA and methoxy-terminated PEG

PLGA-PEG-SH. PLGA-PEG block co-polymer containing a terminal thiol group

PLGA-PEG-SH. PLGA-PEG nanoparticles expressing surface thiol groups

PLGA. Poly(D,L-lactic-co-glycoclic acid)

PPD. Passive paracellular diffusion

PTD. Passive transcellular diffusion

RES. Reticuloendothelial system

RMT. Receptor-mediated transcytosis

SCP. Solute carrier proteins

SFB. P-succinimidyl 4-formylbenzoate

SH-PEG-COOH. Heterobifunctional polyethylene glycol polymer containing terminal thiol and carboxylic acid groups

siRNA. Small interfering ribonucleic acid

TEM. Transmission electron microscopy

Tf-C. Nanoparticle formulation containing transferrin bound through acid-cleavable link

Tf-N. Nanoparticle formulation containing transferrin bound through non-cleavable link

Tf. Transferrin

TfR. Transferrin receptor

THR-AF488. THR peptide tagged with an Alexa Fluor 488 fluorescent probe

THR-PEG. THR peptide tagged with a polyethylene glycol molecule

THR. Anti-transferrin receptor peptide with sequence THRPPMWSPVWP

TJM. Tight junction modulation

Tyr. L-tyrosine

Chapter I

INTRODUCTION

1.1 Chronic Diseases of the Central Nervous System, Their Treatment Limitations and Outlook

Improvements in treatment and prevention over the past fifty years have led to a significant decrease in mortality from cardiovascular disease and cancer, the two leading causes of death in the US (1). The age-adjusted death rate from malignant neoplasms has decreased 16% since 1950 while the death rate from heart disease has dropped an impressive 70% over that same period (2). Despite these remarkable achievements, chronic diseases of the central nervous system (CNS), such as Alzheimer's disease (AD), have not benefited similarly (Fig 1A). In fact, the proportion of deaths from AD has increased 68% over the past decade (3), moving AD from outside the top ten in 1980 to the sixth leading cause of death in the US in 2013 (2). AD currently affects over five million people in the US, and is expected to increase to over thirteen million by 2050. The estimated total cost of care in 2012 for people with AD was over $200 billion and is projected to rise to $1.2 trillion within the next forty years (Fig 1B) (3). In comparison, the direct healthcare costs in 2010 for heart disease and cancer were estimated at $109 billion and $77 billion, respectively (4), making AD one of the most costly diseases in the US. A similar trend, in both high societal cost and a relative lack of progress in treatment, is seen with many other neurodegenerative diseases, including Huntington's disease (5), Parkinson's disease (PD) (6), and certain forms of multiple sclerosis (7).

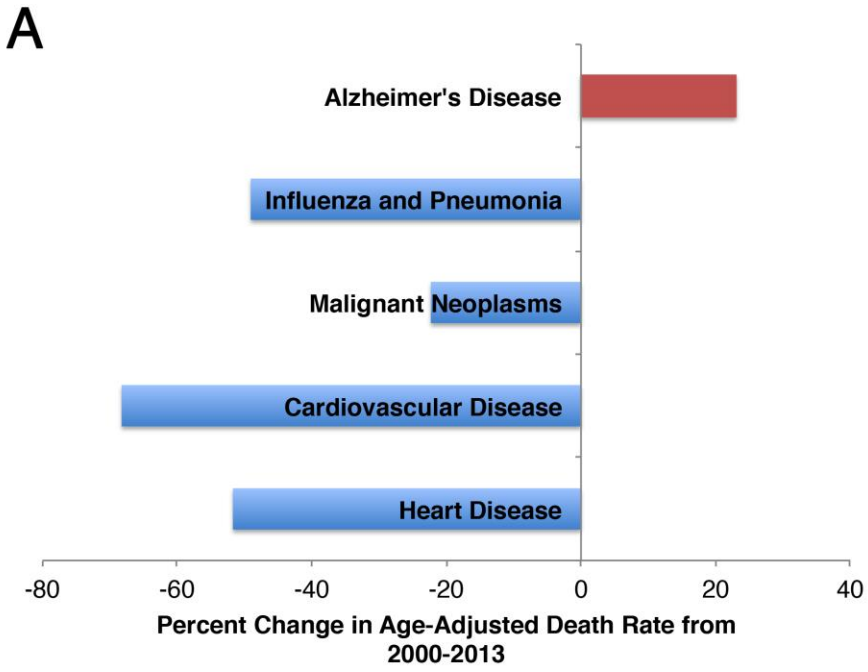

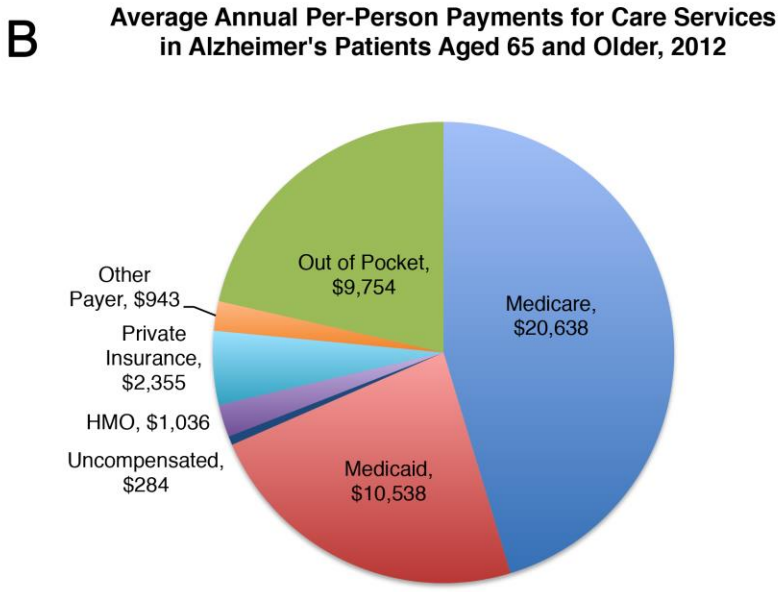

Fig 1.1 Societal impact of Alzheimer's disease in the US. (A) Change in age-adjusted death rate from 2000-2013 for major causes of death in the US. AD is one of the few causes to increase over this period [Data from (2)]. (B) Per-annum cost per person for care services in patients with AD aged 65 and older. The average cost of care services exceeded $40K per AD patient in 2012 [Data from (3)].

Investigating the current treatment modalities for AD and their limitations is useful to demonstrate the obstacles that inhibit better treatments for CNS diseases as a whole. AD is a neurodegenerative disease that causes memory impairment and affects cognitive function. The key pathological signs are atrophy of the cerebral cortex and hippocampus, accumulation of extracellular β-amyloid plaques, and aggregated intracellular tau protein (neurofibrillary tangles). The disease is also characterized by decreased cerebral synthesis of the neurotransmitter acetylcholine (ACh). First-line treatment for AD includes the cholinesterase inhibitors donepezil, rivastigmine, and galantamine (Fig 1.2). These molecules reduce breakdown of endogenous ACh restoring some degree of cholinergic function. Memantine, an N-methyl-D-aspartate (NMDA) receptor antagonist, is also commonly given to treat AD and believed to be neuroprotective. These drugs are all small (<400 Da) and strongly lipophilic, two key structural characteristics that allow them to enter the CNS (discussed in section 1.4). They are also only symptomatic treatments and fail to either influence the poorly understood underlying pathophysiology or significantly reduce disease progression.

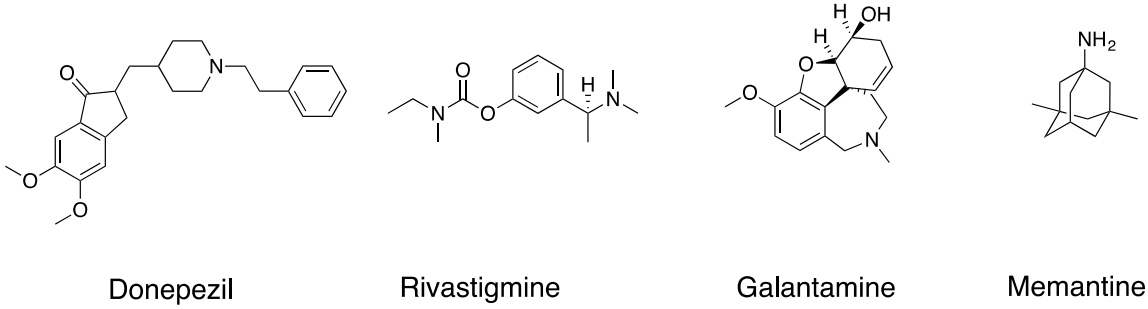

Fig 1.2. Molecular structures of FDA-approved treatments for Alzheimer's disease. Each molecule is small and hydrophobic with few atoms capable of forming hydrogen bonds.

With the tremendous social burden AD is poised to place on the US in the upcoming decades, significant investment has been made recently to improve treatment for the disease; however, few new therapies are expected in the near future. From 2002-2012, 99.6% of new AD therapies, primarily small molecules and immunotherapies, investigated in clinical trails failed due to either poor efficacy or unacceptable toxicity. This is among the lowest success

rates for therapeutic development. More concerning is that, over this same time period, none of the 221 disease-modifying drugs successfully progressed through clinical trials (8).

The example of AD illustrates factors common to most chronic neurological conditions, namely, (i) complex and multifactorial pathogenesis reducing the possibility of a single "silver bullet" treatment, (ii) limited or no disease-modifying therapies currently available, and (iii) few promising disease-modifying candidates in the drug pipeline. Novel and innovative treatment approaches are desperately needed before the societal impact of these chronic diseases becomes overwhelming.

1.2 Blood-Brain Barrier Structure and Function

A major reason for the limited progress in treating CNS diseases is the inability to deliver therapeutic quantities of drug to the CNS from the blood. Drug delivery is inhibited by the blood-brain barrier (BBB), an anatomical and physiological barrier between the CNS parenchyma and vasculature. It is composed of endothelial cells, pericytes, and astrocyte end-foot processes and plays a critical role in maintaining homeostasis within the CNS, with functions including influx of nutrients and efflux of waste, maintenance of optimum ion concentrations, control of immune surveillance, and separation of central and peripheral neurotransmitter pools (9).

One of the major reasons that the BBB is able to engage in such a diverse and finely controlled range of functions is the presence of zonulae occludentes (tight junctions) between endothelial cells. These tight junctions greatly inhibit paracellular diffusion of polar molecules, macromolecules, and cells, forcing solute transport into the CNS to occur primarily across individual endothelial cells. The junctions are so effective that individual sodium ions (hydrated radius of 3.6 Å) are prevented from crossing paracellularly. Maintenance of the tight junctions is controlled by soluble factors secreted by nearby astrocytes, highlighting the importance of nearby supporting cells in maintaining and influencing BBB permeability (10).

1.2.1 Solute Transport Across the Blood-Brain Barrier

Though the BBB severely limits passive transport of solutes into the CNS, many different transport systems exist at the BBB for influx of necessary nutrients. There are six main transport mechanisms at the BBB: (i) passive paracellular diffusion (PPD), (ii) passive transcelluar diffusion (PTD), (iii) solute carrier proteins (SCP), (iv) receptor-mediated transcytosis (RMT), (v) adsorptive-mediated transcytosis (AMT), and (vi) tight junction modulation (TJM) (Fig 1.3) (9).

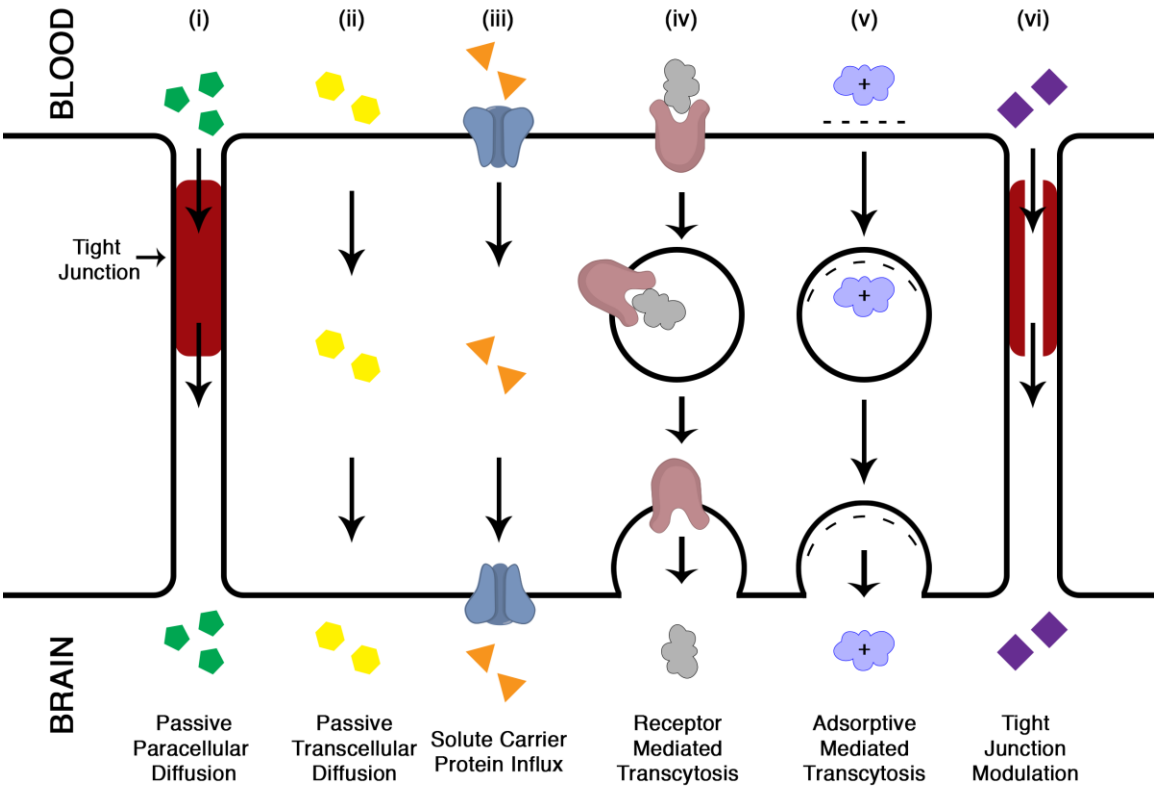

Fig 1.3. Solute transport systems at the blood-brain barrier. Solutes can cross the BBB through six different pathways. (i) Passive paracellular diffusion, (ii) passive transcellular diffusion, (iii) solute carrier protein influx, (iv) receptor-mediated transcytosis, (v) adsorptive-mediated transcytosis, and (vi) tight junction modulation. Nearly all FDA-approved medications for chronic CNS diseases cross through PTD.

PTD is primarily restricted to small (<500 Da), lipophilic molecules capable of diffusing through the cell membrane lipid bilayer. Molecules capable of forming >6 hydrogen bonds and with polar surface areas >80 Å are severely restricted from crossing by PTD due to the high free energy requirement to partition from the aqueous blood to lipid membrane. Some bases are capable of crossing via this pathway due to the ability of the cationic group to interact with the negatively charged phospholipid membrane head, but they are still limited by the size restriction needed for diffusion (10). The only way for polar solutes to passively move through the BBB is through PPD; however, due to the presence of the tight junctions, this pathway is virtually non-existent in the healthy BBB.

Many polar solutes, though, are required for normal function in the CNS. To accommodate these needs, specific transport proteins for many different nutrients, including amino acids, glucose, and small peptides, exist at the BBB. SCP's on the apical surface of the BBB recognize their solute in the blood and transport it into the BBB endothelial cells through facilitative diffusion. As concentration within the endothelial cell builds, equivalent transport proteins on the basal membrane transport solute into the CNS parenchymal space. SCP's are highly specific for their solute and have limited ability to transport different or novel compounds. This method of facilitative diffusion is also restricted to small molecules capable of moving through the protein channels.

To transport macromolecules across the BBB, transcytosis pathways are used. In this process, events on the apical side of the BBB trigger invagination of the cell membrane to form an endocytic vesicle encapsulating the macromolecules. The vesicle is then transported to the basolateral side of the endothelial cell where it fuses with the membrane, releasing the enclosed macromolecules to the CNS parenchyma. In RMT, specific binding of a serum protein to its transcytosing receptor on the apical side induces formation of the transcytosis vesicle. Several serum proteins, including transferrin (Tf), insulin, and apolipoprotein E (ApoE) use this process to enter the brain from the circulation (10). An alternative method to induce transcytosis is through AMT. AMT is a non-specific process where a highly cationic protein induces transcytosis by interacting with negatively charged proteins on the

endothelial cell surface. The exact mechanisms by which AMT occurs are less understood than those for RMT (11).

The final mechanism solutes use to cross the BBB is through TJM though this process does not readily occur in the healthy BBB. Circulating leukocytes are believed to use this pathway to enter the brain and become resident microglia, though there is some debate regarding whether the tight junctions themselves are transiently disrupted (10). TJM mainly occurs in pathological conditions, such as malignant gliomas, where astrocyte endfoot coupling to the endothelium is disrupted, leading to loss of BBB integrity (12).

1.3 Current Methods of Drug Delivery to the CNS

The vast majority of drugs currently used to treat neurological diseases are small and lipophilic, reaching the CNS through PTD. This includes benzodiazepines, many anti-psychotics and anti-depressants, and the AD treatments in Fig 1.2. Not coincidentally, most diseases that can be treated with these drugs, such as depression, anxiety, and psychosis, have significantly better prognoses than diseases where small, lipophilic drugs are unavailable.

Invasive methods that physically bypass the BBB have been investigated for several decades to treat CNS diseases that are poorly treated systemically. Three similar techniques that involve direct introduction of drug to the parenchyma have been developed with varying, but overall limited, degrees of success: (i) intracerebral implantation (ICI), (ii) intracerebroventricular infusion (ICV), and (iii) convection enhanced diffusion (CED) (13). Two other methods, hyperosmotic shrinkage (HOS) and focused ultrasound (FUS), involve transient disruption of BBB tight junctions to allow circulating drugs to enter the CNS (14).

ICI involves direct implantation of drugs into the CNS parenchyma. It was first crudely applied in patients with gliomas, where a chemotherapeutic-soaked sponge was placed in the resulting cavity after sub-total tumor resection. This technique was further refined to incorporate external cannulas allowing multiple chemotherapy doses to be introduced directly into the glioma site or implantation of drug-loaded, biodegradable devices (15). ICV introduces drugs directly into the ventricular system to take advantage of cerebrospinal fluid (CSF) circulation to deliver drug to a large brain area while avoiding

uptake into systemic circulation. This method has been applied in a variety of conditions, including AD (16) and chronic pain (17).

Clinically, these two techniques have shown limited to no improvement over systemic treatments. The main reason for this failure is the poor drug diffusion from the site of introduction. Solute diffusion in the brain decreases by the square of the distance from its origin, leading to logarithmic decay in drug concentration. In practical applications, the concentration of small molecule drugs introduced by ICV to Rhesus monkeys was found to decrease by 98% only 1-2mm from the ependymal surface (contact point between the CNS parenchyma and CSF) (13). The extremely limited diffusional capacity of drugs introduced by these methods and their failure to significantly improve outcomes for focal diseases like primary neoplasm bodes poorly for their application in diffuse conditions such as AD where neurons throughout the brain are affected.

CED attempts to improve upon the diffusional limitations of ICI and ICV through use of an infusion pump. This produces a small positive pressure gradient to drive bulk flow of drug into the CNS parenchyma, leading to delivery of therapeutic concentrations over a much larger volume than previously possible. Two CED treatments have reached Phase III clinical trials for glioblastoma multiforme (GBM) but failed to show statistically significant survival benefit as monotherapy compared to conventional therapy, though there is some evidence they may have a role in combination therapies. Research is ongoing with CED devices to improve biocompatibility and technical reproducibility as well as deliver novel therapeutics (18).

An alternative method to physically bypass the BBB is to temporarily disrupt the tight junctions between endothelial cells, allowing for transient permeability to systemic drug molecules. This is done commonly in the clinical through arterial injection of a hyperosmotic solution, such as mannitol. The high salt concentration in the blood causes BBB endothelial cells to shrink and stretch the tight junctions (19,20). Expansion of the tight junctions creates space in between cells for circulating drug molecules to cross and enter the CNS. HOS suffers, however, from difficult administration and significant side effects, including seizures and hypotension (14). These problems are likely due to the widespread, nonspecific nature of BBB disruption in HOS, allowing toxic substances to enter the brain.

Similar to the development of CED in response to ICI and ICV's shortcomings, FUS was investigated as a method to safely disrupt the BBB. In FUS, microbubbles are administered systemically, followed by focal application of ultrasound waves. The microbubbles oscillate within the ultrasound field allowing them to interact with endothelial cells. At the BBB, the exact mechanism that leads to BBB disruption is unclear. Current understanding is that the microbubbles either physically stretch the endothelium similar to HOS or trigger a physiologic response that temporarily increases permeability. Regardless of the true biological cascade leading to BBB disruption, FUS has garnered considerable attention due to the abilities to both control the magnitude of disruption and spatially locate disruption by controlled application of the ultrasound. It is also reproducible, capable of delivering a wide variety of therapeutic agents, and has not shown significant side effects in animal models (14). Concerns persist regarding the long-term safety of FUS and its efficacy in humans. The technique has very recently begun investigation in a pilot clinical trial to deliver doxorubicin to GBM patients (21). Of particular concern is whether this method will cause similar neurological side effects as HOS by non-specifically regulating what crosses the BBB.

One final aspect affecting small molecule drug delivery to the CNS—either systemically or by invasively bypassing the BBB—is the presence of efflux pumps on the basal side of BBB endothelial cells. Similar to the influx SCP's on the apical cell membrane, specific efflux transporters exists to clear neurotoxins from the CNS. There are numerous different ATP Binding-Cassette (ABC) transporters expressed for this purpose, including P-glycoprotein, Multidrug Resistance-associated Proteins, and Breast Cancer Resistance Protein (10). These proteins can actively transport a diverse array of molecules out of the CNS, including a large number of prescribed medications. In fact, many drugs that showed promise in vitro have failed either in animal models or during clinical trials because they are cleared from the CNS by ABC transporters (22). Novel therapeutics that not only diffuse through significant portions of the brain but can also avoid rapid efflux by ABC proteins are needed to improve on these current paradigms.

1.4 Targeted Drug Delivery to the Brain

Compared to invasive, local introduction of drugs described above, therapies that are capable of entering the brain from the blood show much greater potential to treat diffuse CNS diseases such as AD and PD. The brain is highly vascular, with a total surface area for exchange between 12-18 m^2 in an adult human. Furthermore, no brain cell is greater than 25 μm from a capillary, allowing for significantly shorter diffusional distances from the blood to reach functional cells compared to locally administered treatments (10).

As detailed above, very few drugs are capable of using PTD to enter the brain and restraining candidate drugs within the limited design parameters for PTD significantly diminishes the available pool of potential treatments. Developing a method to deliver large, macromolecular therapeutics to the CNS provides the most promising route as normally excluded treatments, such as potent biologics and circulating drug delivery devices, will be available for use. Delivery methods that do not affect BBB integrity are also desired so only the therapeutic enters the CNS and not potentially toxic substances.

In order to meet these requirements, large therapeutics must cross by transcytosis (detailed in section 1.3). The idea of using endogenous transcytosis pathways to shuttle a therapeutic into the brain was first proposed several decades ago (13). The general approach has been to conjugate a BBB-impermeable drug molecule to a ligand that binds a transcytosing receptor at the apical side of the BBB. Binding of the ligand portion of the drug-ligand conjugate to its receptor will shuttle the drug through the BBB via the transcytosing vesicle. Then, once inside the CNS, the drug can diffuse to its site of action. This method of "masking" the drug molecule by binding it to a transcytosing ligand has been coined the "Trojan-horse" approach for CNS drug delivery (13). RMT across the BBB has already been investigated extensively to deliver antibody-drug conjugates (23, 24, 25), liposomes (26, 27), and nanoparticles (28, 29, 30) to the CNS.

1.4.1 Drug Delivery Across the Blood-Brain Barrier Using Anti-Transferrin Receptor Antibodies

Several receptors are known to undergo RMT at the BBB. The insulin receptor (InR), transferrin receptor (TfR), melanotransferrin receptor (MTfR), low-density lipoprotein receptor-related protein 1 (LRP1), and the folate receptor (FR) have each been investigated for targeted drug delivery (30). Of these ligands, Tf has been the most studied and is of greatest relevance to this work.

Tf is an iron-binding protein that transports free iron in biological fluids. Iron-loaded Tf (holo-Tf) has high binding affinity for TfR (K_D = 15 nM). In most cells, once Tf binds to TfR, the protein-receptor complex is internalized via clathrin-mediated endocytosis. A drop in pH within the endosome causes a conformational shift in Tf, leading to iron release from holo-Tf and disassociation of apo-Tf (Tf without any bound Fe, K_D > 700 nM) from TfR. The endocytic vesicle is recycled back to the plasma membrane where apo-Tf is released back to the extracellular fluid to find more iron (Fig 1.4) (31).

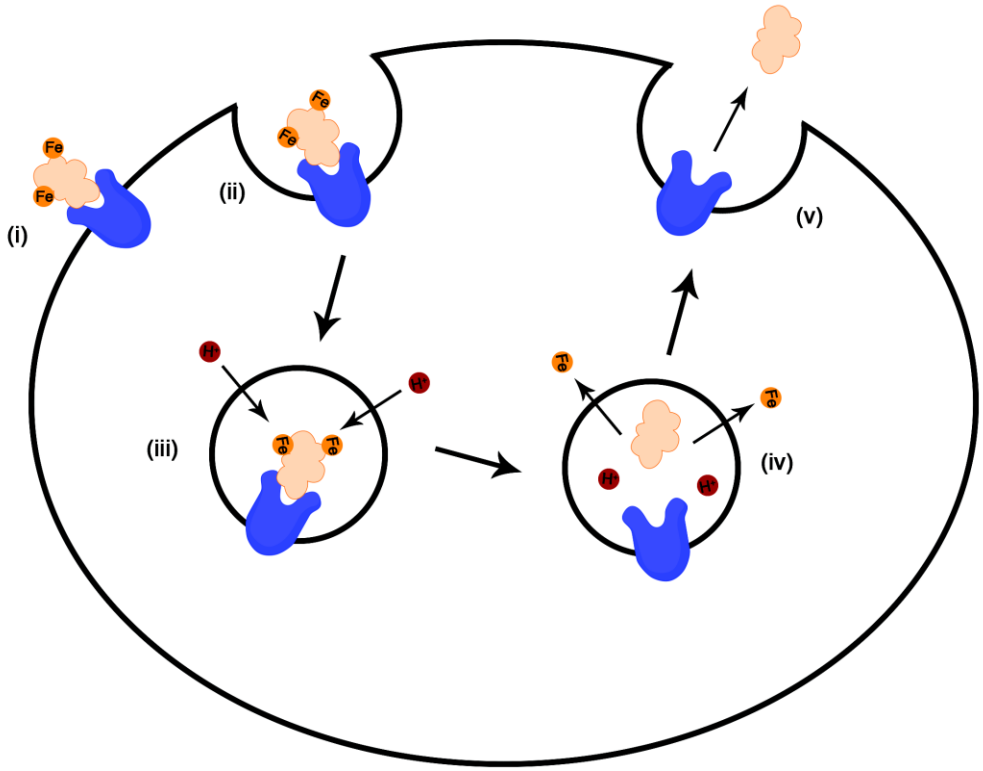

Fig 1.4. The transferrin cycle in apolar cells. (i) Holo-Tf binds TfR on the plasma membrane. (ii) Binding induces endocytosis of the Tf-TfR complex. (iii) Protons are actively pumped into the endosome, reducing the pH to ~5.5. (iv) Acidification of the endosome causes a conformational change in Tf, leading to release of bound iron and detachment from TfR, (v) The vesicle is recycled back to the cell surface, releasing iron-free Tf (apo-Tf) back to the extracellular space.

In BBB endothelium, however, Tf is transcytosed across the cells, allowing it to enter the CNS (discussed in detail in Section 2.1). TfR is a useful target for drug delivery because it is highly expressed on BBB endothelium and not saturated by endogenous Tf as seen in other tissues (32,33) presenting available binding sites for targeted therapies. TfR is similarly upregulated in many different forms of cancer and Tf has been used successfully as a targeting molecule for an siRNA-containing nanoparticle in clinical trials (34).

Anti-TfR antibodies have been primarily investigated as transcytosis ligands because of their specificity for TfR, high binding affinity and ability to induce endocytosis by binding a different epitope on TfR than native Tf (30). In the early 90's, a mAb against the rat TfR (OX26) was first found to cross the BBB and enter the CNS (25). Subsequent work focused on the development of antibody-drug conjugates (ADC's) where one to several drug molecules are conjugated to the Fc region of the antibody. Anti-TfR ADC's containing therapies for stroke (35-37), Huntington's disease (38), and AD (39) have been developed and investigated in animal models.

Despite the wide variety of experimental anti-TfR RMT therapies developed, there is yet to emerge a viable clinical candidate using this technique. A major reason for this failure is the very low numbers of antibodies that reach the CNS from systemic injection. For example, only 0.44% of injected OX26 antibody is within the rat brain after 24 hours (25). Similar results have been found with Tf-containing liposomes (40,41) and nanoparticles (19,42,43). In BBB endothelium, there is some debate over the extent of transcytosis versus endocytic recycling of Tf. Experiments in mice using radioactively labeled holo-Tf to measure accumulation in the brain found increased brain Fe content relative to injected Tf, suggesting endocytic recycling was the primary pathway taken by Tf (44,45). However, other investigations in animals using radioactivity and electron microscopy have shown successful transcytosis of Tf into the brain, indicating at least some portion of internalized holo-Tf undergoes transcytosis into the CNS (46,47). Furthermore, successful delivery of Tf-containing agents to the brain (29,42,48,49) reinforces the potential of Tf RMT as a pathway for drug delivery to the CNS.

In 2011, a group from Genentech first began to uncover the mechanism preventing accumulation of large numbers of anti-TfR mAb's in the CNS. High-affinity antibodies allow the ADC to bind TfR and initiate uptake into the BBB endothelium from the blood, but these strong interactions prevent the therapeutic from releasing into the CNS. By preparing an anti-TfR antibody with reduced affinity for TfR and dosing at therapeutic quantities, the authors were able to show increased parenchymal penetration of the low-affinity antibody relative to a high-affinity one. The authors proposed that high-affinity antibodies induce transcytosis but remain bound to the TfR once the transcytosis vesicle fuses to the brain side of the

endothelium and cannot penetrate the CNS. The low-affinity antibody, however, was able to undergo transcytosis due to its high serum concentration but could also disassociate from TfR once on the brain side because of its reduced affinity to TfR (Fig 1.5). With this approach they were able to deliver nearly 1% of the injected low-affinity antibody to the CNS, an amount deemed therapeutically useful (50); however, in order to obtain this amount of CNS penetration, extraordinarily high quantities of antibody were needed systemically, likely leading to significant side effects.

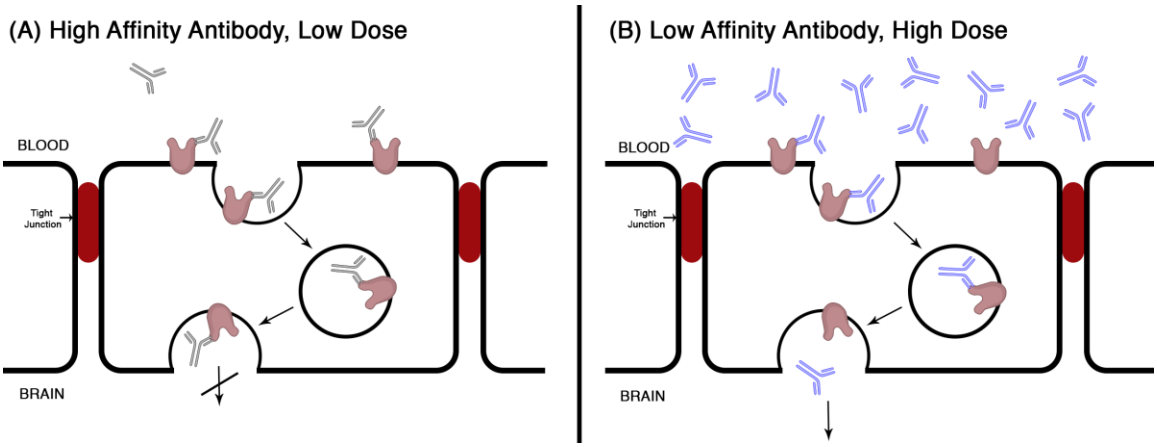

Fig 1.5 (A) High affinity anti-TfR antibodies are restricted from entering the CNS by the BBB endothelium but (B) low affinity ones can cross if given at very high systemic doses.

A different group from Roche proposed an alternative model for ligand processing within the BBB endothelium that may explain this limited transcytosis. They prepared antibodies against brain β-amyloid and engineered a Fab fragment to TfR onto one or both of the C-termini of the IgG heavy chain. This facilitated either monovalent binding or divalent binding to TfR. They found the divalent construct trafficked to the lysosome within an in vitro BBB model and was unable to undergo transcytosis (51) (Fig 1.6). Their results suggest TfR binding mode—not affinity—affects intracellular sorting and therefore transcytosis capacity.

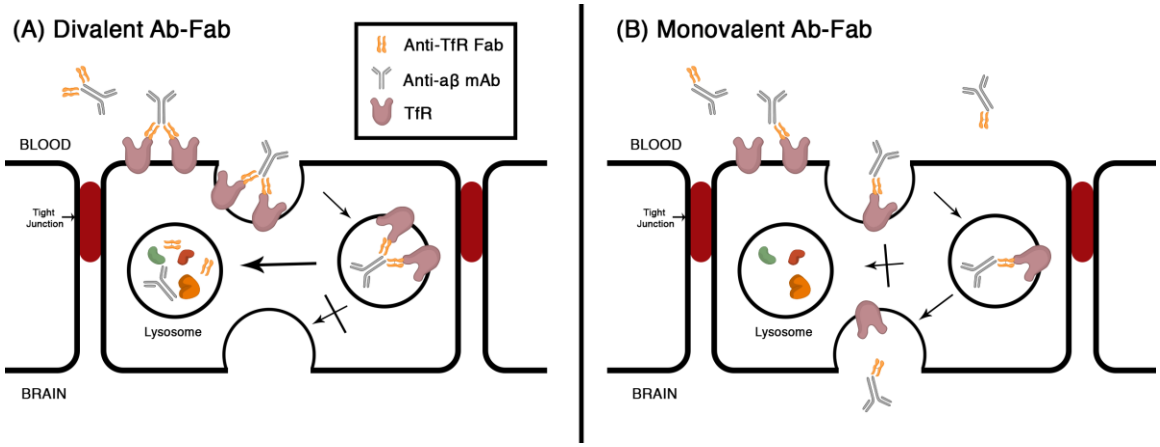

Fig 1.6 Divalent anti-TfR Fab's are sent to the lysosome while monovalent ones successfully enter the CNS. ADC's were synthesized containing either one or two anti-TfR Fab's conjugated to an anti-aβ mAb to shuttle the therapeutic antibody across the BBB. (A) The divalent conjugate was believed to form dimers with TfR that promoted trafficking to the lysosome and inhibited uptake in the brain. (B) The monovalent variant did not experience the same accumulation within the lysosome and was capable of reaching the CNS.

Follow-up work from the Genentech group showed that their high affinity antibody was similarly trafficking to the lysosome both in vitro and in vivo. They also found that exposure to high-affinity anti-TfR antibodies led to downregulation of TfR expression by brain endothelium (52). This finding was critical to recognizing the influence of high affinity mAb's on iron homeostasis in the CNS and the limitations of their use in conditions where multiple doses would be necessary.

Taken together, these results suggest sequestration to the lysosome may be the limiting factor in delivery of TfR-targeted antibody therapeutics to the CNS parenchyma. Understanding how individual ligands are processed at the BBB is critical to promoting transcytosis of therapeutics and avoiding dead-end or non-productive pathways (Fig 1.7).

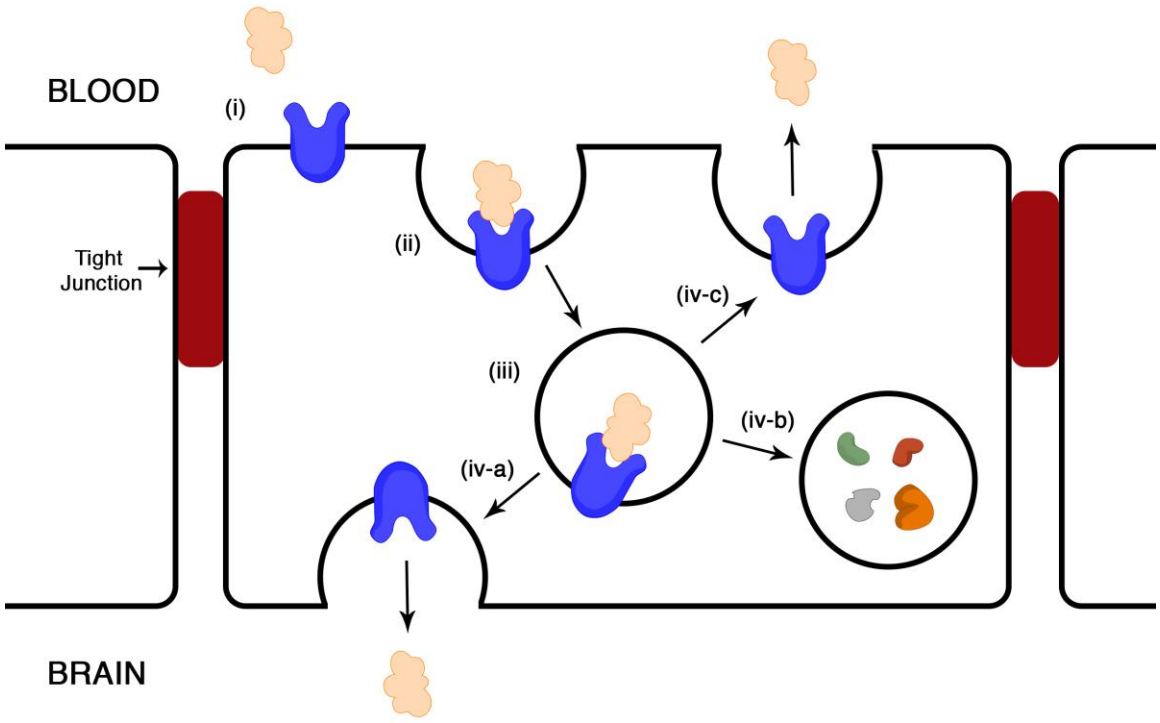

Fig 1.7 Potential pathways within the BBB endothelial cells for TfR targeted therapies. (i) The targeted therapeutic binds TfR from the blood and (ii) is internalized through endocytosis. (iii) Once internalized, the vesicle can be sent to one of three different pathways: (iv-a) transcytosed into the CNS, (iv-b) degraded within the lysosome, or (iv-c) recycled back to the apical cell surface. Ensuring therapies preferentially undergo (iv-a) is critical to developing effective targeted therapies that cross the BBB.

1.4.2 Targeted Nanoparticles and Their Applications in Drug Delivery

Nanoparticles are colloidal particles with diameters ranging from 1-100nm. Nanoparticle therapeutics have garnered tremendous interest in the biomedical community over the last three decades due to the extensive advantages they offer for drug delivery. Most notably, nanoparticle therapeutics can (i) be loaded with large quantities of a drug compared to ligand-drug conjugates (10^3-10^4 times more); (ii) improve the pharmacologic profile of a drug without changing the structure of the drug; (iii) accumulate within a specific biological site, thereby decreasing side effects of the drug while introducing no new side effects; (iv)

release drugs at a tunable rate; and (v) deliver multiple therapeutic and/or imaging agents simultaneously (53). Moreover, nanoparticle therapeutics have proven clinical efficacy, with several formulations receiving FDA approval for use in humans and over 250 products in preclinical or clinical development (54).

Affinity ligands, including antibodies (55,56), proteins (29), and peptides (57,58), can easily be added to the surface of nanoparticles. The targeting ligand allows the nanoparticle to bind antigens on the plasma membranes of cells, facilitating specific interaction and internalization via endocytosis (53). By incorporating ligands to receptors that are overexpressed in diseased tissues, nanoparticles can reach these tissues in greater numbers. Also, targeted nanoparticles have proven more efficacious than non-targeted equivalents due to their ability to be retained by diseased cells and release drug within this population (59,60). Targeted nanoparticles have garnered much attention due to their superior pharmacokinetics and improved therapeutic indices compared to passive nanoparticles. Several candidates are in varying stages of clinical trials (53).

1.4.3 Transferrin Receptor-Targeted Nanoparticles at the Blood-Brain Barrier

Many different experimental targeted nanoparticles have been investigated for drug delivery across the BBB with widely varying results (61,62,63). One of the major issues in assessing the ability of nanoparticles to reach the CNS parenchyma is the difficulty in measuring nanoparticle deposition within different compartments of the brain in vivo. Furthermore, the BBB can easily be disrupted depending on the disease investigated (64, 65), experimental model used in vivo (66), and the characteristics of the nanoparticles used, particularly if the nanoparticles are highly-negatively or positively charged (67).

These difficulties are further complicated in the case of TfR-targeted nanoparticles where a significant portion may be retained within the endothelial cells. Distinguishing whether nanoparticles are within the CNS parenchyma proper or stuck in endothelial cells is paramount to measuring the their true capacity to cross the BBB.

Because of the uncertainty regarding targeted nanoparticle behavior at the BBB, the Davis lab began investigating how the fundamental aspects of nanoparticle design, namely

nanoparticle size, charge, and targeting ligand density, affected transcytosis capacity. We were also motivated by the interesting results regarding antibody affinity from the Genentech group and wanted to determine if similar effects occurred with TfR-targeted nanoparticles.

Wiley et al. prepared a series of gold nanoparticles of varying diameters, ranging from ~20-80nm, with increasing quantities of surface Tf. Zeta potentials of the nanoparticles were kept slightly anionic to near neutral by adding a dense polyethylene glycol (PEG) surface coating, which has been found to have no appreciable negative impact on BBB integrity (67). The authors found that, similar to anti-TfR antibodies, uptake of nanoparticles into the brain parenchyma was influenced by tuning the nanoparticle's avidity for TfR. Of the nanoparticles investigated, those with 80nm diameter and an intermediate avidity (0.89 nM K_D to TfR) had the best delivery to the brain. Similar sized nanoparticles with greater avidity to TfR were restricted from entering the brain and, in fact, associated with BBB endothelial cells in greater amounts compared to the lower avidity formulation, suggesting the nanoparticles were restricted from entering the CNS by these cells. The authors hypothesized that the numerous, multidentate interactions between the surface Tf of the high avidity formulations and TfR were preventing it from releasing from the transcytosis vesicle and into the CNS (Fig 1.8A). The lower avidity nanoparticles did not suffer from the same restriction, but are limited instead by their ability to outcompete endogenous Tf within the blood and induce transcytosis (Fig 1.8B) (29).

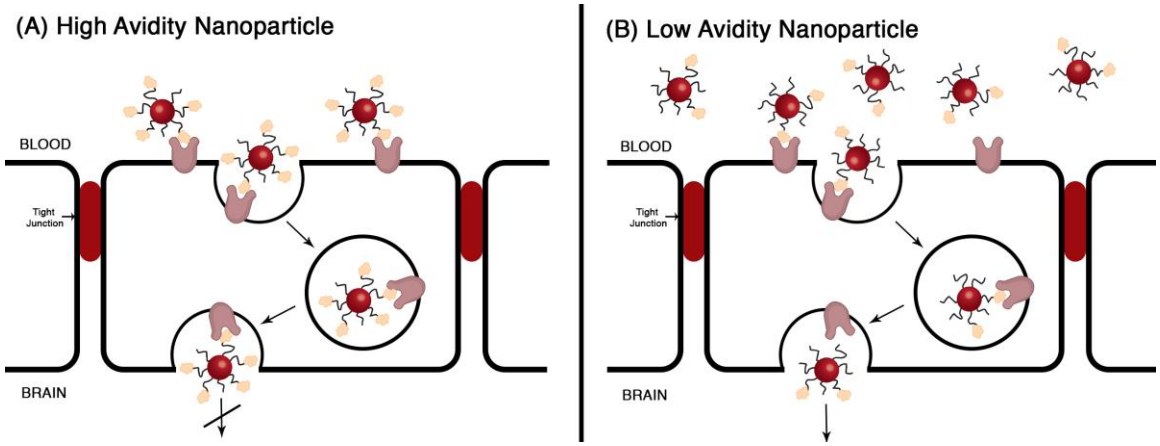

Fig 1.8 Tf-containing nanoparticles are subject to the same constraints as anti-TfR antibodies at the BBB; namely, (A) high avidity nanoparticles are restricted by BBB endothelium, but (B) low avidity ones can enter the CNS but only with high systemic dosing.

The same results regarding targeted nanoparticle avidity were found using nanoparticles targeted with angiopep-2, a peptide that induces transcytosis at the BBB by interacting with LRP1, suggesting binding avidity may be a critical component to the success of other RMT therapeutics at the BBB, not just transferrin (68).

Despite the limited transcytosis capacity, the high avidity, Tf-containing nanoparticles were not seen within lysosomes on TEM (29). In contrast, gold nanoparticles coated with the anti-TfR mAb 8D3 were found to accumulate within the lysosomes of BBB endothelial cells over time (69). These findings suggest that the native ligand may be superior in promoting transcytosis compared to mAb's.

1.5 Thesis Objectives and Organization

Results from Wiley et al. indicated that multidentate interactions between the surface Tf and TfR were preventing nanoparticles from entering the CNS. The goal of this work was to determine whether attaching the TfR-targeting ligand to the nanoparticle core via a link that would sever during transcytosis could overcome this problem and allow high avidity, Tf-containing nanoparticles to successfully cross the BBB (Fig 1.9). If successful, these high-avidity nanoparticles could then be investigated as potential drug delivery devices to the CNS.

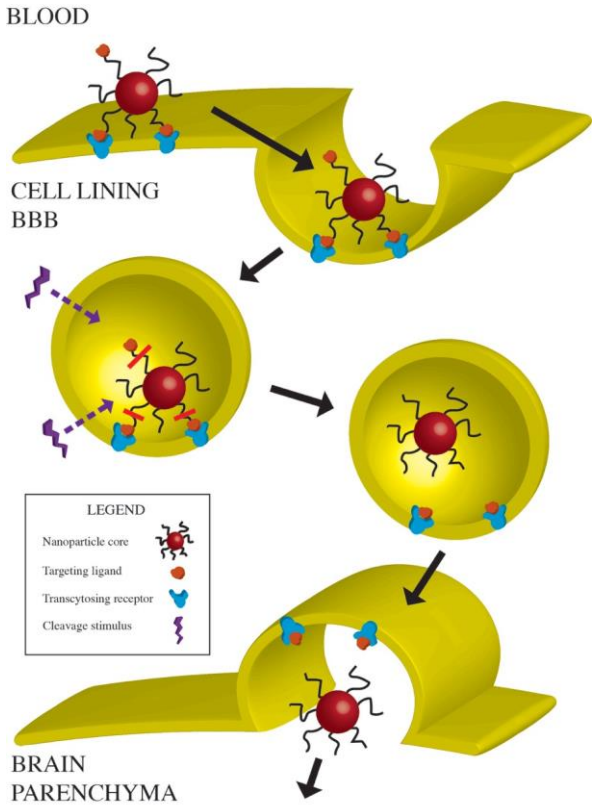

Fig 1.9 High avidity targeted nanoparticles containing Tf bound through a detachable link. The targeting ligand is bound to the nanoparticle core through a chemical link the breaks during transcytosis. High avidity nanoparticles are capable of readily engaging with TfR on the blood side of the BBB and inducing endocytosis, but a chemical stimulus experienced during transcytosis triggers separation of the targeting ligand from the nanoparticle surface, preventing inhibition of the nanoparticle within BBB endothelial cells.

First, polymeric nanoparticles were prepared containing Tf bound through a disulfide bond (Chapter II). A pilot in vivo study was performed to test the viability of this targeting method. Though the method showed promise, questions regarding the magnitude and mechanism of disulfide cleavage within the endosome and potential toxicity from exposing free thiols within tissues led us to consider alternative strategies.

Next, gold nanoparticles with Tf bound through an acid-cleavable link were investigated (Chapter III). By incorporating a small chemical link that breaks at mildly acidic pH between Tf and the nanoparticle core, high avidity nanoparticles were found to cross the BBB in greater amounts compared to those lacking the cleavable link. These nanoparticles were compared with high affinity anti-TfR containing nanoparticles, which showed no improvement in transcytosis when the acid-cleavable link was added.

Finally, polymeric nanoparticles loaded with dopamine (DA) were prepared as a potential therapeutic for Parkinson's disease and tested in vivo using an improved, acid-cleavable linker strategy (Chapter IV). The nanoparticles with Tf bound through chemistry that instantaneously disassociates at mildly acidic pH showed a higher than expected increase in brain DA content when given to healthy mice. This result suggests nanoparticles containing surface Tf that rapidly separates from the nanoparticle core under acidic conditions are able to cross the BBB in increased numbers and deliver therapeutically useful levels of drug to the CNS.

1.6 References

1. National Center for Health Statistics. (2012). 75 Years of Mortality in the United States, 1935–2010, 1–8.
2. National Center for Health Statistics. (2015). Health, United States, 2014 (5/2015), 1–473.
3. Association, A. (2013). 2013 Alzheimer's disease facts and figures. *Alzheimer's & Dementia*, *9*(2), 208–245.
4. Hurd, M. D., Martorell, P., Delavande, A., Mullen, K. J., & Langa, K. M. (2013). Monetary Costs of Dementia in the United States. *New England Journal of Medicine*, *368*(14), 1326–1334.
5. Wakler, F. O. (2007). Huntington's Disease. *The Lancet*, *369*, 218–228.
6. Driver, J. A., Logroscino, G., Gaziano, J. M., & Kurth, T. (2009). Incidence and remaining lifetime risk of Parkinson disease in advanced age. *Neuro-Oncology*, *72*, 432–438.
7. Ramagopalan, S. V., Dobson, R., Meier, U. C., & Giovannoni, G. (2010). Multiple sclerosis: risk factors, prodromes, and potential causal pathways. *The Lancet Neurology*, *9*(7), 727–739.
8. Cummings, J. L., Morstorf, T., & Zhong, K. (2014). Alzheimer's disease drug-development pipeline: few candidates, frequent failures. *Alzheimers Res Ther*. 6:37.
9. Abbott, N. J. (2013). Blood–brain barrier structure and function and the challenges for CNS drug delivery. *Journal of Inherited Metabolic Disease*, *36*(3), 437–449.
10. Abbott, N. J., Patabendige, A. A. K., Dolman, D. E. M., Yusof, S. R., & Begley, D. J. (2010). Structure and function of the blood–brain barrier. *Neurobiology of Disease*, *37*(1), 13–25.
11. Hervé, F., Ghinea, N., & Scherrmann, J.-M. (2008). CNS Delivery Via Adsorptive Transcytosis. *The AAPS Journal*, *10*(3), 455–472.
12. Watkins, S., Robel, S., Kimbrough, I. F., Robert, S. M., Ellis-Davies, G., & Sontheimer, H. (2014). Disruption of astrocyte-vascular coupling and the blood-brain barrier by invading glioma cells. *Nature Communications*, *5*, 4196.

13. Pardridge, W. M. (2004). The Blood-Brain Barrier: Bottleneck in Brain Drug Development. *NeuroRx: the Journal of the American Society for Experimental Neurotherapeutics*, *2*, 3–14.
14. Aryal, M., Arvanitis, C. D., Alexander, P. M., & McDannold, N. (2014). Ultrasound-mediated blood–brain barrier disruption for targeted drug delivery in the central nervous system. *Advanced Drug Delivery Reviews*, *72*(C), 94–109.
15. Tomita, T. (1991). Interstitial chemotherapy for brain tumors: review. *Journal of Neuro-Oncology*, *10*(1), 57–74.
16. Laxton, A. W., Stone, S., & Lozano, A. M. (2014). The neurosurgical treatment of Alzheimer's disease: a review. *Stereotactic and Functional Neurosurgery*, *92*(5), 269–281.
17. Raffa, R. B., & Pergolizzi, J. V., Jr. (2012). Intracerebroventricular opioids for intractable pain. *British Journal of Clinical Pharmacology*, *74*(1), 34–41.
18. Vogelbaum, M. A., & Aghi, M. K. (2015). Convection-enhanced delivery for the treatment of glioblastoma. *Neuro-Oncology*, *17 Suppl 2*(suppl 2), ii3–ii8.
19. Rapoport, S. I. (1970). Effect of concentrated solutions on blood-brain barrier. *Journal of Physiology, 219*(1), 270-274.
20. Rapoport, S.I. (2001) Advances in osmotic opening of the blood–brain barrier to enhance CNS chemotherapy. *Expert. Opin. Investig. Drugs, 10*, 1809–1818.
21. Focused Ultrasound Foundation. Blood-brain barrier opened non-invasively with focused ultrasound for the first time. http://goo.gl/e63tBj (Accessed 26 Mar 2016).
22. Begley, D. J. (2004). ABC transporters and the blood-brain barrier. *Current Pharmaceutical Design*, *10*(12), 1295–1312.
23. Wu, D., & Pardridge, W. M. (1996). Central nervous system pharmacologic effect in conscious rats after intravenous injection of a biotinylated vasoactive intestinal peptide analog coupled to a blood-brain barrier drug delivery system. *The Journal of Pharmacology and Experimental Therapeutics*, *279*(1), 77–83.
24. Lee, H. J., Zhang, Y., Zhu, C., Duff, K., & Pardridge, W. M. (2002). Imaging brain amyloid of Alzheimer disease in vivo in transgenic mice with an AB peptide radiopharmaceutical. *Journal of Cerebral Blood Flow and Metabolism*, *22*, 223–231.

25. Friden, P. M., Walus, L. R., Musso, G. F., Taylor, M. A., Malfroy, B., & Staryzk, R. M. (1991). Anti-transferrin receptor antibody and antibody-drug conjugates cross the blood-brain barrier. *Proceedings of the National Academy of Sciences*, *88*, 4771–4775.
26. Visser, C. C., Stevanović, S., Voorwinden, L. H., Bloois, L. V., Gaillard, P. J., Danhof, M., Crommelin, D. J. A., et al. (2005). Targeting liposomes with protein drugs to the blood–brain barrier in vitro. *European Journal of Pharmaceutical Sciences*, *25*(2-3), 299–305.
27. Schnyder, A., & Huwyler, J. (2004). Drug Transport to Brain with Targeted Liposomes. *NeuroRx: The Journal of the American Society for Experimental Neurotherapeutics*, *2*, 99–107.
28. Kreuter, J., Shamenkov, D., Petrov, V., Ramge, P., Cychutek, K., Koch-Brandt, C., & Alyautdin, R. (2002). Apolipoprotein-mediated Transport of Nanoparticle-bound Drugs Across the Blood-Brain Barrier. *Journal of Drug Targeting*, *10*(4), 317–325.
29. Wiley, D. T., Webster, P., Gale, A., & Davis, M. E. (2013). Transcytosis and brain uptake of transferrin-containing nanoparticles by tuning avidity to transferrin receptor. *Proceedings of the National Academy of Sciences*, *110*(21), 8662–8667.
30. Freskgård, P.-O., & Urich, E. (2016). Antibody therapies in CNS diseases. *Neuropharmacology*, 1–46. Advanced online publication. http://doi.org/10.1016/j.neuropharm.2016.03.014
31. Widera, A., Norouziyan, F., & Shen, W. C. (2003). Mechanisms of TfR-mediated transcytosis and sorting in epithelial cells and applications toward drug delivery. *Advanced Drug Delivery Reviews*, *55*(11), 1439–1466.
32. Jefferies, W. A., Brandon, M. R., Hunt, S. V., & Williams, A. F. (1984). Transferrin receptor on endothelium of brain capillaries. *Nature*, *312*(5990), 162–163.
33. Gatter, K. C., Brown, G., Trowbridge, I. S., Woolston, R. E., & Mason, D. Y. (1983). Transferrin receptors in human tissues: their distribution and possible clinical relevance. *Journal of Clinical Pathology*, *36*(5), 539–545.
34. Zuckerman, J. E., Gritli, I., Tolcher, A., Heidel, J. D., Lim, D., Morgan, R., et al. (2014). Correlating animal and human phase Ia/Ib clinical data with CALAA-01, a

targeted, polymer-based nanoparticle containing siRNA. *Proceedings of the National Academy of Sciences*, *111*(31), 11449–11454.

35. Zhang, Y. & Pardridge, W.M. (2006). Blood-brain barrier targeting of BDNF improves motor function in rats with middle cerebral artery occlusion. *Brain Research, 1111,* 227–229.
36. Lyons, M.K., Anderson, R.E., & Meyer, F.B. (1991) Basic fibroblast growth factor promotes in vivo cerebral angiogenesis in chronic forebrain ischemia. *Brain Research, 558,* 315–320.
37. Song, B.W., Vinters, H.V., Wu D.F., & Pardridge, WM. (2002). Enhanced neuroprotective effects of basic fibroblast growth factor in regional brain ischemia after conjugation to a blood-brain barrier delivery vector. *Journal of Pharmacology and Experimental Therapeutics, 301,* 605–610.
38. Kordower, J.H., Charles, V., Bayer, R., Bartus, R.T., Putney, S., Walus, L.R., & Friden, P.M. (1994). Intravenous administration of a transferrin receptor antibody nerve growth-factor conjugate prevents the degeneration of cholinergic striatal neurons in a model of Huntington disease. *Proceedings of the National Academy of Sciences USA, 91*, 9077–9080.
39. Lee, H.J., Zhang, Y., Zhu, C.N., Duff, K., & Pardridge, W.M. (2002). Imaging brain amyloid of Alzheimer disease in vivo in Transgenic mice with an A beta peptide radiopharmaceutical. *Journal of Cerebral Blood Flow and Metabolism, 22,* 223–231.
40. Zhang, P., Hu, L., Yin, Q., Zhang, Z., Feng, L., & Li, Y. (2012). Transferrin-conjugated polyphosphoester hybrid micelle loading paclitaxel for brain-targeting delivery: Synthesis, preparation and in vivo evaluation. *Journal of Controlled Release*, *159*(3), 429–434.
41. van Rooy, I., Mastrobattista, E., Storm, G., Hennink, W. E., & Schiffelers, R. M. (2011). Comparison of five different targeting ligands to enhance accumulation of liposomes into the brain. *Journal of Controlled Release*, *150*(1), 30–36.
42. Jones, A. R., & Shusta, E. V. (2007). Blood–Brain Barrier Transport of Therapeutics via Receptor-Mediation. *Pharmaceutical Research*, *24*(9), 1759–1771.
43. Wohlfart, S., Gelperina, S., & Kreuter, J. (2012). Transport of drugs across the blood–

brain barrier by nanoparticles. *Journal of Controlled Release*, *161*(2), 264–273.

44. Morgan, E. H., & Moos, T. (2002). Mechanism and Developmental Changes in Iron Transport across the Blood-Brain Barrier. *Developmental Neuroscience*, *24*(2-3), 106–113.
45. Crowe A., Morgan E. H. (1992). Iron and transferrin uptake by brain and cerebrospinal fluid in the rat. *Brain Research*, *24*, 8–16.
46. Broadwell, R. D., Baker-Cairns, B. J., Friden, P. M., Oliver, C., & Villegas, J. C. (1996). Transcytosis of Protein through the Mammalian Cerebral Epithelium and Endothelium. *Experimental Neurology*, *142*, 47–65.
47. Skarlatos, S., Yoshikawa, T., & Pardridge, W. M. (1995). Transport of [^{125}I]transferrin through the rat blood-brain barrier. *Brain Research*, *683*, 164–171.
48. Ulbrich, K., Hekmatara, T., Herbert, E., & Kreuter, J. (2009). Transferrin- and transferrin-receptor-antibody-modified nanoparticles enable drug delivery across the blood–brain barrier (BBB). *European Journal of Pharmaceutics and Biopharmaceutics*, *71*(2), 251–256.
49. Wohlfart, S., Gelperina, S., & Kreuter, J. (2012). Transport of drugs across the blood–brain barrier by nanoparticles. *Journal of Controlled Release*, *161*(2), 264–273.
50. Yu, Y. J., Zhang, Y., Kenrick, M., Hoyte, K., Luk, W., Lu, Y., Atwal, J., et al. (2011). Boosting Brain Uptake of a Therapeutic Antibody by Reducing Its Affinity for a Transcytosis Target. *Science Translational Medicine*, *3*(84), 84ra44–84ra44.
51. Niewoehner, J., Bohrmann, B., Collin, L., Urich, E., Sade, H., Maier, P., et al. (2014). NeuroResource. *Neuron*, *81*(1), 49–60.
52. Bien-Ly, N., Yu, Y. J., Bumbaca, D., Elstrott, J., Boswell, C. A., Zhang, Y., et al. (2014). Transferrin receptor (TfR) trafficking determines brain uptake of TfR antibody affinity variants. *Journal of Experimental Medicine*, *3*(84), 84ra43.
53. Kamaly, N., Xiao, Z., Valencia, P. M., Radovic-Moreno, A. F., & Farokhzad, O. C. (2012). Targeted polymeric therapeutic nanoparticles: design, development and clinical translation. *Chemical Society Reviews*, *41*(7), 2971.
54. J. Marshall, *Nature News,* 2011.

55. Han, H., & Davis, M. E. (2013). Targeted Nanoparticles Assembled via Complexation of Boronic-Acid-Containing Targeting Moieties to Diol-Containing Polymers. *Bioconjugate Chemistry*, *24*(4), 669–677.
56. Pridgen, E. M., Alexis, F., Kuo, T. T., Levy-Nissenbaum, E., Karnik, R., Blumberg, R. S., et al. (2013). Transepithelial transport of Fc-targeted nanoparticles by the neonatal fc receptor for oral delivery. *Science Translational Medicine*, *5*(213), 213ra167–213ra167.
57. Kamaly, N., Fredman, G., Subramanian, M., Gadde, S., Pesic, A., Cheung, L., et al. (2013). Development and in vivo efficacy of targeted polymeric inflammation-resolving nanoparticles. *Proceedings of the National Academy of Sciences*, *110*(16), 6506-6511.
58. Hrkach, J., Hoff, Von, D., Ali, M. M., Andrianova, E., Auer, J., Campbell, T., et al. (2012). Preclinical Development and Clinical Translation of a PSMA-Targeted Docetaxel Nanoparticle with a Differentiated Pharmacological Profile. *Science Translational Medicine*, *4*(128), 128ra39–128ra39.
59. Farokhzad, O. C., Cheng, J., Teply, B. A., Sherifi, I., Jon, S., Kantoff, P. W., et al. (2006). Targeted nanoparticle-aptamer bioconjugates for cancer chemotherapy in vivo. *Proceedings of the National Academy of Sciences of the United States of America*, *103*(16), 6315–6320.
60. Lammers, T., Hennink, W. E., & Storm, G. (2008). Tumour-targeted nanomedicines: principles and practice. *British Journal of Cancer*, *99*(3), 392–397.
61. Costantino, L., Gandolfi, F., Tosi, G., Rivasi, F., Vandelli, M. A., & Forni, F. (2005). Peptide-derivatized biodegradable nanoparticles able to cross the blood–brain barrier. *Journal of Controlled Release*, *108*(1), 84–96.
62. Bommana, M. M., Kirthivasan, B., & Squillante, E. (2012). In vivo brain microdialysis to evaluate FITC-dextran encapsulated immunopegylated nanoparticles. *Drug Delivery*, *19*(6), 298-306.
63. Loureiro, J. A., Gomes, B., Coelho, M. A., Carmo Pereira, M. D., & Rocha, S. (2014). Targeting nanoparticles across the blood–brain barrier with monoclonal antibodies. *Nanomedicine*, *9*(5), 709–722.

64. Cheng, Y., Dai, Q., Morshed, R. A., Fan, X., Wegscheid, M. L., Wainwright, D. A., et al. (2014). Blood-Brain Barrier Permeable Gold Nanoparticles: An Efficient Delivery Platform for Enhanced Malignant Glioma Therapy and Imaging. *Small*, *10*(24), 5137-5150.

65. Yonemori, K., Tsuta, K., Ono, M., Shimizu, C., Hirakawa, A., Hasegawa, T., et al. (2010). Disruption of the blood brain barrier by brain metastases of triple-negative and basal-type breast cancer but not HER2/neu-positive breast cancer. *Cancer*, *116*(2), 302–308.

66. Kodack, D. P., Chung, E., Yamashita, H., Incio, J., Duyverman, A. M. M. J., Song, Y., et al. (2012). Combined targeting of HER2 and VEGFR2 for effective treatment of HER2-amplified breast cancer brain metastases. *Proceedings of the National Academy of Sciences*, *109*(45), E3119–27.

67. Lockman, P. R., Koziara, J. M., Mumper, R. J., & Allen, D. D. (2004). Nanoparticle Surface Charges Alter Blood–Brain Barrier Integrity and Permeability. *Journal of Drug Targeting*, *12*(9-10), 635–641.

68. Gao, X., Qian, J., Zheng, S., Xiong, Y., Man, J., Cao, B., Wang, L., et al. (2013). Up-regulating Blood Brain Barrier Permeability of Nanoparticles via Multivalent Effect. *Pharmaceutical Research*, *30*(10), 2538–2548.

69. Cabezón, I., Manich, G., Martin-Venegas, R., Camins, A., Pelegrí, C., & Vilaplana, J. (2015). Trafficking of gold nanoparticles coated with the 8D3 anti-transferrin receptor antibody at the mouse blood-brain barrier. *Molecular Pharmaceutics*, *12*(11), 4137-4145.

Chapter II

INVESTIGATION OF POLY(LACTIC-CO-GLYCOLIC ACID) NANOPARTICLES CONTAINING TRANSFERRIN BOUND THROUGH A DISULFIDE LINK

2.1 Introduction

2.1.1 Chemical Changes Experienced During Transcytosis - Reduction

To prepare nanoparticles with targeting ligands capable of detaching during transcytosis, potential stimuli occurring during this process first needed to be identified. As discussed in section 1.6, in most cells, holo-Tf is endocytosed, undergoes a conformational change to release bound iron, and then recycles back to the extracellular space. In polarized cells, such as the BBB endothlium, this process is slightly modified to allow Tf to enter the CNS. After endocytosis, intracellular machinery sorts the Tf-containing vesicle to undergo transcytosis, sending it across the cell and to the basal membrane (1,2).

Several chemical differences exist within the endosome compared to the extracellular space. The two most useful for a drug delivery device are (i) slight drop in pH and (ii) exposure to redox agents. Changes in pH will be discussed in section 3.1. Glutathoine (GSH) is the major non-protein redox agent in biological systems (3). In the extracellular space, GSH concentration is low, about 10 μM (4), producing a generally oxidizing environment outside the cell. Intracellularly, however, GSH concentration is in low mM concentrations with the ratio of GSH to its oxidized form (GSSG) at ~100:1. These two factors create a strongly reducing environment within mammalian cells. In the endocytosis pathway several membrane associated enzymes help reduce the vesicle contents. Protein disulfide isomerase (PDI) is a plasma membrane enzyme that reduces macromolecules within the early endosome through disulfide-thiol exchange. GSH is also present within the endosome to maintain the catalytic activity of this and other reducing enzymes (5). Though the exact mechanism by which molecules are reduced in the

endosome occurs is unclear, reduction of a disulfide-containing conjugate within endosomes has been observed. This finding was also important because it occurred in Tf-containing endosomes (6), suggesting it can be taken advantage of during Tf transcytosis.

2.1.2 Stimuli-Responsive Nanodevices

Stimuli-responsive nanomedicines are commonplace (7-9) including those in clinical trials (10). In general, therapeutics are designed to take advantage of physical and/or chemical changes the nanomedicine experiences at the site of action to trigger release of loaded drug. This is typically done by incorporating the appropriate stimuli-responsive chemistry into the backbone of the nanomedicine, causing it to destabilize or degrade once it reaches its desired destination (e.g. a malignant tumor) (11). With polymeric nanoparticles, the chemistry can be implemented either within the polymer chain itself (12-14) or at the point of attachment for polymers that stabilize the nanoparticle core under biological conditions (15-18).

Implementing stimuli-responsive chemistry to facilitate intact nanoparticle transit across cellular barriers has not been performed prior to this work. Because of the reducing potential within the endosome, the first cleavable chemistry investigated was disulfide bonds. Disulfides are easily synthesized, reversible, and commonplace in biological systems (5). These bonds have been implemented in many different nanoparticles, with the vast majority designed to destabilize the device once in the desired intracellular compartment (19-21).

2.1.3 Drug Delivery Using PLGA Nanoparticles

PLGA is an FDA-approved biodegradable co-polymer composed of lactic acid and glycolic acid (Fig 2.1). It is used in a wide variety of medical devices, including sutures, prosthetic devices, and implants (22). The polymer has received much attention from the drug delivery community due to its flexibility, versatility, and excellent biocompatibility. Depending on the synthesis method, PLGA can be formulated into nearly any shape (23) and loaded with either hydrophobic or hydrophilic small (22) and macromolecules (24),

including proteins and nucleic acids (25). PLGA nanoparticles can easily be prepared through simple methods at the desired diameter for BBB transcytosis (26). Targeting molecules can also be added to the surface of the PLGA nanoparticles after synthesis, allowing for controlled quantities of targeting ligand on the nanoparticle surface (27). PLGA nanoparticles are also resistant to degradation under mildly acidic conditions, suggesting the nanoparticles will remain intact within the acidic endosome (28).

The drug payload is encapsulated within the core of PLGA nanoparticles during synthesis. Under biological conditions, the esters comprising the PLGA polymer hydrolyze, slowly breaking apart the polymer (22). The rate of breakdown can be controlled by the ratio of lactic acid:glycolic acid in the co-polymer. The methyl group of lactic acid makes it more hydrophobic compared to glycolic acid, so co-polymers enriched in lactic acid break down more slowly (29). As the nanoparticle breaks down, water-filled pores form, allowing encapsulated molecules to exit the particle core through diffusion (30).

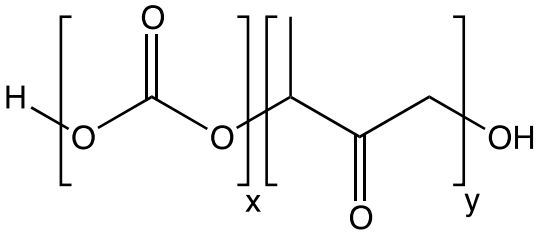

Fig 2.1 Chemical structure of carboxylic acid-terminated PLGA. X and Y refer to the molar ratio of glycolic to lactic acid, respectively.

2.1.4 PLGA-PEG Nanoparticles

Nanoparticles are cleared from circulation primarily through the reticuloendothelial system (RES). Opsonin proteins in the bloodstream bind foreign objects triggering their phagocytosis by macrophages, especially within the liver and spleen (31). To reduce this opsonization process and improve circulation half-life, nanoparticles are routinely decorated with polyethylene glycol (PEG). PEG is a hydrophilic polymer of repeated ether

units that is highly biocompatible and FDA-approved for use in humans. The polymer is typically added to the surface of the nanoparticle to form a corona that inhibits serum protein binding. This, in effect, reduces nanoparticle clearance from the bloodstream by the RES (32).

PEG also provides steric stability to the nanoparticles in serum. Due to their high surface area to volume ratio and surface potentials, spherical nanoparticles are at risk of aggregating in solution (33). Surface PEG reduces nanoparticle aggregation by reducing van der Waals attractive forces and increasing the distance between adjacent particles. Addition of PEG also increases the solubility of the nanoparticle in aqueous solution (34). A final benefit of PEG addition relevant to this work is that nanoparticles under 100nm with a dense surface PEG coating are capable of diffusing through the extracellular space of brain tissue (35).

PEG can be conjugated to PLGA through simple chemistry to form a block co-polymer (36). Nearly all PLGA nanoparticles formulated for drug delivery are prepared in this manner (25).

2.2 Results and Discussion

2.2.1 Synthesis and Characterization of PLGA Nanoparticles

For optimal transcytosis across the BBB, nanoparticles around 70 nm in diameter and with near neutral zeta potential are necessary (37,38). For the reasons outlined in section 2.1.4, a block polymer of PLGA and PEG was initially synthesized. Carboxy-terminated PLGA (PLGA-COOH) was added to amine-terminated PEG (PEG-NH_2) through EDC/NHS chemistry in dichloromethane (DCM) (Scheme 2.1).

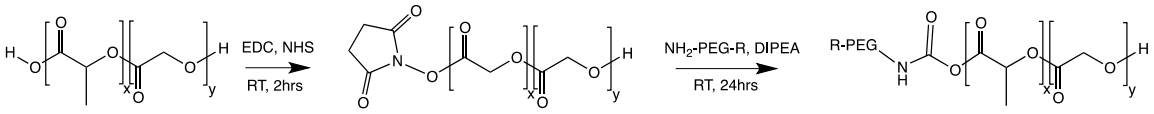

Scheme 2.1 Preparation of PLGA-PEG polymer. R = -OCH_3, -COOH, or –SH.

PLGA nanoparticles can be prepared with these design parameters using nanoprecipitation (26). In nanoprecipitation, PLGA is dissolved in a water-miscible solvent at a predetermined concentration. The PLGA is then added dropwise to water stirring at a high rate. Nanoparticles spontaneously form in the aqueous solution following addition. The organic solvent used, concentration of PLGA in that solvent, and stir rate control the size of the formed nanoparticles (36).

The relationship between starting PLGA concentration and nanoparticle size was initially investigated. Various organic solvents, including dimethylformamide (DMF), dimethylsulfoxide (DMSO), and acetonitrile (ACN), were used to dissolve prepared PLGA-PEG polymer. DMSO was found to be the only solvent capable of producing nanoparticles within the desired size range. Also, nanoparticle diameter could be controlled linearly depending on the initial polymer concentration in DMSO (Fig 2.2). PLGA nanoparticle size formed through nanoprecipitation was indirectly related to organic solvent miscibility in water so a highly miscible solvent like DMSO leads to much smaller nanoparticles compared to a less miscible one such as DCM.

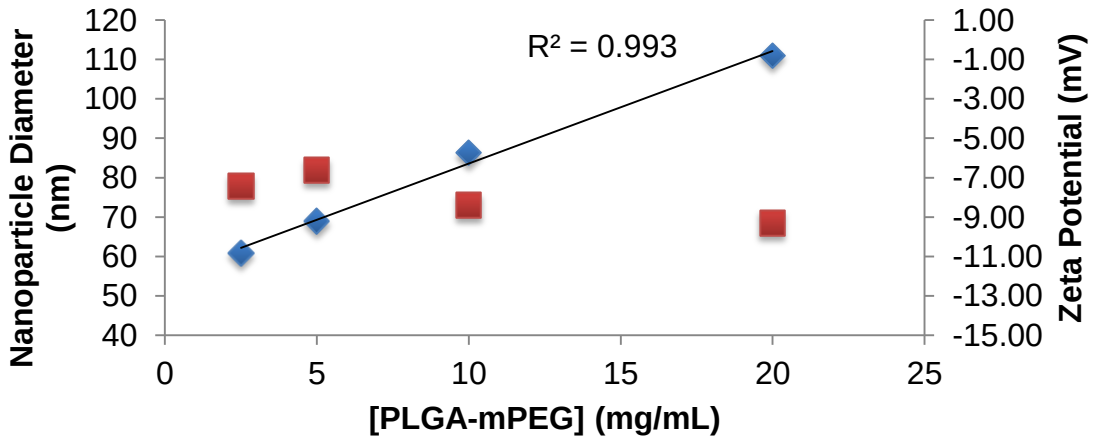

Fig 2.2 Effect of PLGA-mPEG polymer concentration in DMSO on nanoparticle diameter (blue diamonds) and zeta potential (red squares) formed through nanoprecipitation. Correlation coefficient and linear regression indicated for nanoparticle diameter is displayed.

To ensure the nanoparticle cores were stable under mildly acidic conditions experienced during endocytosis, 100 nm PLGA-mPEG nanoparticles were incubated in a pH 5 buffer solution at 37°C for 1 hour. Nanoparticle diameter was monitored during that period by dynamic light scattering (DLS) (Fig 2.3). Evidence of nanoparticle instability appears either as significant increase in nanoparticle diameter indicating aggregation or loss in detected scattering signal indicating breakdown of nanoparticles into non-scattering polymer components. The PLGA-mPEG nanoparticles showed no significant change in size or signal intensity at pH 5 over 60 minutes, demonstrating their stability under the conditions and timecourse of transcytosis.

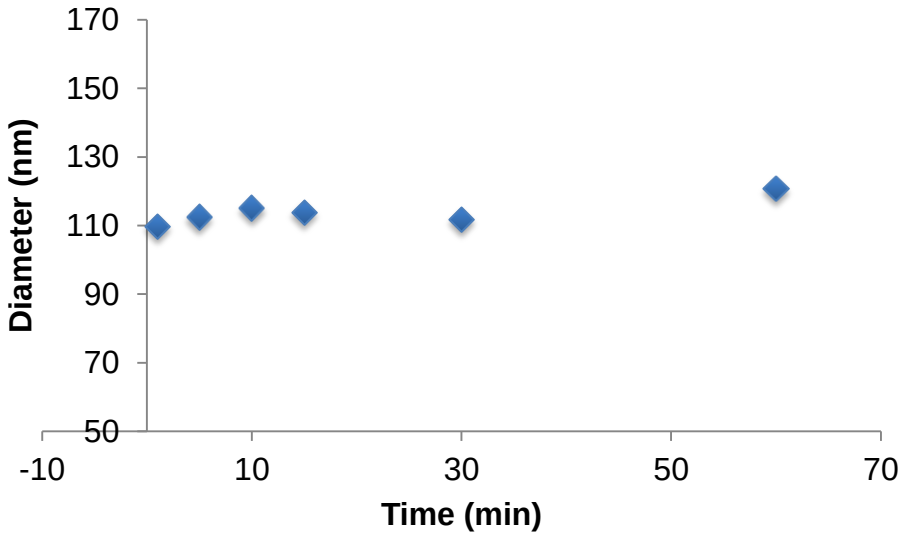

Fig 2.3 Nanoparticle diameter during 60 minute incubation at endosomal pH.

2.2.2 Investigation of an Anti-TfR Peptide as Potential Targeting Agent

With stable nanoparticles of the proper diameter and surface charge prepared, an anti-TfR peptide reported to undergo transcytosis at the BBB (39) was investigated as a potential targeting agent. Peptide targeting agents are considered superior to whole proteins and antibodies due to their small size, low immunogenicity, and facile synthesis (40). Peptides are also stable in organic solvents—unlike proteins and antibodies—allowing them to be conjugated to nanoparticle parent polymers prior to particle formation, allowing finer control of nanoparticle targeting ligand content.

The peptide THR (sequence THRPPMWSPVWP) was found to bind specifically to human TfR with a K_D of 15 nM using a phage display library (39). This binding affinity is similar to Tf itself (11.3 nM) (41) but multiple peptides can be added to a single nanoparticle to significantly increase binding avidity (40). More importantly, 13 nm gold nanoparticles decorated with surface THR were found to cross an in vitro model of the BBB, suggesting the peptide may be capable of undergoing transcytosis at the BBB in vivo.

The possibility of incorporating THR into the PLGA-PEG nanoparticle design was intriguing due to the synthesis flexibility peptides provide compared to protein ligands. Before this was attempted, however, the binding affinity of THR to TfR needed to be validated. A cysteine (Cys) -terminated THR peptide was acquired to introduce a thiol group that could be used to form disulfide bonds. The peptide was first labeled at the Cys residue with a fluorescent tag to provide readout for receptor binding assays (THR-AF488). Peptide binding to TfR was determined using K562 cells, a line known to express human TfR in high amounts (42). Increasing concentrations of fluorescently labeled THR was added to fixed K562 cells and the amount of fluorescence associated with the cells was measured using single-channel flow cytometry (Fig 2.4).

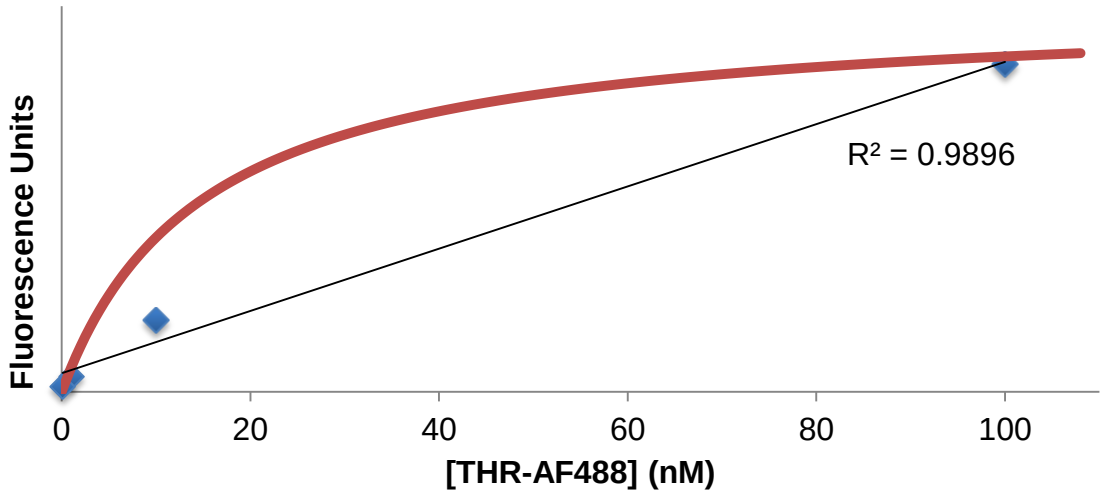

Fig 2.4 THR-AF488 binding to K562 cells. The solid red line indicates the theoretical Langmuir binding isotherm for a ligand with a K_D = 15 nM. Blue diamonds indicate the collected data points. Correlation coefficient and linear regression are shown for the bound THR-AF488 data.

The amount of fluorescence bound to the K562 cells was linearly related to the concentration of THR-AF488 suggesting no specific binding between the peptide and cells was occurring. To ensure the adjacent fluorescent tag was not interrupting with peptide binding capacity, a large PEG was instead conjugated to the Cys residue (THR-PEG) and the binding assay was repeated. Bound peptide was determined by adding a fluorescent anti-PEG antibody to the cell-peptide mixture after washing to detect any cell-associated PEG (Fig 2.5). A similar result was found using immunofluorescence with virtually no fluorescence associated with the K562 cells.

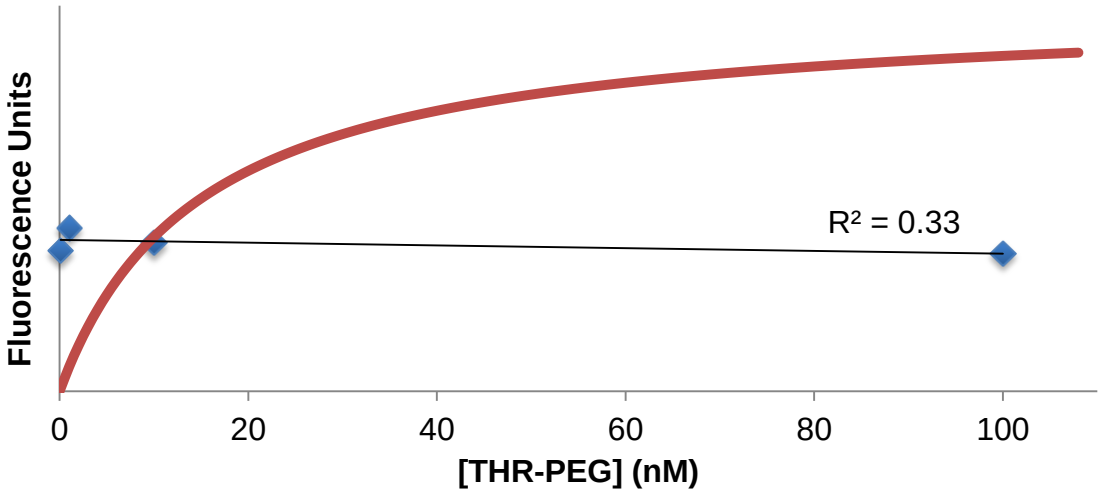

Fig 2.5 THR-PEG bound to K562 cells using immunofluorescence. The solid red line indicates the theoretical Langmuir binding isotherm for a ligand with a K_D = 15 nM. Blue diamonds indicate the collected data points. Correlation coefficient and linear regression are shown for the bound THR-PEG data.

A final measurement using non-labeled THR to compete with THR-AF488 was performed. A constant concentration of THR-AF488 was combined with increasing concentrations of non-labeled THR in the presence of K562 cells. Though a small amount of fluorescence remained associated with the cells at low concentrations of non-labeled peptide, this amount was not significantly greater than background fluorescence (Fig 2.6).

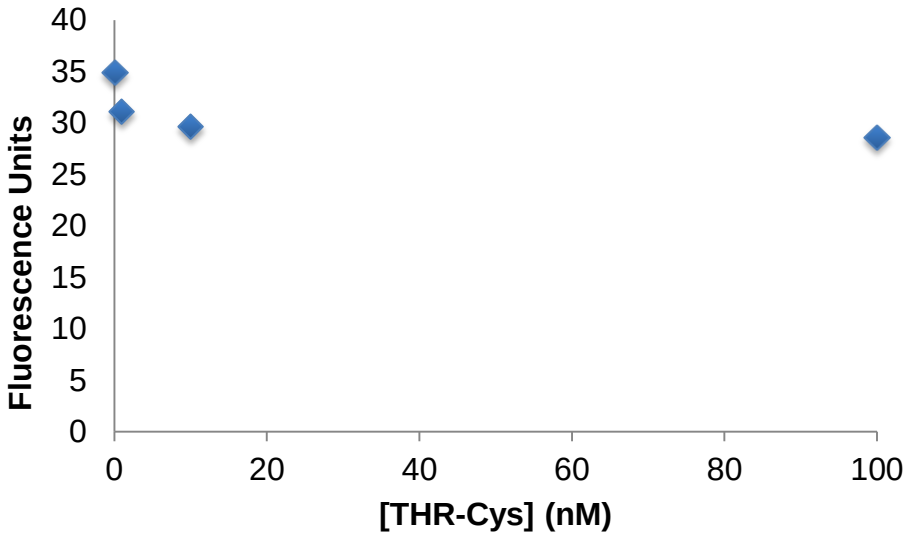

Fig 2.6 Cell-associated fluorescence from bound THR-AF488 in presence of increasing concentrations of non-labeled THR.

Taken together these results indicated the modified THR peptide had limited affinity to human TfR, rendering it a poor option as a targeting agent. The native peptide's affinity for TfR has also been questioned in the literature as THR-labeled gold nanoparticles failed to associate with the CNS in greater numbers than non-targeted ones in vivo (43). The peptide was discovered using a phage library against a chicken embryo fibroblast line engineered to express human TfR (39). The same specific binding to TfR could not be found in human derived cell lines (44) suggesting the artificially expressed TfR was not equivalent to natively expressed human TfR. It is also possible that the addition of the terminal Cys residue or other modifications disrupted THR's ability to bind TfR on K562 cells though the evidence in literature strongly suggests even the native peptide itself has limited to no affinity to endogenously expressed human TfR.

2.2.3 Synthesis of Inter-PEG Disulfide

With the THR peptide failing to serve as a potential targeting ligand, focus shifted towards developing a method to add Tf to the nanoparticle surface through a disulfide bond.

As described in the previous section, to attach whole proteins to the surface of PLGA nanoparticles, the nanoparticles must first form in aqueous solution followed by addition of surface proteins.

There are two potential points for introducing the cleavable disulfide bond PLGA nanoparticles: (i) directly between the native protein and the rest of the nanoparticle or (ii) within the nanoparticle core such that the nanoparticle does not destabilize after it breaks. To form the disulfide between the nanoparticle core and the native protein, a free thiol would be introduced in Tf at a known residue, followed by addition to thiol-expressing PLGA nanoparticles (PLGA-PEG-SH). This approach, however, has kinetic, functional, and technical problems. Kinetically, the concentrations of surface Tf free thiols and PLGA thiols would be exceedingly low in solution, leading to slow reaction time. The harsh oxidizing conditions necessary to form the disulfides at a reasonable rate could also potentially disrupt Tf's structural integrity and, consequently, its ability to bind TfR. Finally, preparing PLGA-PEG-SH nanoparticles in aqueous solution is difficult as thiols on adjacent PLGA nanoparticles can easily form disulfides with one another, leading to rapid nanoparticle aggregation.

To counteract these limitations, the disulfide was placed within a single PEG strand that was bound to Tf. By doing this, the PLGA nanoparticles can react with Tf using fast and well-characterized chemistry without sacrificing nanoparticle core stability. Once the disulfide breaks, a PEG, albeit smaller in length, will remain attached to the PLGA core, preventing any significant change in nanoparticle steric stability. This approach of preparing cleavable PEG's has already been used successfully to prepare unique heterofunctional polymers (45).

Heterobifunctional, thiol-containing PEGs of different molecular weights were added together in DMF in the presence of hydrogen peroxide (H_2O_2) to promote formation of disulfides (Scheme 2.2). Unfortunately, this reaction is not specific for the desired heterobifunctional product. Crosslinking between same-sized PEG molecules was prominently observed using matrix-assisted laser desorption/ionization time-of-flight mass spectrometry (MALDI-TOF) (Fig 2.7). The reaction was also unable to reach completion over the measured timecourse as significant quantities of the parent PEG molecules

remained. An excess quantity of small molecule thiol (2-mercaptoethanol, BME) was added to undergo thiol-disulfide exchange with the products, regenerating the parent polymers and indicating the three products were indeed linked through disulfide bonds (Fig 2.8).

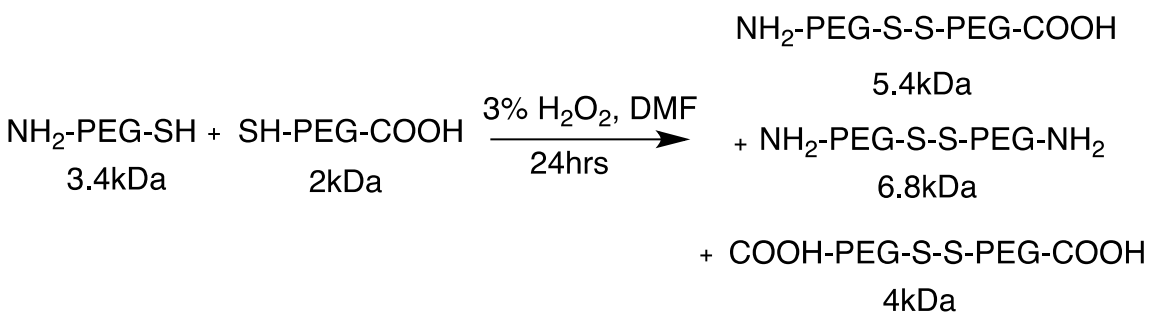

Scheme 2.2 Formation of disulfide bonds between two PEG molecules. Two thiol-terminated PEG molecules were reacted to form a heterobifunctional (5.4kDa), disulfide containing PEG. Homobifunctional side products (6.8kDa and 4kDa) were also formed.

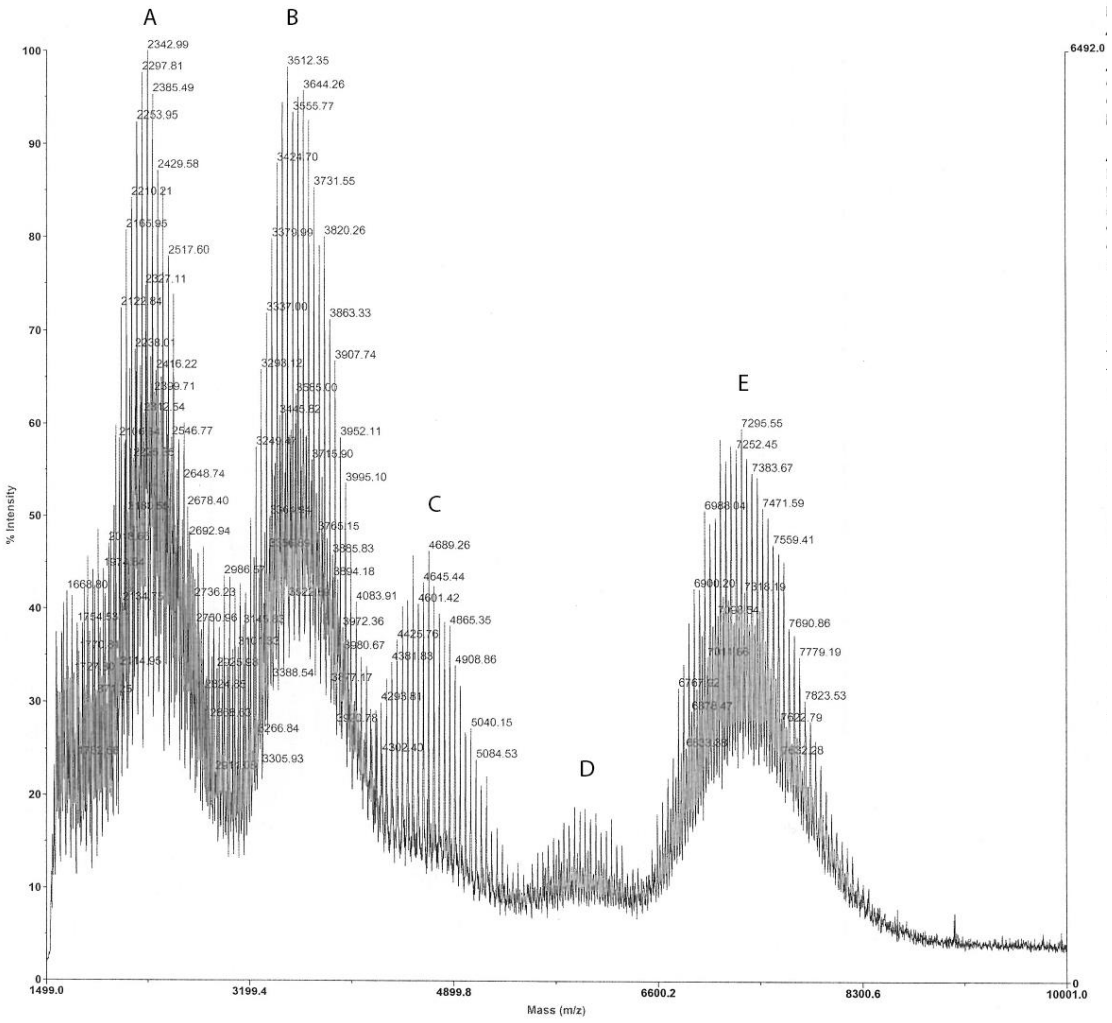

Fig 2.7 MALDI-TOF analysis of PEG coupling reaction. MALDI spectra of NH2-PEG-SH (3.4kDa) and COOH-PEG-SH (2kDa) reaction at 24hrs. Peaks A and B correspond to the reactants, COOH-PEG-SH and NH2-PEG-SH, respectively. Peaks C, D, and E correspond to the three potential products shown in Scheme 2.2, the 4kDa, 5.4kDa, and 6.8kDa polymers, respectively.

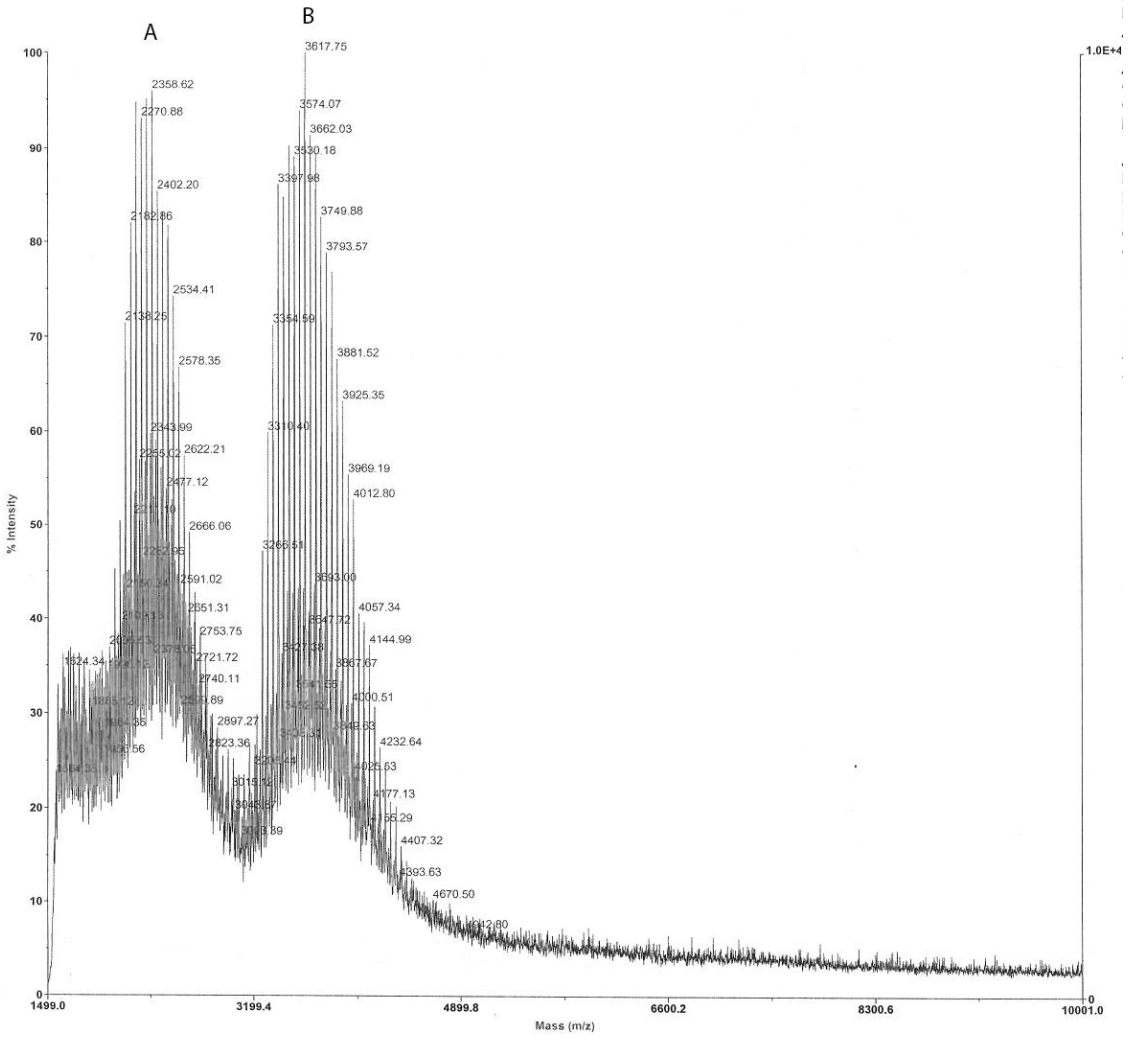

Fig 2.8 MALDI-TOF analysis of disulfide cleavage reaction. MALDI spectra of NH2-PEG-SH (3.4kDa) and COOH-PEG-SH (2kDa) reaction after addition of excess BME. Peaks A and B correspond to the parent polymers, COOH-PEG-SH and NH2-PEG-SH, respectively. There is no evidence of products from disulfide bond formation between PEG polymers due to thiol-disulfide exchange caused by the excess BME.

2.2.4 Preparation and Characterization of PLGA Nanoparticles Containing Surface Tf Bound Through a Disulfide Bond

To prepare PLGA nanoparticles containing an intra-PEG disulfide bond, thiol-terminated PLGA-PEG polymer (PLGA-PEG-SH) was prepared as shown in Scheme 2.1.

After the diblock-polymer was formed, a heterobifunctional PEG containing terminal thiol and carboxylic acid groups (SH-PEG-COOH) was added (Scheme 2.3). This particular polymer was chosen for its ability to form a disulfide bond with the PLGA-PEG block polymer while reintroducing a terminal carboxylic acid capable of reacting with Tf once the nanoparticle is assembled. By using a large molar excess of SH-PEG-COOH, disulfide cross-linking between adjacent PLGA-PEG-SH polymers was minimized. The cross-linked SH-PEG-COOH species could also be removed easily through size separation to yield the desired block co-polymer product.

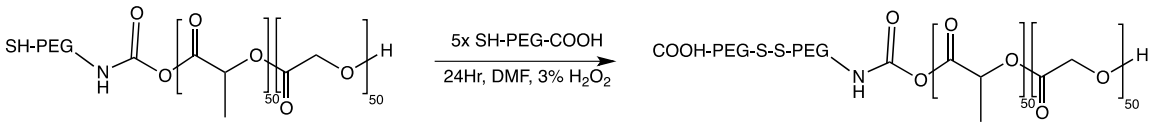

Scheme 2.3 Incorporation of intra-PEG disulfide bond to PLGA-PEG copolymer.

The PLGA nanoparticles were prepared by mixing the disulfide-containing polymer with non-functional polymer strands prior to nanoprecipitation. Mixing functional and non-functional PLGA-PEG polymers before nanoparticle formulation provides control over surface ligand density by controlling the number of reactive sites on the nanoparticle surface (26). In this design, varying the composition of these two polymers in the pre-formulation mixture will affect the carboxylic acid quantity expressed on the nanoparticle surface, controlling the number of available reactive sites for Tf.

A third component was also included in the polymer mixture to serve as a fluorescent reporter. A fluorescent dye molecule was conjugated to non-PEGylated PLGA polymer (PLGA-AF488) and a small percentage (2.5 wt%) of this polymer was included in the pre-formulation mixture. Including the fluorescently tagged PLGA polymer in this manner allows creation of highly fluorescent nanoparticles without affecting nanoparticle stability (46). Also, by conjugating the fluorophore to non-PEGylated PLGA, it is hidden within the surface PEG corona formed by the majority PLGA-PEG component of the nanoparticle. This prevents the fluorescent dye from interfering with surface protein addition or nanoparticle interactions once within biological systems.

Following nanoprecipitation, targeted nanoparticles were prepared by conjugating different quantities of Tf to the nanoparticle surface through EDC/NHS chemistry (Fig 2.12). Four different nanoparticle formulations were prepared: (i) non-targeted (PLGA-mPEG), (ii) low-Tf containing, (iii) high-Tf containing, and (iv) high-Tf bound through disulfide bond. The polymer composition of each formulation is shown in Table 2.1. Nanoparticle diameter and zeta potential were measured using DLS (Table 2.2). The nanoparticle hydrodynamic diameter did not vary significantly between non-targeted and non-cleavable Tf-containing formulations. The disulfide containing formulation was slightly larger, which is consistent with a larger PEG corona formed by the longer disulfide-containing PEG's. Zeta potentials were similar and near neutral for all formulations.

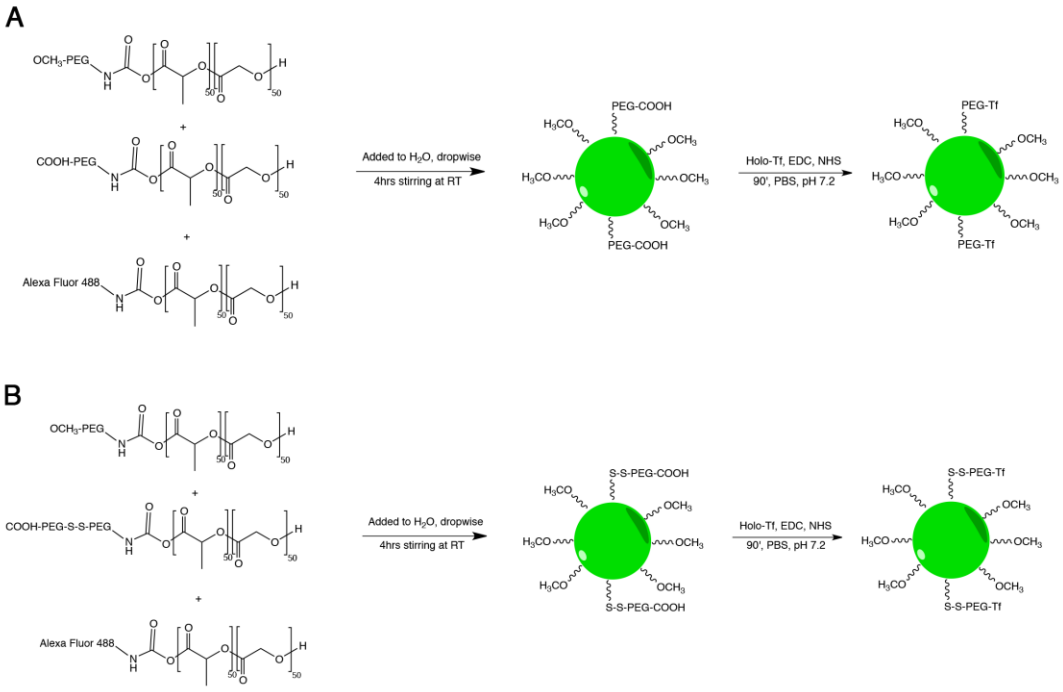

Scheme 2.4 Synthesis of Tf-labeled PLGA-PEG nanoparticles. Panel A shows the preparation of non-cleavable nanoparticles. Panel B shows the preparation of disulfide-containing nanoparticles. Each polymer mixture was prepared in DMF at a total PLGA concentration of 10mg/mL prior to formation of the nanoparticles through nanoprecipitation. The relative amounts of each polymer used to make the four different nanoparticle formulations are shown in Table 2.1. Each formulation contained 2.5% PLGA-AF488.

Formulation	% PLGA-mPEG	% PLGA-PEG-COOH	% PLGA-PEG-S-S-PEG-COOH
mPEG	100	0	0
Low Tf	90	10	0
High Tf	70	30	0
High Tf + S-S	70	0	30

Table 2.1 Polymer composition of PLGA-PEG nanoparticle formulations. Values shown are wt %.

Formulation	Diameter (nm)	Zeta potential (mV)
mPEG	56.6	-6.6 ± 2.6
Low-Tf	58.7	-5.8 ± 3.8
High-Tf	56.2	-8.5 ± 1.6
High-Tf + S-S	65.6	-5.9 ± 3.0

Table 2.2. Characterization of PLGA-PEG nanoparticles. Zeta potential values are given as the average value plus or minus one standard deviation

The binding avidity to TfR of the disulfide-containing formulation was measured before and after exposure to a reducing agent. Neuro2A cells that express TfR were incubated with varying concentrations of methoxy-terminated PLGA-PEG particles (PLGA-mPEG), disulfide-containing PLGA-PEG-Tf (PLGA-PEG-S-S-PEG-Tf), and disulfide containing PLGA-PEG-Tf after treatment with reducing agent, dithiothreitol (DTT). The binding curves of each of these formulations are presented in Fig. 2.9. The calculated K_D for the disulfide-containing formulation without exposure to DTT was 2.5 nM.

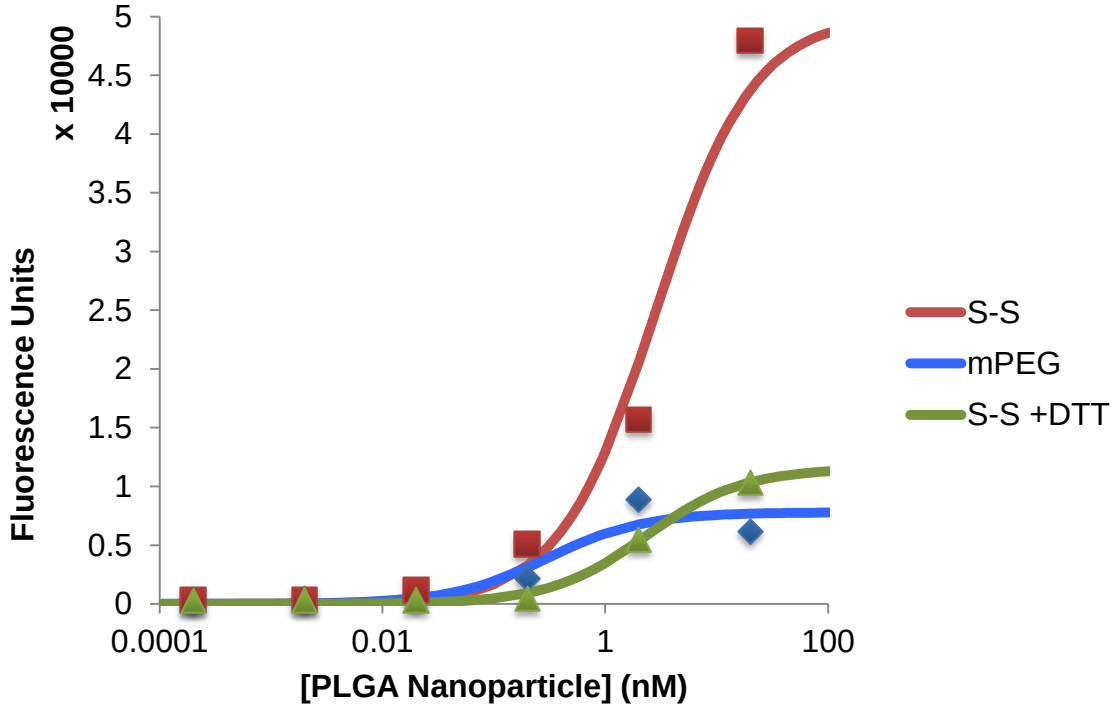

Fig 2.9 Disulfide-containing nanoparticle binding avidity to Neuro2A cells. Measured data points are indicated by squares, diamonds or triangles for the disulfide-containing PLGA-PEG-Tf nanoparticles (S-S), disulfide-containing PLGA-PEG-Tf nanoparticles after treatment with DTT (S-S +DTT), and methoxy-terminated PLGA-PEG nanoparticles (mPEG), respectively. The model curves for each formulation are based on the Langmuir binding isotherm.

The Tf targeted, disulfide-containing nanoparticles bind the most to Neuro2A cells and have the highest avidities for the TfRs. Cleavage of the disulfide bond by treatment with DTT and subsequent dissociation of Tf from the nanoparticle significantly lowers the nanoparticles' binding to the Neuro2A cells, seen by the decreased maximal fluorescence intensity (Fig. 2.13). Non-targeted (PLGA-mPEG) nanoparticles have essentially the same binding curves as the DTT-treated nanoparticles, which suggests that most of the binding by the DTT-treated particles is due to non-specific interaction of nanoparticles with the cell surface. These results demonstrate that the disulfide-containing nanoparticles bind with

high avidity to TfRs, but once Tf falls off the nanoparticles they bind non-specifically to the Neuro2A cells just as the non-targeted nanoparticles. This indicates that a disulfide bond is present between the Tf and PLGA nanoparticle core and when cleaved causes loss of the targeting ligand from the nanoparticle and subsequent loss of binding avidity for the targeting ligand's receptor.

2.2.5 In Vivo Investigation of PLGA Nanoparticles Containing Surface Tf Bound Through a Disulfide Bond

BALB/c mice were intravenously administered four PLGA nanoparticle formulations: (i) non-targeted nanoparticles (mPEG); (ii) low avidity nanoparticles (30 Tf per nanoparticle); (iii) high avidity nanoparticles (3000 Tf per nanoparticle); and (iv) a high avidity nanoparticle containing a disulfide linker between the targeting ligand and nanoparticle core (3000 Tf per nanoparticle + S-S). Thin tissues sections were prepared and imaged using fluorescence microscopy to identify the location of nanoparticles within the brain. Initially, this was performed using fresh-frozen tissue sections. Non-targeted nanoparticles showed little overall fluorescence with a few, large areas of signal likely indicating nanoparticles within vessels (Fig 2.10). The low Tf formulation showed greater overall fluorescence and small, diffuse punctate signal, suggesting they were from nanoparticles within the brain parenchyma (Fig 2.11). The high Tf formulation, in contrast, lacked these diffuse, punctate points (Fig 2.12). These results are consistent with previous reports that high avidity nanoparticles fail to enter the CNS (37,47). The disulfide-containing group showed staining pattern similar to the low Tf formulation, suggesting they were able to reach the parenchyma (Fig 2.13).

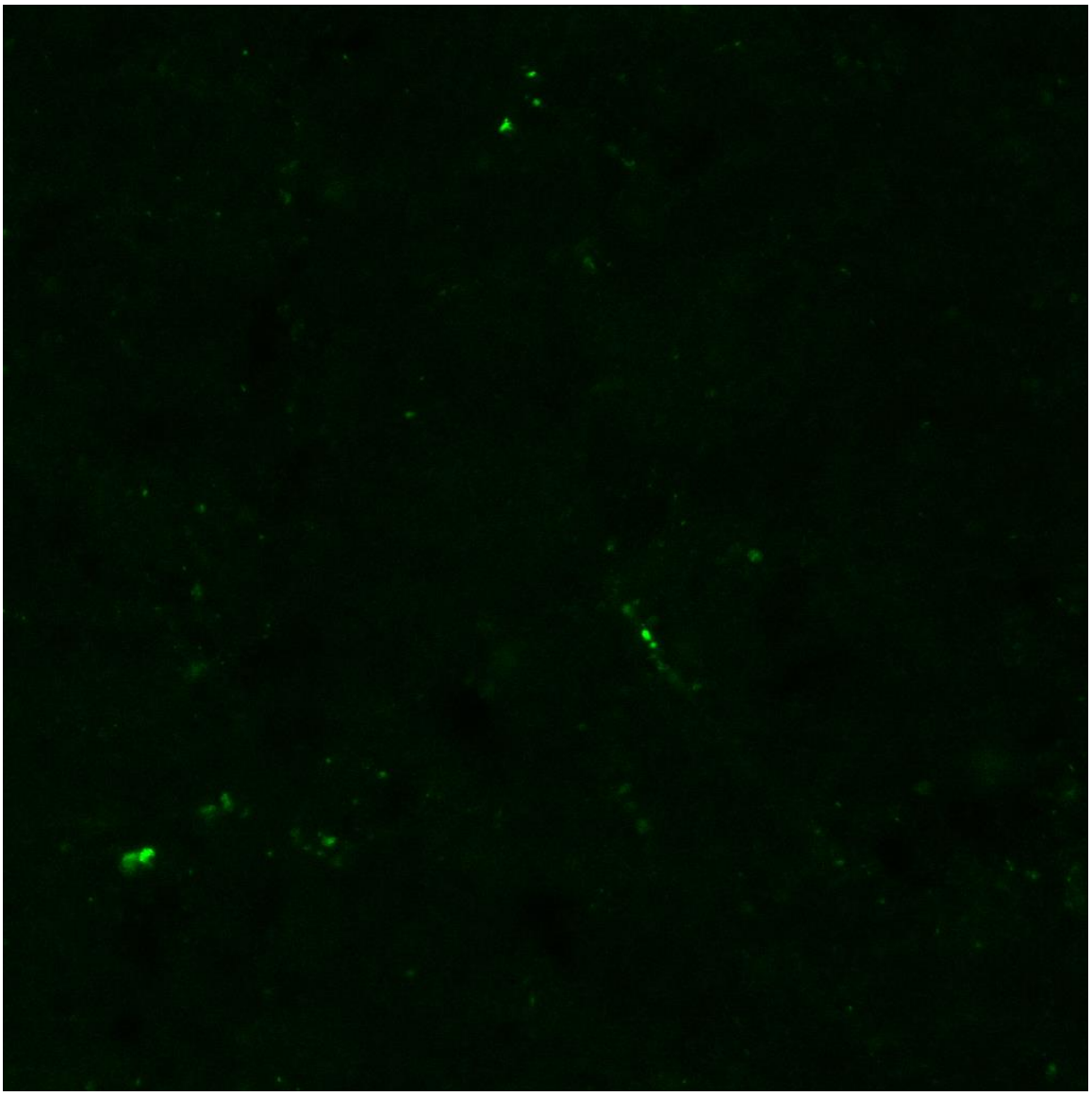

Fig 2.10 Fluorescent image of fresh-frozen brain section of mouse injected with non-targeted PLGA-PEG nanoparticles.

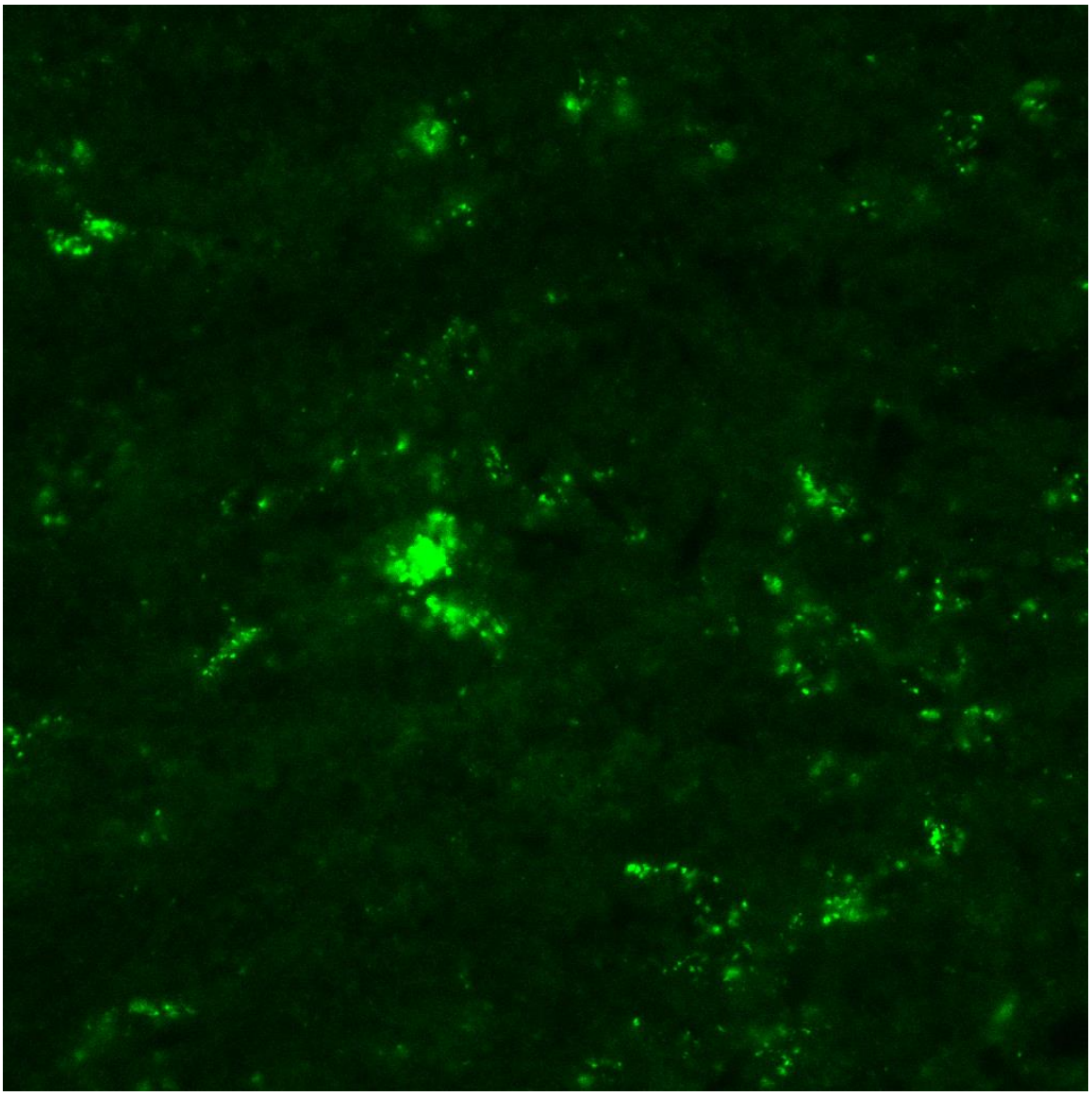

Fig 2.11 Fluorescent image of fresh-frozen brain section of mouse injected with low-Tf PLGA-PEG nanoparticles.

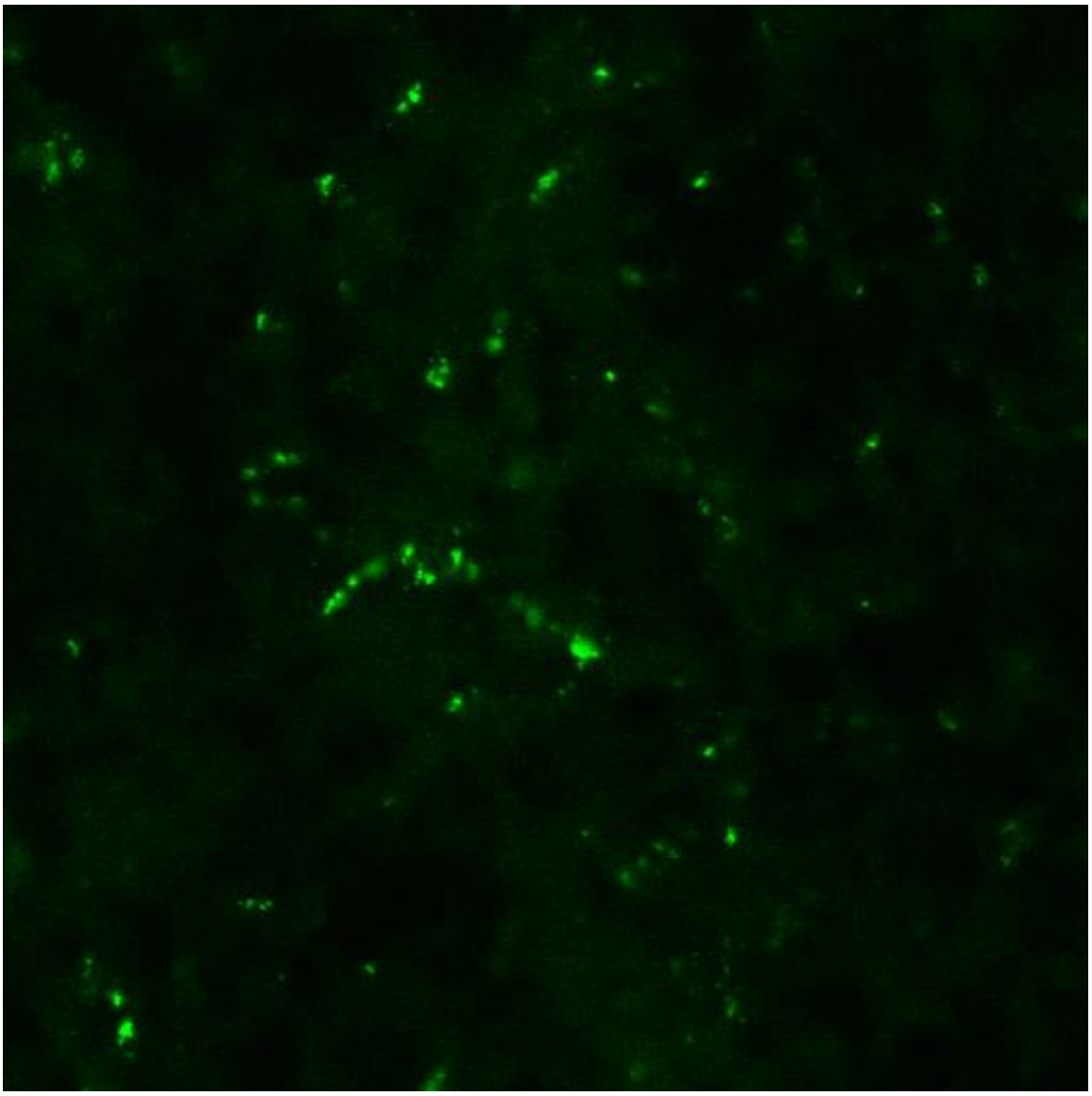

Fig 2.12 Fluorescent image of fresh-frozen brain section of mouse injected with high-Tf PLGA-PEG nanoparticles.

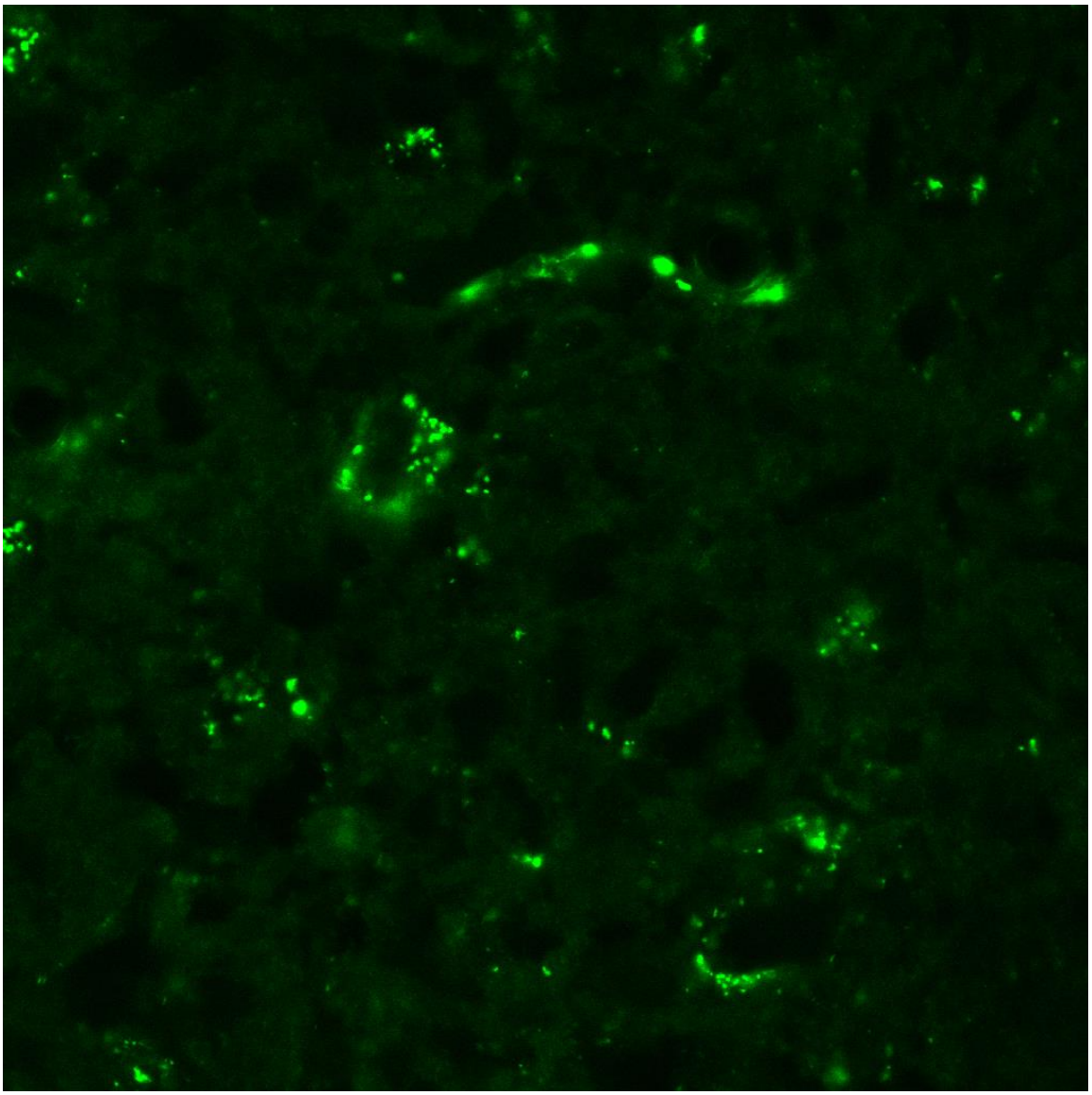

Fig 2.13 Fluorescent image of fresh-frozen brain section of mouse injected with high-Tf PLGA-PEG nanoparticles containing a disulfide link between Tf and the nanoparticle core.

Making conclusions using fresh-frozen sections, however, is limited due to the poorly preserved tissue architecture preventing definitive morphological identification of vessels, so the assay was repeated using formalin-fixed paraffin-embedded brain tissue sections. Figures 2.14-2.17 illustrate to what extent each nanoparticle formulation reaches the brain parenchyma using this method. Nanoparticles were positively identified as

distinct fluorescent signal above autofluorescence and clearly away from the blood vessels and in the parenchyma. Fluorescence associated with cell nuclei was seen in the negative controls and was therefore not considered to be specific to nanoparticles.

Untargeted PLGA-mPEG nanoparticles did not access the brain parenchyma and remained exclusively in the vasculature (Fig 2.14). Low-Tf PLGA-PEG nanoparticles were present in the parenchyma (Fig 2.15). High-Tf PLGA-PEG nanoparticles were not clearly seen in the brain parenchyma, with a similar fluorescent pattern to the PLGA-mPEG formulation (Fig 2.16). This is consistent with the necessity for the nanoparticles' avidity to be tuned for successful release into the brain parenchyma. High-Tf with disulfide nanoparticles showed the greatest amount of fluorescence within the brain parenchyma (Fig 2.17).

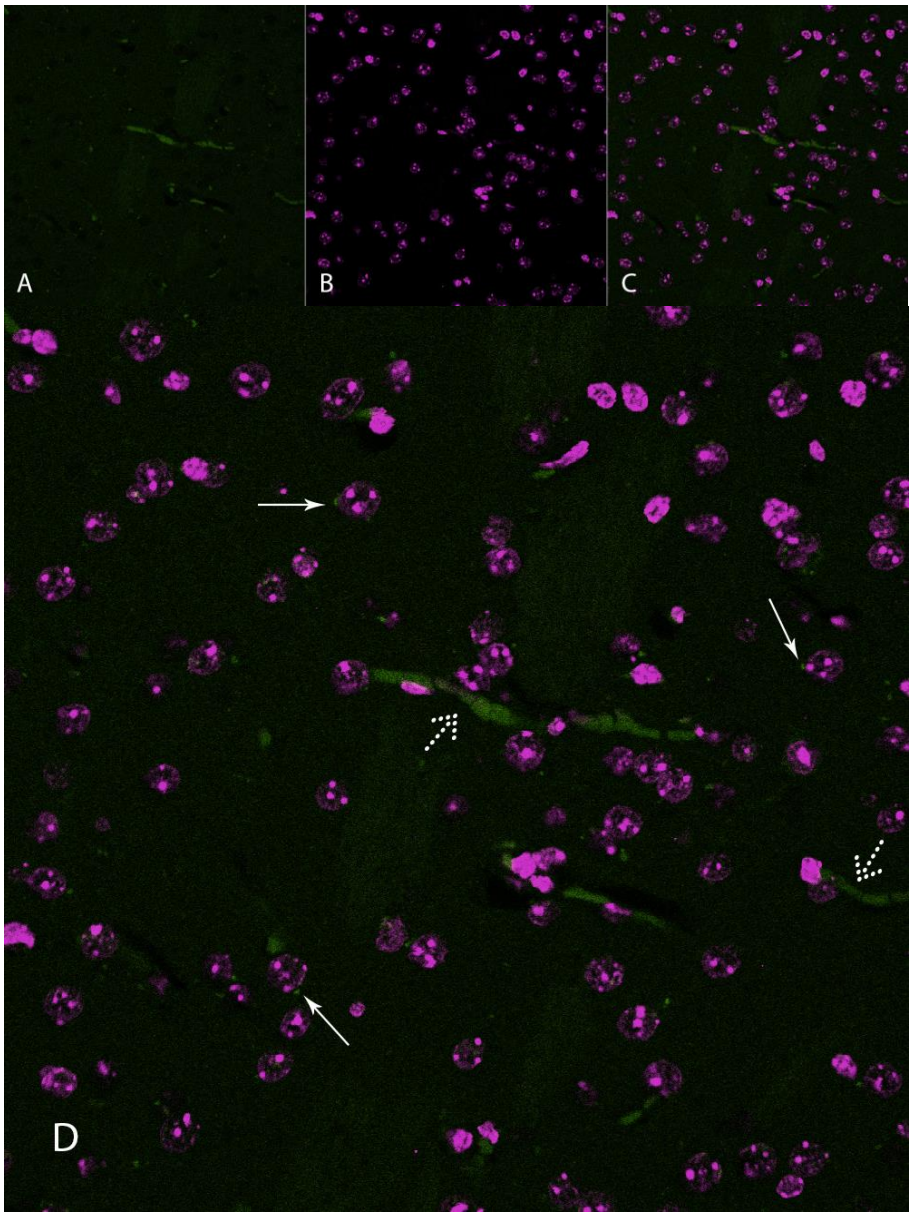

Fig 2.14 Confocal images of PLGA-mPEG nanoparticle in formalin-fixed mouse brain sections. Panel A: 488nm excitation, panel B: DAPI signal, panel C: merged image of Panels A and B. Panel D shows an enlarged view of the merged image in Panel C. Solid white arrows indicate fluoresecence co-localized with cell nuclei. Since this phenomenon was seen with non-targeted particles, it was considered normal tissue background fluorescence. Dotted white arrows indicate blood vessels.

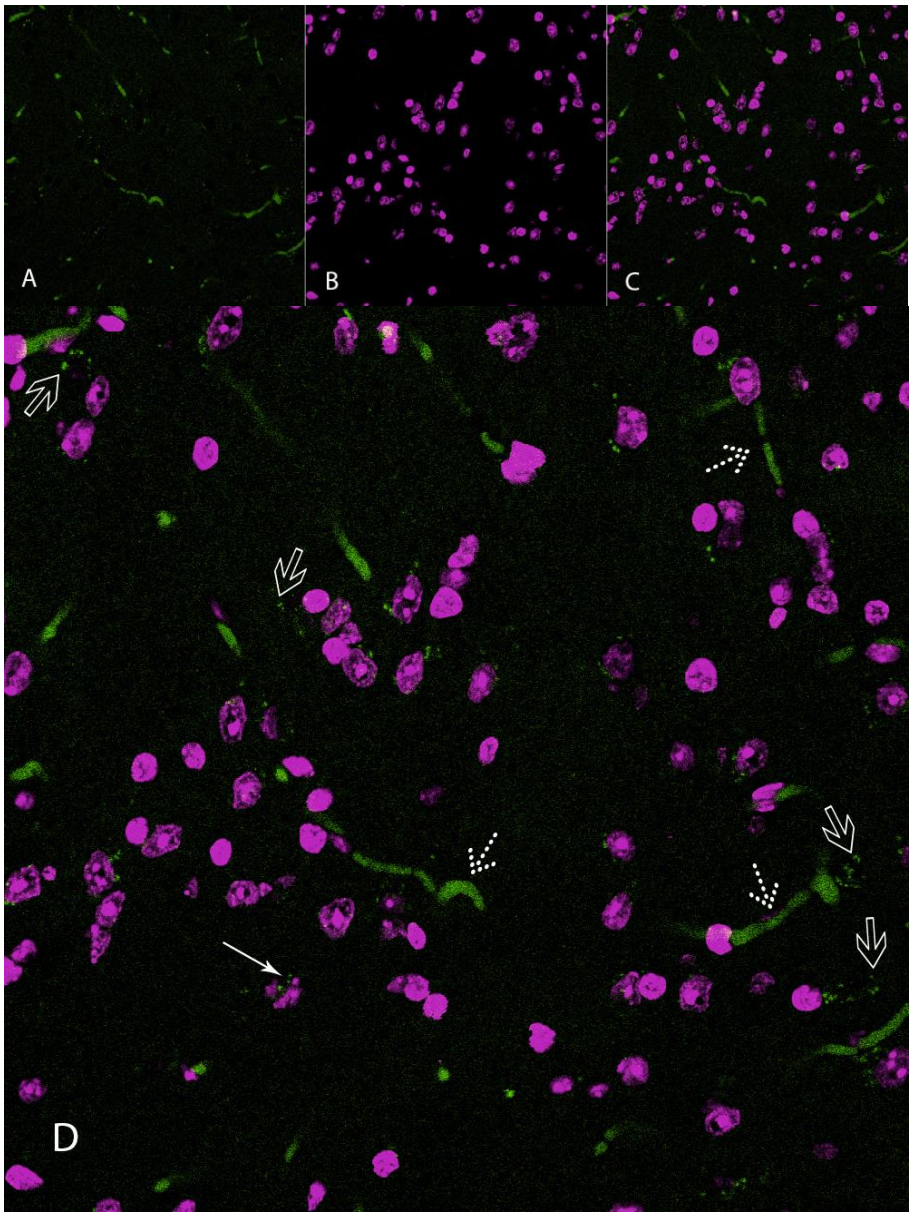

Fig 2.15 Confocal images of low-Tf PLGA-PEG nanoparticles in formalin-fixed mouse brain sections. Panel A shows fluorescence from 488nm excitation. Panel B shows the DAPI signal. Panel C shows a merged image of Panels A and B. Panel D shows an enlarged view of the merged image in Panel C. Solid white arrows indicate fluoresecence co-localized with cell nuclei. Dotted white arrows indicate blood vessels. Hollow white arrows indicate fluorescence in the parenchyma not associated with cell nuclei determined to be nanoparticle signal.

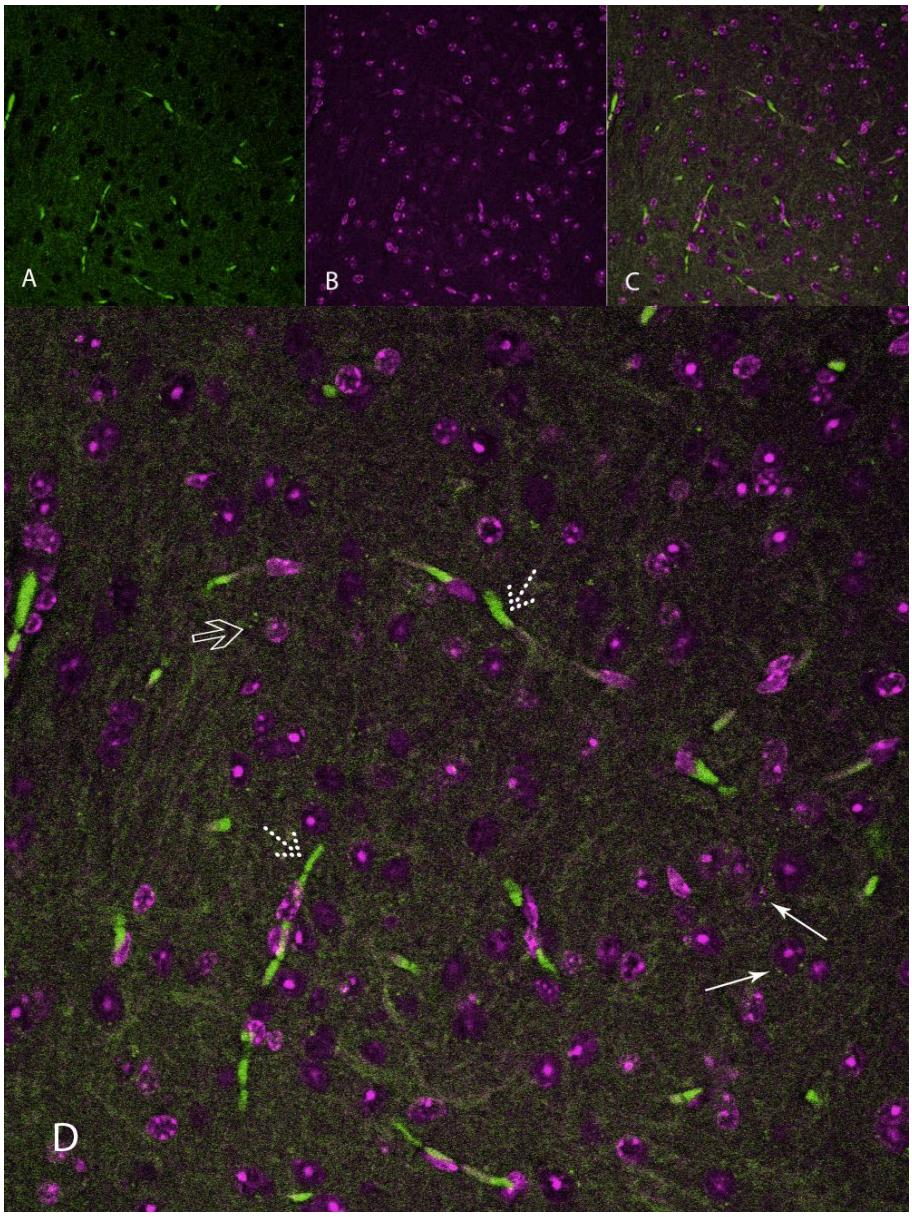

Fig 2.16 Confocal images of high-Tf PLGA-PEG nanoparticles in formalin-fixed mouse brain sections. Panel A shows fluorescence from 488nm excitation. Panel B shows the DAPI signal. Panel C shows a merged image of Panels A and B. Panel D shows an enlarged view of the merged image in Panel C. Solid white arrows indicate fluoresecence co-localized with cell nuclei. Dotted white arrows indicate blood vessels. Hollow white arrows indicate fluorescence in the parenchyma not associated with cell nuclei determined to be nanoparticle signal.

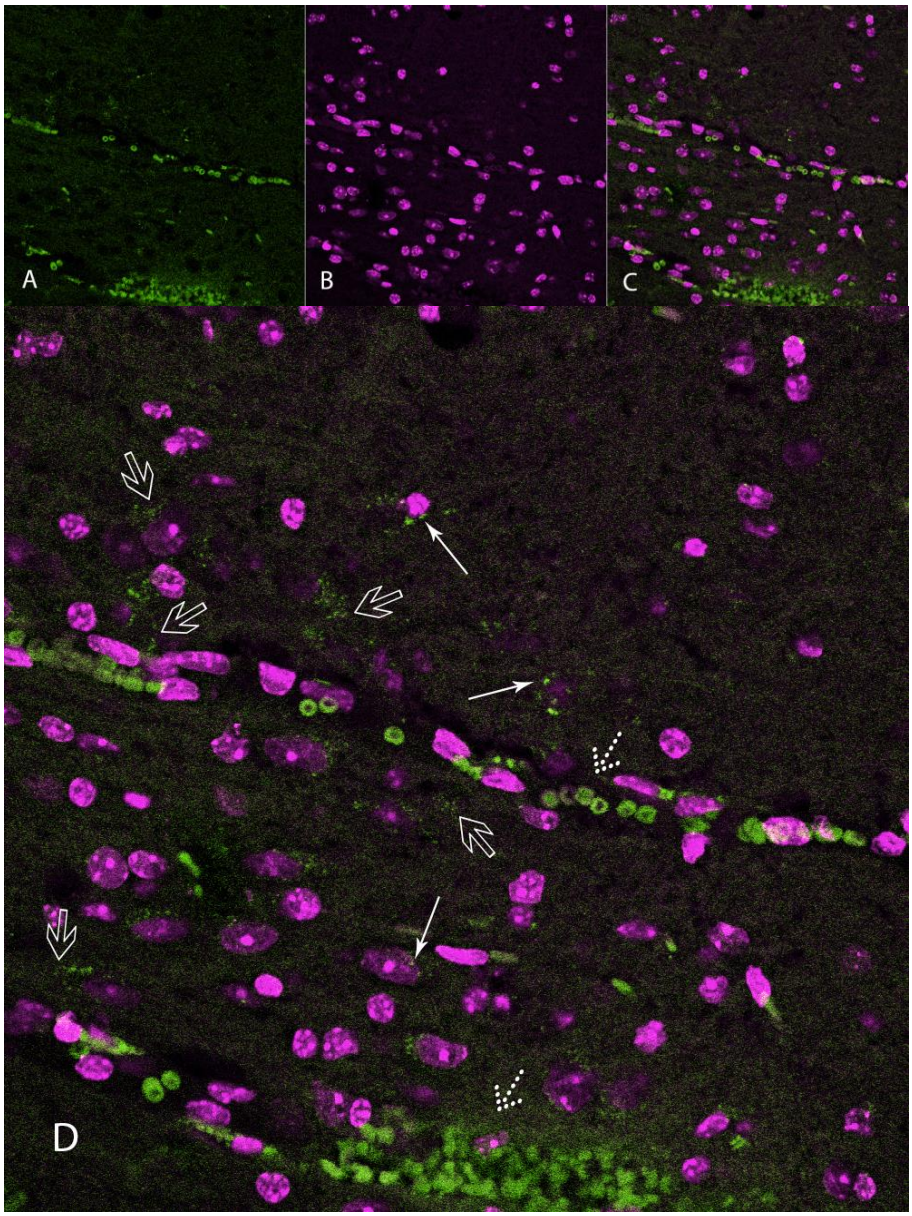

Fig 2.17 Confocal images of high-Tf plus disulfide PLGA-PEG nanoparticle in formalin-fixed mouse brain sections. Panel A shows fluorescence from 488nm excitation. Panel B shows the DAPI signal. Panel C shows a merged image of Panels A and B. Panel D shows an enlarged view of the merged image in Panel C. Solid white arrows indicate fluoresecence co-localized with cell nuclei. Dotted white arrows indicate blood vessels. Hollow white arrows indicate fluorescence in the parenchyma not associated with cell nuclei determined to be nanoparticle signal.

Recent work by Wiley et al. demonstrated that nanoparticle avidity to transcytosing receptors need to be tuned to deliver the nanoparticles into the brain parenchyma. In this work, nanoparticles of intermediate avidity were able to attach to receptors on the blood-side of the BBB and detach from the receptors on the brain side of the BBB. These optimally tuned nanoparticles reached the brain parenchyma; however, they did so in very small numbers (much less than 1% of the injected dose reached the brain parenchyma). Nanoparticles of high avidity accumulated more in the bulk of the brain mainly by remaining stuck to receptors in or on the endothelial cells of the BBB.

Here we demonstrate that nanoparticles whose targeting molecules are attached to the nanoparticle core through a disulfide bond can access the brain in greater numbers than nanoparticles with fixed targeting molecules. Nanoparticles of high avidity can associate with receptors in larger numbers, and these nanoparticles, when released from their targeting ligand while en route through the BBB, can accumulate more in the brain parenchyma.

Disulfide bonds inserted into PEG linkers between the nanoparticle and the targeting molecules can be cleaved by reducing agents including BME, DTT, and GSH. When nanoparticles of high avidity are injected, they do not appreciably enter the brain parenchyma. However, when nanoparticles of high avidity with the disulfide-based linker are injected, the nanoparticles access the brain parenchyma in much greater numbers. Nanoparticles of high avidity with disulfide linkers also access the brain parenchyma to a greater extent than nanoparticles of tuned avidity. Therefore nanoparticles with targeting molecules that fall off may be better able to deliver drugs to the brain than nanoparticles of tuned avidity.

2.3 Conclusions

Disulfide bonds are cleaved in biological systems through interactions with reducing agents such as GSH or cysteine or enzymes such as PID. In this work, targeted nanoparticles were prepared using PLGA polymer coupled to targeting molecule transferrin (Tf) through a PEG chemical spacer. A disulfide-bond was incorporated into

the PEG chemical spacer that allows the targeting molecules to come off the nanoparticles while en route across the BBB. This disulfide bond is cleaved by redox agents present in transcytosing vesicles, separating the targeting ligand from the nanoparticle core. Once the nanoparticle finishes its transit through the cell, it can diffuse, free of any interference from the targeting ligand interactions with its receptor, into the CNS tissue.

In-vitro studies using the disulfide-containing nanoparticles demonstrated reduced avidity to TfR in vitro after exposure to a reducing agent. In vivo investigations showed increased delivery of high avidity nanoparticles to the parenchyma when targeting molecules were attached through the disulfide bond suggesting the cleavable link strategy was able to overcome the avidity limitations of previous nanoparticle designs (37).

Despite these initial intriguing results, using disulfide bonds as the cleavable component in the nanoparticle design has several important constraints. First, the magnitude and mechanisms of reduction within the endosome are poorly characterized. Though reduction of a small molecule fluorescence resonance energy transfer (FRET) reporters was observed in Tf-containing endosomes (6), the opposite result was not seen with a much larger, antibody-based FRET reporter (48). In the latter case, a trastuzumab antibody was bound to a rhodamine molecule through a disulfide bond and used to measure endosomal reduction in a HER2 positive breast cancer cell line. The antibody failed to separate from the fluorescent probe once within the endosome, which, according to the authors, indicates the endosome is oxidizing, rather than reducing. It is possible that endosomal behavior is modified in breast cancer cells, but more likely—and more important to this work—is that the large antibody conjugate could not interact with redox machinery within the endosome, preventing its reduction. Though it is well known that the cytosol is strongly reductive due to the high concentration of GSH, the exact redox conditions and components controlling these conditions in the endosome are less understood. Reduction in the cytosol occurs primarily through thiol-disulfide exchange using a thiolate anion. Formation of this anion within the acidic endosome is highly unfavorable (pKa = 8.3), suggesting reduction occurs enzymatically (6). If redox enzymes control endosomal reduction, a disulfide would need to be capable of accessing the enzyme active site in order to be reduced. In the nanoparticle design presented here, this would be

very difficult. The disulfide is within the PEG brush layer, creating tremendous steric interference from enzyme interaction. Because of this, the ability of endosomal enzymes to bind and reduce disulfides within the dense PEG layer during the course of transcytosis is expected to be extremely limited. Without being able to cleave sufficient numbers of targeting ligands from the nanoparticle surface, the nanoparticle will be subject to the same avidity limitations of previous designs.

It is possible that the disulfide could be placed in a more flexible location to allow easier access to redox enzymes. The most likely location would be at the nanoparticle surface; however, that would lead to problems with exposing free thiols to the CNS. Free thiols are well known to be toxic within biological systems by forming free radical species (49), and thus designing the nanoparticle such that surface thiols are present after transcytosis may lead to tissue damage once within the CNS, an unacceptable side effect. The disulfide was designed to hide within the PEG brush layer of the investigated nanoparticle to minimize thiol exposure once within the CNS, but, as described above, this may preclude its ability to undergo enzymatic digestion.

A final limitation of this design is the implication of drug loading on the choice of using PLGA as the nanoparticle component polymer. PLGA-PEG is an amphiphilic co-polymer. In nanoprecipitation, this property drives spontaneous nanoparticle formation in aqueous solution with the hydrophobic PLGA portion densely packed to form the nanoparticle interior and surface PEG interacting with solvent molecules (22). This synthesis technique is most commonly used to encapsulate small, hydrophobic drug molecules since they easily pack within the PLGA nanoparticle core. For delivery to the brain, however, drugs of interest are usually large and hydrophilic, necessitating an alternative nanoparticle synthesis method. Hydrophilic macromolecules can be encapsulated within PLGA nanoparticles using a double emulsion method (25) but stable nanoparticles cannot be formed using this method at the sub-100nm sizes needed for BBB transcytosis. An alternative polymer is necessary for drug delivery to the brain.

2.4 Methods

Synthesis of THR-AF488. N-terminally Cys-modified THR peptide (CTHRPPMWSPVWP) was purchased from Anaspec Inc. The peptide was dissolved at 0.01 mg/mL in PBS pH 7.2. Tris(2-carboxyethyl)phosphine (TCEP) was added to give a final concentration of 5 mM and reacted at room temperature for 5 mins. Alexa Fluor-488 maleimide (Thermo Scientific) was dissolved in DMSO at a concentration of 6 mg/mL. The Alexa-Fluor was added to Cys-THR at a 10 times molar excess and reacted at room temperature for 2 hrs. The mixture was purified using a Spectra Por dialysis membrane (Spectrum Labs) [100-500Da molecular weight cutoff (MWCO)] with four buffer changes of PBS over the course of four days.

Synthesis of THR-PEG. THR-Cys was dissolved in DMF at a concentration of 50 mg/mL and diluted to 5 mg/mL in 50 mM NaH_2PO_4 pH 7.2. A ten times molar excess of TCEP was added to the solution and sat at room temperature for 10 min. A ten times molar excess of maleimide-PEG-amine (5kDa, Laysan Bio) was then added and reacted with stirring at room temperature for 2 hrs. To quench remaining maleimide activity, a ten times molar excess (to the maleimide-PEG) of BME was added to the solution and stirred for 30 mins. Excess BME and unreacted peptide was removed through ultracentrifugation using a 3kDa MWCO filter (EMD Millipore). For the binding assay, the crude mixture was added to the cells using the theoretical maximum concentration of synthesized THR-PEG to determine ligand concentration.

Investigation of THR Binding Affinity. K562 cells were grown at 37°C, 5% CO2 in DMEM+10% FBS with penicillin/streptomycin. Cells were washed with PBS and removed using a cell scraper. After centrifugation at 300 g for 3 min, the cells were fixed using BD Cytofix (BD Biosciences) for 20 min at 4°C. The cells were then washed and resuspended in PBS + 4% BSA. Increasing concentrations of nanoparticles were added to $1x10^6$ cells at $5x10^6$ cells/mL and sat at RT with light agitation every 15 min to prevent cells from settling. After 90 min, the cells were added to 12 mL PBS and centrifuged at 300 g for 3 min. The cells were resuspended in 12 mL fresh PBS and centrifuged again. This washing procedure

was performed for a total of three times. Fluorescent cells were measured using a Becton Dickson FACSCalibur flow cytommerty. Viable cell populations were identified and gated using forward-scatter and side-scatter values from the blank (no THR) sample. For the cells incubated with THR-AF488 (either directly or in competition with unlabeled peptide), cells fluorescence was directly measured after exposure to the peptide. For the cells incubated with THR-PEG, an anti-PEG rat IgG (1:1000 dilution) was added to each sample for 60 min at room temperature after exposure to the PEGylated peptide. The cells were then washed in PBS and incubated with an anti-rat IgG Alexa Fluor 488 antibody for 60 min at room temperature. Following a final wash in PBS, cell fluorescence was measured using the flow cytometer. In both conditions, the geometric mean of measured fluorescence values was recorded.

Preparation of intra-PEG disulfide bond. Amine-PEG-thiol (NH2-PEG-SH, 3.4kDa) was dissolved in DMF at a concentration of 20mg/mL. Carboxy-PEG-thiol (COOH-PEG-SH, 2kDa) was added at an equimolar concentration (Scheme 1). Hydrogen peroxide (H2O2) was added to give a final concentration of 3% H2O2. The reaction mixture was stirred at room temperature for 24 hrs and analyzed by MALDI-TOF (Figure 3). Disulfide bonds were confirmed to link the PEG polymers by adding 1000x molar excess beta-mercaptoethanol to the polymer and validating by MALDI-TOF that the disulfide cleaved and polymers dissociated (Figure 4).

Synthesis of PLGA-PEG block copolymers. PLGA-NHS was prepared by dissolving 250mg carboxy-terminated poly(D,L-lactic-co-glycolic acid) (50/50) (PLGA-COOH) in 1.1mL of acetonitrile. Ten molar excess 1-ethyl-3-(3-dimethylaminopropyl)carbodiimide (EDC) and N-hydroxysuccinimide (NHS) were added to this solution and stirred for 90 minutes at room temperature. The product was precipitated out of solution by addition of 30mL of methanol followed by centrifugation at 2700g for 10min. The supernatant was discarded and the product was washed with 30mL of methanol and collected again by centrifugation. This process was repeated twice more for a total of three washes. The purified PLGA-NHS was dried under vacuum.

Various hetero-bifunctional polyethylene glycol (PEG) polymers were added to PLGA-NHS to form PLGA-PEG block copolymers. All PEG polymers contained an amine terminus to react with the NHS ester on the PLGA polymer and either a carboxyl (NH2-PEG-COOH; 5kDa); methoxy (NH2-PEG-OCH3, 5kDa); or sulfhydryl (NH2-PEG-SH; 3.4kDa) terminus at the other end. Dried PLGA-NHS was dissolved in acetonitrile at a concentration of 5mM followed by addition of 1.5x molar excess hetero-bifunctional PEG and 10x molar excess N,N-diisopropylethanolamine (DIPEA). The product was precipitated by addition of 30mL diethyl ether after 24hrs at room temperature with gentle stirring. The PLGA-PEG block copolymer was collected by centrifugation at 2700g for 10min. The supernatant was discarded and the product was washed with another 30mL of ether and collected again by centrifugation. This process was repeated twice more for a total of three washes. The product was dried under vacuum.

Synthesis of disulfide-containing PLGA-PEG copolymer. PLGA-PEG-S-S-PEG-COOH was prepared by dissolving 100mg of PLGA-PEG-SH in 2mL of DMF. To this was added 5x molar excess SH-PEG-COOH (2kDa). Following dissolution of the SH-PEG-COOH, 200uL of 30% hydrogen peroxide (H2O2) was added to the reaction mixture to give a final concentration of 3% H2O2. The reaction was left stirring at room temperature for 24hours.

Synthesis of PLGA-AF488. Fluorescently-labeled PLGA polymer was prepared by dissolved 50mg of PLGA-NHS in 1mL of DMF followed by addition of 1mg of Alexa-fluor 488 cadaverine (AF488) dissolved in 0.5mL of DMF. The product was collected after one hour by precipitation with 20mL of methanol followed by centrifugation at 2700g for 10mins. The product was washed in another 20mL of methanol and collected again by centrifugation. This process was repeated twice more for a total of three washes. The purified product was dried under vacuum.

Preparation of PLGA-PEG nanoparticles. PLGA-PEG nanoparticles were prepared by nanoprecipitation. Various combinations of PLGA-PEG block copolymers were dissolved in 3mL DMF at a total concentration of 10mg/mL PLGA-PEG copolymer. Each formulation

contained 2.5% PLGA-AF488 by weight. The polymer mixture was added dropwise to 30mL of stirring water and allowed to mix for 2hrs. The resulting nanoparticle mixture was passed through a 0.2μm filter and purified through ultrafiltration with a 50kDa MWCO centrifugal filter at 2700g for 10mins. The nanoparticle retentate was resuspended in 10mL of water and collected by ultrafiltration twice more for a total of three washes. Following the final wash cycle, the concentrated nanoparticles were resuspended in 1mL of PBS.

Addition of human holo-transferrin to nanoparticles. Nanoparticle concentration was determined using nanoparticle tracking analysis (NTA). Nanoparticle formulations were diluted to 0.0001mg/mL in PBS and the particle concentration was determined using a Nanosight NS500. EDC and NHS were added to the nanoparticles at 10x molar excess to the total amount of carboxy-terminated PLGA-PEG block copolymer (PLGA-PEG-COOH or PLGA-PEG-S-S-PEG-COOH) present in the formulation and allowed to stir at room temperature for 10mins. Based on the nanoparticle concentration determined by NTA, human holo-transferrin (Tf) prepared in PBS, pH 7.2 was added at 30x molar excess for the low-Tf formulations and 3000x molar excess for the high-Tf and disulfide-containing formulations. The reaction mixture was stirred for 90mins at room temperature and then purified by ultrafiltration with a 100kDa MWCO centrifugal filter at 3000g for 10mins. The nanoparticle retentate was resuspended in 0.5mL of PBS and collected again by ultrafiltration. This process was repeated twice more for a total of three washes.

Characterization of PLGA-PEG nanoparticles. Particle sizes and zeta potentials were measured with a Brookhaven Instruments DLS and ZetaPALS. Particle diameter was measured in PBS over 2mins. Zeta potentials were taken in 1.5mM KCl (pH 7.0) and averaged from 3 runs at target residual of 0.018.

In vitro determination of disulfide-containing nanoparticle binding affinity. Neuro2A cells were cultured in DMEM, 10% FBS, and penicillin/streptomycin. Prior to incubation with nanoparticles, cells were fixed in BD Cytofix ® for 15mins at 4°C, washed, and resuspended in PBS + 4% BSA. Various concentrations of three nanoparticle formulations

were incubated with $2x10^6$ cells at $1x10^6$ cells/mL for 90mins. In order to cleave the disulfide-bond present in the disulfide-containing nanoparticle formulation, these particles were treated with dithiothreitol (DTT) for 30mins at room temperature prior to addition to the Neuro2A cells. Excess DTT was removed by washing the nanoparticles in PBS and collecting them by ultrafiltration. Cells were pelleted at 200g for 5mins and resuspended in 200uL PBS. Nanoparticle binding was determined by measuring fluorescence intensity at 488nm excitation, 525nm emission. The data were fit to the Langmuir binding isotherm with Bmax and KD numerically determined using Matlab function nlinfit.

Animal studies. All animals were treated according to the NIH Guidelines for Animal Care and Use approved by the Caltech Institutional Animal Care and Use Committee. Nanoparticle formulations containing 1x1010 to 1x1011 particles were prepared in 150uL of PBS and injected into female Balb/c mice via lateral tail vein. The mice were sacrificed one hour after injection by CO2 asphyxiation. The brain was removed and fixed in 4% paraformaldehyde overnight for further tissue processing.

Confocal Microscopy. Formaldehyde-fixed tissues were embedded in paraffin, sectioned, and deparaffinized. The tissue was mounted using Prolong Gold ® Antifade Reagant with DAPI (nuclear stain). Sections were imaged on a Zeiss LSM 510 inverted confocal scanning microscope with a Zeiss PlanNeofluar 40x/1.3 oil objective. The excitation wavelength for DAPI was 710 nm (two-photon laser) and 488 nm for Alexafluor488 labeled nanoparticles. Their corresponding emission filters were 390-465 nm and 530-560 nm, respectively.

2.5 References

1. Sahay, G., Alakhova, D. Y., & Kabanov, A. V. (2010). Endocytosis of nanomedicines. *Journal of Controlled Release*, *145*(3), 182–195.
2. Harush-Frenkel, O., Rozentur, E., Benita, S., & Altschuler, Y. (2008). Surface Charge of Nanoparticles Determines Their Endocytic and Transcytotic Pathway in Polarized MDCK Cells. *Biomacromolecules*, *9*(2), 435–443.
3. Meister, A., & Anderson, M. E. (1983). Glutathione. *Annual Review of Biochemistry*, *52*(1), 711–760.
4. Meister, A. (1991). Glutathione deficiency produced by inhibition of its synthesis, and its reversal; applications in research and therapy. *Pharmacology & Therapeutics*, *51*(2), 155–194.
5. Saito, G., & Swanson, J. A. (2003). Drug delivery strategy utilizing conjugation via reversible disulfide linkages: role and site of cellular reducing activities. *Advanced Drug Delivery Reviews*, (55), 199–215.
6. Yang, J., Chen, H., Vlahov, I. R., Cheng, J. X., & Low, P. S. (2006). Evaluation of disulfide reduction during receptor-mediated endocytosisby using FRET imaging. *Proceedings of the National Academy of Sciences*, *103*(37), 13872–13877.
7. Mahmoud, E. A., Sankaranarayanan, J., Morachis, J. M., Kim, G., & Almutairi, A. (2011). Inflammation Responsive Logic Gate Nanoparticles for the Delivery of Proteins. *Bioconjugate Chemistry*, *22*(7), 1416–1421.
8. Guk, K., Lim, H., Kim, B., Hong, M., Khang, G., & Lee, D. (2013). Acid-cleavable ketal containing poly(β-amino ester) for enhanced siRNA delivery. *International Journal of Pharmaceutics*, *453*(2) 541–550.
9. Shao, W., Miao, K., Liu, H., Ye, C., Du, J., & Zhao, Y. (2013). Acid and reduction dually cleavable amphiphilic comb-like copolymer micelles for controlled drug delivery. *Polymer Chemistry*, *4*(11), 3398.
10. Eliasof, S., Lazarus, D., & Peters, C. G. (2013). Correlating preclinical animal studies and human clinical trials of a multifunctional, polymeric nanoparticle. *Proceedings of the National Academy of Sciences*, 110(37), 15127-15132.

11. Binauld, S., & Stenzel, M. H. (2013). Acid-degradable polymers for drug delivery: a decade of innovation. *Chemical Communications*, *49*(21), 2082.
12. Paramonov, S. E., Bachelder, E. M., Beaudette, T. T., Standley, S. M., Lee, C. C., Dashe, J., & Fréchet, J. M. J. (2008). Fully Acid-Degradable Biocompatible Polyacetal Microparticles for Drug Delivery. *Bioconjugate Chemistry*, *19*(4), 911–919.
13. Li, Y., Du, W., Sun, G., & Wooley, K. L. (2008). pH-Responsive Shell Cross-Linked Nanoparticles with Hydrolytically Labile Cross-Links. *Macromolecules*, *41*(18), 6605–6607.
14. Cai, X., Dong, C., Dong, H., Wang, G., Pauletti, G. M., Pan, X., et al. (2012). Effective Gene Delivery Using Stimulus-Responsive Catiomer Designed with Redox-Sensitive Disulfide and Acid-Labile Imine Linkers. *Biomacromolecules*, *13*(4), 1024–1034.
15. Nie, Y., Günther, M., Gu, Z., & Wagner, E. (2011). Pyridylhydrazone-based PEGylation for pH-reversible lipopolyplex shielding. *Biomaterials*, *32*(3), 858–869.
16. Knorr, V., Allmendinger, L., Walker, G. F., Paintner, F. F., & Wagner, E. (2007). An Acetal-Based PEGylation Reagent for pH-Sensitive Shielding of DNA Polyplexes. *Bioconjugate Chemistry*, *18*(4), 1218–1225.
17. Murthy, N., Campbell, J., Fausto, N., Hoffman, A. S., & Stayton, P. S. (2003). Bioinspired pH-Responsive Polymers for the Intracellular Delivery of Biomolecular Drugs. *Bioconjugate Chemistry*, *14*(2), 412–419.
18. Gao, W., Langer, R., & Farokhzad, O. C. (2010). Poly(ethylene glycol) with Observable Shedding. *Angewandte Chemie International Edition*, *49*(37), 6567–6571.
19. Wang, Y.-C., Wang, F., Sun, T.-M., & Wang, J. (2011). Redox-Responsive Nanoparticles from the Single Disulfide Bond-Bridged Block Copolymer as Drug Carriers for Overcoming Multidrug Resistance in Cancer Cells. *Bioconjugate Chemistry*, *22*(10), 1939–1945.

20. Jia, L., Li, Z., Zhang, D., Zhang, Q., Shen, J., Guo, H., et al. (2012). Redox-responsive catiomer based on PEG-ss-chitosan oligosaccharide-ss-polyethylenimine copolymer for effective gene delivery. *Polymer Chemistry*, *4*(1), 156-165.
21. Cheng, R., Feng, F., Meng, F., Deng, C., Feijen, J., & Zhong, Z. (2011). Glutathione-responsive nano-vehicles as a promising platform for targeted intracellular drug and gene delivery. *Journal of Controlled Release*, *152*(1), 2–12.
22. Dinarvand, R., Sepehri, N., Manouchehri, Rouhani, & Atyabi, F. (2011). Polylactide-co-glycolide nanoparticles for controlled delivery of anticancer agents. *International Journal of Nanomedicine*, *6*, 877-895.
23. Champion, J. A., Katare, Y. K., & Mitragotri, S. (2007). Particle shape: A new design parameter for micro- and nanoscale drug delivery carriers. *Journal of Controlled Release*, *121*(1-2), 3–9.
24. Lee, Y.-K., Hong, S. M., Kim, J. S., Im, J. H., Min, H. S., Subramanyam, E., et al. (2007). Encapsulation of CdSe/ZnS quantum dots in poly(ethylene glycol)-poly(D,L-lactide) micelle for biomedical imaging and detection. *Macromolecular Research*, *15*(4), 330–336.
25. Danhier, F., Ansorena, E., Silva, J. M., Coco, R., Le Breton, A., & Préat, V. (2012). PLGA-based nanoparticles: An overview of biomedical applications. *Journal of Controlled Release*, *161*(2), 505–522.
26. Gu, F. X., Zhang, L., Teply, B., Mann, N., Wang, A. Z., Radovic-Moreno, A. F., et al. (2008). Precise engineering of targeted nanoparticles by using self-assembled biointegrated block copolymers. *Proceedings of the National Academy of Sciences*, *105*(7), 2586–2591.
27. Cheng, J., Teply, B. A., Sherifi, I., Sung, J., Luther, G., Gu, F. X., et al. (2007). Formulation of functionalized PLGA-PEG nanoparticles for in vivo targeted drug delivery. *Biomaterials*, *28*(5), 869–876.
28. Zolnik, B. S., & Burgess, D. J. (2007). Effect of acidic pH on PLGA microsphere degradation and release. *Journal of Controlled Release*, *122*(3), 338–344.
29. Makadia, H. K., & Siegel, S. J. (2011). Poly Lactic-co-Glycolic Acid (PLGA) as Biodegradable Controlled Drug Delivery Carrier. *Polymers*, *3*(4), 1377–1397.

30. Fredenberg, S., Wahlgren, M., Reslow, M., & Axelsson, A. (2011). The mechanisms of drug release in poly(lactic-co-glycolic acid)-based drug delivery systems—a review. *International Journal of Pharmaceutics*, *415*(1-2), 34–52.
31. Alexis, F., Pridgen, E., Molnar, L. K., & Farokhzad, O. C. (2008). Factors Affecting the Clearance and Biodistribution of Polymeric Nanoparticles. *Molecular Pharmaceutics*, *5*(4), 505–515.
32. Acharya, A. P., Lewis, J. S., & Keselowsky, B. G. (2013). Combinatorial co-encapsulation of hydrophobic molecules in poly(lactide-co-glycolide) microparticles. *Biomaterials*, *34*(13), 3422–3430.
33. Dunphy Guzman, K. A., Finnegan, M. P., & Banfield, J. F. (2006). Influence of Surface Potential on Aggregation and Transport of Titania Nanoparticles. *Environmental Science & Technology*, *40*(24), 7688–7693.
34. Jokerst, J. V., Lobovkina, T., Zare, R. N., & Gambhir, S. S. (2011). Nanoparticle PEGylation for imaging and therapy. *Nanomedicine*, *6*(4), 715–728.
35. Nance, E. A., Woodworth, G. F., Sailor, K. A., Shih, T. Y., Xu, Q., Swaminathan, G., et al. (2012). A Dense Poly(Ethylene Glycol) Coating Improves Penetration of Large Polymeric Nanoparticles Within Brain Tissue. *Science Translational Medicine*, *4*(149), 149ra119–149ra119.
36. Karve, S., Werner, M. E., Cummings, N. D., Sukumar, R., Wang, E. C., Zhang, Y.-A., & Wang, A. Z. (2011). Formulation of Diblock Polymeric Nanoparticles through Nanoprecipitation Technique. *Journal of Visualized Experiments*, (55), e3398.
37. Wiley, D. T., Webster, P., Gale, A., & Davis, M. E. (2013). Transcytosis and brain uptake of transferrin-containing nanoparticles by tuning avidity to transferrin receptor. *Proceedings of the National Academy of Sciences*, *110*(21), 8662–8667.
38. Canton, I., & Battaglia, G. (2012). Endocytosis at the nanoscale. *Chemical Society Reviews*, *41*(7), 2718–2739.
39. Lee, J. H., Engler, J. A., Collawn, J. F., & Moore, B. A. (2001). Receptor mediated uptake of peptides that bind the human transferrin receptor. *European Journal of Biochemistry*, *268*, 2004–2012.

40. Kamaly, N., Xiao, Z., Valencia, P. M., Radovic-Moreno, A. F., & Farokhzad, O. C. (2012). Targeted polymeric therapeutic nanoparticles: design, development and clinical translation. *Chemical Society Reviews*, *41*(7), 2971-3010.
41. Descamps, L., Dehouck, M. P., Torpier, G., & Cecchelli, R. (1996). Receptor-mediated transcytosis of transferrin through blood-brain barrier endothelial cells. *American Journal of Physiology Heart and Circulatory Physiology*, *270*(4), H1149–H1158.
42. Klausner, R. D., Harford, J., & van Renswoude, J. (1984). Rapid internalization of the transferrin receptor in K562 cells is triggered by ligand binding or treatment with a phorbol ester. *Proceedings of the National Academy of Sciences of the United States of America*, *81*(10), 3005–3009.
43. Prades, R., Guerrero, S., Araya, E., Molina, C., Salas, E., Zurita, E., et al. (2012). Delivery of gold nanoparticles to the brain by conjugation with a peptide that recognizes the transferrin receptor. *Biomaterials*, *33*(29), 7194–7205.
44. Wängler, C., Nada, D., Höfner, G., Maschauer, S., Wängler, B., Schneider, S., et al. (2010). In Vitro and Initial In Vivo Evaluation of 68Ga-Labeled Transferrin Receptor (TfR) Binding Peptides as Potential Carriers for Enhanced Drug Transport into TfR Expressing Cells. *Molecular Imaging and Biology*, *13*(2), 332–341.
45. Dingels, C., Müller, S. S., Steinbach, T., Tonhauser, C., & Frey, H. (2013). Universal Concept for the Implementation of a Single Cleavable Unit at Tunable Position in Functional Poly(ethylene glycol)s. *Biomacromolecules*, *14*(2), 448–459.
46. Valencia, P. M., Hanewich-Hollatz, M. H., Gao, W., Karim, F., Langer, R., Karnik, R., & Farokhzad, O. C. (2011). Effects of ligands with different water solubilities on self-assembly and properties of targeted nanoparticles. *Biomaterials*, *32*(26), 6226–6233.
47. Gao, X., Qian, J., Zheng, S., Xiong, Y., Man, J., Cao, B., Wang, L., et al. (2013). Up-regulating Blood Brain Barrier Permeability of Nanoparticles via Multivalent Effect. *Pharmaceutical Research*, *30*(10), 2538–2548.
48. Austin, C. D., Wen, X., Gazzard, L., Nelson, C., Scheller, R. H., & Scales, S. J. (2005). Oxidizing potential of endosomes and lysosomeslimits intracellular cleavage

of disulfide-basedantibody–drug conjugates. *Proceedings of the National Academy of Sciences*, *102*(50), 17987–17992.

49. Munday, R. (1989). Toxicity of thiols and disulphides: involvement of free-radical species. *Free Radical Biology & Medicine*, *7*(6), 659–673.

Chapter III

INVESTIGATION OF GOLD NANOPARTICLES CONTAINING TRANSFERRIN BOUND THROUGH AN ACID-CLEAVABLE LINK*

3.1 Introduction

3.1.1 Chemical Changes Experienced During Transcytosis – Reduced pH

Though the disulfide strategy outlined in Chapter II showed promise, significant drawbacks to this approach (detailed in Section 2.3) necessitated development of a different cleavable link. Endocytosis is a well-studied process, including endocytosis of nanomaterials (1,2). In general, endocytosis has three stages: (i) engulfment of the cargo into a membrane-bound vesicle, (ii) sorting of the cargo towards its destination, and (iii) delivery of the cargo to its destination (2). The second step, in which vesicles are sorted to their destination, occurs primarily in the endosome (3). One critical chemical difference persists in the endosome relative to the extracellular fluid: decreased pH (5-6 versus 7.4) (3,4). Although there is still debate over the exact sorting mechanism of Tf once it is within the BBB endothelium, it is well established that Tf internalization can be prevented using endocytosis inhibitors (5), indicating Tf must undergo some portion of the endocytosis pathway initially before diverting to transcytosis.

Since any Tf-containing therapeutic will experience this pH drop en route to the adluminal side of the cell, chemical bonds sensitive to mildly acidic pH should break during transcytosis. Therefore, if the targeting ligand is attached to the therapeutic through an acid-sensitive chemical bond, it will disassociate from the rest of the therapeutic, allowing free movement into the CNS (Fig 3.1). Also, an acid-cleavable strategy will not require any interaction between the nanoparticle and small molecules or enzymes, allowing flexibility of cleavable link placement within the nanoparticle design.

*Excerpts from this chapter are reprinted from Clark, A. J., & Davis, M. E. (2015). Increased brain uptake of targeted nanoparticles by adding an acid-cleavable linkage between transferrin and the nanoparticle core. *Proceedings of the National Academy of Sciences*, *112*(40), 12486-12491 with permissions from *PNAS*.

3.1.2 Acid-Cleavable Chemical Bonds

Chemical bonds of interest have two essential characteristics: (i) stability under extracellular conditions and (ii) quick and irreversible breakage at mildly acidic pH. Incorporation of acid-cleavable bonds into nanomedicines has gained much interest due to the pH gradients that exist between the blood and endosomes, lysosomes, and tumor tissue (6,7). Most work has been focused towards selective release of a drug in an acidic environment through destabilization/breakdown of the delivery device or release of the drug from a drug-polymer conjugate. The chemical bonds under investigation include orthoesters, acetals/ketals, imines, hydrazones, and cis-aconityls. These groups have garnered interested because of their sensitivity in mildly acidic media while maintaining stability at neutral pH. The variety of chemical bonds investigated highlights one of the major advantages—as well as one of the current limitations—of acid-cleavable systems: namely, that the rate of breakdown can be tuned based on the structure of the cleavable-bond and its surrounding chemical groups; however, there is yet to be a systematic review comparing chemical structure and pH sensitivity so the cleavage rate must be determined empirically for each candidate (8).

The cleavage rate is critical for choosing the proper acid-cleavable link for this system. Following endocytosis of the targeted nanomedicine, the endosome rapidly acidifies to a pH <6 within 2-3 mins (7). Experiments with radiolabeled Tf have found significant amounts of the protein in the brain parenchyma within 30 minutes of systemic injection (9). These two findings suggest that Tf-containing nanomedicines will experiences an acidic environment on the order of tens of minutes. Therefore, potential acid-cleavable linkers must undergo significant cleavage within this timeframe in order to effectively separate Tf from the rest of the nanomedicine.

Of the previously mentioned chemical groups, only acetals/ketals have been shown to have cleavages half-lives that are compatible with Tf transcytosis at the BBB (6). Consequently, subsequent investigation focused on incorporating acetals/ketals in between Tf and the rest of the nanoparticle.

3.1.3 Biological Applications of Gold Nanoparticles

In this investigation, transferrin was bound to the surface of gold nanoparticles (AuNP's). AuNP's have been widely used for labeling applications in biological tissues (10-12). The high electron density of AuNP's makes them superb contrast agents for transmission electron microscopy (TEM) while their unique optical properties have applications in both light and confocal microscopy. AuNP's can also be used for drug delivery where drug molecules are directly adsorbed to the nanoparticle surface, though this method is less flexible than delivery using polymeric systems (13). Finally, AuNP's are well tolerated in vivo with no toxicity evident even at very high concentrations (14,15).

Important to this work is the ability to prepare AuNP's with well-controlled diameters and surface characteristics. Surface ligands can then easily be added to AuNP's through thiol-dative bonds. Our lab previously developed an imaging assay that can specifically detect AuNP's in tissue using light microscopy, allowing identification of nanoparticle location within different compartments of the brain (16). In this method, a silver solution is applied to fixed tissues containing gold nanoparticles. The silver solution catalytically deposits to the surface of the gold nanoparticles, increasing the size of individual nanoparticles until they are visible under light microscopy (Fig 3.1). The specificity of gold in biological samples was also used to quantitate AuNP's in an in vitro assay using inductively coupled plasma mass spectrometry (ICP-MS).

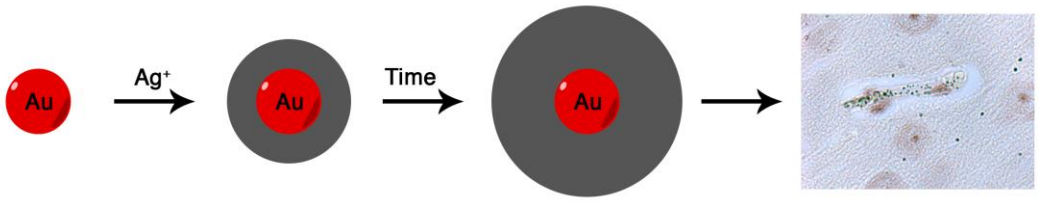

Fig 3.1 Silver staining of gold nanoparticles. Addition of metallic silver catalytically deposits on the AuNP surface, increasing individual nanoparticle size and allowing visualization by light microscopy (black dots).

3.1.4 Ligand-Dependent Trafficking Dynamics at the Blood-Brain Barrier

TfR has been one of the primary targets investigated for RMT across the BBB, due to its high expression on BBB endothelium (17). Anti-TfR antibody-drug conjugates (ADCs) have received the most attention because of their ability to bind TfR with high affinity without interfering with endogenous Tf (18-20). Despite the perceived potential of anti-TfR ADCs, a BBB-permeable drug using this approach has yet to reach the clinic. Yu et al. showed that anti-TfR Abs enter the brain in greater numbers when their affinity to TfR is reduced (21). Follow-up work from the same group showed that high-affinity, bispecific anti-TfR Abs preferentially trafficked to the lysosome within BBB endothelium rather than transcytosing, while low-affinity Abs did not (22). A similar effect was seen with a divalent anti-TfR Ab, which entered the lysosome in significantly greater amounts than the monovalent variant (Detailed in section 1.4.1) (23).

Recently, our group demonstrated that Tf-containing, 80nm AuNP's with near neutral zeta potentials are capable of accessing the brain parenchyma from the blood when their avidity to TfR is appropriately tuned (16). If the avidity is too high, the nanoparticles remain strongly associated with the endothelial cells of the BBB, whereas nanoparticles of lower avidity are able to release into the brain following transcytosis (Detailed in section 1.4.3). Although the lower avidity nanoparticles showed the greatest ability to enter the brain, the higher avidity nanoparticles still were able to cross the BBB in greater amounts than non-Tf containing nanoparticles.

Recently, in vitro results using an anti-TfR Ab with reduced affinity at pH 5.5 showed the ability to transcytose across hCMEC/D3 cells while Abs with high affinity independent of pH were trafficked to the lysosome (24), suggesting vesicle trafficking may be affected by a particular targeting ligand. Thus, we also investigated whether Tf, the natural ligand for the TfR, and anti-TfR Abs behaved differently when used as the targeting agents for the nanoparticles.

3.1.5 Design of Nanoparticles with Tf Bound Through an Acid-Cleavable Link

As with Ab BBB transcytosis, the nanoparticles with reduced avidity to TfR showed the greatest ability to cross the BBB. A major obstacle to translating these agents to viable therapeutics is the need to dose very high quantities in the blood in order for an appreciable amount of drug to reach the CNS (16,20,21). We attempted to increase the ability of Tf-containing nanoparticles to reach the brain parenchyma by incorporating a small, chemical linker between the Tf and AuNP cores that cleaves at mildly acidic pH. This design provides for high avidity interactions with TfR at the blood side of the BBB to enable practical, systemic dosing amounts. Then, as the targeted nanoparticles transcytose, we use the drop in pH (3,4) that the bound nanoparticles would experience during the transcytosis process to trigger the cleavage of the linkage between the Tf and the nanoparticle core. Thus, when the transcytosing vesicle reaches the brain, the nanoparticles will no longer be bound and can be released into the parenchyma. With this design, the nanoparticle will retain high avidity interactions with TfR on the blood side of the BBB, but not be restricted once within the endothelium (Fig 3.2). Our results show a nearly 3-fold increase in the ability of high avidity nanoparticles to reach the brain parenchyma in vivo after incorporation of an acid-cleavable, diamino ketal (DAK) linker. We also observed a direct relationship between brain penetration of nanoparticles and surface Tf-DAK content. Furthermore, no improvement was seen in the ability for anti-TfR Ab-containing nanoparticles to cross the BBB with addition of the DAK linker, suggesting that there are significant differences in their intracellular trafficking compared to that of Tf-containing nanoparticles.

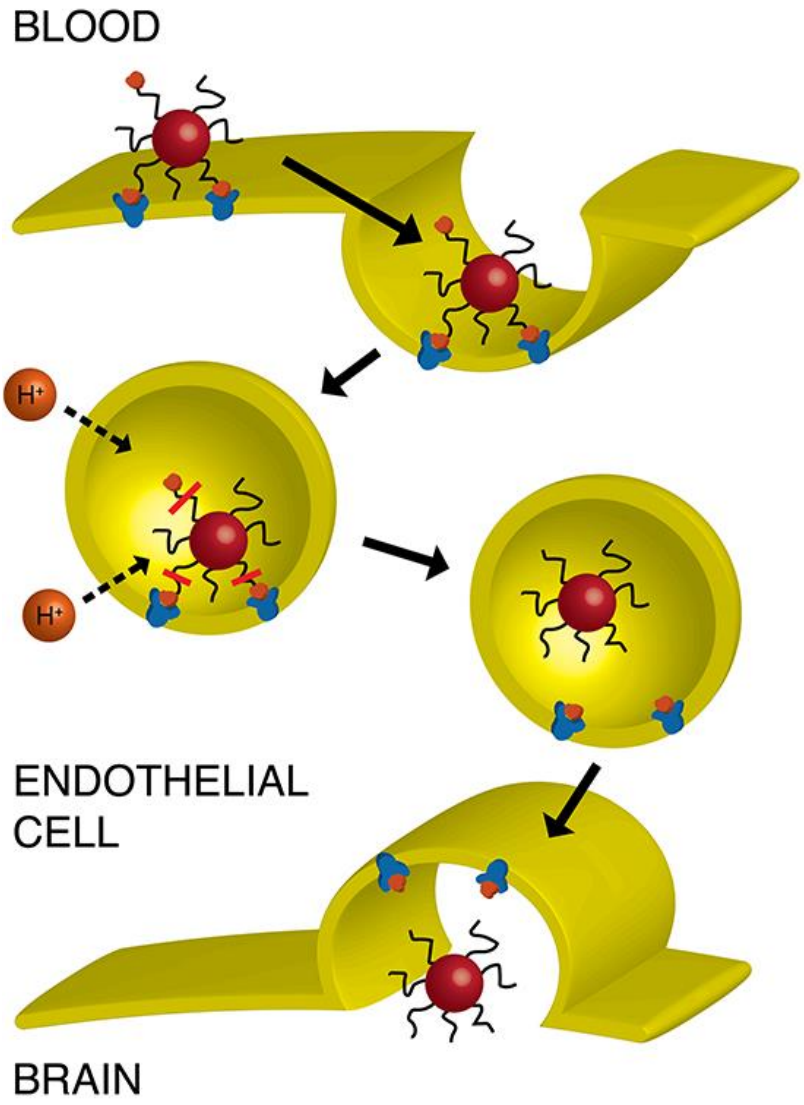

Fig 3.2 Transcytosis of nanoparticles containing Tf bound to the nanoparticle core through an acid-cleavable link. Following endocytosis, rapid acidification of the endosome causes separation of the Tf ligand from the nanoparticle core, allowing free movement of the nanoparticle into the brain parenchyma once transcytosis is completed.

3.2 Results

3.2.1 Synthesis and Characterization of Acid-Cleavable, Ligand-PEG Conjugates

The acid-sensitive DAK (2,2-bis(aminoethoxy)propane) moiety was added to a 5kDa polyethylene glycol (PEG) followed by conjugation of the polymer to either human holo-Tf or R17217 anti-mouse TfR Ab (Fig 3.3). DAK was chosen because its reported hydrolysis half-life is 60 min at pH 5.5 but over 24 hrs at pH 7.4 and 37°C (6). These hydrolysis kinetics should provide sufficient Ligand-DAK-PEG stability for the Tf/Ab to remain associated with the nanoparticle while it is circulating in the blood, but cleave in the acidic vesicles during the transcytosis process so that the majority of the ligand disassociates from the nanoparticle core during that time. The R17217 anti-TfR antibody was chosen because it binds mouse TfR with high affinity (25) and has been suggested as a BBB-permeable targeting ligand for nanoparticles (26). This antibody has very low uptake by the mouse liver and kidney, suggesting some degree of brain selectivity (27). The stability of the Tf-DAK-PEG (Tf-C) conjugate was monitored by MALDI-TOF and found to release Tf within 2 hrs once placed in pH 5.5 buffer at 37°C (Fig 3.4A). The conjugate remained virtually unchanged at pH 8 after 2 hrs and could still be detected after 24 hrs (Fig 3.4B).

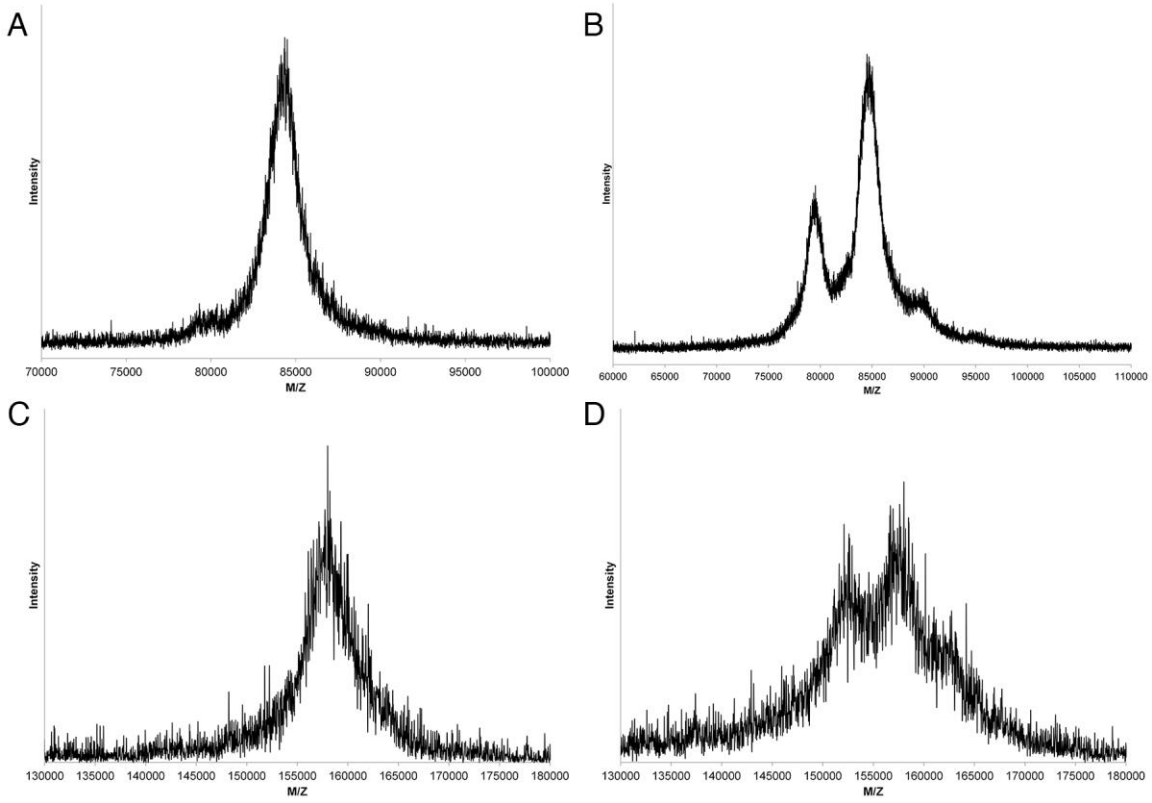

Fig 3.3 MALDI-TOF spectra of purified conjugates. (A) Mono-PEGylated Tf-PEG-OPSS. (B) Mixture of unreacted Tf (79kDa) and mono-PEGylated Tf-DAK-PEG-OPSS (84kDa). (C) Mono-PEGylated R17217-PEG-OPSS. (D) Mixture of unreacted Ab (153kDa) and mono-PEGylated R17217-DAK-PEG-OPSS (158kDa).

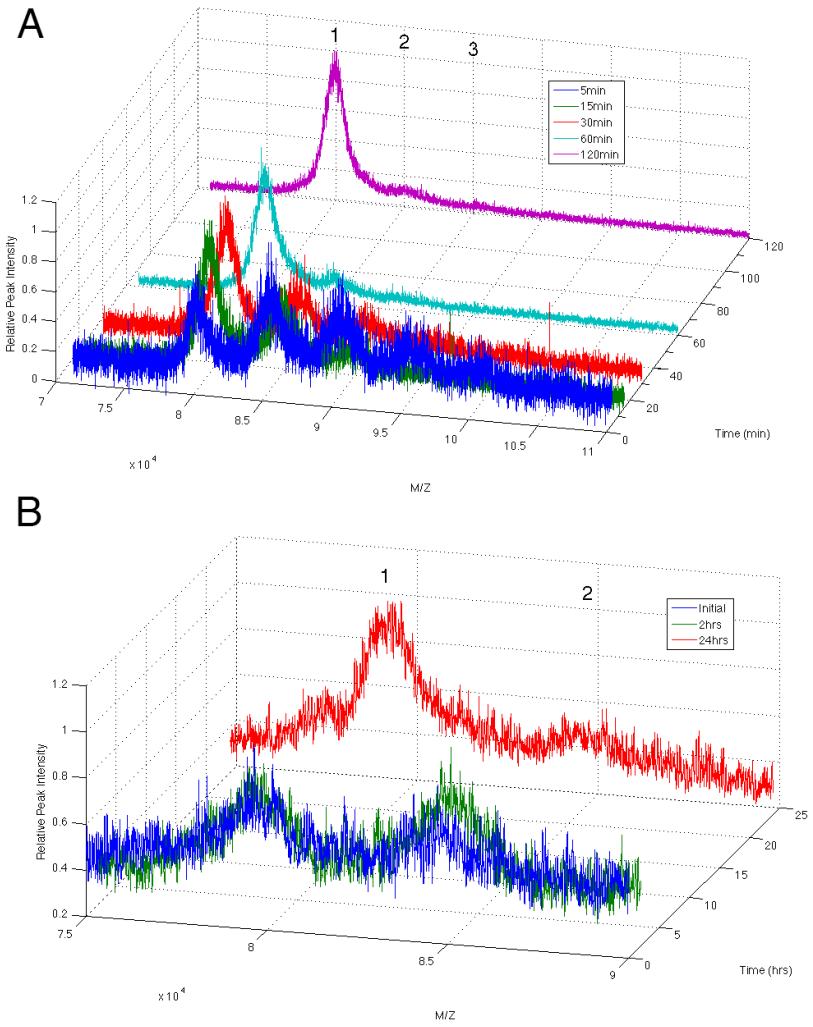

Fig 3.4 Tf-DAK-PEG-OPSS pH-dependent stability. (A) The conjugate rapidly cleaves to native Tf (peak 1, 79kDa) from a mixture of monoPEGylated (peak 2, 84kDa) and diPEGylated (peak 3, 89kDa) conjugate over the course of 120 min when placed in pH 5.5 buffer at 37°C. (B) The same conjugate as in (A) placed at pH 8, 37°C shows much slower degradation. At two hours (green trace) the amount of monoPEGylated Tf-DAK-PEG (peak 2) is virtually unchanged and the conjugate is still present 24 hrs later (red trace).

3.2.2 Tf/Ab-DAK-PEG-containing nanoparticles have decreased avidity to TfR after exposure to mildly acidic pH

To prepare the targeted nanoparticles, various quantities of either cleavable (Tf-C/Ab-C) or non-cleavable ligand (Tf-N/Ab-N) were added to 50 nm AuNPs followed by an addition of excess, non-functionalized PEG (mPEG) (Scheme 3.1). AuNPs were chosen for the utility of their detection within biological systems, either through transmission electron microscopy (TEM), inductively coupled plasma mass spectrometry (ICP-MS) or silver enhancement. Nanoparticles were prepared in this manner in order to preserve the characteristics we found useful in our previous formulations, which showed ~80nm nanoparticles with near-neutral zeta potentials (<-15mV) best enter the brain (16). Also, sub-100nm nanoparticles with dense PEG coating and near-neutral zeta potentials have shown the ability to diffuse throughout the brain's extracellular space (28). All nanoparticle formulations prepared here had hydrodynamic diameters near 80 nm measured by dynamic light scattering (DLS) and zeta potentials between -11 and -5mV when measured in 1mM KCl (Table 3.1).

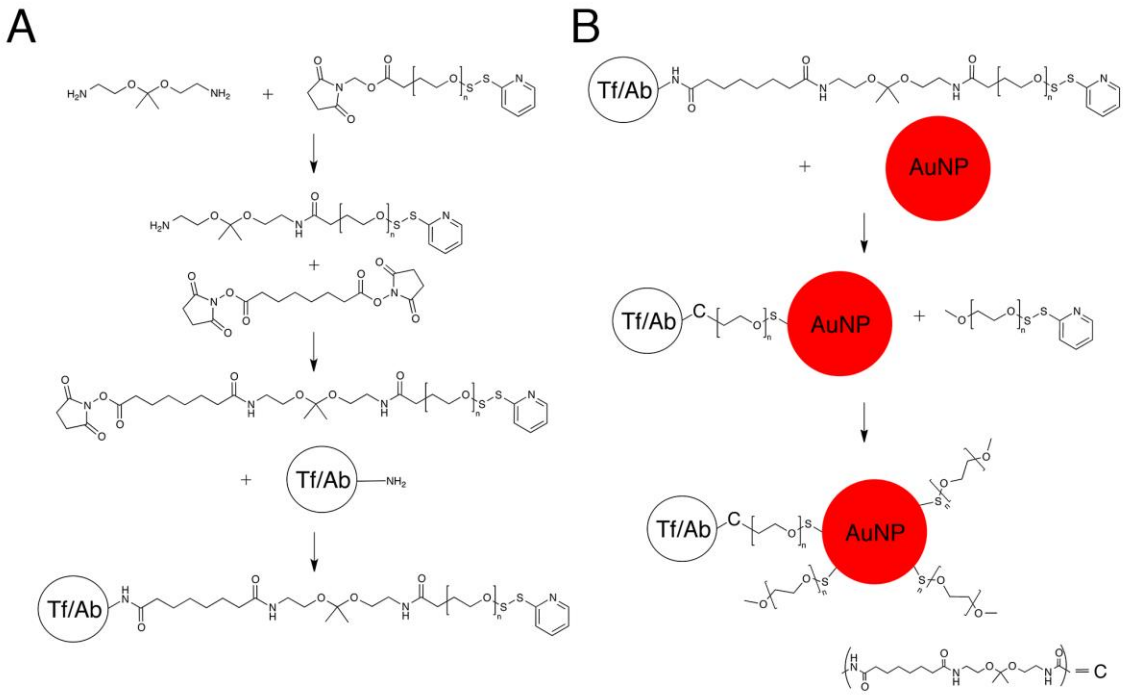

Scheme 3.1 Synthesis of targeted nanoparticles with ligand bound by an acid-cleavable link. (A) Preparation of acid-cleavable DSS-DAK-PEG-OPSS and addition to the targeting ligand (Tf/Ab) to create the cleavable conjugate. (B) Addition of the Tf/Ab-DAK-PEG-OPSS ligand followed by excess mPEG-SH to prepare targeted gold nanoparticles. n ~120 for 5kDa PEG.

Formulation	Diameter (nm)	Zeta Potential (mV)	Kd (nM)
mPEG	75.1±2.4	-5.75±4.12	N.D.
20Tf-N	79.1±0.9	-5.77±2.21	0.408
200Tf-N	78.1±6.2	-7.78±3.73	0.029
20Tf-C	75.7±4.4	-11.25±1.81	0.788
120Tf-C	77.2±0.2	-7.93±0.60	0.096
200Tf-C	73.6±1.6	-7.47±3.12	0.030
2Ab-N	76.1±4.3	-6.26±2.00	0.441
10Ab-N	84.4±6.9	-8.83±2.19	0.039
2Ab-C	72.9±4.9	-6.36±2.44	0.619
10Ab-C	77.4±1.9	-5.10±2.31	0.021

Table 3.1 Nanoparticle formulations and characteristics. Number indicates the number of ligands per particle, -N indicates non-cleavable PEG conjugate, and -C indicates cleavable PEG conjugate. Data shown for hydrodynamic diameter and zeta potential are the average of 5 measurements ± 1 SD. N.D. = not determined.

An in vitro, cell-binding assay was performed using the Neuro2A mouse brain endothelial cell line to determine the avidity of the nanoparticles to mouse TfRs. Cells were incubated with increasing quantities of nanoparticles. Then the bound nanoparticles were quantified by silver enhancement, a highly sensitive AuNP detection method (29). The binding data were fit to a Langmuir binding isotherm in order to calculate Kd (Fig 3.5). The binding avidity was directly dependent on the ligand content of the nanoparticle (Table 3.1), as we have shown previously (16). Also, by increasing the quantity of Tf contained on the nanoparticle, avidities similar to those of the nanoparticles containing the R17217 Ab with lower protein numbers could be obtained. The cell-binding assay was repeated for the 200Tf-C and 10Ab-C formulations after incubating the particles to pH 5.5 for 4 hrs at 37°C. Both formulations showed lower avidity to TfR (Kd = 1.16 nM for 200Tf-C, Kd = 0.512 nM for 10Ab-C) following exposure to decreased pH, indicating loss of the surface ligand (Fig 3.6).

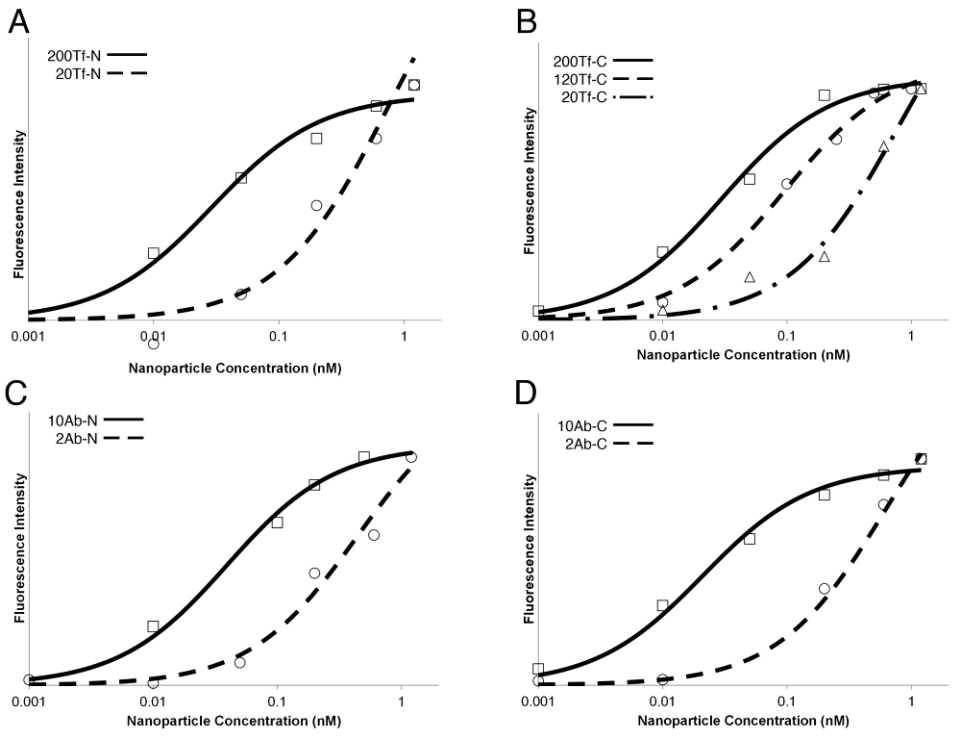

Fig 3.5 Nanoparticle binding avidity to Neuro2A cells. Binding data for (A) Tf-N, (B) Tf-C, (C) Ab-N and (D) Ab-C formulations are shown. Model curves are based on the Langmuir binding isotherm with Kd and Bmax determined by fitting the data (Matlab).

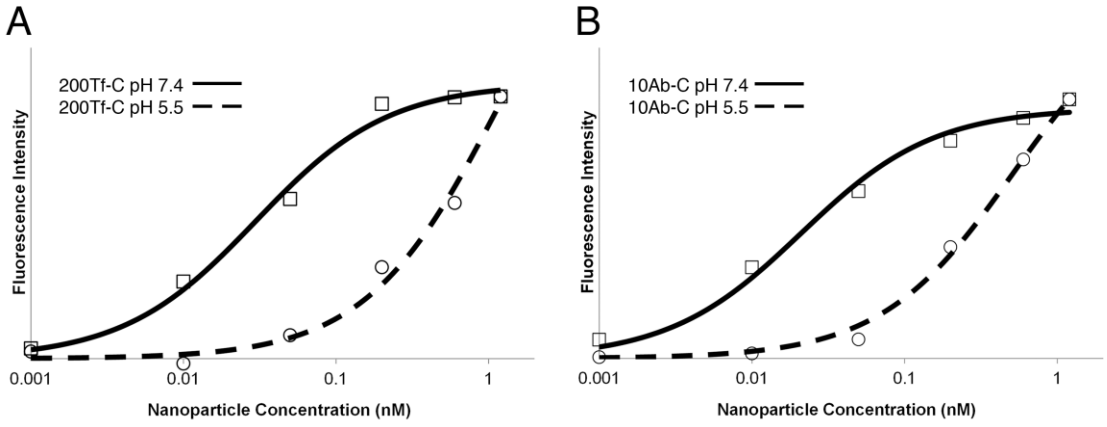

Fig 3.6 Tf/Ab-DAK-PEG-containing nanoparticles have decreased avidity for mouse TfR after exposure to mildly acidic pH. (A) Nanoparticle binding to Neuro2A cells for 200Tf-C

formulation after exposure to either neutral or acidic pH. 200Tf-C nanoparticles bind with high avidity (K_d = 0.040 nM) when kept at pH 7.4, but avidity is reduced after incubating nanoparticles at pH 5.5 (K_d = 1.16 nM). (B) The same effects are observed with 10Ab-C formulation (K_d = 0.021 nM at pH 7.4, K_d = 0.512 nM after pH 5.5), as in (A) with 200Tf-C. Curves are fitted Langmuir binding isotherms.

3.2.3 High avidity Tf-DAK-PEG-containing nanoparticles cross an in vitro model of the BBB rapidly and in greatest amounts

In order to assess how the addition of the DAK linker may affect the ability of the targeted nanoparticles to cross the BBB in vivo, we employed the bEnd.3 cell line, an immortalized mouse brain endothelial line, in a commonly used in vitro model of the BBB (30). Nanoparticles were added to the apical compartment of bEnd.3-coated transwells in serum-free DMEM and allowed to cross the cellular border over 8 hours. The full volume of the basal compartment was removed and replaced by fresh, serum-free DMEM at various time points. These samples were then measured for gold content using ICP-MS.

After 8 hrs, the 200Tf-C formulation showed the greatest capacity to cross the BBB model membrane (Fig 3.7). These nanoparticles reach the basal compartment at a 10-fold increased quantity compared to the 200Tf-N formulation. All Tf-containing formulations reveal decreased ability to cross the bEnd.3 cells when co-incubated with greater than serum concentrations of Tf, indicating specific binding of TfR is responsible for crossing (Fig 3.8). Unlike the high avidity Tf-C formulations, the Ab-C formulations did not show a significant difference in basal well accumulation compared to Ab-N. In fact, all Ab-containing formulations showed similar or less crossing than non-targeted mPEG particles (Fig 3.9). After the 8 hr incubation, the cells exposed to the high avidity formulations (200Tf-N, 200Tf-C, 10Ab-N) were lysed and intracellular gold content measured (Fig 3.10). The 10Ab-N formulation had significantly more gold within the cells compared to 200Tf-C, consistent with high affinity Abs being primarily retained by endothelial cells rather than transcytosing.

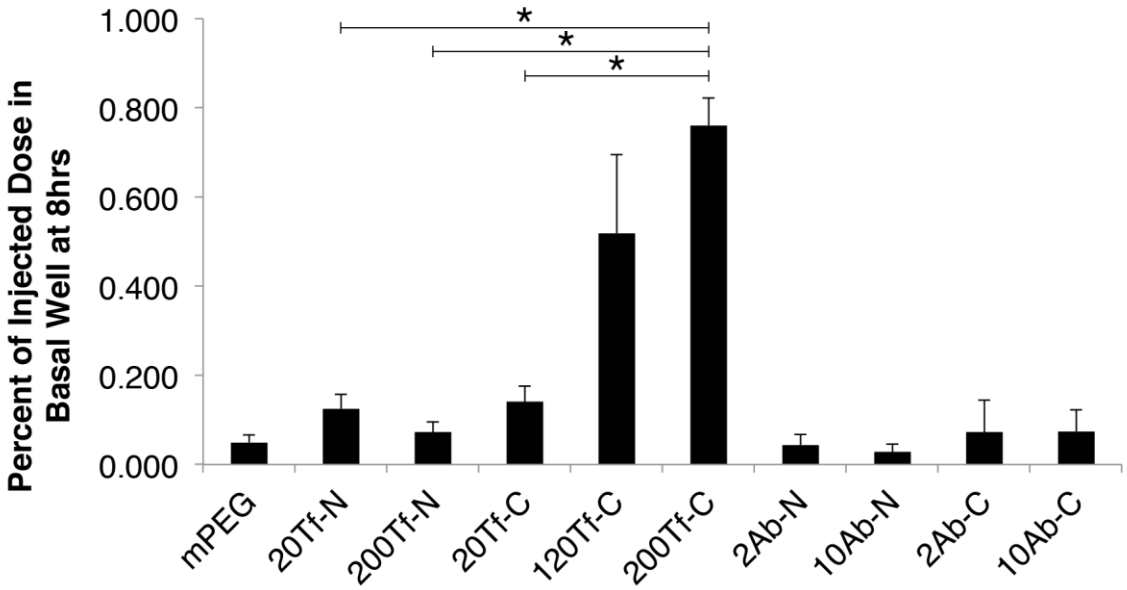

Fig 3.7 120Tf-C and 200Tf-C nanoparticles cross an in vitro model of the BBB in greater amounts than 20Tf-N and 200Tf-N. Percent of injected nanoparticles reaching the basal well of bEnd.3 coated transwells 8 hrs after introduction. 120Tf-C and 200Tf-C show greater ability to cross the transwells compared to 200Tf-N, whereas both Ab-C formulations did not show a significant increase compared to equivalent Ab-N formulations. The average of three wells for each group is shown (except for 20Tf-C, n = 4). Error bars given are SE. * = $p<0.001$.

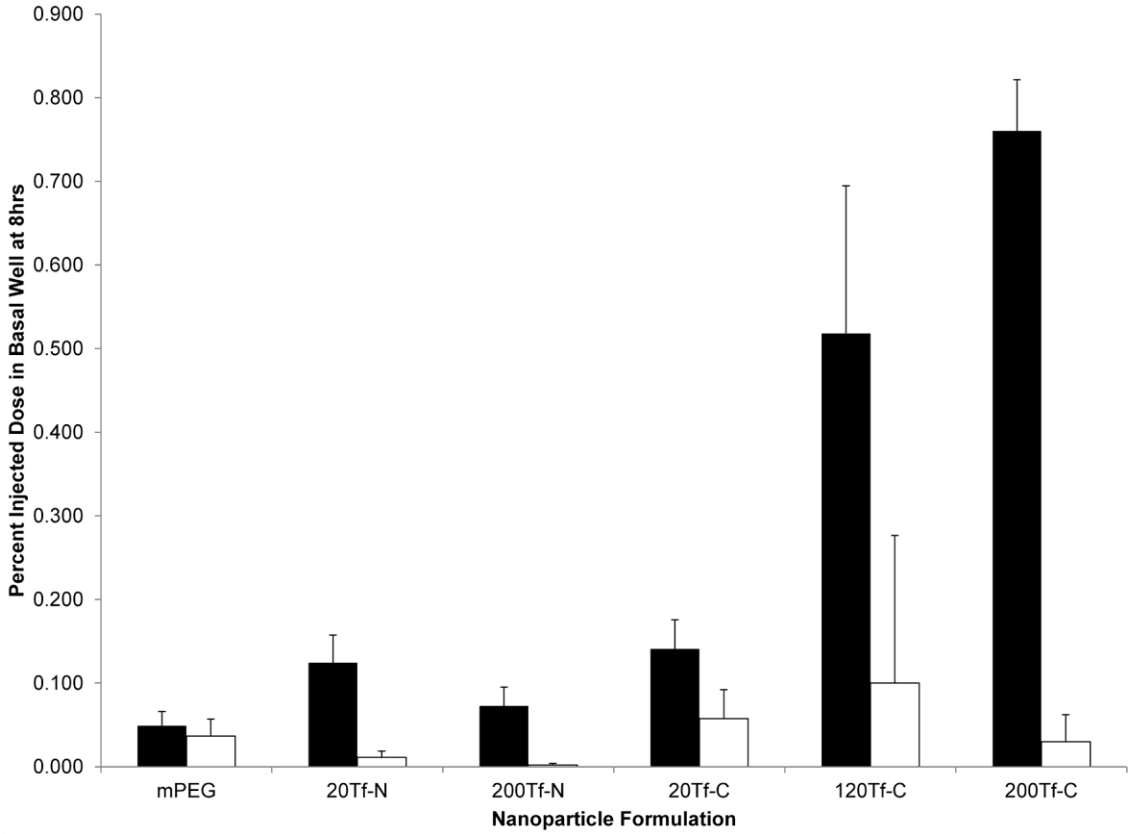

Fig 3.8 Tf-containing nanoparticles show decreased ability to cross bEnd.3 transwells in the presence of high concentrations of hTf. Nanoparticles were added to apical wells in either serum-free DMEM (black bars) or in the presence of 2.5 mg/mL hTf (white bars). Total nanoparticles reaching the basal well at 8 hrs was measured by ICP-MS. Error bars indicate SE (n = 3 for each Tf-competition group).

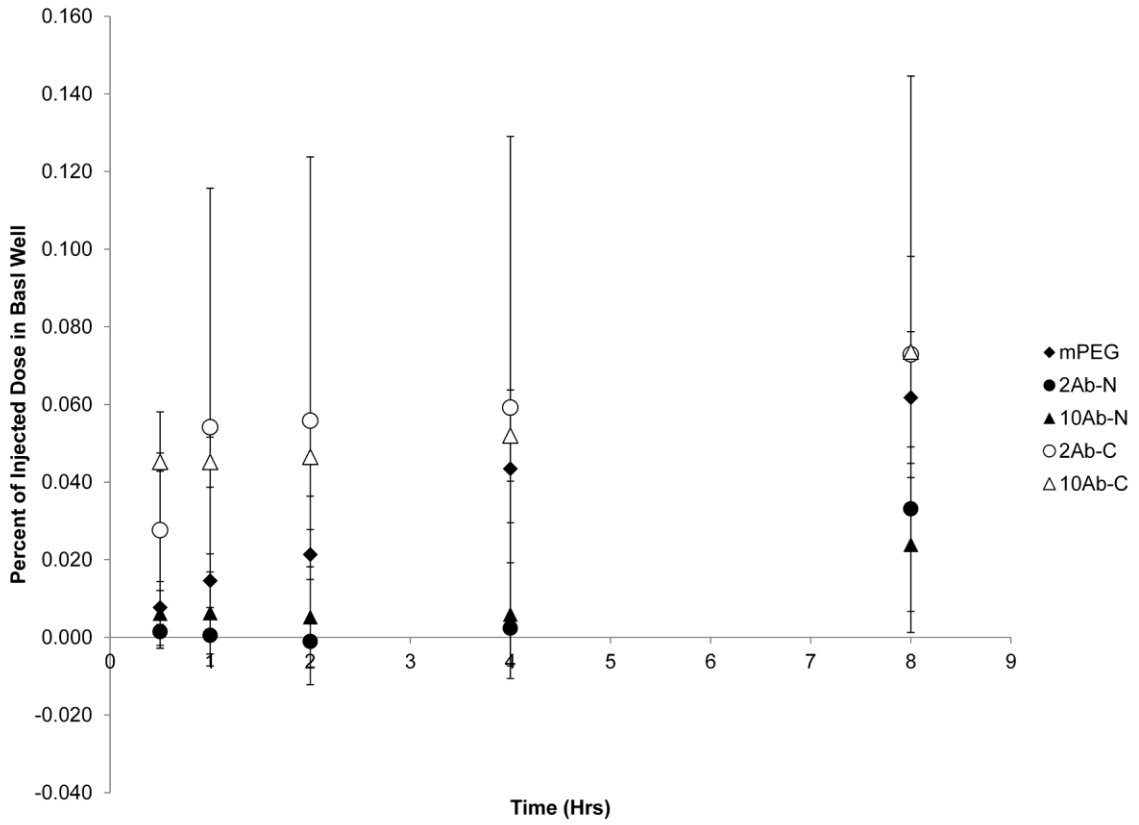

Fig 3.9 bEnd.3 transwell crossing over time for Ab-containing nanoparticles. Data shown are an average of three transwells per group. Error shown is SE.

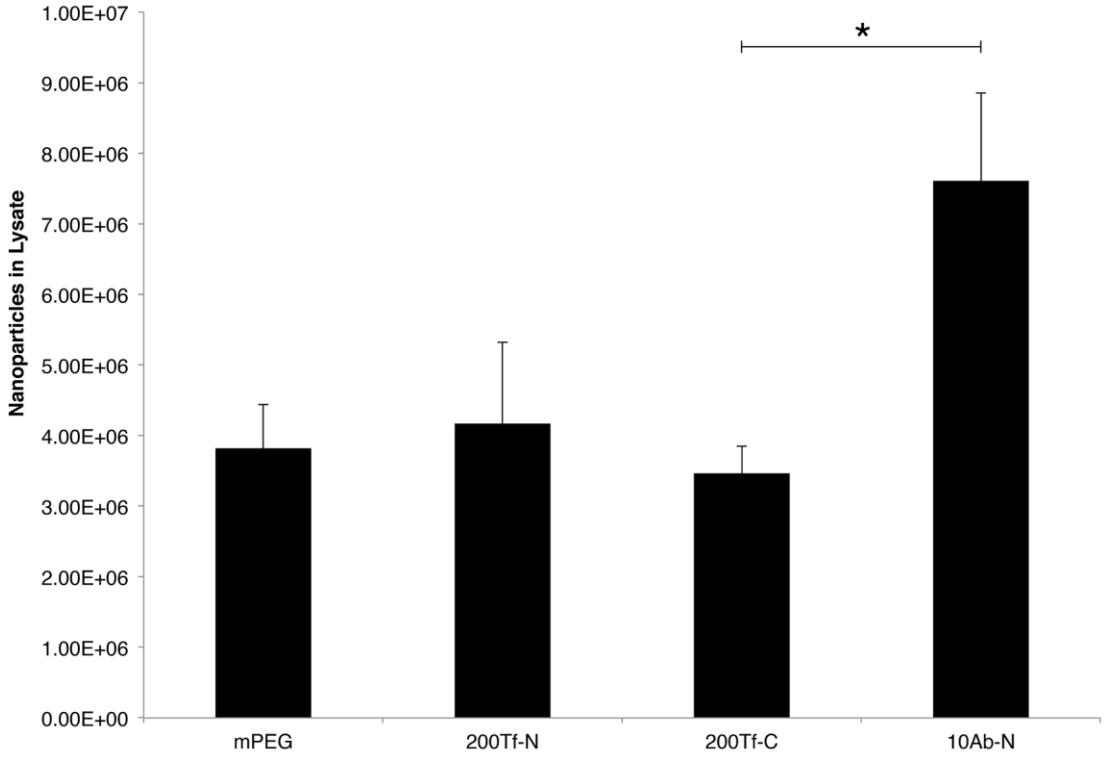

Fig 3.10 Intracellular gold content for bEnd.3 cells exposed to high avidity formulations. After 8 hrs, cells exposed to high avidity formulations were lysed and intracellular gold content determined. Data shown are an average of three transwells. Error bars indicate SE. * = $p<0.05$

Interestingly, all three Tf-C formulations underwent the majority of their total crossing within the first 60 min after introduction (Fig 3.9). The Tf-N formulations, conversely, showed slower basal well accumulation over the 8 hrs (Table 3.2). For example, by 60 min, only 18% of the total 20Tf-N quantity reached the basal well compared to 61% of the total 20Tf-C. AuNPs with diameters between 50-100nm have been shown to rapidly sediment within in vitro systems using an upright cell orientation (31). This causes the particle concentration at the cell surface to be higher than the rest of the solution. Since each Tf-C formulation crossed the bEnd.3 cells rapidly after introduction, these results suggest that these nanoparticles are undergoing transcytosis upon initial contact with the cells, while the Tf-N formulations may have a larger portion recycled back to the cell surface or retained by the cells. Also, the 120Tf-C and 200Tf-C formulations reached near maximum crossing

within 2 hrs (93% and 94% of total, respectively) compared to 200Tf-N (47%). These data indicate that the high-avidity, cleavable nanoparticles may be saturating the transcytosis pathway within 2 hrs of exposure.

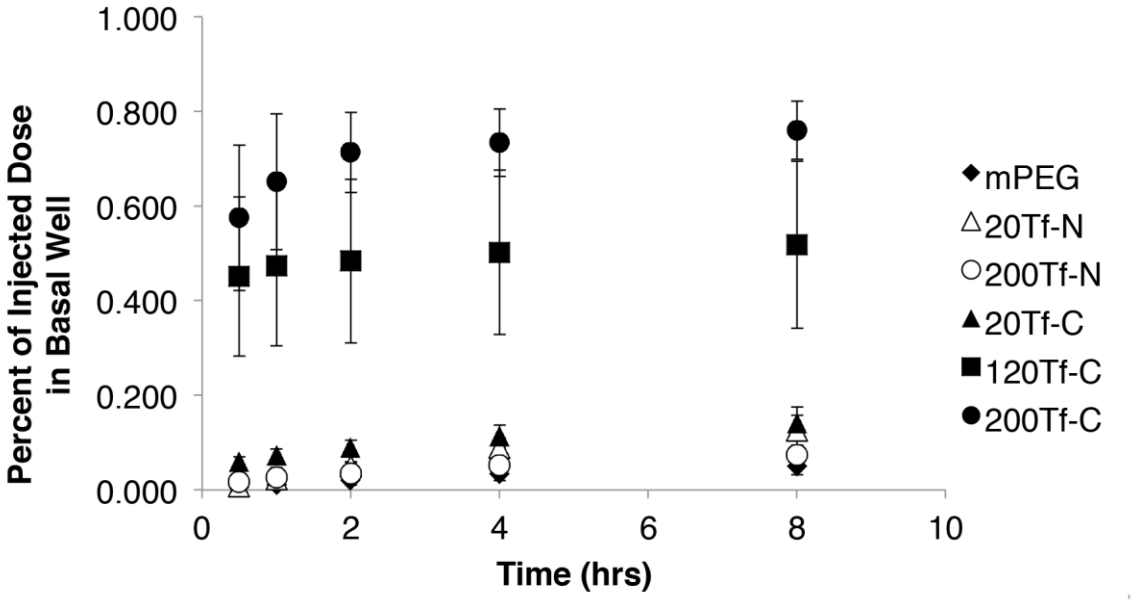

Fig 3.11 Tf-containing nanoparticles crossing the model BBB over time. All Tf-C formulations show the majority of crossing within the first 2 hrs.

Time (hrs)	mPEG	20Tf-N	200Tf-N	20Tf-C	120Tf-C	200Tf-C
0.5	9.34	5.63	22.27	56.51	87.07	75.62
1	22.08	18.39	36.81	61.75	91.38	85.69
2	42.29	39.76	47.68	71.47	93.34	93.84
4	68.88	71.00	70.40	83.66	96.90	96.54
8	100.00	100.00	100.00	100.00	100.00	100.00

Table 3.2 Percentage of total nanoparticle crossing bEnd.3-coated transwells over time per formulation for Tf-containing nanoparticles. All Tf-C formulations cross rapidly within the first 2 hrs compared to the analogous Tf-N formulations.

3.2.4 Addition of DAK linkage increases the ability of high-avidity, Tf-containing nanoparticles to enter the brain, but does not affect those with anti-TfR Abs

Nanoparticles of each formulation listed in Table 3.1 were injected into BALB/c mice, and assessed for their ability to enter the brain parenchyma. A total of 3 mice were used for each formulation. Nanoparticles were systemically administered by injection via the lateral tail vein, and allowed to circulate for 12 hrs. Mice were then euthanized, and the brains resected and processed for histological examination. The locations of nanoparticles within the brain were determined using silver enhancement. Deposition of metallic silver onto gold nanoparticles allows individual nanoparticles to become visible by light microscopy. Nanoparticles present within the brain parenchyma were manually counted in 40 images per mouse. The median number of nanoparticles in the parenchyma for each group is shown in Fig 3.12. As with the in vitro experiment, the 200Tf-C formulation showed the highest penetration into the brain, and a significantly higher quantity compared to 200Tf-N. Also, incorporation of the cleavable link did not increase the ability of either Ab-C formulation to enter the parenchyma. The 20Tf-C formulation did not significantly differ from 20Tf-N, but more nanoparticles localized into the brain as the surface content of Tf-DAK increased. The 120Tf-C and 200Tf-C nanoparticles entered the brain best, but did not significantly differ from one another [they have relatively similar Kd values (Table 3.1)]. Results from mPEG, 20Tf-N, and 200Tf-N are essentially the same as we reported previously using formulations of those type (16), and indicate the good reproducibility of our methods. The 20Tf-N formulation reached the parenchyma in significantly higher amounts than 200Tf-N (Table 3.3) indicating the high avidity Tf-containing nanoparticles are retained and/or stuck to the endothelium without the presence of the cleavable linker.

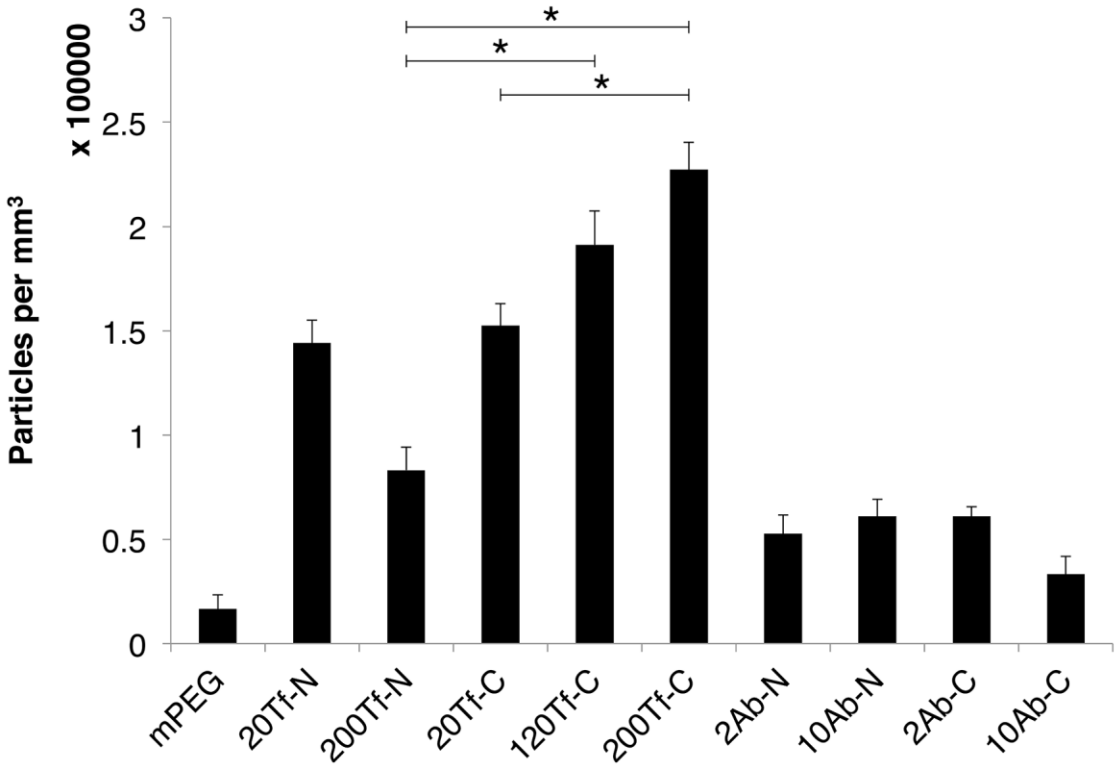

Fig 3.12 Addition of DAK increases the ability of high avidity Tf-containing nanoparticles to enter the brain in vivo. Nanoparticles within the brain parenchyma were manually counted after silver enhancement of brain sections. Three BALB/c mice were injected for each formulation. A total of 40 images per mouse brain were analyzed. Median values and SE are shown. Significant differences are displayed for select group comparisons (* = $p<0.0001$).

Nanoparticle Formulation	mPEG	20Tf-N	200Tf-N	20Tf-C	120Tf-C	200Tf-C	2Ab-N	10Ab-N	2Ab-C	10Ab-C
mPEG	X									
20Tf-N	<0.0001	X								
200Tf-N	<0.0001	<0.0001	X							
20Tf-C	<0.0001	0.590	<0.0001	X						
120Tf-C	<0.0001	<0.0001	<0.0001	0.0005	X					
200Tf-C	<0.0001	<0.0001	<0.0001	<0.0001	0.114	X				
2Ab-N	<0.0001	<0.0001	0.5344	<0.0001	<0.0001	<0.0001	X			
10Ab-N	<0.0001	<0.0001	0.2342	<0.0001	<0.0001	<0.0001	0.999	X		
2Ab-C	<0.0001	<0.0001	0.0186	<0.0001	<0.0001	<0.0001	0.243	0.2352	X	
10Ab-C	0.0008	<0.0001	0.0003	<0.0001	<0.0001	<0.0001	0.0095	0.00014	0.0026	X

Table 3.3 P-values for all potential pairwise comparisons for in vivo quantitative analysis. Values were calculated using the Wilcoxon rank-sum test.

Sample images for each formulation are shown in Fig 3.13-3.16. All slides were silver-stained simultaneously with a blank brain (no AuNPs injected) to assess for any non-specific staining [some areas of non-specific silver stain were observed in the blank sample (Fig 3.17), and similar staining patterns observed in AuNP-containing samples were not included in the analysis].

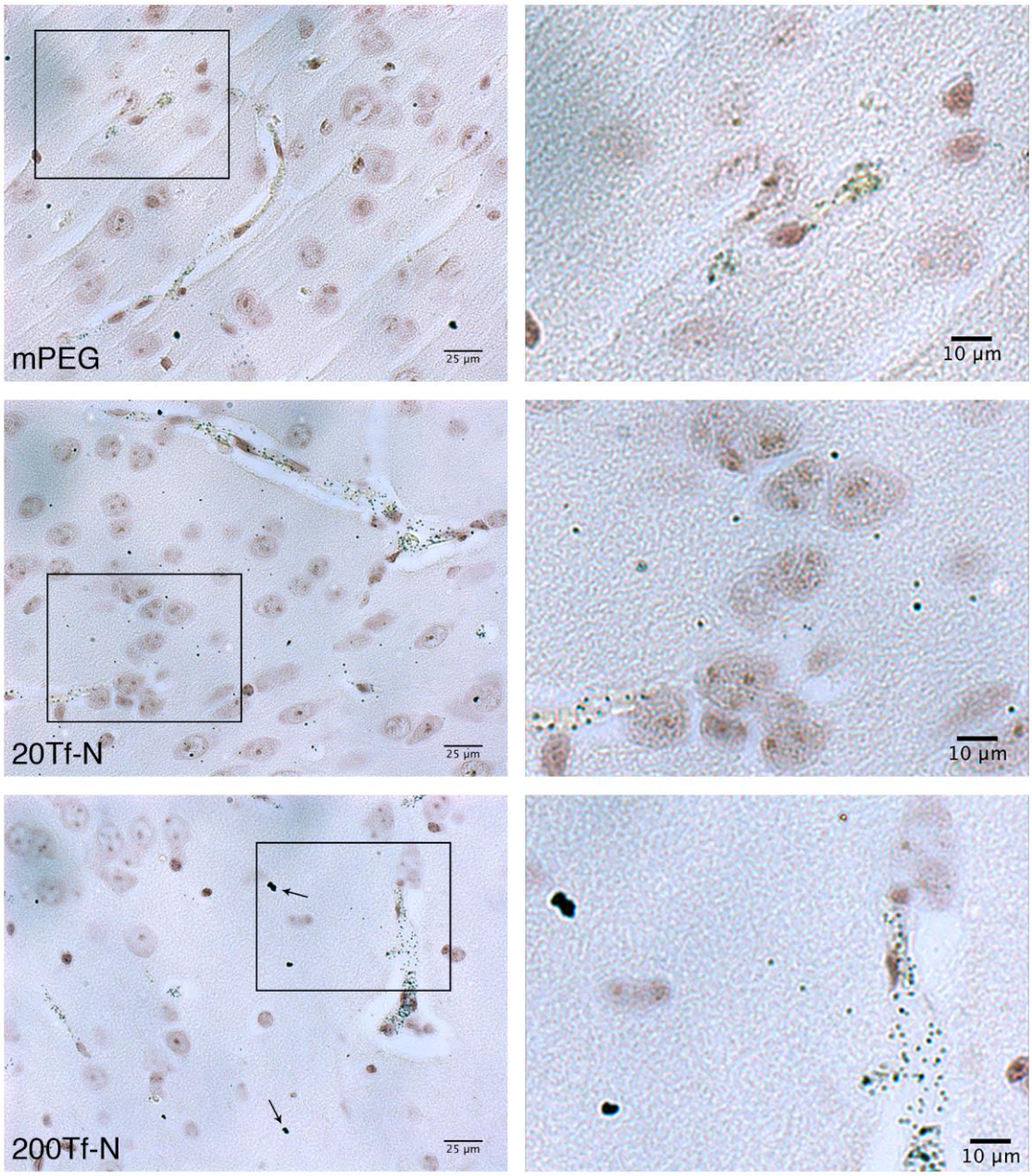

Fig 3.13 Images from silver-stained brains of mPEG, 20Tf-N and 200Tf-N formulations. Left column contains full sized image and right column contains area highlighted in black box. Arrows indicate amorphous silver stain determined to be non-specific silver deposition and were not included in the quantitative analysis.

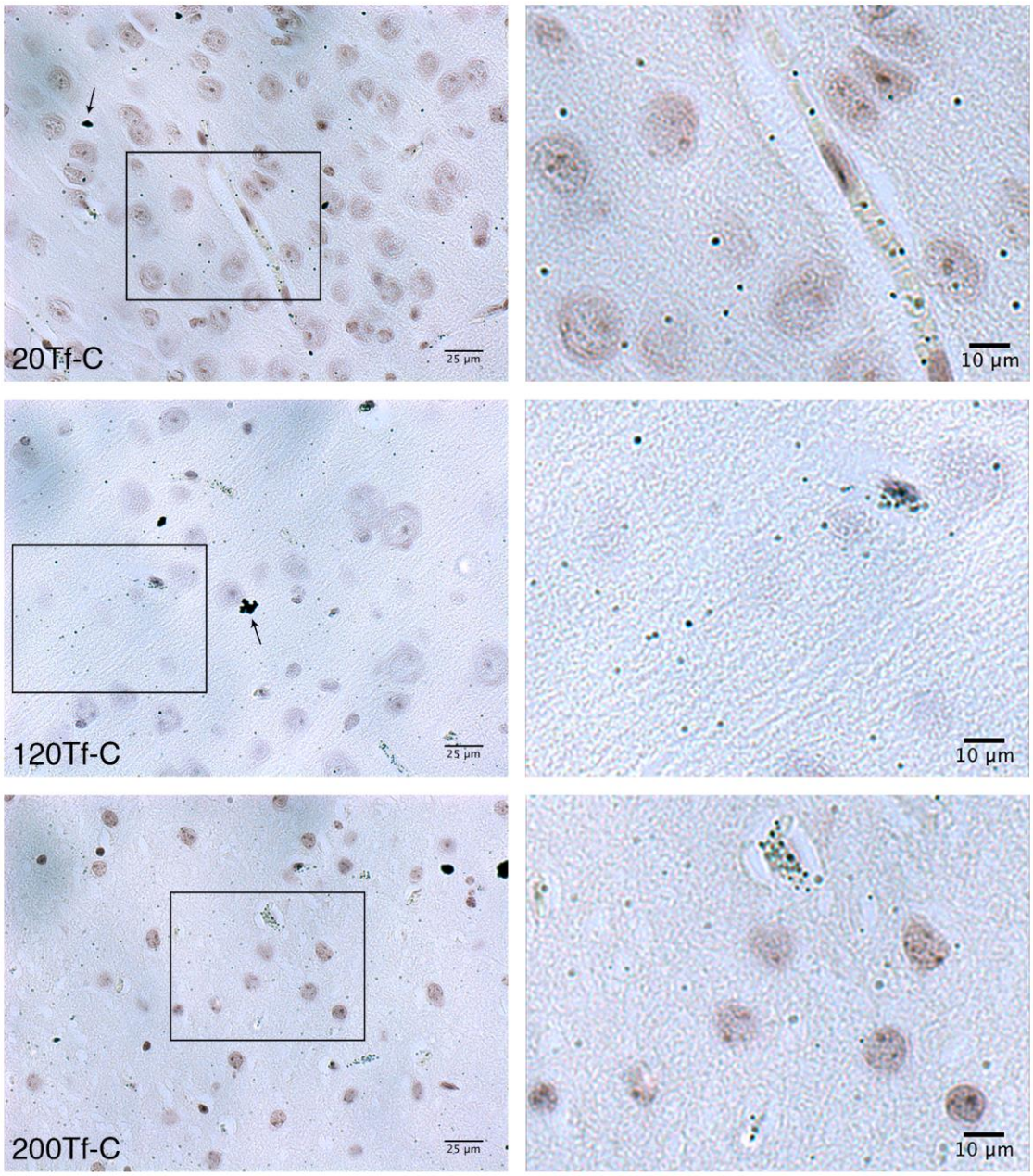

Fig 3.14 Images from silver-stained brains of 20Tf-C, 120Tf-C, and 200Tf-C formulations. Left column contains full sized image and right column contains area highlighted in black box. Arrows indicate amorphous silver stain determined to be non-specific silver deposition and were not included in the quantitative analysis.

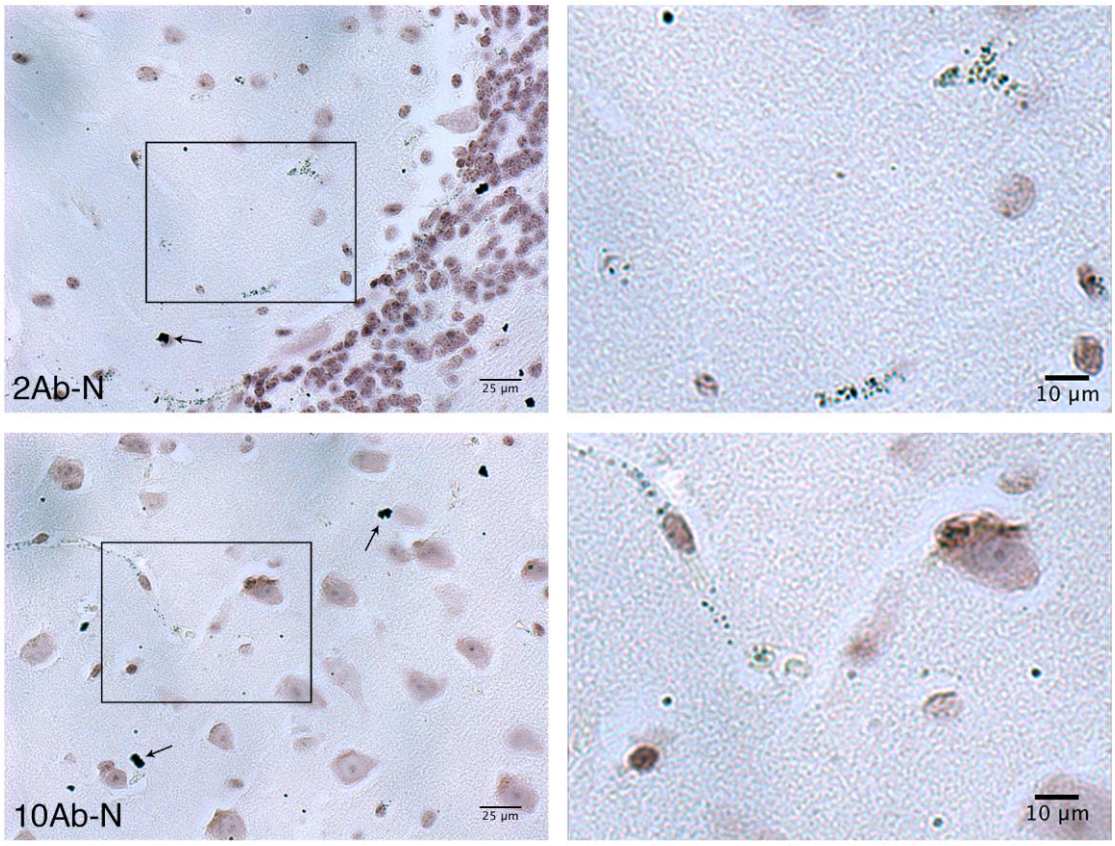

Fig 3.15 Images from silver-stained brains of 2Ab-N and 10Ab-N formulations. Left column contains full sized image and right column contains area highlighted in black box. Arrows indicate amorphous silver stain determined to be non-specific silver deposition and were not included in the quantitative analysis.

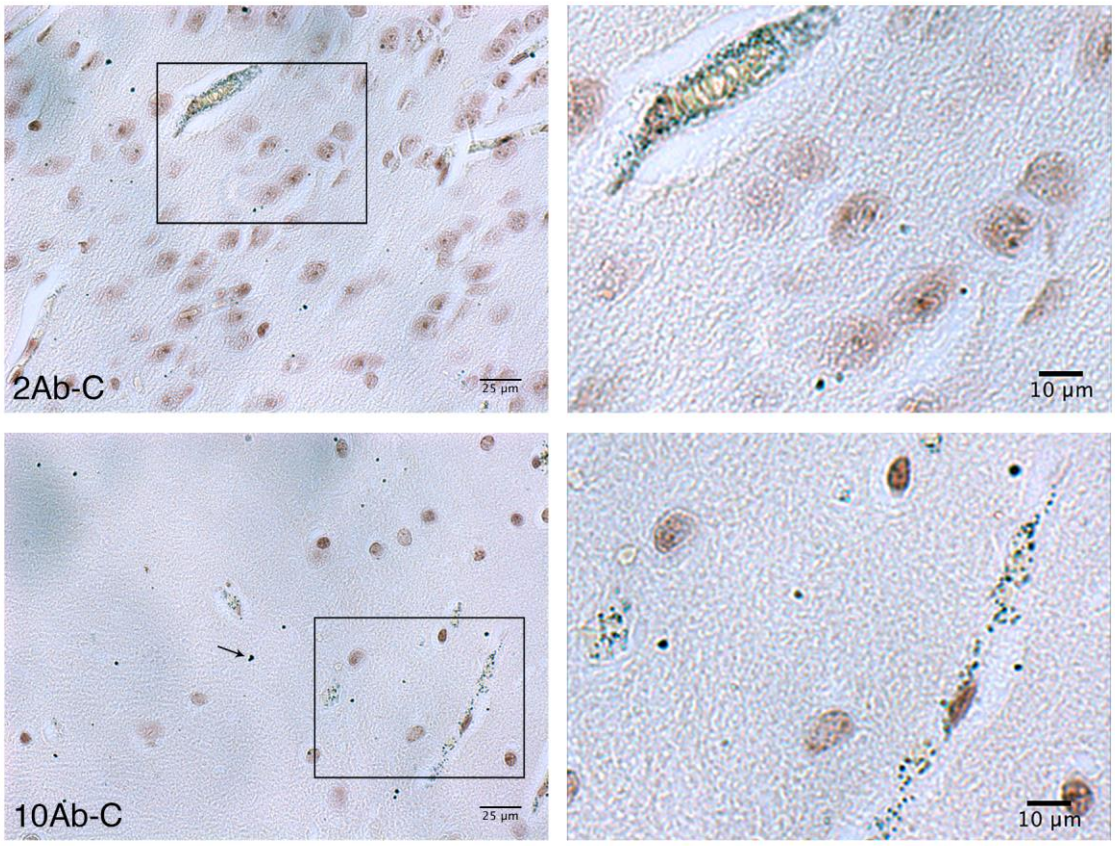

Fig 3.16 Images from silver-stained brains of 2Ab-C and 10Ab-C formulations. Left column contains full sized image and right column contains area highlighted in black box. Arrows indicate amorphous silver stain determined to be non-specific silver deposition and were not included in the quantitative analysis.

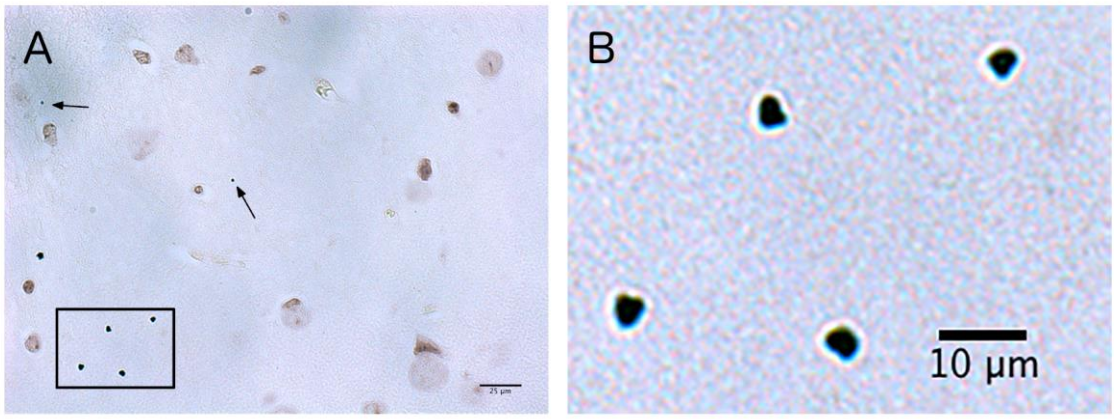

Fig 3.17 Silver staining of brain containing no gold nanoparticles. (A) Blood vessels are absent of silver stain. Rare occurrences of nanoparticle-like signal (arrows) were present in the blank brain. These instances were counted and the median value subtracted from the experimental groups. (B) Larger, amorphous silver deposition was observed in all samples, including the blank brain, and determined to be non-specific silver stain. These instances were neither counted nor included in the quantitative analysis.

3.3 Discussion

Here, we show that high-avidity, Tf-containing nanoparticles can enter the brain in vivo in mice from systemic administrations if Tf is attached to the nanoparticle through an acid-cleavable link. This improvement over our previous design where high avidity nanoparticles were restricted by the brain endothelium (16) should allow for higher brain accumulation of therapeutic agents contained in nanoparticles from a more practical, systemic dosing amount. The 20Tf-C nanoparticles did not significantly differ from the 20Tf-N, indicating, at lower avidity, the ability to outcompete endogenous Tf for TfR on the blood side of the BBB is likely the limiting factor for the processes of entering the brain. Despite the increased ability for 200Tf-C nanoparticles to enter the brain, only a 2.7-fold increase in nanoparticle accumulation was observed compared to 200Tf-N. This is likely due to the cleavage kinetics of the DAK linker. DAK was chosen because of its good stability at pH 7.4, simple incorporation into the nanoparticle design, and biologically compatible cleavage

product. The tradeoff, however, is slower cleavage at acidic pH. Radiolabeled-Tf has been observed in the brain parenchyma within 30 mins of systemic injection (9), suggesting the length of transcytosis is on the order of tens of minutes. The Tf-DAK-PEG conjugate likely does not cleave rapidly enough during this time period to dissociate all the Tf from the nanoparticle surface, causing the remaining fraction to limit entry to the brain. There is certainly room for improvement on this design using a linkage with well-controlled cleavage kinetics. An ideal linker will cleave fully at mildly acidic pH within the timespan of transcytosis but remain stable at neutral pH long enough to allow for adequate biodistribution of the nanoparticle. Unfortunately, there is yet to be a systematic study comparing pH stability with chemical structure (32).

Unlike Tf-DAK-containing nanoparticles, both Ab-C and Ab-N formulations have limited ability to enter the brain in vivo. These results are consistent with previous reports of high affinity anti-TfR Abs trafficking to the lysosome (3,21,23). If Ab-TfR interactions dictate trafficking of the endocytic vesicle, whether the nanoparticle core is covalently attached to the ligand or a separate entity should have no effect on the transcytosis capacity. The mechanism that triggers trafficking to the lysosome, however, is unclear. Experiments with anti-TfR Abs have suggested either high affinity (22) or multivalent binding (23) disrupts TfR processing. We did not observe the same limitations with high avidity, multivalent Tf-containing nanoparticles, which were able to enter the brain parenchyma, albeit at reduced amounts compared to lower-avidity nanoparticles. These results suggest that the native ligand may not adversely affect intracellular sorting of the targeted therapeutic in the same way or to the same degree as with Abs. It is well established that Tf disassociates from TfR at mildly acidic pH (33). Also, the Tf-TfR complex is known to undergo significant conformational changes following the pH change (34). It is possible that continuous occupation of TfR by pH-independent, high-affinity Abs inhibits necessary conformational changes in the Tf-TfR complex, causing sorting to the lysosome. The cleavable nanoparticles containing Tf (e.g., 200Tf-C), however, decrease the influence of the nanoparticle core on Tf-TfR interactions by physically separating the nanoparticle from the ligand. Thus, Tf sorting may be able to occur more normally, while the rest of the nanoparticle remains a passenger in the transcytotic vesicle.

The ultimate goal of our work is to develop a safe method to deliver a wide spectrum of therapeutic agents to the CNS (we have already translated to the clinic nanoparticles carrying small molecule chemotherapeutics and siRNAs). Though 200Tf-C revealed the best results here for entering the brain, the amounts achieved are still on the order of 1% of the injected dose reaching the brain parenchyma. Whether this quantity is sufficient to deliver enough therapeutic and/or imaging agent to the brain for practical use is currently under investigation. As we mentioned previously, we believe that faster release kinetics could be advantageous to increasing the amounts that reach the brain. Other chemical linkers that are sensitive to endosomal changes may also benefit from this cleavable ligand strategy, provided they break rapidly enough during transcytosis.

3.4 Conclusions

Here, we show that high avidity, Tf-containing nanoparticles are capable of entering the brain parenchyma when Tf is bound to the nanoparticle through an acid-cleavable link. Exposure to the decreased pH during the transcytosis process causes the nanoparticle core to separate from surface Tf bound to TfR and increases the nanoparticle's ability to enter the brain parenchyma. In contrast, nanoparticles containing anti-TfR Abs were essentially excluded from the brain independent of the cleavable link, likely by their trafficking to lysosomes. All Tf-containing formulations with or without the cleavable link showed greater ability to enter the brain than any Ab-containing ones. These results suggest that TfR-targeted therapeutics using the native ligand rather than a high-affinity Ab may have a greater ability to cross the BBB. Our results suggest that better understanding of TfR trafficking within the brain endothelium on a ligand-by-ligand basis is necessary to develop therapeutics that can readily engage and be successful in the TfR-mediated transcytosis process at the BBB.

3.5 Methods

Synthesis of DSS-DAK-PEG-OPSS. NHS-PEG-OPSS (5kDa, Laysan Bio) was dissolved in dry DCM at 10 mg/mL. To this was added both 20x molar excess triethylamine (TEA) and 20x DAK (2,2-bis(aminoethoxy)propane, Sigma Aldrich). The solution was stirred for 5 hrs under argon at room temperature. N-(2-aminoethyl)aminomethyl polystyrene beads (NH2-bead, EMD Millipore) presoaked in dry DCM were added at 10x molar excess to DAK and stirred for one hour under the same conditions. The solution was filtered and then precipitated by addition of diethyl ether. After sitting at room temperature for 15 min, the precipitate was isolated by centrifugation at 3220 g for 15 min. The solid was washed with ether and collected by centrifugation twice more. The product was dried under vacuum to yield a dense, white solid. The resulting DAK-PEG-OPSS was dissolved in dry DCM at 10 mg/mL. Disuccinimidyl suberate (DSS, Pierce) and TEA were added at 10x molar excess. The reaction was stirred under argon at room temperature for 90 min. The product was precipitated by addition of diethyl ether. After sitting at room temperature for 30 min, the precipitate was isolated by centrifugation at 3220 g for 15 min. The solid was washed with ether and collected by centrifugation twice more. It was dried under vacuum to yield a dense, white solid.

Preparation of Ligand-DAK-PEG-OPSS: Human holo-Tf (Sigma) or R17217 anti-TfR Ab (Biolegend) was dissolved in 100 mM NaHCO3 pH 8.5 at 10 mg/mL. DSS-DAK-PEG-OPSS (2.5x molar excess) was dissolved in DMSO at 30 mg/mL and added to the ligand. The solution reacted at room temperature for 60 min with light agitation. Excess PEG was removed and the reaction was quenched by centrifugation through a 50 kDa MWCO spin filter (EMD Millipore) at 14000 g for 5 min. The retentate was washed with 10 mM NaH2PO4 pH 8.0. This process was repeated for a total of three washes. Conjugation was verified by MALDI-TOF (Voyager DE Pro, PerSeptive Biosystems) using a sinapinic acid matrix. Multi-PEGylated species were removed from the mixture by hydrophobic interaction chromatography (HIC) on a AKTA Prime Plus FPLC System (GE Healthcare, 5mL HiTrap Phenyl column) using a high salt buffer of 1 M ammonium sulfate with 50 mM sodium

phosphate pH 7.5 and an elution buffer consisting of the latter salt only (Fig. S1B,D). Iron citrate (2.5x molar excess) in 100 mM NaHCO3 pH 8.5 was added to the Tf-DAK-PEG conjugate following HIC. Excess iron was removed through centrifugation using a 50 kDa MWCO spin filter, then the conjugate was washed with 10 mM NaH2PO4 pH 8.0. This process was repeated for a total of five washes. The amount of iron loaded to the Tf was measured by UV-VIS using the ratio of A465/A280. This value was compared to the A465/A280 ratio of the non-processed holo-Tf. A value ≥80% of the unprocessed ratio indicated adequate iron reloading.

The amount of mono-PEGylated ligand remaining in the separated mixture was determined by a dipyridyl disulfide cleavage assay. The Ligand-DAK-PEG mixture was diluted in 10 mM NaH2PO4 pH 8.0 with 1 mM ethylenediaminetetraacetic acid (EDTA) and the absorbance at 343 nm was recorded. Dithiothreitol (DTT) was added to the protein solution to give a final concentration of 1.5 mg/mL DTT. After sitting for 15 min at room temperature, the absorbance at 343 nm was recorded again. The difference in A343 was calculated and compared to a standard curve prepared from pure, noncleavable, mono-PEGylated Tf-PEG-OPSS or Ab-PEG-OPSS as necessary. The calculated OPSS concentration was used to determine the concentration of Ligand-DAK-PEG-OPSS in the mixture.

pH-Dependent Stability of Tf-DAK-PEG-OPSS: Purified Tf-DAK-PEG-OPSS was prepared at approximately 5 mg/mL in either 10 mM NaH2PO4 pH 8.0 or 100 mM NaOAc pH 5.5 at 37°C. Aliquots were removed at various time points and diluted 1:10 in 10 mM NaH2PO4 pH 8.0 and frozen on CO2(s). After all aliquots were taken, samples were thawed and analyzed simultaneously by MALDI-TOF as described above.

Preparation of Ligand-PEG-OPSS: Either human holo-Tf or R17217 Ab was dissolved in 100 mM NaHCO3 pH 8.5 at 0.5 mg/mL. NHS-PEG-OPSS (5 kDa, Laysan Bio) was added at 2.5x molar excess. The reaction sat at room temperature for 60mins under light rocking. Excess PEG was removed and the reaction was quenched by centrifugation through a 50 kDa MWCO spin filter at 14000 g for 5 mins. The retentate was washed with 10 mM NaH2PO4

pH 8.0 twice more. Conjugation was verified by MALDI-TOF using a sinapinic acid matrix. For Tf-PEG-OPSS, the monoPEGylated fraction was isolated by HPLC (Agilent 1200 series) using two TOSOH TSK gel G3000swxl columns in series followed by HIC and iron reloading as described previously (Fig. S1A). The monoPEGylated Ab-PEG-OPSS was isolated solely through HIC (Fig. S1C). Both conjugates were stored in 10 mM NaH2PO4 pH 8.0 at 4°C until use.

Preparation of Nanoparticles: Either Ligand-DAK-PEG-OPSS or Ligand-PEG-OPSS was added to 50 nm gold nanoparticles (BBI International) at the appropriate molar excess (e.g. nanoparticles dosed with 20x molar excess Tf-PEG produced 20 Tf/NP). The solution was stirred vigorously for 60 min then methoxy-PEG-thiol (mPEG-SH) (5kDa, Laysan Bio) was added at 10,000x molar excess and stirred for another 30 min. The nanoparticles were collected by centrifugation at 20,000 g for 10 min, washed with dH2O and sonicated for 5 min. This process was repeated twice more to give three total washes. After the final centrifugation, the particles were resuspended in 10 mM NaH2PO4 pH 8.0. To prepare untargeted nanoparticles (mPEG), only mPEG-SH was added to 50 nm gold cores for 60 min with vigorous stirring. The nanoparticles were purified as described above.

Nanoparticle Characterization: Nanoparticles were characterized using a Brookhaven Instruments ZetaPALS. Nanoparticles were diluted in PBS and hydrodynamic diameter was measured using dynamic light scattering (DLS). Zeta potential was measured in 1 mM KCl (pH 7.0) using a target residual of 0.02. Five runs were performed for both the nanoparticle diameter and zeta potential measurements.

Nanoparticle Binding Assay: Neuro2A cells (ATCC) were grown at 37°C, 5% CO2 in DMEM+10% FBS with penicillin/streptomycin. Cells were washed with PBS and removed using a cell scraper. After centrifugation at 300 g for 3 min, the cells were fixed using BD Cytofix (BD Biosciences) for 20 min at 4°C. The cells were then washed and resuspended in PBS + 4% BSA. Increasing concentrations of nanoparticles were added to $1x10^6$ cells at $5x10^6$ cells/mL and sat at RT with light agitation every 15 min to prevent cells from settling.

After 90 min, the cells were added to 12 mL PBS and centrifuged at 300 g for 3 min. The cells were resuspended in 12 mL fresh PBS and centrifuged again. This washing procedure was performed for a total of three times. Finally, the cell solution was added to a 96 well plate, silver enhancement solution (Ted Pella) was added and fluorescence read (310 nm excitation, 400 nm emission) using a plate reader (Tecan, infinite M200). Data were fit to a Langmuir binding isotherm using Matlab, and KD and Bmax were calculated.

To measure avidity after exposure to mild acid, 200Tf-C and 10Ab-C formulations were incubated for four hours at 37°C in 100 mM NaOAc, pH 5.5. The nanoparticles were collected by centrifugation at 20,000 g for 10 min and washed in dH2O twice. After the final wash, they were resuspended in PBS + 4% BSA, added to Neuro2A cells and analyzed as described above.

Nanoparticle Transcytosis Across bEnd.3-coated Transwells: bEnd.3 cells (ATCC) were grown in 37°C, 5% CO2 in DMEM+10% FBS with penicillin/streptomycin. The cells were seeded on 12 mm polyester-coated transwell supports (Corning) at 82,500 cells/well. Media was replaced in the apical and basal wells every two-three days. Transepithelial electrical resistance (TEER) was measured in an Endohm chamber and using an EVOM resistance meter (World Precision Instruments). Once TEER had reached ≥30 Ohms*cm2, transcytosis experiments were performed. Prior to introduction of nanoparticles, both compartments of the transwell were washed with serum-free DMEM and allowed to equilibrate for 1hr. Nanoparticles were added at 1x1010 particles/well to the apical well. At various time points, the entire volume was removed from the basal well and replaced with fresh media. The aliquot was diluted in water and measured for gold content using an HP 7500 ICP-MS (Agilent). A Babington type nebulizer in a Pyrex Scott-type spray chamber was used for nebulization at a carrier flow rate of 1.3 L/min of argon. The argon plasma power was 1200 W with a flow of 15 L/min and an auxiliary flow of 1.1 L/min. A calibration curve of known concentrations of non-targeted AuNPs (mPEG) was prepared and used to determine gold concentration in the aliquots. Reported values are the average of three wells per group, except for the 20Tf-C, group which contains four measurements. The error shown is standard error

of the mean. Pairwise group comparisons testing for statistically significant differences were performed using a two-sample t-test in Matlab.

For the Tf-competition assay, both compartments of the transwell were washed and incubated in DMEM + 2.5 mg/mL hTf for 1 hr prior to nanoparticle introduction. The assay was performed as described above using DMEM + 2.5 mg/mL Tf as the replacement media. Three wells were performed for each nanoparticle formulation in the competition assay.

To determine intracellular gold content, the transwells were removed from the basal compartment after 8 hrs and the apical volume was removed. Cells were washed 8 times with 200 μL PBS to clear unbound nanoparticles then lysed by addition of 100 μL RIPA buffer (Pierce) to each transwell. The lysate was centrifuged at 14000 g for 5 min to pellet cell debris and the supernatant prepared for ICP-MS as described above. The lysates were quantitated with an Agilent 8800 triple quadrupole (ICP-QQQ) ICP-MS using a MicroMist nebulizer and Scott-type spray chamber with a carrier gas flow rate of 1.05 L/min of argon. The plasma power was 1600 W with a flow of 15 L/min.

Animal Injections and Tissue Processing: All animals were treated according to the NIH Guidelines for Animal Care and Use as approved by the Caltech Institutional Animal Care and Use Committee. Three female BALB/c mice (Jackson Laboratory) were each injected with 4.5x1011 nanoparticles via lateral tail vein for all nanoparticle formulations. The mice were euthanized by CO2 asphyxiation after 12 hrs. The brains were resected and bisected with a manual mid-sagittal cut before fixing both hemispheres overnight in 10% neutral buffered formalin (Sigma). Individual hemispheres were dehydrated in increasing concentrations of ethanol (3 x 30 min each for 50, 70, 95 and 100% EtOH), followed by xylenes (3 x 30 min) and 50:50 xylene:paraffin mixture (1 x 30 min). The tissues were then incubated in molten paraffin (3 x 1 hr) at 60°C. The brains were placed in a paraffin mold and stored at 4°C until sectioning. A Leica 1512 microtome was used to cut 5 μm sections.

Silver Enhancement Staining of Mouse Brains: All glassware used was washed with Farmer's Solution (9 parts 10% sodium thiosulfate and 1 part 10% potassium ferricyanide) for 20 min prior to tissue processing to reduce non-specific silver staining. Paraffin-

embedded sections were deparaffinized in xylenes, rehydrated using decreasing concentrations of ethanol and washed in pure water (3 x 1min). Silver enhancement solution (Ted Pella) was added to the sections for 20 min. The stained sections were immediately placed in water for 5 min followed by counterstaining with haematoxylin for 2 min. They were then dehydrated with increasing concentration of ethanol and xylenes and mounted with Permount (Fisher).

Image Analysis, Nanoparticle Counting and Statistics: Processed sections were imaged using an Olympus IX50 microscope with a 40x objective and QCapture Pro 6 imaging software (QImaging). Images were acquired from sections near the mid-sagittal plane. A total of 40 images were acquired from each tissue section, consisting of ten images taken from rostral, ventral, dorsal and cerebellar regions of the brain. For each region, an arbitrary starting point was chosen and imaged. Subsequent images were obtained at consistent, transverse intervals along the entire length of the region. Nanoparticles observed distinctly outside the margins of blood vessels were counted as parenchymal particles. All image acquisition and particle counting steps were performed blindly. A brain containing no AuNP's (blank) was processed and imaged simultaneously with the experimental groups. Instances of nanoparticle-like signal (Fig 3.17, arrows) were observed in the blank brain and determined to be non-specific silver stain deposition. The median value of these phenomena was subtracted from all the experimental groups. Large, amorphous areas of silver stain (Fig 3.17, inset) were also observed in both the blank and experimental groups and concluded to be non-specific silver deposition. These instances were not counted and were excluded from the quantitative analysis. Pairwise group comparisons testing for statistically significant differences were performed using the Wilcoxon rank-sum test in Matlab (Table 3.3).

3.5 References

1. Canton, I., & Battaglia, G. (2012). Endocytosis at the nanoscale. *Chemical Society Reviews*, *41*(7), 2718-2739.
2. Sahay, G., Alakhova, D. Y., & Kabanov, A. V. (2010). Endocytosis of nanomedicines. *Journal of Controlled Release*, *145*(3), 182–195.
3. Mellman, I. (1996). Endocytosis and Molecular Sorting. *Annual Reviews of Cell and Developmental Biology*, *12*, 575–625.
4. Mellman, I., Fuchs, R., & Helenius, A. (1986). Acidification of the endocytic and exocytic pathways. *Annual Review of Biochemistry*, *55*, 663–700.
5. Visser, C. C., Voorwinden, L. H., Crommelin, D. J. A., Danhof, M., & Boer, A. G. de. (2004). Characterization and Modulation of the Transferrin Receptor on Brain Capillary Endothelial Cells. *Pharmaceutical Research*, *21*(5), 761–769.
6. Binauld, S., & Stenzel, M. H. (2013). Acid-degradable polymers for drug delivery: a decade of innovation. *Chemical Communications*, *49*(21), 2082.
7. Gao, W., Chan, J. M., & Farokhzad, O. C. (2010). pH-Responsive Nanoparticles for Drug Delivery. *Molecular Pharmaceutics*, *7*(6), 1913–1920.
8. Leriche, G., Chisholm, L., & Wagner, A. (2012). Cleavable linkers in chemical biology. *Bioorganic & Medicinal Chemistry*, *20*(2), 571–582.
9. Fishman, J. B., Rubin, J. B., Handrahan, J. V., Connor, J. R., & Fine, R. E. (1987). Receptor-mediated transcytosis of transferrin across the blood brain barrier. *Journal of Neuroscience Research*, *18*(2), 299–304.
10. Choi, C. H. J., Alabi, C. A., Webster, P., & Davis, M. E. (2010). Mechanism of active targeting in solid tumors with transferrin-containing gold nanoparticles. *Proceedings of the National Academy of Sciences*, *107*(3), 1235–1240.
11. Choi, C. H. J., Zuckerman, J. E., Webster, P., & Davis, M. E. (2011). Targeting kidney mesangium by nanoparticles of defined size. *Proceedings of the National Academy of Sciences*, *108*(16), 6656–6661.
12. Cabezón, I., Manich, G., Martin-Venegas, R., Camins, A., Pelegrí, C., & Vilaplana, J. (2015). Trafficking of gold nanoparticles coated with the 8D3 anti-transferrin

receptor antibody at the mouse blood-brain barrier. *Molecular Pharmaceutics*, *12*(11), 4137-4145.

13. Sperling, R. A., Rivera Gil, P., Zhang, F., Zanella, M., & Parak, W. J. (2008). Biological applications of gold nanoparticles. *Chemical Society Reviews*, *37*(9), 1896–1915.
14. Dykman, L. A., & Khlebtsov, N. G. (2011). Gold nanoparticles in biology and medicine: recent advances and prospects. *Acta Naturae*, *3*(2), 34–55.
15. Sykes, E. A., Dai, Q., Tsoi, K. M., Hwang, D. M., & Chan, W. C. W. (2014). Nanoparticle exposure in animals can be visualized in the skin and analysed via skin biopsy. *Nature Communications*, *5*, 3796.
16. Wiley, D. T., Webster, P., Gale, A., & Davis, M. E. (2013). Transcytosis and brain uptake of transferrin-containing nanoparticles by tuning avidity to transferrin receptor. *Proceedings of the National Academy of Sciences*, *110*(21), 8662–8667.
17. Uchida, Y., Ohtsuki, S., Katsukura, Y., Ikeda, C., Suzuki, T., Kamiie, J., & Terasaki, T. (2011). Quantitative targeted absolute proteomics of human blood-brain barrier transporters and receptors. *Journal of Neurochemistry*, *117*(2), 333–345.
18. Widera, A., Norouziyan, F., & Shen, W. C. (2003). Mechanisms of TfR-mediated transcytosis and sorting in epithelial cells and applications toward drug delivery. *Advanced Drug Delivery Reviews*, *55*(11), 1439–1466.
19. Friden, P. M., Walus, L. R., Musso, G. F., Taylor, M. A., Malfroy, B., & Staryzk, R. M. (1991). Anti-transferrin receptor antibody and antibody-drug conjugates cross the blood-brain barrier. *Proceedings of the National Academy of Sciences*, *88*(11), 4771–4775.
20. Lajoie, J. M., & Shusta, E. V. (2014). Targeting Receptor-Mediated Transport for Delivery of Biologics Across the Blood-Brain Barrier. *Annual Review of Pharmacology and Toxicology*, *55*(1), 141023145729002.
21. Yu, Y. J., Zhang, Y., Kenrick, M., Hoyte, K., Luk, W., Lu, Y., Atwal, J., et al. (2011). Boosting Brain Uptake of a Therapeutic Antibody by Reducing Its Affinity for a Transcytosis Target. *Science Translational Medicine*, *3*(84), 84ra44–84ra44.

22. Bien-Ly, N., Yu, Y. J., Bumbaca, D., Elstrott, J., Boswell, C. A., Zhang, Y., et al. (2014). Transferrin receptor (TfR) trafficking determines brain uptake of TfR antibody affinity variants. *Journal of Experimental Medicine*, *3*(84), 84ra43.
23. Niewoehner, J., Bohrmann, B., Collin, L., Urich, E., Sade, H., Maier, P., et al. (2014). NeuroResource. *Neuron*, *81*(1), 49–60.
24. Sade, H., Baumgartner, C., Hugenmatter, A., Moessner, E., Freskgård, P.-O., & Niewoehner, J. (2014). A Human Blood-Brain Barrier Transcytosis Assay Reveals Antibody Transcytosis Influenced by pH-Dependent Receptor Binding. *PLoS ONE*, *9*(4), e96340.
25. Lee, H. J., Engelhardt, B., Lesley, J., Bickel, U., & Pardridge, W. M. (2000). Targeting rat anti-mouse transferrin receptor monoclonal antibodies through blood-brain barrier in mouse. *Journal of Pharmacology and Experimental Therapeutics*, *292*(3), 1048–1052.
26. Ulbrich, K., Hekmatara, T., Herbert, E., & Kreuter, J. (2009). Transferrin- and transferrin-receptor-antibody-modified nanoparticles enable drug delivery across the blood–brain barrier (BBB). *European Journal of Pharmaceutics and Biopharmaceutics*, *71*(2), 251–256.
27. Jones, A. R., & Shusta, E. V. (2007). Blood–Brain Barrier Transport of Therapeutics via Receptor-Mediation. *Pharmaceutical Research*, *24*(9), 1759–1771.
28. Nance, E. A., Woodworth, G. F., Sailor, K. A., Shih, T. Y., Xu, Q., Swaminathan, G., et al. (2012). A Dense Poly(Ethylene Glycol) Coating Improves Penetration of Large Polymeric Nanoparticles Within Brain Tissue. *Science Translational Medicine*, *4*(149), 149ra119–149ra119.
29. Cao, X., Ye, Y., & Liu, S. (2011). Gold nanoparticle-based signal amplification for biosensing. *Analytical Biochemistry*, *417*(1), 1–16.
30. Brown, R. C., Morris, A. P., & O'Neil, R. G. (2007). Tight junction protein expression and barrier properties of immortalized mouse brain microvessel endothelial cells. *Brain Research*, *1130*(1), 17–30.

31. Cho, E. C., Zhang, Q., & Xia, Y. (2011). The effect of sedimentation and diffusion on cellular uptake of gold nanoparticles. *Nature Nanotechnology*, *6*(6), 385–391.
32. Leriche, G., Chisholm, L., & Wagner, A. (2012). Cleavable linkers in chemical biology. *Bioorganic & Medicinal Chemistry*, *20*(2), 571–582.
33. Dautry-Varsat, A., Ciechanover, A., & Lodish, H. F. (1983). pH and the Recycling of Transferrin during Receptor-Mediated Endocytosis. *Proceedings of the National Academy of Sciences*, *80*, 2258–2262.
34. Luck, A. N., & Mason, A. B. (2012). Structure and dynamics of drug carriers and their interaction with cellular receptors: Focus on serum transferrin. *Advanced Drug Delivery Reviews*, *65*(8), 1012–1018.

Chapter IV

DEVELOPMENT OF DOPAMINE-LOADED MUCIC ACID POLYMER NANOPARTICLES FOR DELIVERY TO THE BRAIN

4.1 Introduction

4.1.1 Parkinson's Disease – Pathology and Pharmacologic Treatment

With successful delivery of high avidity nanoparticles to the brain using the DAK linker described in the previous chapter, focus shifted to determining whether nanoparticles could be prepared that deliver therapeutic quantities of drug across the BBB.

One condition that could greatly benefit from nanoparticle drug delivery is Parkinson's disease (PD). PD is a complex neuropsychiatric disorder characterized by rest tremors, bradykinesia, rigidity, and autonomic dysfunction. The disease is caused by breakdown of dopaminergic neurons within the substantia nigra leading to decreased quantities of the neurotransmitter dopamine in the striatum.

PD, similar to AD described in Section 1.1, can currently be treated only with limited, symptomatic therapy. Dopamine (DA) replacement through oral levodopa (L-DOPA) is the foundation of treatment for PD. DA is a small, hydrophilic molecule incapable of crossing the BBB from the blood. L-DOPA contains a carboxylic acid off a chiral carbon also bonded to an amine group. This structure is very similar to the amino acid L-tyrosine (Tyr) (Fig 4.1), a small molecule with an influx carrier protein (SCP) expressed on the BBB (see section 1.2.1) (1). L-DOPA is so structurally similar Tyr that it can enter the CNS through the same SCP. Once in the CNS, it is taken up by presynaptic neurons and metabolized to DA through the enzyme aromatic amino acid decarboxylase (2). Cotzias discovered L-DOPA as an effective treatment for PD in 1967 (3) and its use was widely adapted by clinicians soon after.

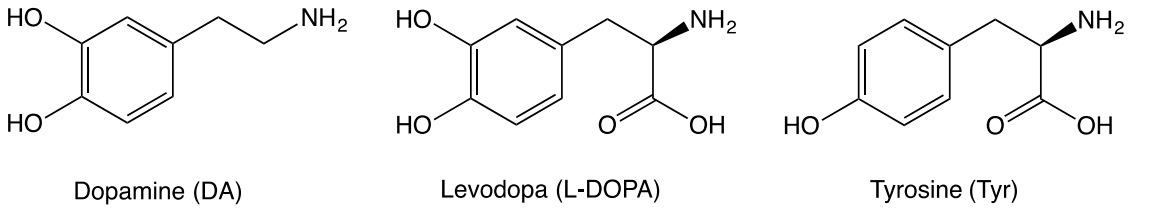

Fig 4.1 Structure of dopamine, L-DOPA and tyrosine. Structural similarities between L-DOPA and Tyr allow the DA analog to cross the BBB through the same solute channel as Tyr where it is then metabolized to DA by pre-synaptic neurons.

Despite L-DOPA's ability to relieve symptoms of PD, its efficacy over time begins to diminish. This occurs for two major reasons: (i) decreased dopamine buffering by pre-synaptic neurons and (ii) loss of tonic dopamine release. PD is a progressive neurodegenerative condition, so despite treatment with L-DOPA, DA-producing neurons will continue to breakdown without disease-modifying intervention. Early on in the disease, when there is still a good amount of viable, dopaminergic neurons, L-DOPA that enters the brain is taken up by pre-synaptic neurons and used as a reserve for when endogenous dopamine stores run low. As these dopaminergic neurons die, less L-DOPA can be retained and used only when necessary and the drug is instead rapidly converted to DA and released into the synapse. This process leads to the second problem. In healthy individuals, DA is constantly released from dopaminergic neurons causing continuous stimulation of post-synaptic neurons. As the PD patient becomes more dependent on L-DOPA, the DA stimulation becomes more and more pulsatile based on the plasma L-DOPA concentration. It's believed that this shift from continuous to pulsatile stimulation affects the behavior of postsynaptic receptors leading to unusual motor movements, known as levodopa-induced dyskinesia (LID) (Fig 4.2). There's been some suggestion this may also affect downstream neural pathways causing some debate that in the very long term (>10yrs treatment) L-DOPA may actually be neurotoxic. The goal of all treatment regimes is to prevent motor complications for as long as possible through minimal L-DOPA dose and adjunctive therapies (4).

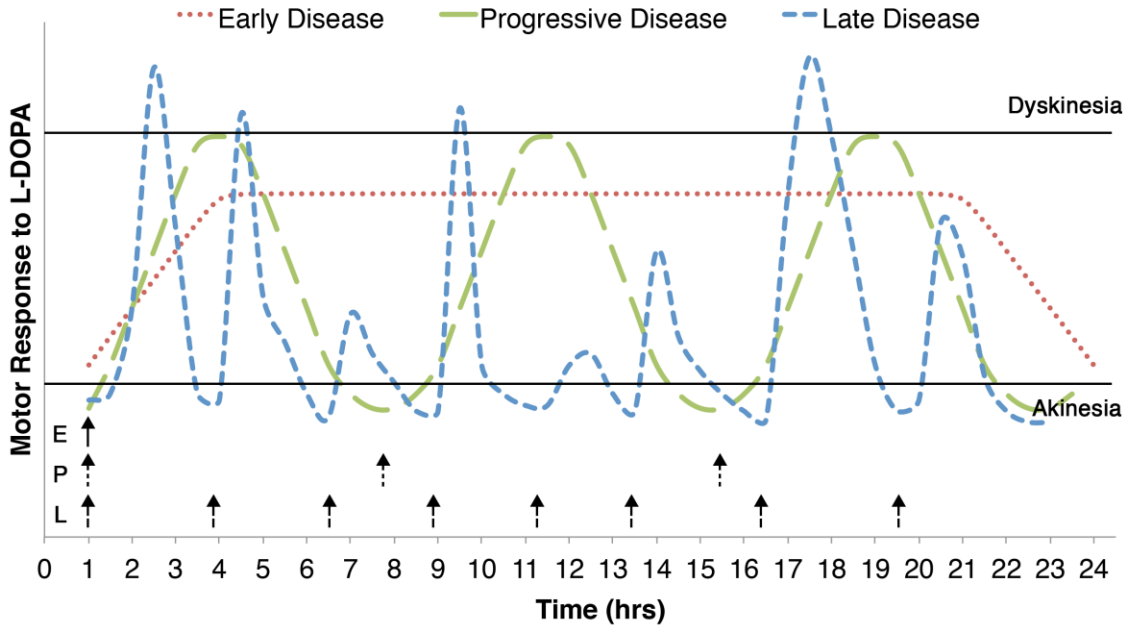

Fig 4.2 Changes in patient response to oral L-DOPA over time. Patients typically respond well to L-DOPA initially due to buffering capacity of still healthy neurons (early disease). As the disease advances, patients require more exogenous L-DOPA and begin to experience motor abnormalities but responses to treatment are consistent (progressive disease). As more and more dopaminergic neurons breakdown, greater amounts of L-DOPA are required and responses greatly fluctuate from dose to dose. Motor abnormalities are common (late disease). Solid black lines indicate thresholds for akinesias (inability to move) and dyskinesias (unwanted, excessive movement). Arrows indicate dosing times for early (E), progressive (P) and late (L) disease.

4.1.2 Mucic Acid Polymer Nanoparticles for Dopamine Delivery

Developing a therapeutic that can deliver native DA to the striatum in a tonic fashion can potentially overcome these long-term complications. Nanoparticles are a promising platform to achieve this goal due to their ability to deliver large quantities of drugs to specific tissues at well-controlled release rates (5) (see section 1.4.2). Despite the significant benefit nanoparticles offer to PD treatment, at the time of writing and to this author's knowledge,

only one study has been published detailing DA-loaded nanoparticles designed to cross the BBB from the blood (6). In this work, PLGA nanoparticles were loaded with DA and given to parkinsonian rats intravenously with a single or double dose of 5 mg/kg DA. Even at this low dosing, the authors found a significant increase in brain DA and DA metabolites seven days after a single dose. The rats also exhibited significantly improved motor function when given the nanoparticles with no signs of either central or peripheral toxicity.

It is interesting that these improvements were made using non-targeted nanoparticles with diameters around 120 nm. Theoretically, non-targeted nanoparticles should be prevented from crossing a healthy BBB. There is suggestion that the PD model used in this study causes increased BBB permeability at the site of the lesion, allowing normally excluded molecules to enter the CNS (7). It is also possible that circulating proteins bound to residual surfactant on the nanoparticle surface, causing random transcytosing proteins to be present on the nanoparticle (8). Regardless of the mechanism that allowed nanoparticle entry to the brain, Pahuja et al.'s results indicate delivery of DA to the brain using nanoparticles is a viable approach for PD treatment.

Using the acid-cleavable targeting strategy detailed in Chapter III, it may be possible to increase the delivery of DA-loaded nanoparticles to the brain. The Davis lab has previously synthesized a novel drug-delivery polymer (mucic acid polymer, MAP) (9). MAP is a hydrophilic polymer composed of mucic acid and PEG repeat units. Carboxylic acid groups are present on the polymer backbone to allow conjugation of drug molecules whose release rate can be tailored depending on the conjugation chemistry. The MAP-drug conjugate will spontaneously form nanoparticles in water and express vicinal diols on its surface (Scheme 4.1). The surface diols can then be used to attach targeting ligands to the nanoparticle (detailed in section 4.1.3). The MAP polymer has already been used to prepare antibody-containing, chemotherapeutic-loaded nanoparticles that can effectively treat cancer xenografts over several weeks with few doses (10). A similar, cationic MAP variant has also been prepared and used to deliver small interfering RNA's (11), showing that the MAP polymer can be modified to deliver different types of therapeutics. A DA-loaded MAP nanoparticle could serve as an effective PD treatment.

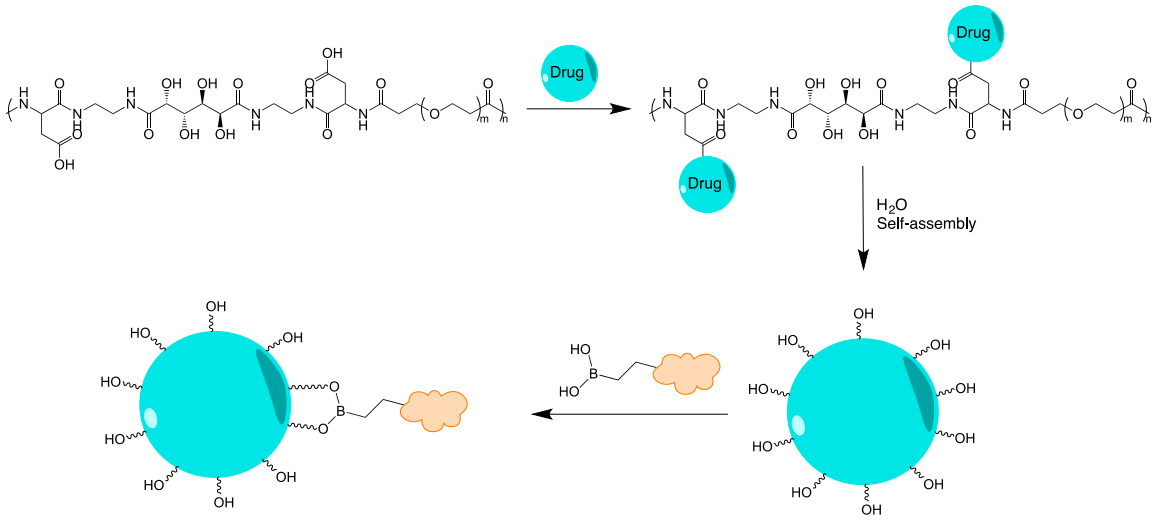

Scheme 4.1 The MAP polymer and formation of targeted MAP nanoparticles. Drugs are conjugated to carboxylic acid groups on the MAP polymer. The MAP-drug conjugate spontaneously assembles into spherical nanoparticles in water with vicinal diols on the nanoparticle surface. Targeting molecules containing boronic acid moieties can be added to the nanoparticle surface through boronic acid ester formation with the vicinal diols.

4.1.3 Boronic Acid-PEG Targeting Ligands

The surface diols on the MAP nanoparticles are capable of forming covalent bonds with boronic acid (BA)-functionalized targeting ligands. This chemistry was used to add trastuzumab, an anti-HER2 mAb, to the surface of chemotherapy-loaded MAP nanoparticles (10). BA can only react with vicinal diols to form a boronic acid ester when it is in its tetrahedral, anionic form. The MAP diol stereochemistry and BA structure was modified to maximize ligand binding to the nanoparticle. A phenyl-BA with a meta nitro group (nPBA) was found to attach to the nanoparticle with a binding constant of 1420 M^{-1} at physiologic pH. Interestingly, the pKa of this reaction was determined to be 6.8. This means that at extracellular pH, the nPBA will strongly bind MAP, but under mildly acidic conditions, the nPBA will convert to its non-reactive, trigonal form, releasing the nPBA from the nanoparticle surface (Scheme 4.2). Adding Tf to the nanoparticle through a boronic ester will allow rapid disassociate of the targeting ligand at mildly acidic pH and should provide

superior brain uptake compared to the slower cleavage of the previously investigated DAK linker (Chapter III). The near instantaneous disassociation of nPBA-PEG-Tf from the nanoparticle surface at pH < 6.8 will remove all possible restrictions imposed by either the receptor-bound Tf restricting movement of the nanoparticle into the CNS or the nanoparticle core restricting conformational changes in the Tf-TfR complex needed for transcytosis. Because of this pKa, an nPBA-PEG-Tf conjugate will be ideal as an acid-cleavable targeting ligand for the nanoparticle.

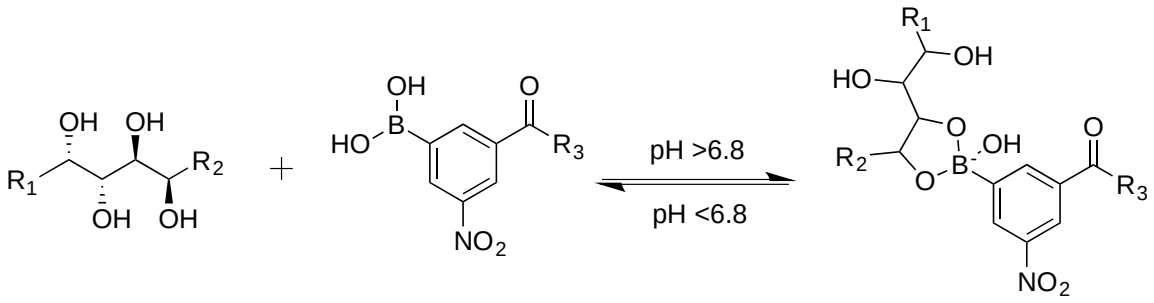

Scheme 4.2 pH-dependent interaction between MAP vicinal diols and nPBA.

4.2 Results and Discussion

4.2.1 Dopamine Forms Stable Aryl Imines Under Mild Conditions

To first determine whether MAP polymers could be used in PD, the ability of the MAP polymer to bind and release native DA was determined. Since the goal of this work was to prepare nanoparticles that can release native DA molecules in the brain, focus was placed on combining DA and MAP such that the DA would release from the polymer under extracellular conditions within the brain. Using this approach Tf-containing MAP-DA nanoparticles can accumulate within extracellular space of the brain and slowly release DA in a controlled fashion over a long period of time (Fig 4.3).

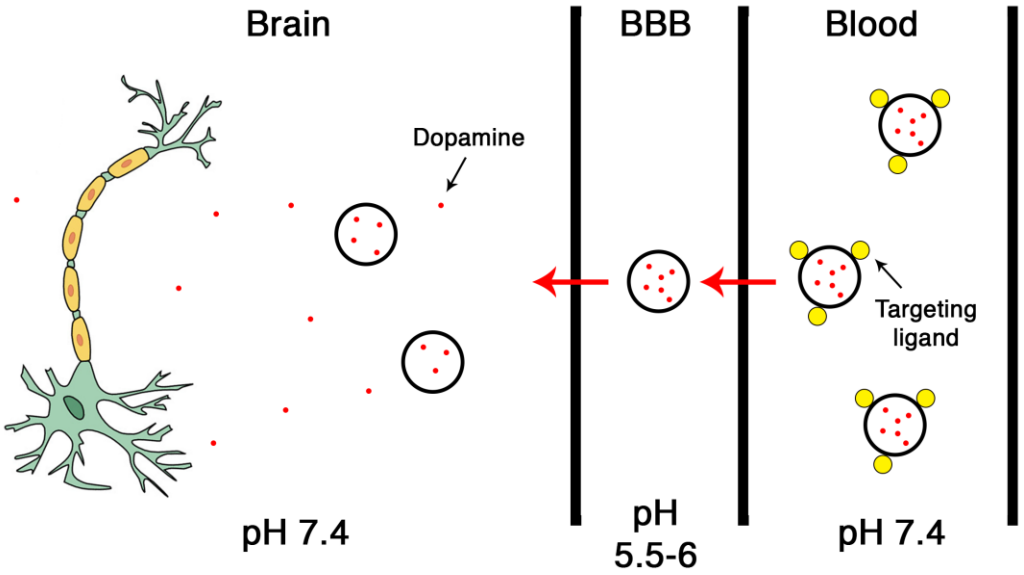

Fig 4.3 Delivery of dopamine to the brain using targeted MAP-DA nanoparticles. Tf-containing MAP nanoparticles loaded with DA are injected intravenously. The targeting ligand detaches during transcytosis to increase brain accumulation of intact nanoparticles. The nanoparticles then reside in the CNS extracellular space and slowly release dopamine over time.

DA has limited functional groups available for modification that can exhibit the desired behavior. The most promising approach is formation of an imine between the primary amine of DA and the MAP polymer. Imines are labile chemical bonds formed from the condensation of aldehydes and amines. They are rarely used in drug delivery devices because they are typically highly unstable at acidic pH; however, in this context where drugs are designed to release at neutral pH, imines may be capable of breaking under these conditions while other acid-cleavable bonds, such as acetals/ketals and hydrazones, may not. Several examples exist in the literature of imine-based drug delivery devices that show rapid drug release in acidic conditions but slow, prolonged release over days at neutral pH (12,13).

Formation of an imine between DA and small molecule aldehydes was first investigated before adding the molecule to MAP. Imines were formed as previously described (14) using equimolar concentrations of DA and aldehyde in the presence of

catalytic pyrrolidine and activated molecular sieves. The most stable and reproducible imine formation occurred between DA and 4-formylbenzoic acid. Unfortunately, the catechol group of DA also oxidizes under the optimal reaction conditions, forming a quinone product (Fig 4.4). Efforts were made in reactions with MAP to minimize potential sources of oxidation in the DA-containing reaction steps.

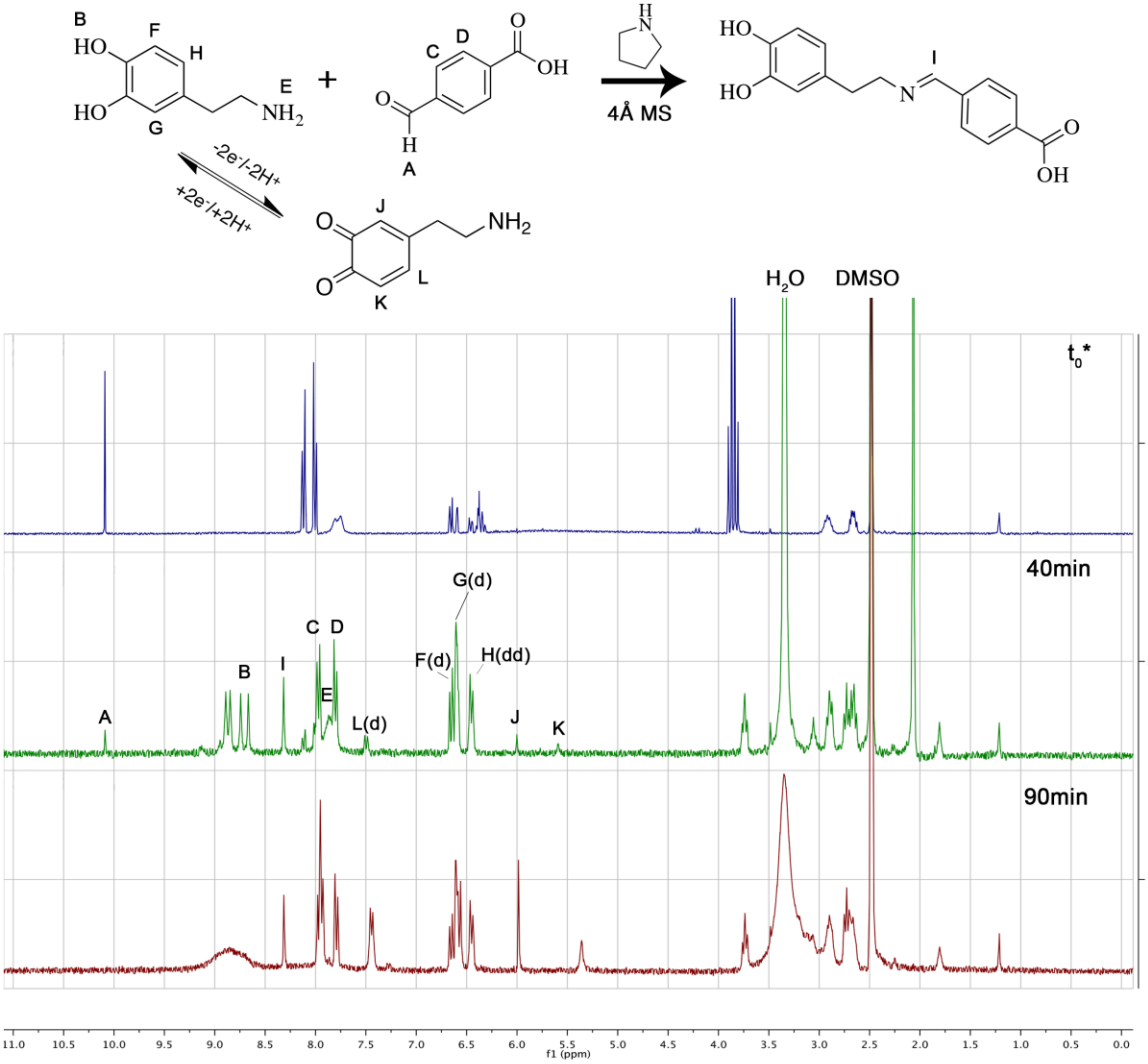

Fig 4.4 Imine formation between DA and 4-formylbenzoic acid. An imine was formed through condensation of the primary amine of DA and the aldehyde of 4FB. The imine proton peak (I) was clearly evident after 40 mins but unreacted aldehyde remained (A). By 90mins, all aldehyde had reacted but peaks from the quinone product of DA oxidation were also

clearly evident (J,K,L). * the t_0 time point spectrum was taken in MeOD so peaks from the hydroxyl groups of DA did not appear.

4.2.2 Addition of Dopamine to MAP through an imine bond

After verifying that DA imines could be prepared, DA was added to the MAP polymer using similar chemistry. The MAP polymer was prepared as previously described (9) and kindly donated by Emily Wyatt. The carboxylic acid groups of MAP were first converted to amine moieties to allow addition of *p*-succinimidyl 4-formylbenzoate (SFB). This particular aldehyde was chosen because it is hydrophobic and highly reactive with amines on the MAP polymer. Previous studies in our group have shown that MAP will not form sterically stable nanoparticles in PBS without some degree of hydrophobicity within the nanoparticle core (data not published). SFB was chosen to serve as a hydrophobic spacer while also introducing an aldehyde capable of forming an imine with DA. MAP-DA was prepared using similar chemistry as described in 4.2.1 (Scheme 4.3, Fig 4.5).

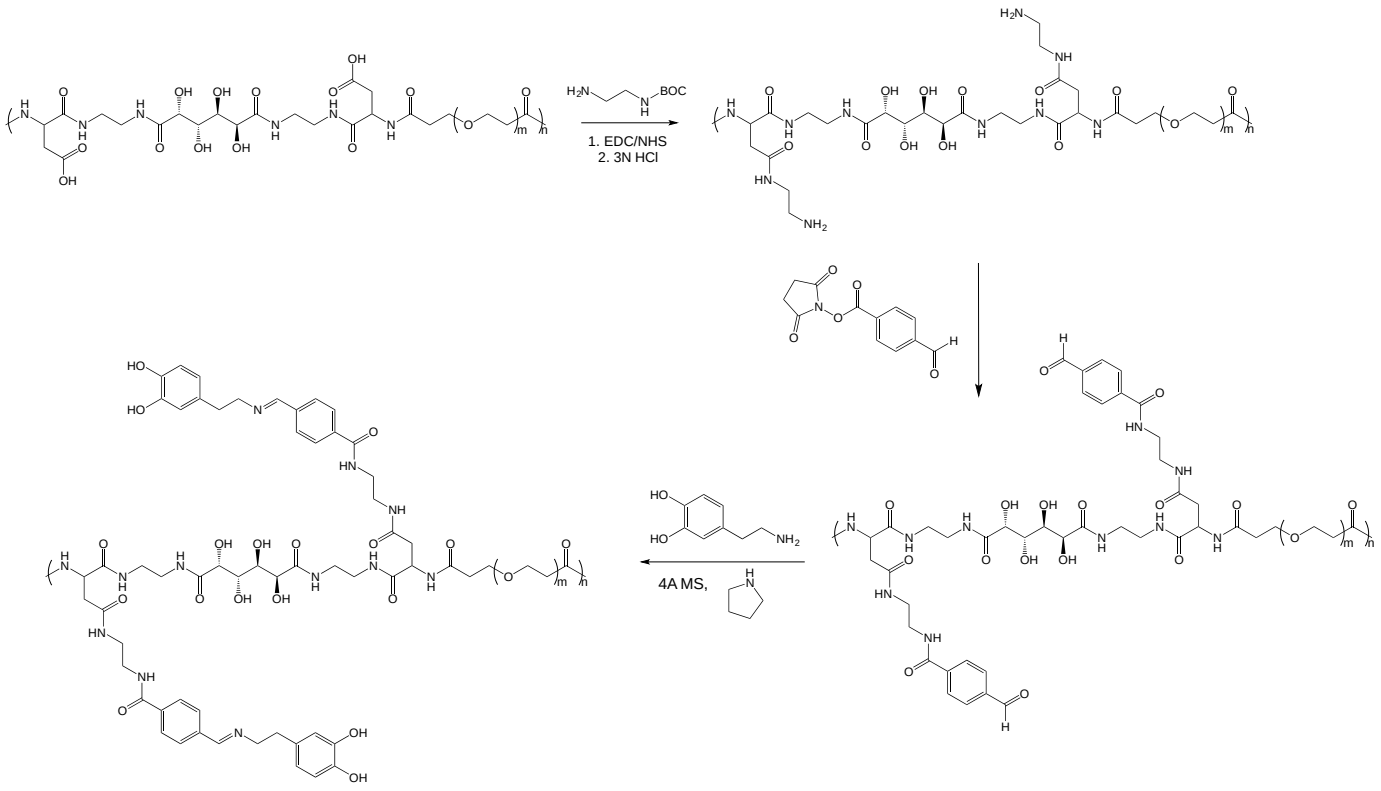

Scheme 4.3 Addition of DA to MAP through an imine.

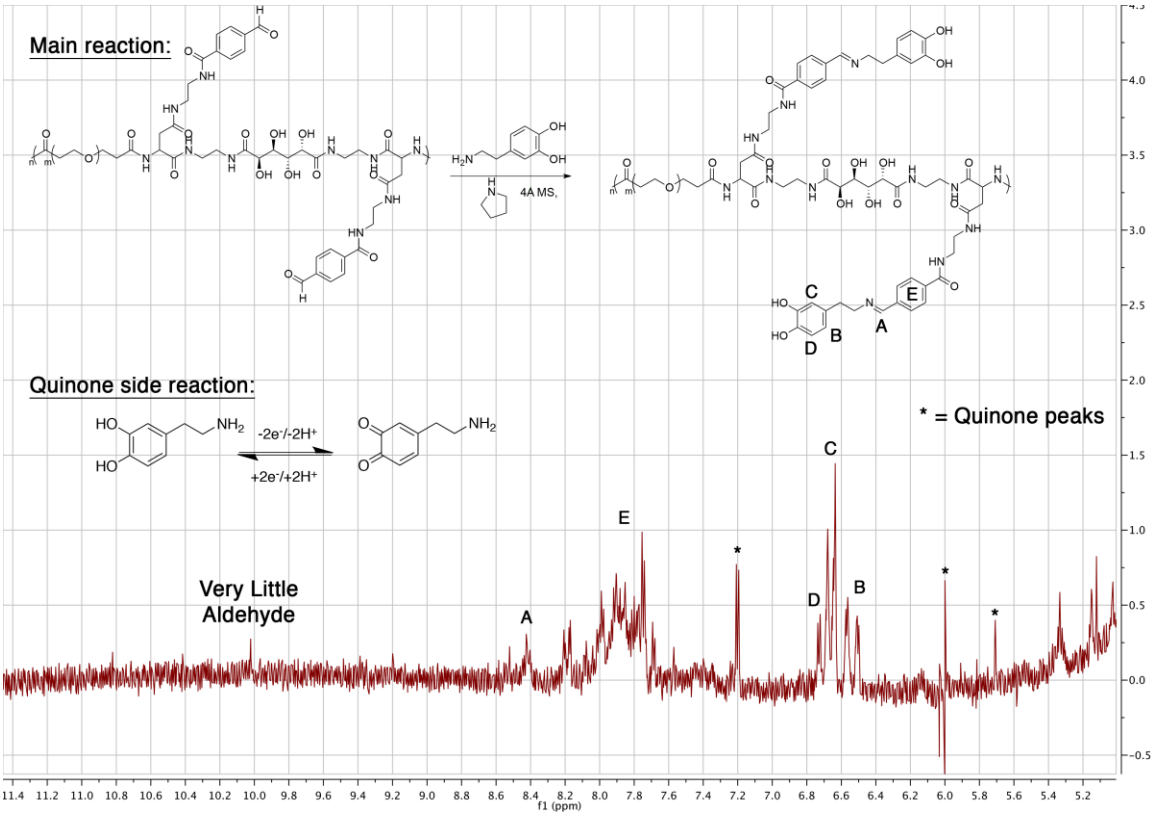

Fig 4.5 Relevant region of MAP-DA polymer ^{1}H NMR. Peaks from the aryl groups of SFB (E) and DA (B,C,D) are both present in the purified MAP-DA polymer. The imine peak is also present (A) along with little unreacted aldehyde and small quinone peaks (*).

After synthesis of the MAP-DA polymer, the quantity of DA loaded on the polymer was determined using fluorescent detection and HPLC (15). Though the amount of DA that was loaded on the polymer increased significantly with the final batch (Fig 4.6), the highest amount was well below the theoretical maximum (81.7 μg DA/mg MAP) giving a drug loading of 4.25%. The main reason for this limited loading is likely due to the inability to fully react available aldehyde with DA without excessive DA oxidation. It is possible to prevent DA oxidation by converting the DA catechol to an acetonide (16,17), but this modification requires breakdown of the acetonide ketal, a process that typically occurs under acidic conditions the nanoparticle may not experience in brain extracellular space. Despite the limited drug loading capacity of the MAP polymer under these reaction conditions, the

nanoparticle may still be able to deliver measurable quantities of drug, particularly in diseased models.

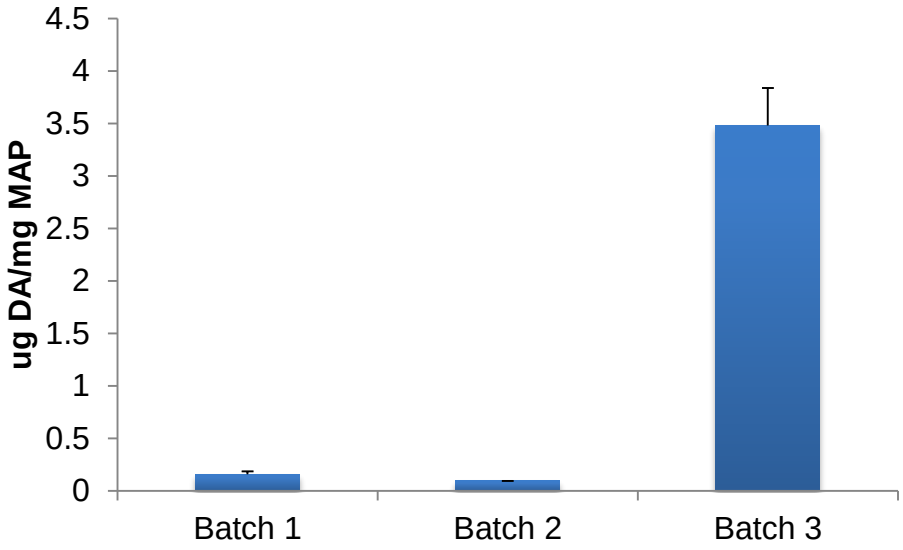

Fig 4.6 Dopamine loading on MAP polymer per synthesis batch. Error bars indicate one standard deviation from the mean.

The stability of the MAP-DA imine was determined by placing the conjugate in either neutral or mildly acidic pH at 37 °C and measuring the amount of DA in solution over time. As expected, DA released from the particle in acidic solution but, surprisingly, the imine proved very stable at neutral pH (FIG 4.7). Imines adjacent to aryl groups (aryl imines) have been shown to be significantly more stable than those next to alkyl groups (alkyl imines) (14). To increase DA release rate at neutral pH, an alkyl aldehyde, such as the modified amino acid phenylalinal, may be a superior hydrophobic spacer to attach to MAP.

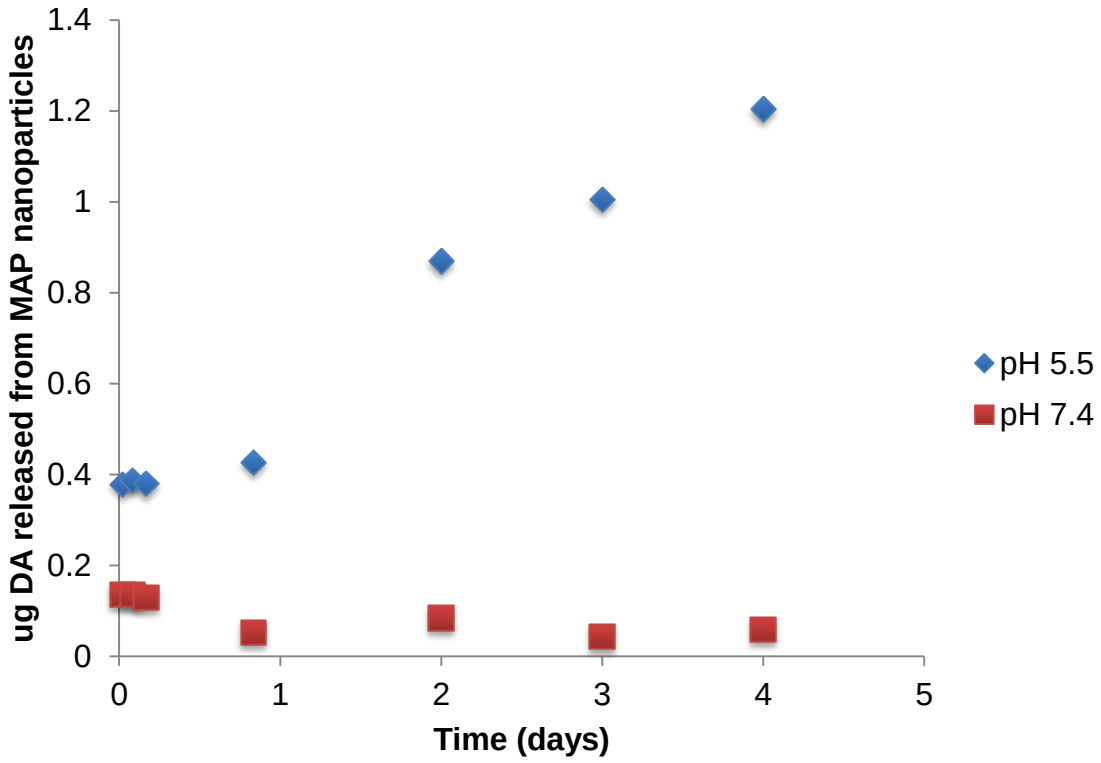

Fig 4.7 pH-dependent release of dopamine from MAP-DA nanoparticles over several days.

4.2.3 Preparation of Dopamine-Loaded, Tf-containing MAP nanoparticles

Tf was bound to MAP nanoparticles using an nPBA terminated PEG polymer. nPBA-PEG-NH_2 was synthesized as previously described (11) and added to Tf through EDC/NHS chemistry (Scheme 4.4).

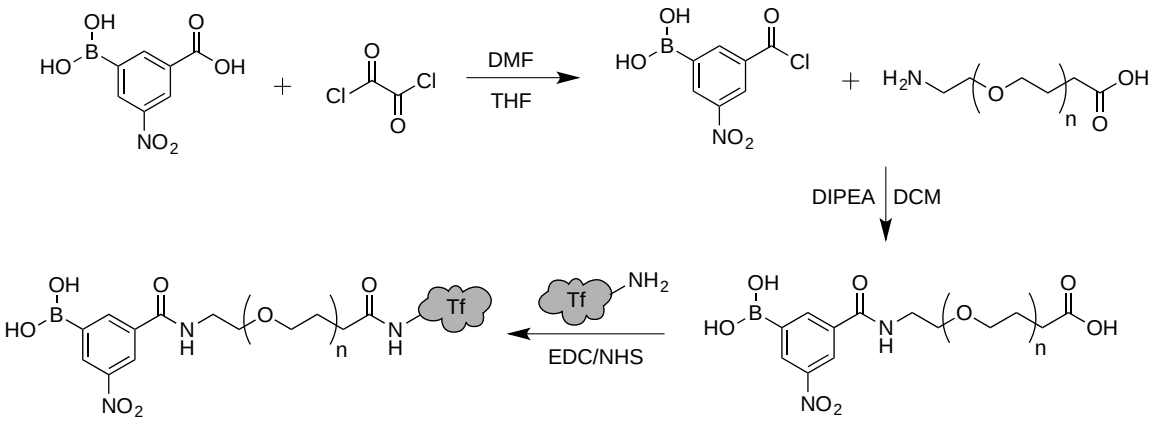

Scheme 4.4 Synthesis of nPBA-PEG-Tf.

Previously, mono-PEGylated ligands had been isolated by extensive HPLC separation (10), though, recently, our lab has discovered Tf's binding affinity to TfR following this process may be significantly diminished. To avoid damage to the PEGylated ligand through purification, the effect of adding a crude mixture of nPBA-PEG-Tf to the MAP nanoparticles was investigated (Fig 4.8). To determine the quantity of nPBA-PEG-Tf in the reaction mixture a fluorescence assay was developed using Alizarin Red, a diol containing dye that shows increased fluorescence at 570 nm when it reacts with nPBA-PEG (Fig 4.9).

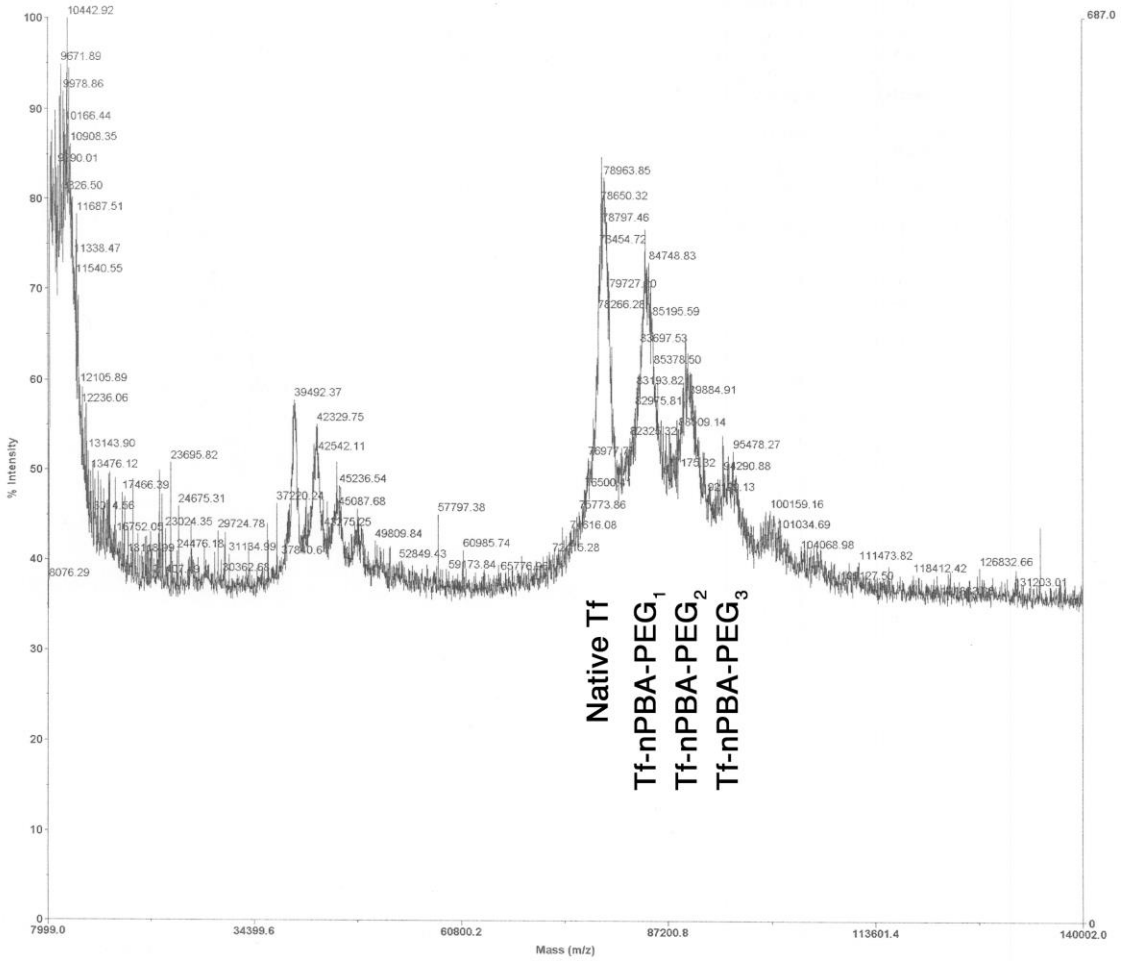

Fig 4.8 Crude nPBA-PEG-Tf reaction mixture. nPBA-PEG-NHS reacts with native Tf to yield PEGylated products. The MALDI of the crude mixture shows significant amounts of unreacted protein along with the different PEGylated species. The number in subscript following PEG indicates the number of PEG molecules reacted with Tf in that peak.

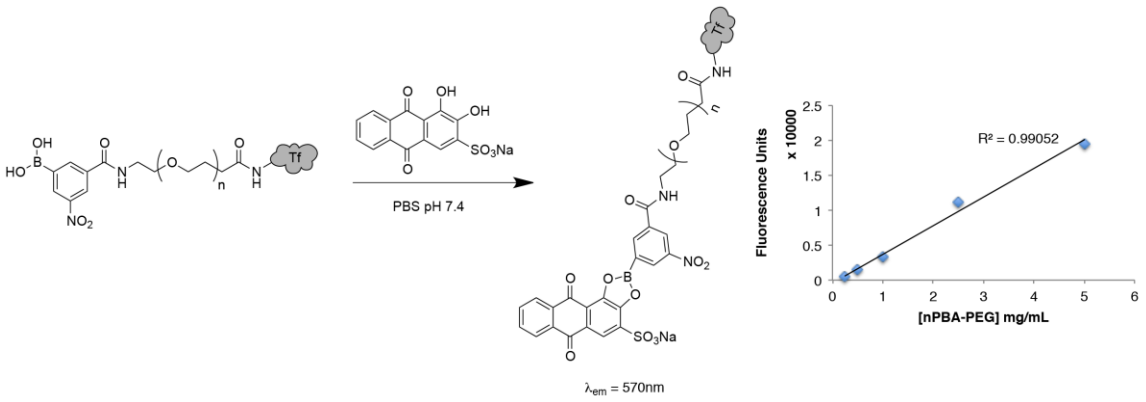

Fig 4.9 Quantitation of nPBA-PEG in reaction mixture using Alizarin Red. At pH 7.4, Alizarin Red will complex with nPBA and fluoresce at 570 nm. The amount of fluorescence correlates linearly with the concentration of nPBA-PEG in solution.

Different quantities of nPBA-PEG-Tf were added to MAP-DA nanoparticles and the effect on nanoparticle diameter and zeta potential was measured (Fig 4.10). MAP-DA nanoparticles were prepared by vortexing the polymer in PBS pH 7.4 at 1 mg/mL. The non-targeted MAP-DA nanoparticles were significantly larger than previously synthesized camptothecin (CPT)-loaded MAP nanoparticles (9). It is likely that the small, mildly hydrophilic SFB-DA on the MAP backbone did not undergo close association with adjacent polymer strands to promote formation of spherical nanoparticles. In comparison, CPT is a large chemotherapeutic that is virtually insoluble in water. When MAP-CPT polymer is added to water, the hydrophobic CPT molecules preferentially cluster together within the nanoparticle core where water can be excluded, driving the formation of spherical nanoparticles (9). DA, in contrast, is highly hydrophilic and does not have the same magnitude of thermodynamic forces dictating its tight packing within the nanoparticle core.

After addition of Tf, however, the particles shrunk in size, possibly due to stabilizing forces introduced through the nPBA-diol formation (18). This effect is clearly due to the nPBA-PEG-Tf as nanoparticle diameter was reduced when more protein was added. Importantly, no overt nanoparticle aggregation or diameter increase was observed after 24 hrs, indicating the multi-PEGylated ligands were not causing crosslinking between nearby nanoparticles (Fig 4.11). Using this method, Tf-containing MAP-DA nanoparticles could be

prepared in the ideal size range for nanoparticle circulation and transcytosis (20-100 nm) (19).

Though the ability to control MAP-DA nanoparticle diameter through the quantity of added nPBA ligand is useful, the fact that non-targeted MAP-DA nanoparticles were so much larger limited their use as an equivalent non-targeted control. To reduce nanoparticle diameter in a similar manner without introducing any BBB-targeting functionality, bovine serum albumin (BSA) was conjugated to nPBA-PEG and added to the MAP-DA nanoparticles. As with the nPBA-PEG-Tf, addition of nPBA-PEG-BSA reduced the nanoparticle size without significantly affecting zeta potential (Fig 4.10).

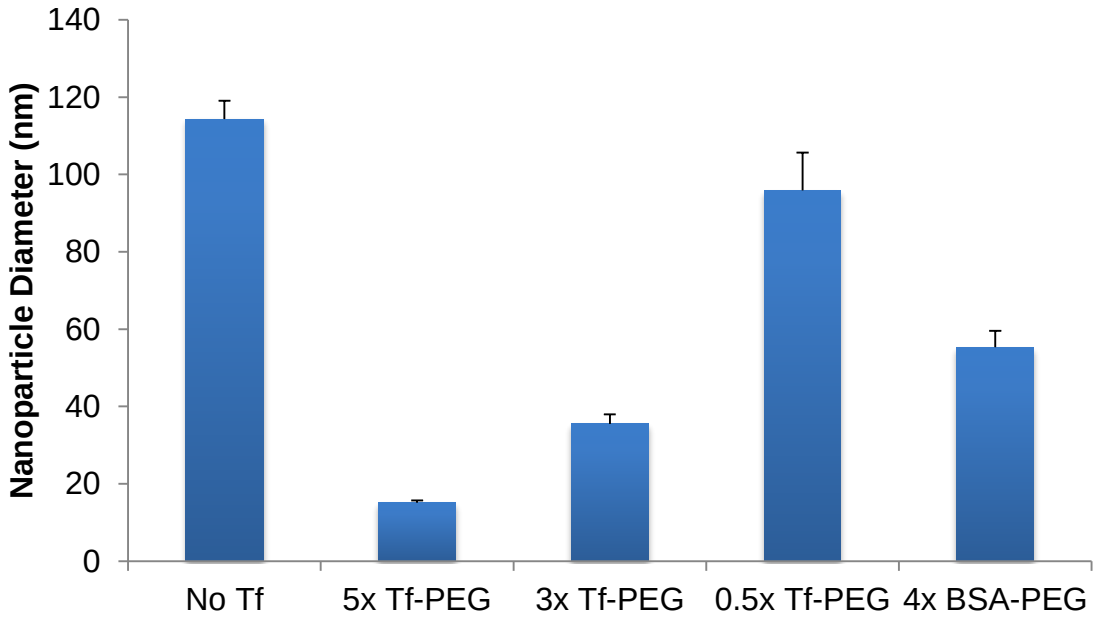

Fig 4.10 Nanoparticle diameter after addition of either nPBA-PEG-Tf or nPBA-PEG-BSA. The nanoparticles shrunk in size as more Tf was added to the nanoparticle surface. The numerical values in front of the ligands indicate the molar excess of PEGylated ligand relative to the number of nanoparticles that was added to the sample. Error bars indicate one standard deviation from the mean.

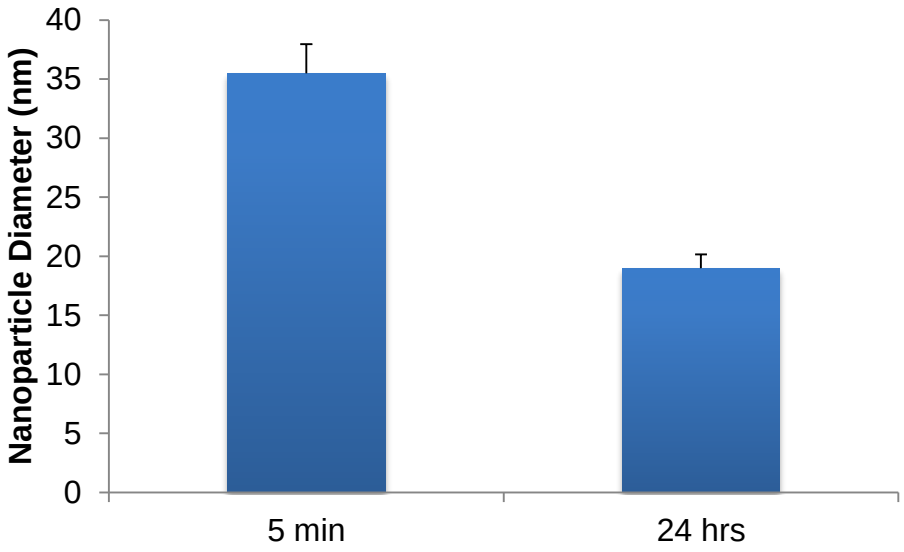

Fig 4.11 Tf-containing MAP-DA nanoparticle diameter over time. No aggregation or increase in size was evident in the sample after 24hrs, indicating the nanoparticles were not crosslinking due to introduction of multiple nPBA-PEG groups per Tf. Error bars indicate one standard deviation from the mean.

4.2.4 Investigation of Dopamine Delivery Across the Blood-Brain Barrier of Healthy Mice using MAP Nanoparticles

Tf-containing MAP-DA nanoparticles were prepared for injection into healthy BALB/c mice. Due to the lower than expected DA loading on MAP, nanoparticles were initially prepared at a concentration of 17 mg/mL MAP polymer to provide a DA dose of ~0.67 mg/kg. Unfortunately at this concentration, the MAP-DA polymer aggregates rather than forming nanoparticles. The initial concentration of polymer had to be adjusted to 5 mg/mL to form stable nanoparticles in solution. Attempts were made to concentrate the solution through ultracentrifugation but the nanoparticles rapidly aggregated even under mild centrifugal force. Because of this, a dose of only ~0.23 mg/kg DA could be safely given to the mice.

Proteins were added to the nanoparticles by introducing a five times molar excess to the solution of either nPBA-PEG-Tf to prepare targeted nanoparticles or nPBA-PEG-BSA

to prepare non-targeted ones (Fig 4.12). At the higher concentration MAP polymer (5 mg/mL vs. 1 mg/mL), the naked MAP-DA nanoparticles are about 50 nm larger in diameter. Addition of nPBA-PEG-Tf led to formation of ~75 nm nanoparticles, which is slightly larger than the 1mg/mL MAP-DA preparation though the absolute change in nanoparticle diameter was similar between the two concentrations after addition of Tf. The BSA-containing nanoparticles were slightly smaller at ~50 nm in diameter but had virtually the same zeta potential (-8.38 mV vs. -9.07 mV for the Tf-containing formulation).

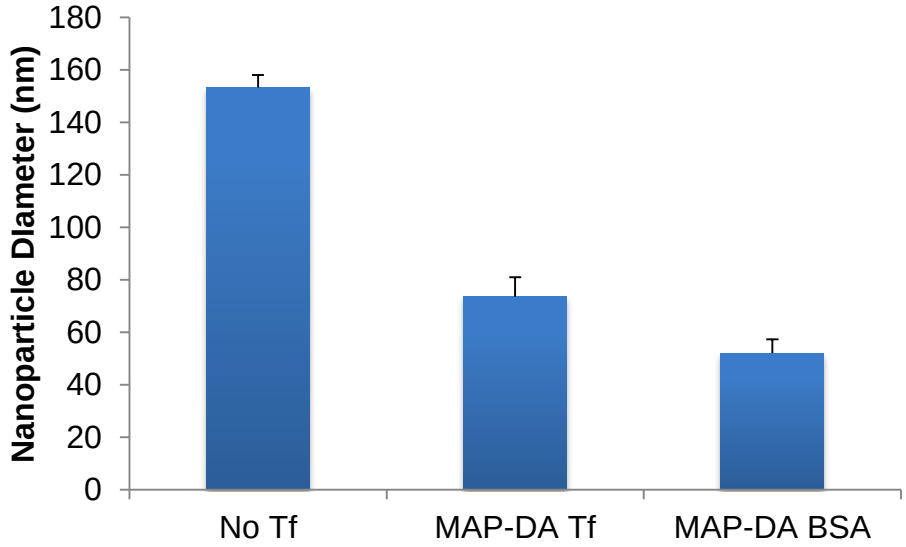

Fig 4.12 Diameters of MAP-DA nanoparticles used for injection before and after addition of protein to the nanoparticle surface. MAP-DA was prepared at 5 mg/mL in PBS pH 7.4 and PEGylated-ligands were added at a five times molar excess to the number of nanoparticles in solution. Error bars indicate one standard deviation from the mean.

Both nanoparticle formulations were injected intravenously into mice and allowed to circulate for 24 hrs. A third group was given L-DOPA with benserazide intravenously at a dose of 1.5 mg/kg L-DOPA and 0.625 mg/kg benserazide. Benserazide is a peripheral dopa-decarboxylase inhibitor that prevents breakdown of L-DOPA while circulating in blood. The combination of L-DOPA with a decarboxylase inhibitor is standard practice and increases the half-life of L-DOPA in the blood from 50 mins to roughly 2 hrs (20). The L-DOPA dose

chosen is equivalent to the amount of drug absorbed into circulation for patients given a high dose of oral L-DOPA (21).

After 24 hrs, the mice were anesthetized and perfused with a 10% sucrose solution to clear any remaining nanoparticles or free drug from the bloodstream. Brains were resected and different regions dissected and stored for DA quantitation as previously described (22). Tissues were homogenized and DA quantity per mass of tissue was measured in the cerebellum, cerebral cortex, and striatum (Fig 4.13). The striatum was the primary region of interest because DA quantity is decreased here in PD. The L-DOPA group showed no difference from a brain that received no injection. This is the expected result, since after 12 half lives, L-DOPA should be essentially cleared from the blood stream and whatever amount reached the brain was likely metabolized by 24 hrs. The MAP-DA-Tf formulation did show greater mean DA values in each brain region compared to blank and L-DOPA treatment, but this increase was not significant (e.g. $p = 0.195$ in the striatum). The reason for this minimal increase is likely due to the limited DA amount available for delivery to the brain. As described above, limitations in MAP-DA nanoparticle stability allowed only a dose of only 0.23 mg/kg DA to be given. Previous work quantitating Tf-containing gold nanoparticle accumulation in the brain showed less than 1% of the injected dose (38 mg AuNP/kg) reaching the brain (23). Assuming the nPBA-PEG-Tf targeting strategy increased nanoparticle accumulation in the brain to 1% of the injected dose (0.23 mg DA/kg), brain DA levels are expected increase by 87 ng/g tissue if homogenously distributed. The measured change in average striatal DA quantity between the Tf-containing and L-DOPA group was actually 487 ng/g tissue, higher than expected if only 1% of the injected dose reached the brain (Table 4.1). Similar increases were seen in other brain regions, indicating this change was not unique to the striatum. This result suggests the targeted nanoparticles may have successfully reached the brain in significant numbers but due to the low DA loading, a statistically significant change could not be identified with a sample size of only three mice. It is also important to note that any increase in brain DA is due to intact nanoparticles reaching the brain since free DA cannot cross a healthy BBB in any appreciable amount.

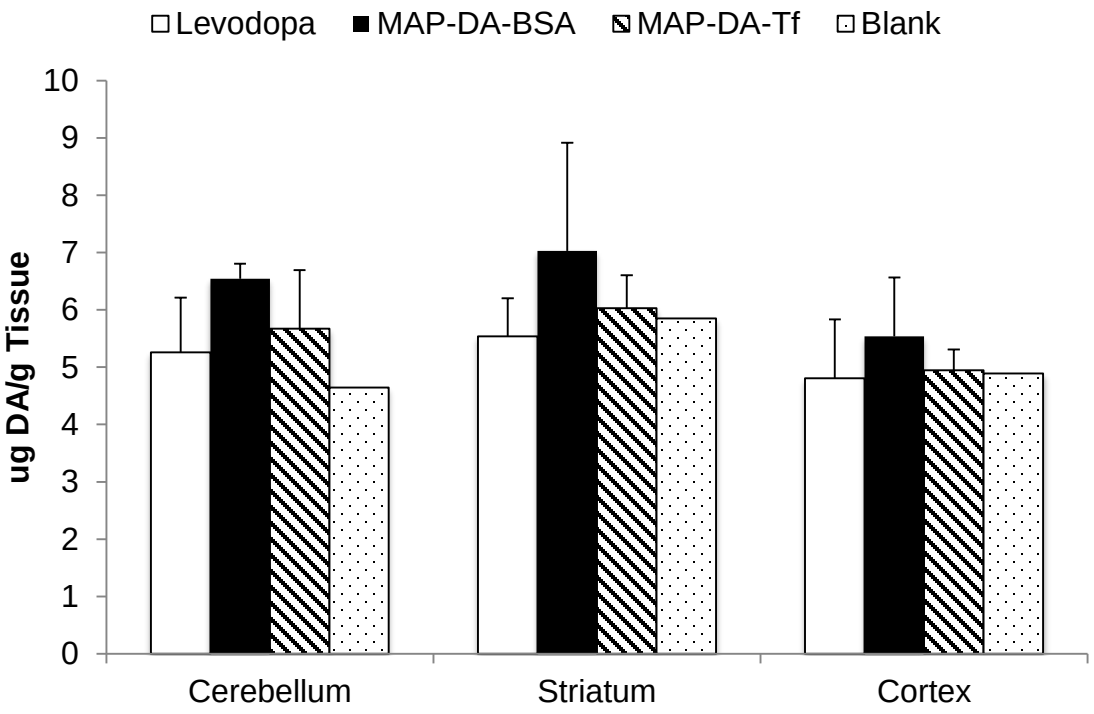

Fig 4.13 Dopamine content in different brain regions for each treatment group. N = 3 for each treatment group. N = 1 for the blank brain (no injection). Error bars indicate one standard deviation from the mean.

Theoretical DA Increase

DA Dose	3.479	ug
mg MAP-DA	1	mg
Brain DA uptake (1%)	0.03479	ug
Mouse Brain Mass	0.4	g
Brain DA Increase	**0.086975**	**µg /g tissue**

Measured DA Change vs. L-DOPA (µg DA/g tissue)

Cerebellum	Striatum	Cortex
+0.412	+0.487	+0.139

Table 4.1 Estimated (top) versus measured (bottom) changes in brain DA content between MAP-DA Tf and L-DOPA group. Assuming only 1% of injected nanoparticles reach the brain and are homogenously distributed, brain DA content is expected to raise 87 ng/g tissue. The measured changes for the MAP-DA Tf group are much larger, suggesting >1% of the

dose reached the CNS. Also, the non-homogenous spread may indicate variable uptake in different brain regions, possibly due to variations in TfR expression.

Interestingly, the mice given non-targeted nanoparticles (MAP-DA BSA) had the highest brain DA amounts. In fact, in the striatum, the DA amount was significantly higher than the L-DOPA group even when only treating three mice ($p < 0.05$). Albumin is the most common serum protein whose primary role is to regulate blood oncotic pressure. Hormones bound to albumin in circulation are capable of crossing the BBB but no specific albumin receptor has been identified on BBB endothelium (24). Nanoparticles containing surface cationized albumin have been observed crossing the BBB through AMT (25) though this is unlikely occurring with the MAP-DA BSA nanoparticles since the BSA used was not modified to introduce positive charges to the protein. One other possible explanation is fluid-phase transcytosis (FMT). FMT is a non-specific uptake pathway used for transendothelial delivery of circulating proteins. In this process a bulk of plasma volume is randomly taken up by an endothelial cell and rapidly sent to the basal cell membrane in a transport vesicle (26). FMT was not discussed among other solute transport systems in Section 1.2.1 because its characteristic membrane invaginations (caveolae) are very rare in BBB endothelium so this transport process is not believed to significantly contribute to solute influx (27). Albumin, however, has been noted to cross the BBB through this process, though in very small amounts (28).

How is it that MAP-DA BSA nanoparticles were capable of entering the brain in greater amounts than Tf-containing ones despite the fact that Tf transcytosis occurs much more readily at the BBB than non-specific albumin uptake? One major concern with adding crude mixtures of PEGylated protein to the MAP-DA nanoparticles is the significant amount of non-PEGylated, free protein in the nanoparticle solution. The MAP-DA nanoparticles could not be size separated from unbound protein rapidly using ultracentrifugation or slowly through dialysis for risk of aggregation or nanoparticle disassembly, respectively. This necessitated inclusion of high quantities of free Tf in the injection mixture, artificially raising the serum Tf concentration possibly high enough to occupy available receptors at the BBB

immediately upon introduction and possibly cause decreased TfR expression over the course of the experiment (29).

To further understand whether the nanoparticles were reaching the brain parenchyma, fixed brain sections were stained with an anti-PEG antibody and imaged using confocal microscopy. The L-DOPA group showed no fluorescent signal above background autofluoresence (Fig 4.14). Occasional points of positive fluorescent signal were seen in the MAP-DA BSA treated mice, again suggesting that these nanoparticles were able to enter the brain in small amounts through some non-specific pathway (Fig 4.15). In the MAP-DA Tf group, however, clusters of fluorescent signal were observed near blood vessels indicating greater numbers of these nanoparticles were within the parenchyma (Fig 4.16). This likely occurred in regions of high TfR expression where receptor sites were not fully saturated with introduced free Tf, allowing the nanoparticles to bind and transcytose.

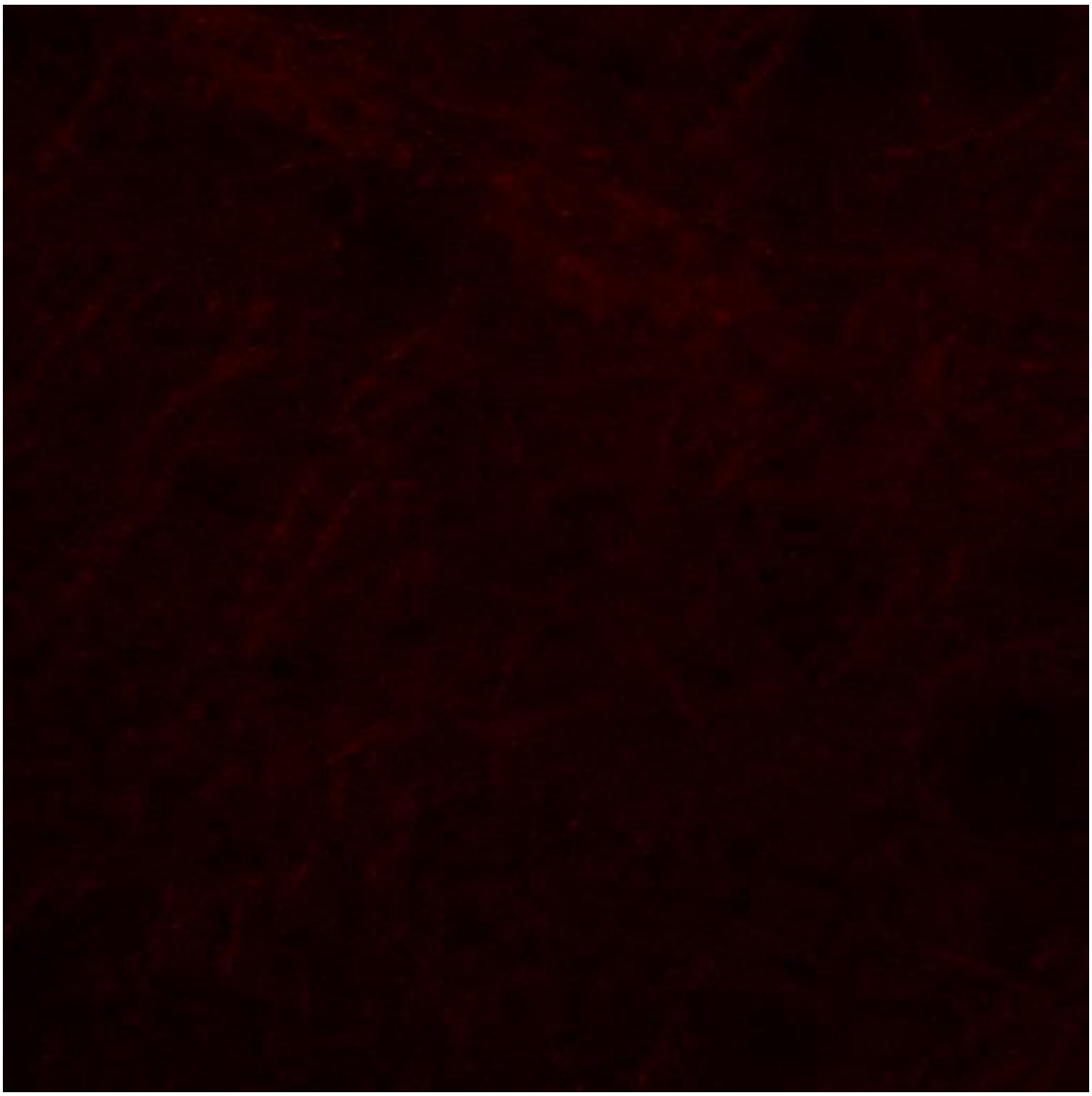

Fig 4.14 Confocal microscopy image of fixed brain section from an L-DOPA treated mouse. No fluorescence is present above tissue auto-fluorescence.

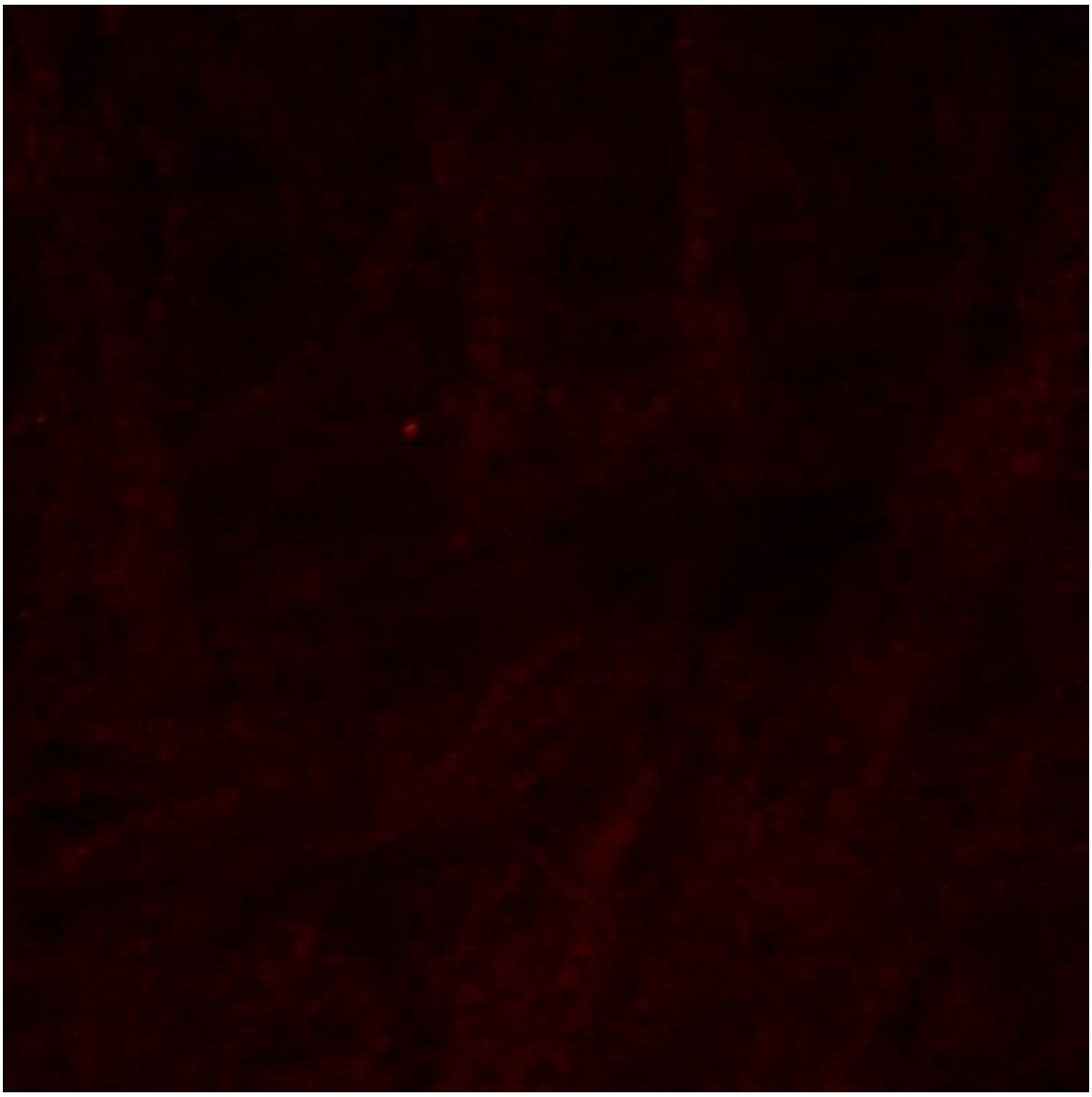

Fig 4.15 Confocal microscopy image of fixed brain section from a MAP-DA BSA treated mouse. Rare points of positive signal were observed in the brain parenchyma, indicating the presence of the PEG portion of the MAP-DA nanoparticle.

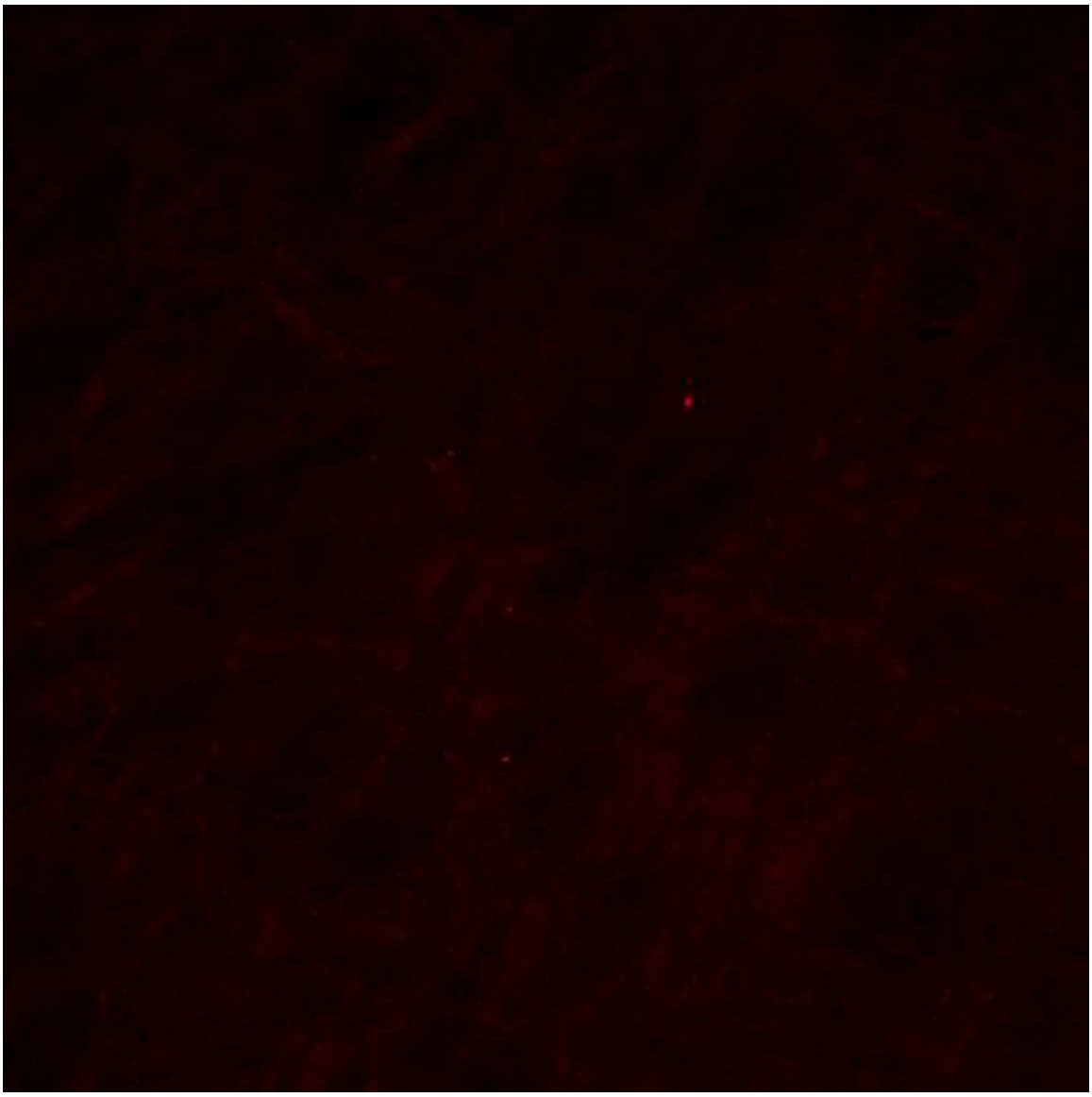

Fig 4.16 Confocal microscopy image of fixed brain section from a MAP-DA Tf treated mouse. Clusters of positive signal were observed near blood vessels within the brain parenchyma, suggesting this formulation was capable of crossing the BBB.

4.3 Conclusions

Targeted nanoparticles offer a compelling approach to deliver dopamine across the BBB into the brain. Development of a nanoparticle with high DA loading capacity, long residence time, and good drug release kinetics could profoundly improve upon current PD

treatment regimes. MAP nanoparticles are promising candidates because of the unique surface functionalization chemistry providing ideal cleavage kinetics superior to the Tf-DAK-PEG construct (Chapter III). MAP-DA nanoparticles were prepared by conjugating the native neurotransmitter to the MAP polymer through a labile imine bond. Though the imine bond was chosen because of its usual poor stability, the aryl imine formed with DA proved surprisingly stable at neutral pH. Before use in a disease model, the drug release kinetics would need to be adjusted to allow more rapid DA release so it can be utilized within the CNS.

The MAP-DA nanoparticles were found to be much larger than previously prepared MAP nanoparticles but the diameter could be reduced into the ideal range for transcytosis through addition of surface proteins (either functional or non-functional). Formation of small, spherical MAP nanoparticles is driven by covalently attached hydrophobic drugs that preferentially pack into the nanoparticle core. Since both MAP and DA are strongly hydrophilic, a more hydrophobic spacer than SFB may be needed to prepare smaller, more stable nanoparticles.

The DA loading capacity on the MAP polymer was, unfortunately, lower than expected. It is likely that a different nanoparticle-forming polymer would prove more effective at DA loading than MAP, ideally one that can passively pack DA into the nanoparticle core during formation and release drug via breakdown of the polymer matrix in vivo. This could also improve upon drug release kinetics, as they would be dictated by the structure of the polymer, a much more chemically flexible unit, than through metabolism of a covalent bond with DA. A rapid drug-loading step is also preferred because nano-encapsulated DA is shielded from oxidation in aqueous solution (6). Use of a different polymer, however, would require presentation of surface vicinal diols with similar boronic ester formation characteristics to retain the ideal disassociation of nPBA-PEG-Tf from the nanoparticle surface during transcytosis.

Despite the shortcomings in loading capacity and release kinetics of MAP-DA nanoparticles, a measurable increase in brain DA was found 24 hrs after a single treatment of 0.23 mg/kg MAP-DA nanoparticles. The fact that any increase in DA was observed in nanoparticle-treated mice with such a low dose highlights the potential of targeted

nanoparticles for DA delivery. The DA quantity in the healthy mouse striatum is around 5 μg/g tissue but that value drops by nearly 75% in rat models of PD. Significant increases in motor function were observed in these rats seven days after a single dose of DA-loaded PLGA nanoparticles when the brain DA concentration was only 1.5 μg/g higher than the untreated controls (6). Even with a very low DA dose, striatal DA content was increased by 0.49 μg/g 24 hrs after treatment with MAP-DA Tf nanoparticles, indicating these nanoparticles could be effective therapeutics if the DA loading capacity of the MAP polymer was only modestly increased. The measured brain DA change is also a promising result for the nPBA targeting strategy as the increased values suggest greater than 1% of the injected dose reached the brain.

The fact that the MAP-DA BSA nanoparticles showed the greatest increase in brain DA was a surprising result. One possible explanation is that these nanoparticles were retained within the BBB endothelial cells similar to other targeted therapeutics (see section 1.4.1). Brains were perfused before dissection to clear any nanoparticles from the blood, but this process does not clear nanoparticles trapped in the endothelium. The limited presence of intact MAP-DA BSA nanoparticles in the brain parenchyma observed through imaging compared to the clusters of positive signal from the Tf-containing formulation supports this possibility, though many follow up experiments would be necessary to verify this conclusion.

Ideally, this work would be expanded to prepare nanoparticles capable of safely dosing high quantities of DA systemically (e.g. 20 mg/kg). If these nanoparticles are capable of crossing the BBB in relatively high quantities (1-2%), residing in the brain extracellular space, and releasing native DA at a constant rate, they could potentially treat PD symptoms for weeks to months at a time without causing undesirable motor dysfunctions.

4.4 Methods

Synthesis of DA-4FB Imine: The imine reaction was preformed as previously described (14). Dopamine (DA)-HCl (Sigma) was prepared in DMSO-d_6 at 0.1 M and placed over dry, activated 4Å molecular sieves. An equimolar quantity of 4-formylbenzoic acid was added along with 20 mol % pyrrolidine. The reaction was placed under Ar and heated to 60°C. Aliquots were removed over time and ^{1}H NMR spectra taken (300 MHz, DMSO-d_6): 8.31 (s, 1H), 8.70 (d, 2H), 7.96 (d, 2H), 7.79 (d, 2H), 6.65 (d, 1H), 6.60 (d, 1H), 6.45 (dd, 1H).

Synthesis of MAP-DA: MAP polymer was prepared as previously described (9) and generously donated by Emily Wyatt. To a dry, two necked vacuum flask was added 115 mg MAP (3.93 μmol), 36 mg 1-Ethyl-3-(3-dimethylaminopropyl)carbodiimide (EDC) (0.208 mmol), 22 mg N-hydroxysuccinimide (NHS) (0.208 mmol), 20 μL dry N,N-diisopropylethylamine (DIPEA) (0.208 mmol) and 33 μL N-Boc-ethylenediamine (Sigma) (0.208 mmol). The flask was purged with Ar and 3.75 mL of dry MeOH was added. The reaction was stirred at RT overnight under Ar. Solvent was removed from the flask under vacuum and the solid was disolved in 1:1 MeOH:water. Impurities were removed through ultracentrifugation using a 10kDa MWCO filter (EMD Millipore). Solvent was evaporated under vacuum until a gel remained. Boiling THF was added followed by immediate cooling on ice. The solution was dried under vacuum to yield a pasty, white solid (MAP-BOC, 92mg, 78% yield).

MAP-BOC was dissolved in 2 mL 3N HCl in MeOH. The reaction was stirred for 3 hr at RT. The solution was dried under vacuum and dissolved in fresh MeOH. This process was repeated for a total of three washes. The resulting amine-containing MAP (MAP-NH_2) (92 mg, 3.14 μmol) was added to a dry, two-necked flask along with 63 mg N-succinimidyl 4-formylbenoate (SFB, Fisher Scientific) (0.255 mmol) and 24.5 μL dry DIPEA (0.255 mmol). The flask was purged with Ar and 12 mL dry MeOH was added. The reaction was stirred overnight at RT under Ar. Solvent was evaporated under vacuum and the solid was dissolved

and purified using ultracentrifugation and THF recrystallization as previously described. A slightly yellow, pasty solid remained (MAP-Ald, 37.4 mg, 41% yield).

MAP-Ald (37.4 mg, 1.27 μmol) was added to a dry, two-necked vacuum flask, along with 9.6 mg DA-HCl (50.6 μmol) and 1 μL pyrrolidine (20 % mol cat.). The flask was purged with Ar and 4 mL Dry, degassed DMSO was added to dissolve the solids. The mixture was transferred to an inert flask containing 1 g dry, activated 4Å molecular sieves. The reaction was heated to 60°C and allowed to react under Ar for 5 hr. The reaction was dialyzed against DMSO followed by MeOH using a 10 kDa MWCO Spectro Por 7 dialysis membrane (Spectrum Labs). After purification, 24.9 mg MAP-DA remained (66% yield). ^{1}H NMR (600 MHz, MeOD): 8.43 (s, 1H), 7.85 (m, 4H), 6.73 (d, 1H), 6.65 (d, 1H). 6.54 (dd, 1H).

Measurement of DA Loading on MAP Polymer: DA quantitation was performed as previously described (15). MAP-DA polymer was prepared at 1 mg/mL in 0.2 M $HClO_4$ with 3 mM cysteine (Cys). The solution was filtered (0.4 μm Supor filter membrane) and 20 μL was injected onto an HPLC column (Synergi 4u Hydro-RP 80A, Phenomenex) using a mobile phase of acetate (12 mM acetate, pH 3.5 with 0.26 mM Na_2EDTA)-methanol (86:14 v/v). DA was detected by fluorescence using λ_{ex} = 279 nm and λ_{em} = 320 nm.

pH-Dependent DA Release from MAP-DA: MAP-DA nanoparticles were prepared in either PBS pH 7.4 or PBS pH 5.5 at 1 mg MAP polymer/mL. Solutions were incubated at 37°C and aliquots were removed and measured for DA quantity at various times.

nPBA-PEG-Ligand Synthesis: nPBA-PEG-COOH was prepared as previously described (11). 3-Carboxyl-5-nitrophenylboronic acid (200 mg, 0.94 mmol) was added to a dry, two-necked vacuum flask. The flask was purged with Ar and sealed. Anhydrous THF containing a BHT inhibitor was added (5 mL) followed by anhydrous DMF (14.6 μL, 0.19 mmol). The flask was cooled in an ice-water bath and oxalyl chloride (195 μL, 2.27 mmol) was added dropwise to the solution. After addition of the oxalyl chloride, the solution was removed from the ice-water bath and allowed to stir at RT for two hours under Ar. Solvent was evaporated under vacuum to yield 3-acyl chloride-5-nitrophenyl boronic acid.

3-acyl chloride-5-nitrophenyl boronic acid (45.8 mg, 0.2 mmol) was added to a dry, two-necked vacuum flask. The flask was sealed, purged with Ar and cooled in an ice-water bath. Anhydrous DCM (4 mL) was added to dissolve the boronic acid. Amine-PEG-carboxylic acid (500 mg, 0.1 mmol) (5 kDa, Jenkem) was prepared in a separate flask along with dry DIPEA (34.8 μL, 0.2 mmol). The flask was purged with Ar and sealed and the PEG was dissolved in 5 mL dry DCM. The PEG solution was added to the boronic acid dropwise. The flask was removed from the ice-water bath, protected from light, and allowed to react at RT overnight. Solvent was removed under vacuum and the solid was reconstituted in 0.5 N HCl (5 mL) and stirred for 15 min. The solution was filtered through a 0.2 μm Supor filter and dialyzed against nanopure water until constant pH using ultracentrifugation (3 kDa, Amicon Ultra, EMD Millipore). The polymer was lyophilized dryness to yield 249.2 mg nPBA-PEG (50% yield).

To prepare nPBA-PEGylated Tf or BSA, 100 mg nPBA-PEG-COOH (0.2 mmol) was dissolved in PBS pH 7.4. EDC (30.6 mg) and NHS (18.4 mg) were added at eight times molar excess and the reaction proceeded under light stirring for 20 min. Excess EDC and NHS were removed through ultracentrifugation (3 kDa, Amicon Ultra, EMD Millipore). The activated nPBA-PEG was added to either 50 mg of Tf (0.63 μmol) or BSA (0.75 μmol) at a ten times molar excess. The reaction proceeded with light agitation for four hours. Unreacted PEG was removed from the protein solutions through ultracentrifugation (50 kDa MWCO). The reaction mixture composition was determined using MALDI-TOF.

The amount of nPBA-PEG in the solution was determined through fluorescence with Alizarin Red. Alizarin Red was added to wells in a 96 well plate at a constant concentration of 0.5 mg/mL. Standards of nPBA-PEG were prepared containing 10 mg/mL Tf to account for the effect of protein in solution on fluorescence. The concentration of protein in the nPBA-PEG-Tf or nPBA-PEG-BSA solutions was determined and the appropriate volume of protein was added to the Alizarin Red solution to give a final concentration of 10 mg/mL total protein in the well. Well fluorescence was measured using λ_{ex} = 530 nm and λ_{em} = 570 nm and nPBA-PEG concentration in the PEGylated protein mixtures calculated.

Preparation of Targeted and Non-Targeted MAP-DA Nanoparticles: MAP-DA was prepared at 1 mg/mL in PBS pH 7.4. Either nPBA-PEG-Tf or nPBA-PEG-BSA was added to the nanoparticle solution at various molar excesses. The nanoparticles were filtered and physical characteristics measured. Nanoparticle diameter and zeta potentials were measured with a Brookhaven Instruments ZetaPALS. Values shown are from an average of five runs for nanoparticle size and five runs with a target residual of 0.02 for zeta potential.

Animal Studies: All animals were treated according to the NIH guidelines for animal care and use as approved by the Caltech Institutional Animal Care and Use Committee. MAP-DA was prepared at 5 mg/mL in 200 μL PBS pH 7.4. Either nPBA-PEG-Tf or nPBA-PEG-BSA was added to the nanoparticle solution at a five times molar excesses. The nanoparticles were filtered (0.22 μm Supor filter), administered intravenously to nine-week old female BALB/c mice. For the L-DOPA group, L-DOPA and benserazide were given intravenously in PBS pH 7.4 at a dose of 1.5 mg/kg and 0.625 mg/kg, respectively. After 24 hours, the mice were anaesthetized and transcardially perfused with a 10% sucrose solution. The brains were resected and different brain regions were dissected and stored for DA quantitation as previously described (21). One hemisphere was retained for imaging studies (described below).

Quantitation of Brain DA Content: Brain tissues were weighed and placed in 200-250 μL 0.2 M $HClO_4$ with 3 mM Cys. The tissues were placed in a Lysing Matrix A homogenizer tube containing a ¼ in ceramic sphere (MP Biomedicals) and homogenized using a FastPrep-24 homogenizer (MP Biomedicals) at a rate of 6 m/s for 30s. A total of three homogenization steps occurred with a 1 min rest on ice between steps. After the final homogenization step, samples were centrifuged at 14000 g for 15 min. The supernatant was withdrawn, filtered (0.4 μm filter) and 20 μL injected and quantitated through HPLC as described above. Statistical significance for pairwise group comparisons was tested using student's t-test.

Tissue imaging: The freshly dissected brain hemispheres were fixed in 10% formalin overnight then embedded in paraffin, sectioned and deparaffinized. Antigen retrieval was performed by baking the tissues at 90°C in 10 mM citrate pH 6.0. The tissues were than

washed in PBS, blocked with a 1 %BSA solution for 30 mins and stained with an anti-PEG primary antibody (1:50 dilution, 4°C overnight) (Life Diagnostics, 9B5-6-25-7). A fluorescent secondary antibody was then added for 1 hr (1:500 dilution) (Abcam ab96876). Tissues were mounted using Prolong Gold antifade reagent and images acquired on a Zeiss LSM 510 inverted confocal scanning microscope using a Zeiss Plan Neofluar 63×/1.25 oil objective. The excitation wavelength for the fluorescent antibody was 543 nm with a corresponding emission filter of 545-590 nm.

4.5 References

1. Duffy, K. R., & Pardridge, W. M. (1987). Blood-brain barrier transcytosis of insulin in developing rabbits. *Brain Research*, *420*(1), 32–38.
2. Sahin, G., Thompson, L. H., Lavisse, S., Ozgur, M., Rbah-Vidal, L., Dollé, F., et al. (2014). Differential Dopamine Receptor Occupancy Underlies L-DOPA-Induced Dyskinesia in a Rat Model of Parkinson's Disease. *PLoS ONE*, *9*(3), e90759–17.
3. Cotzias, G. C., Van Woert, M. H., & Schiffer, L. M. (1967). Aromatic amino acids and modification of parkinsonism. *New England Journal of Medicine*, *276*(7), 374–379.
4. Thanvi, B. R., & Lo, T. C. N. (2004). Long term motor complications of levodopa: clinical features, mechanisms, and management strategies. *Postgraduate Medical Journal*, *80*(946), 452–458.
5. Kamaly, N., Xiao, Z., Valencia, P. M., Radovic-Moreno, A. F., & Farokhzad, O. C. (2012). Targeted polymeric therapeutic nanoparticles: design, development and clinical translation. *Chemical Society Reviews*, *41*(7), 2971.
6. Pahuja, R., Seth, K., Shukla, A., Shukla, R. K., Bhatnagar, P., Chauhan, L. K. S., et al. (2015). Trans-Blood Brain Barrier Delivery of Dopamine-Loaded Nanoparticles Reverses Functional Deficits in Parkinsonian Rats. *ACS Nano*, *9*(5), 4850–4871.
7. Carvey, P. M., Zhao, C. H., Hendey, B., Lum, H., Trachtenberg, J., Desai, B. S., et al. (2005). 6-Hydroxydopamine-induced alterations in blood-brain barrier permeability. *European Journal of Neuroscience*, *22*(5), 1158–1168.
8. Olivier, J.-C. (2005). Drug transport to brain with targeted nanoparticles. *NeuroRx: the Journal of the American Society for Experimental Neurotherapeutics*, *2*(1), 108–119.
9. Han, H., & Davis, M. E. (2013). Targeted Nanoparticles Assembled via Complexation of Boronic-Acid-Containing Targeting Moieties to Diol-Containing Polymers. *Bioconjugate Chemistry*, *24*(4), 669–677.
10. Han, H., & Davis, M. E. (2013). Single-Antibody, Targeted Nanoparticle Delivery of Camptothecin. *Molecular Pharmaceutics*, *10*(7), 2558–2567.

11. Pan, D. W., & Davis, M. E. (2015). Cationic Mucic Acid Polymer-Based siRNA Delivery Systems. *Bioconjugate Chemistry*, *26*(8), 1791–1803.
12. Saito, H., Hoffman, A. S., & Ogawa, H. I. (2007). Delivery of Doxorubicin from Biodegradable PEG Hydrogels Having Schiff Base Linkages. *Journal of Bioactive and Compatible Polymers*, *22*(6), 589–601.
13. Xu, X., Flores, J. D., & McCormick, C. L. (2011). Reversible Imine Shell Cross-Linked Micelles from Aqueous RAFT-Synthesized Thermoresponsive Triblock Copolymers as Potential Nanocarriers for "pH-Triggered" Drug Release. *Macromolecules*, *44*(6), 1327–1334.
14. Morales, S., Guijarro, F. G., García Ruano, J. L., & Cid, M. B. (2014). A General Aminocatalytic Method for the Synthesis of Aldimines. *Journal of the American Chemical Society*, *136*(3), 1082–1089.
15. De Benedetto, G. E., Fico, D., Pennetta, A., Malitesta, C., Nicolardi, G., Lofrumento, D. D., et al. (2014). A rapid and simple method for the determination of 3,4-dihydroxyphenylacetic acid, norepinephrine, dopamine, and serotonin in mouse brain homogenate by HPLC with fluorimetric detection. *Journal of Pharmaceutical and Biomedical Analysis*, *98*, 266–270.
16. Liu, Z., Hu, B.-H., & Messersmith, P. B. (2010). Acetonide protection of dopamine for the synthesis of highly pure N-docosahexaenoyldopamine. *Tetrahedron Letters*, *51*(18), 2403–2405.
17. Soloshonok, V., & Ueki, H. (2008). Efficient and Practical Protection of the Catechol Residue of 3,4-Dihydroxyphenylalanine (DOPA) Derivative as Acetonide. *Synthesis*, *2008*(5), 693–695.
18. Sperling, R. A., & Parak, W. J. (2010). Surface modification, functionalization and bioconjugation of colloidal inorganic nanoparticles. *Philosophical Transactions of the Royal Society a: Mathematical, Physical and Engineering Sciences*, *368*(1915), 1333–1383.
19. Canton, I., & Battaglia, G. (2012). Endocytosis at the nanoscale. *Chemical Society Reviews*, *41*(7), 2718–2739.

20. Brooks, D. J. (2008). Optimizing levodopa therapy for Parkinson's disease with levodopa/carbidopa/entacapone: implications from a clinical and patient perspective. *Neuropsychiatric Disease and Treatment*, *4*(1), 39–47.
21. Porras, G., De Deurwaerdere, P., Li, Q., Marti, M., Morgenstern, R., Sohr, R., et al. (2014). L-dopa-induced dyskinesia: beyond an excessive dopamine tone in the striatum. *Scientific Reports*, *4*, 1–5.
22. Jackson-Lewis, V., & Przedborski, S. (2007). Protocol for the MPTP mouse model of Parkinson's disease. *Nature Protocols*, *2*(1), 141–151.
23. Pardridge, W. M., Eisenberg, J., & Cefalu, W. T. (1985). Absence of albumin receptor on brain capillaries in vivo or in vitro. *The American Journal of Physiology*, *249*(3 Pt 1), E264–7.
24. Lu, W., Zhang, Y., Tan, Y.-Z., Hu, K.-L., Jiang, X.-G., & Fu, S.-K. (2005). Cationic albumin-conjugated pegylated nanoparticles as novel drug carrier for brain delivery. *Journal of Controlled Release*, *107*(3), 428–448.
25. Tuma, P. L., & Hubbard, A. L. (2003). Transcytosis: Crossing Cellular Barriers. *Physiological Reviews*, 871–932.
26. Hervé, F., Ghinea, N., & Scherrmann, J.-M. (2008). CNS Delivery Via Adsorptive Transcytosis. *The AAPS Journal*, *10*(3), 455–472.
27. Poduslo, J. F., Curran, G. L., & Berg, C. T. (1994). Macromolecular permeability across the blood-nerve and blood-brain barriers. *Proceedings of the National Academy of Sciences of the United States of America*, *91*(12), 5705–5709.
28. Bien-Ly, N., Yu, Y. J., Bumbaca, D., Elstrott, J., Boswell, C. A., Zhang, Y., et al. (2014). Transferrin receptor (TfR) trafficking determines brain uptake of TfR antibody affinity variants. *Journal of Experimental Medicine*, *3*(84), 84ra43.

Chapter V

OVERALL SUMMARY AND CONCLUSIONS

Novel therapeutics and treatment methods are desperately needed to combat the rising impact of chronic CNS diseases on individuals, families, and society as a whole. The major reason for the lack of progress in treating diseases such as AD and PD is the inability for most therapeutics to cross the BBB from circulation and enter the CNS (1). Developing a versatile method to safely deliver different classes of drugs across the BBB will open a tremendous number of new therapeutic options for poorly treated diseases of the brain and spinal cord.

One promising method for accomplishing this goal is the use of drug-loaded targeted nanoparticles. Targeted nanoparticles are capable of selectively accumulating in desired tissues through specific interaction of surface ligands with their receptors in the body (2). Several targeted nanoparticle therapies are currently under investigation in clinical trials (3,4).

By attaching ligands that undergo transcytosis at the BBB, drug-loaded nanoparticles have the potential to cross the BBB and deliver a wide variety of entrapped therapeutics to the brain, including small molecules, macromolecules, and biologics. Tf, an iron-carrying serum protein, is well known to undergo transcytosis at the BBB (5). Antibodies targeted to TfR at the BBB have long been hypothesized as potential shuttles for therapeutics across the BBB through RMT. Despite several decades of investigation using this approach, no viable clinical candidates have emerged. The main reason for this was recently discovered: anti-TfR mAb's are preferentially sent to the lysosome of BBB endothelial cells, rather than transcytosing (6,7).

Our group investigated whether the Tf-containing nanoparticles experienced the same restrictions at the BBB and did observe uptake of high avidity nanoparticles was limited in a similar fashion as high affinity mAb's (8). The primary goal of this work was to determine whether high avidity, Tf-containing nanoparticles could be made capable of accumulating in the brain in high numbers. To do this, Tf was added to the surface of nanoparticles through chemical bonds capable of breaking during transcytosis. With this design, the nanoparticles would retain strong interactions with TfR while in the blood, but would not be limited from entering the brain by restrictive ligand-receptor interactions or deleterious intracellular vesicle trafficking.

Polymeric nanoparticles containing Tf bound through a disulfide bond were first investigated. Though this method showed promising initial results in vivo, concerns regarding the mechanism of disulfide cleavage in the endosome and its compatibility with macromolecular therapeutics, along with potential toxicity introduced by exposing free thiols precluded further investigation of this design.

Instead, focus shifted on exploiting an alternative chemical change experienced during transcytosis: decreased pH. A small ketal that breaks at mildly acidic pH was incorporated between surface Tf and gold nanoparticle cores. Addition of the acid-cleavable link allowed the high avidity nanoparticles to accumulate within the brain in vivo at nearly three-times the amount of those lacking the cleavable link. Furthermore, nanoparticles containing an anti-TfR mAb showed no improvement in crossing the BBB when attached through the acid-cleavable link, further supporting the idea that anti-TfR mAbs are sent to the lysosome while simultaneously underscoring the importance of understanding how each targeting ligand behaves at the BBB to design the best drug delivery device (9).

Despite this improvement, the ketal linker investigated did not provide optimal cleavage kinetics during transcytosis to remove all surface protein. A boronic acid-based chemistry was next used to attach Tf to dopamine-loaded MAP nanoparticles. The pKa of boronic ester formation nPBA and MAP is ideal for ligand detachment during transcytosis as the nPBA will disassociate from MAP nearly instantaneously at pH < 6.8. Initial in vivo experiments using this targeting approach showed both increased amounts of DA within the brain and evidence of intact nanoparticles within the brain parenchyma. Further refinement

and validation of this nanoparticle could lead to an effective treatment for PD, particularly to prevent complications experienced from chronic oral L-DOPA treatment without sacrificing efficacy.

These promising results using the acid-cleavable targeting strategy warrant investigation of similarly prepared nanoparticles for drug delivery to other significant CNS diseases, including AD and GBM. In particular, the flexibility of this approach in regards to which types of therapeutics can be delivered should be investigated. Nanoparticles are very good at delivering small molecule therapeutics (2,10) but have recently been investigated as potential shuttles for macromolecules and proteins (11-13). Delivery of mAbs across the BBB could revolutionize treatment for AD as several highly potent mAb's investigated in clinical trials for AD have failed due to poor penetration into the CNS (14). Several of these antibodies showed measureable effects in humans even when brain uptake was extremely limited (1 nM estimated brain concentration), suggesting that if the brain accumulation of these mAb's could increase even slightly, disease-modifying treatment for AD may be possible.

Nanoparticles with detachable targeting ligands also have applications in areas beyond drug delivery across the BBB. Taking a broader view, the detachable ligand system works to facilitate nanoparticle transit across cellular borders in the body. This could be exploited to help nanoparticles enter the bloodstream from the gut. A system of regulated solute transport exists in the gut similar to the BBB and severely limits the passive uptake of nanoparticles from the GI tract. For this reason, oral administration of nanoparticles for systemic disease is not currently possible. Nanoparticles targeted against the neonatal Fc receptor (FcRN) have recently been shown cross the gut through RMT (15). Unfortunately, FcRN is expressed in many tissues in the body and may restrict uptake of these nanoparticles in desired tissues through FcRN-mediated sequestration. Attaching the targeting ligand through a compatible cleavable linker would allow the nanoparticle to circulate independent of FcRN-interactions once in the blood.

Future designs using detachable ligands would also include a secondary targeting moiety to facilitate uptake by cells of interest. In this design, a primary targeting ligand would be attached through a cleavable link and capable of interacting with its transcytosing receptor

while circulating. Once this ligand separates from the nanoparticle, a second, different ligand (one that is either inert while circulating or unveiled after cleavage of the primary ligand) is expressed and promotes uptake by a specific population of cells within the diseased tissues. For example, if a nanoparticle was designed to treat HER2-positive breast cancer metastases in the brain, a Tf ligand could be used to facilitate nanoparticle crossing of the BBB. Once in the brain, however, a trastuzumab antibody could be displayed on the nanoparticle surface to promote uptake by the cancerous cells. This type of multi-targeted nanoparticle could provide highly precise and efficacious treatments for conditions where drug delivery is limited by cellular barriers.

Despite the promise of this detachable ligand approach, several critical questions require investigation before future pre-clinical and, hopefully, clinical investigations can begin. First, the distribution of these nanoparticles throughout the brain is poorly understood. Though gross regional differences were measured in the ketal linker work (9), differences between functional regions were not determined. Determining whether nanoparticle uptake correlates to local TfR expression and whether any differences can be exploited to increase accumulation in diseased tissues with high endothelial TfR expression is an important consideration. Depending on what therapeutic is delivered, it is also vital to ensure these high avidity nanoparticles are not outcompeting endogenous Tf on tissues with decreased TfR expression (relative to the BBB) and delivering toxic drugs to non-diseased tissue.

It is also immensely important to understand how treatment with these Tf-containing nanoparticles affects iron homeostasis and TfR expression on the BBB and throughout the body. Use of high affinity anti-TfR antibodies was found to reduce TfR expression at the BBB, rendering subsequent doses less effective at penetrating the brain (6). If treatment with these nanoparticles downregulates BBB TfR in a similar fashion, their use in chronic diseases may be limited.

One final consideration is the need to investigate and validate other potential TfR ligands. Though the limits of high affinity anti-TfR mAb's have been thoroughly discussed in this text (see section 1.4.1), this does not preclude their use as targeting ligands at the BBB entirely. Recently, an anti-TfR mAb that has reduced binding affinity at pH 5.5 was reported to cross an in vitro model of the BBB while variants with pH independent binding could not

(16). It is possible that continuous TfR occupation after endocytosis, rather than ligand affinity, avidity or binding epitope, is the event that triggers sequestration to the lysosome. If this is true, mAb's with similar changes in affinity in response to pH changes could be synthesized and used to target TfR at the BBB.

In summary, this work details the design, development and investigation of high-avidity Tf-containing nanoparticles capable of crossing the BBB by incorporating Tf into the nanoparticle design through a cleavable chemical link. Attaching the Tf through chemistry that breaks at mildly acidic pH showed the greatest potential for increased brain uptake of nanoparticles. Polymeric nanoparticles using this targeting design are capable of delivering dopamine across the healthy mouse BBB and have tremendous potential in treating diseases of the CNS.

5.1 References

1. Pardridge, W. M. (2004). The Blood-Brain Barrier: Bottleneck in Brain Drug Development. *NeuroRx: the Journal of the American Society for Experimental Neurotherapeutics*, *2*, 3–14.
2. Kamaly, N., Xiao, Z., Valencia, P. M., Radovic-Moreno, A. F., & Farokhzad, O. C. (2012). Targeted polymeric therapeutic nanoparticles: design, development and clinical translation. *Chemical Society Reviews*, *41*(7), 2971.
3. Zuckerman, J. E., Gritli, I., Tolcher, A., Heidel, J. D., Lim, D., Morgan, R., et al. (2014). Correlating animal and human phase Ia/Ib clinical data with CALAA-01, a targeted, polymer-based nanoparticle containing siRNA. *Proceedings of the National Academy of Sciences*, *111*(31), 11449–11454.
4. Hrkach, J., Hoff, Von, D., Ali, M. M., Andrianova, E., Auer, J., Campbell, T., et al. (2012). Preclinical Development and Clinical Translation of a PSMA-Targeted Docetaxel Nanoparticle with a Differentiated Pharmacological Profile. *Science Translational Medicine*, *4*(128), 128ra39–128ra39.
5. Tuma, P. L., & Hubbard, A. L. (2003). Transcytosis: Crossing Cellular Barriers. *Physiological Reviews*, 871–932.
6. Bien-Ly, N., Yu, Y. J., Bumbaca, D., Elstrott, J., Boswell, C. A., Zhang, Y., et al. (2014). Transferrin receptor (TfR) trafficking determines brain uptake of TfR antibody affinity variants. *Journal of Experimental Medicine*, *3*(84), 84ra43.
7. Niewoehner, J., Bohrmann, B., Collin, L., Urich, E., Sade, H., Maier, P., et al. (2014). NeuroResource. *Neuron*, *81*(1), 49–60.
8. Wiley, D. T., Webster, P., Gale, A., & Davis, M. E. (2013). Transcytosis and brain uptake of transferrin-containing nanoparticles by tuning avidity to transferrin receptor. *Proceedings of the National Academy of Sciences*, *110*(21), 8662–8667.
9. Clark, A. J., & Davis, M. E. (2015). Increased brain uptake of targeted nanoparticles by adding an acid-cleavable linkage between transferrin and the nanoparticle core. *Proceedings of the National Academy of Sciences*, *112*(40), 12486-12491.

10. Eliasof, S., Lazarus, D., Peters, C. G., Case, R. I., Cole, R. O., Hwang, J., et al. (2013). Correlating preclinical animal studies and human clinical trials of a multifunctional, polymeric nanoparticle. *Proceedings of the National Academy of Sciences*, *110*(37), 15127–15132.
11. Gdowski, A., Ranjan, A., Mukerjee, A., & Vishwanatha, J. (2015). Development of Biodegradable Nanocarriers Loaded with a Monoclonal Antibody. *International Journal of Molecular Sciences*, *16*(2), 3990–3995.
12. Bilati, U., Allémann, E., & Doelker, E. (2008). Poly(D,L-lactide- co-glycolide) protein-loaded nanoparticles prepared by the double emulsion method—processing and formulation issues for enhanced entrapment efficiency. *Journal of Microencapsulation*, *22*(2), 205–214.
13. Mundargi, R. C., Babu, V. R., Rangaswamy, V., Patel, P., & Aminabhavi, T. M. (2008). Nano/micro technologies for delivering macromolecular therapeutics using poly(d,l-lactide-co-glycolide) and its derivatives. *Journal of Controlled Release*, *125*(3), 193–209.
14. Freskgård, P.-O., & Urich, E. (2016). Antibody therapies in CNS diseases. *Neuropharmacology*, 1–46. (Ahead of print)
15. Pridgen, E. M., Alexis, F., Kuo, T. T., Levy-Nissenbaum, E., Karnik, R., Blumberg, R. S., et al. (2013). Transepithelial transport of Fc-targeted nanoparticles by the neonatal fc receptor for oral delivery. *Science Translational Medicine*, *5*(213), 213ra167–213ra167.
16. Sade, H., Baumgartner, C., Hugenmatter, A., Moessner, E., Freskgård, P.-O., & Niewoehner, J. (2014). A Human Blood-Brain Barrier Transcytosis Assay Reveals Antibody Transcytosis Influenced by pH-Dependent Receptor Binding. *PLoS ONE*, *9*(4), e96340.

Appendix A

CRLX101 NANOPARTICLES LOCALIZE IN HUMAN TUMORS AND NOT IN ADJACENT, NONNEOPLASTIC TISSUE AFTER INTRAVENOUS DOSING*

A.1 Preamble

During my thesis work I was given the opportunity to work on a clinical trial investigating the behavior of a nanoparticle therapeutic in humans. In this study, CRLX101 (formerly IT-101), a nanoparticle therapeutic developed by the Davis lab and currently under investigation in a variety of clinical trials, was given to patients with gastric cancer. The goal of this study was to determine if CRLX101 behaves in humans as predicted and described in animal models; namely, that the nanoparticles accumulate specifically in tumors and not healthy tissue. After the first intravenous dose of CRLX101, biopsies were taken of the primary tumor and nearby, uninvolved tissue. The accumulation of the nanoparticle drug in either tumor or nonneoplastic tissue was measured using confocal microscopy. The following is work published from that investigation.

*Excerpts from this chapter are reprinted from Clark, A. J., et al. (2016). CRLX101 nanoparticles localize in human tumors and not in adjacent, nonneoplastic tissue after intravenous dosing. *Proceedings of the National Academy of Sciences*, *113*(14), 3850-3854 with permissions from *PNAS*.

A.2 Introduction

Nanoparticle-based experimental therapeutics are being used to deliver a variety of different drug molecules to patients with solid tumors (1). Nanoparticle delivery seeks to improve pharmacokinetic (PK) properties (e.g., enhanced solubility of the drug, increased circulation times), altered biodistribution of the drug molecules to have low amounts of drugs in non-target tissues and increased amounts in tumors, and enhanced pharmacodynamics (PD) (e.g., tunable release of the drug at the site of action in the tumor) in order to produce enhanced efficacy while simultaneously reducing side effects (and most importantly, introducing no new side effects due to the nanoparticle) in patients. These properties can: (i) enable drug combinations formerly prohibited by toxicity limits, (ii) enable new classes of drug delivery (for example, short interfering RNAs (siRNAs)), and (iii) provide cell specific targeting within a tumor.

Delivery of drugs to solid tumors using nanoparticle technology relies on the enhanced permeability and retention (EPR) effect. The mechanistic data regarding the EPR effect come from animal models, primarily xenografted human tumors in mice. Because these xenografted tumors poorly recapitulate the architecture of true human tumors, there is skepticism about whether or not intact nanoparticles can localize in human tumors. Radiolabeled liposomes have been used to assess tumor accumulation in humans (2,3). In those studies, the amounts of radioactivity accumulated in tumors did correlate with the number of microvessels measured from 9 patient biopsies (3). Increased microvessel density may be an indication of increasing potential for the EPR effect. Also, Davis et al. demonstrated dose dependent deposition of the CALAA-01 polymer-siRNA nanoparticle system in human subcutaneous melanoma metastases using a stain specific for the nanoparticle (4), Eliasof et al. showed the presence of the camptothecin (CPT) component of CRXL101 in a single human gastric tumor biopsy (5), and Weiss et al. provided a single biopsy showing CRLX101 and CPT in a human breast cancer (6). Thus, there remains a need for further evidence of intact nanoparticle localization in solid, human tumors when they are systemically administered to cancer patients.

Here, we use fluorescence microscopy to demonstrate the presence of an intact polymer-drug nanoparticle (CRLX101) in human gastric tumors that have been obtained from endoscopic capture prior to, and 24 to 48 hours after, dosing. Adjacent, non-neoplastic tissues are also obtained to assist in determining the specificity for tumor localization. Further, immunohistochemistry (IHC) was used to label various biomarkers within the tumor tissue to better understand the pharmacodynamics effect of CRLX101 on solid human tumors.

CRLX101 is a nanoparticle consisting of a cyclodextrin-containing polymer conjugate of CPT. The individual polymer strands self-assemble into nanoparticles (approximately five strands) of approximately 20 to 30 nm diameter and 10 wt% CPT by multiple, interstrand, inclusion complex formation between cyclodextrin and the CPT molecules (Fig A.1A). CRLX101 is currently in a number of human cancer Phase II trials [early results from some of the Phase I/II trials are available (6,7)]. Here, a clinical trial was performed at and sponsored by the City of Hope (ClinicalTrials.gov identifier: NCT01612546). CRLX101 was supplied by Cerulean Pharma Inc. The primary endpoint of this study was to test the hypothesis that intact CRLX101 nanoparticles localize in primary human tumors and not adjacent, non-neoplastic tissue after intravenous administration. The results presented here show that CRLX101 does localize in tumor tissue and not the non-neoplastic tissue leading to the expected pharmacodynamics effect.

A.3 Results

A.3.1 Trial design and tissue biopsies

Patients with progression on at least one prior line of systemic therapy were enrolled in a pilot study to assess CRLX101 activity in gastric, esophageal, or gastroesophageal adenocarcinoma or squamous cell carcinoma (Fig A.1B). Patients consented to have endoscopic assisted biopsies of both their primary tumor and healthy, adjacent tissue prior to, and 24 to 48 hours after, the first dose of CRLX101. The first dose of CRLX101 for all patients was given at the recommended Phase II dosing of 15 mg/m^2 Three individual samples of both tumor and non-neoplastic tissue were acquired and divided in the following

ways: (i) frozen in optimized cutting temperature compound (Tissue-Tek OCT) for fluorescence microcopy studies, (ii) fixed in 10% formalin for antibody staining, or (iii) placed in formalin for standard histology. A total of 10 patients consented for this study, of which 9/10 had histologically confirmed tumor tissue present in both pre- and post-CRLX101 treatment biopsies.

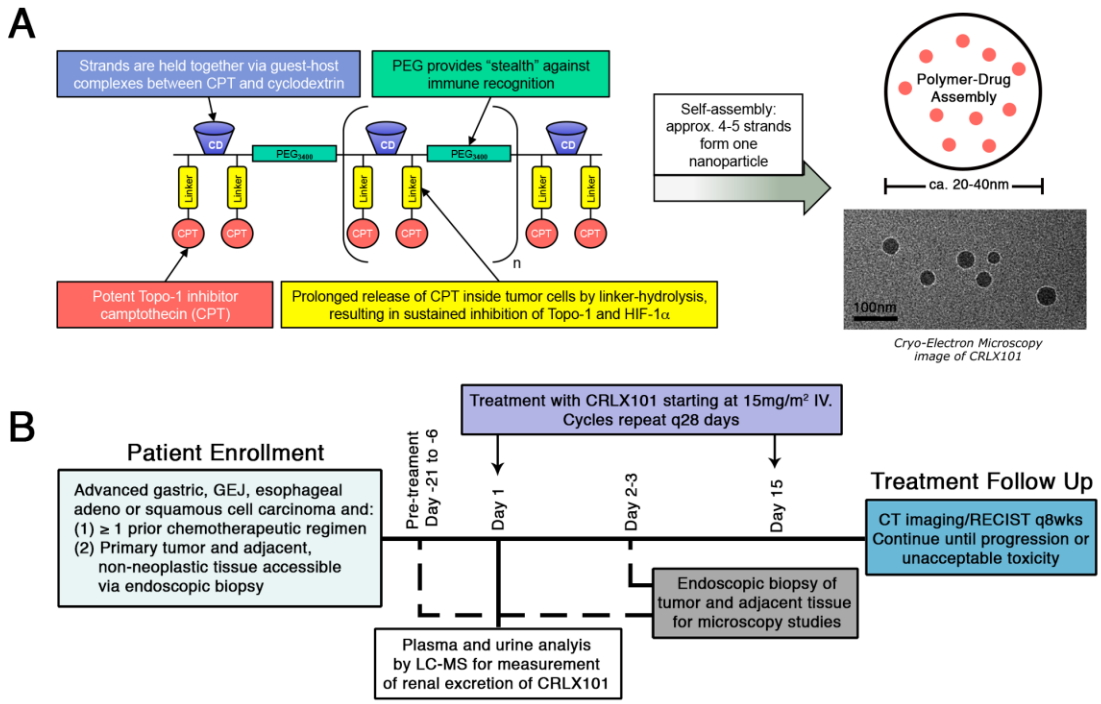

Fig A.1 Schematic of CRLX101 and study design. (A) CRLX101 nanoparticle design and particle formation including image of particles under cryo-electron microscopy. (B) Design of clinical trial.

A.3.2 Detection of CRLX101 fluorescence in human gastric tumors

The pharmacologically active component of CRLX101 – camptothecin (CPT) – has intrinsic fluorescence ($Excitation_{max}$ = 370 nm and $Emission_{max}$ = 435 nm), and can be used for the detection of CRLX101 in tissue via fluorescence microscopy (5,6,8). Fig A.2A illustrates detection of CPT fluorescence in two different types of human tumor xenografts in mice 24 hours after intravenous dosing of CRLX101. The fluorescence signal has a patchy

distribution throughout the tumor with some areas of densely clustered punctate fluorescence signal while other areas are devoid of signal.

Figs A.2B-C illustrate detection of CPT fluorescence in human gastric tumor biopsy specimens. The CPT signal observed was qualitatively similar to that obtained from the xenograft tumors (Examples of CPT signal observed in other patients are shown in Fig A.3). Distribution of CPT fluorescence was focal and punctate. To verify that observed signal was indeed CPT, regions of interest were repeatedly scanned using the confocal laser. CPT is a weak fluorophore, and rapidly photobleaches upon repeated interrogation, as compared to non-specific tissue autofluorescence. Thus, punctate fluorescence that rapidly diminished upon multiple scans was determined to be from CPT (Fig A.4). In total, CPT fluorescence was detected in all 9 post-treatment tumors. No definitive CPT fluorescent signal was observed in any of the adjacent non-tumor biopsy specimens (Table A.1). One patient showed potential CPT signal in the non-tumor tissue biopsy; however, this signal did not fully quench from repeated laser scans, thereby not meeting our criteria for definitive CPT signal (Fig A.5). Fluorescence was considerably rarer in the patient samples than in the xenograft tumors. However, the patient biopsies were only a fraction of the size of pieces of xenograft tumor that we investigated. Tissue samples were also stained with an antibody against the PEG component of CRLX101 (Fig A.6). In 5 of 9 patients, the PEG antibody co-localized with the CPT fluorescence, suggesting intact nanoparticles were present within the post-treatment tumors.

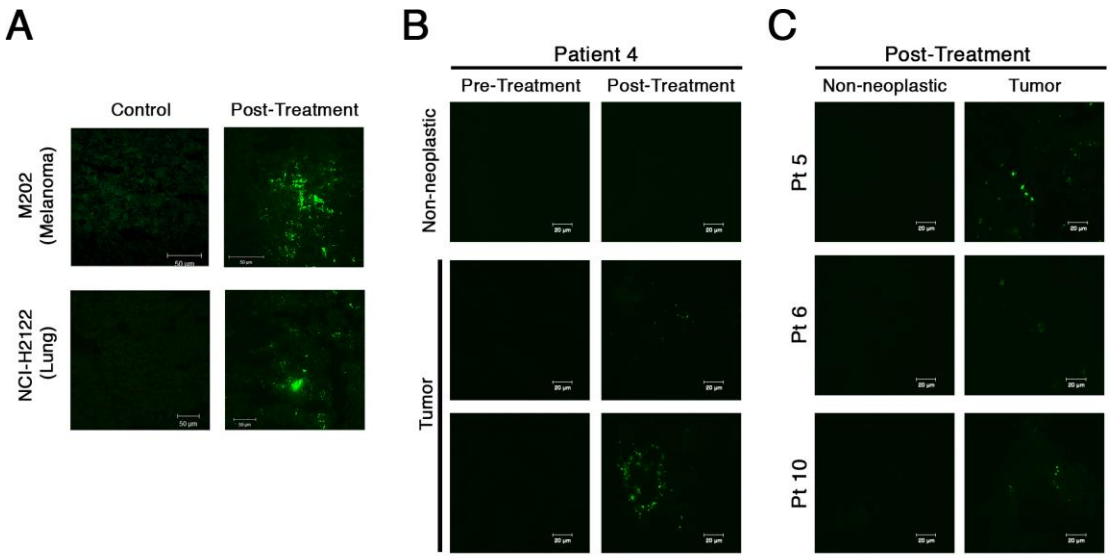

Fig A.2 Detection of camptothecin (CPT) fluorescence following CRLX101 treatment in mice and humans. (A) Presence of CPT in mice bearing two different human tumor xenografts. CPT is apparent 24hrs after a single CRLX101 dose and appears as bright, punctate dots (green dots) with a patchy distribution throughout the tissue. (B) CPT signal in non-neoplastic and tumor tissue of a single patient under different dosing states. Positive CPT signal (green dots) is seen only in the post-treatment tumor tissue. (C) CPT signal in post-treatment non-neoplastic and tumor tissue for three other patients.

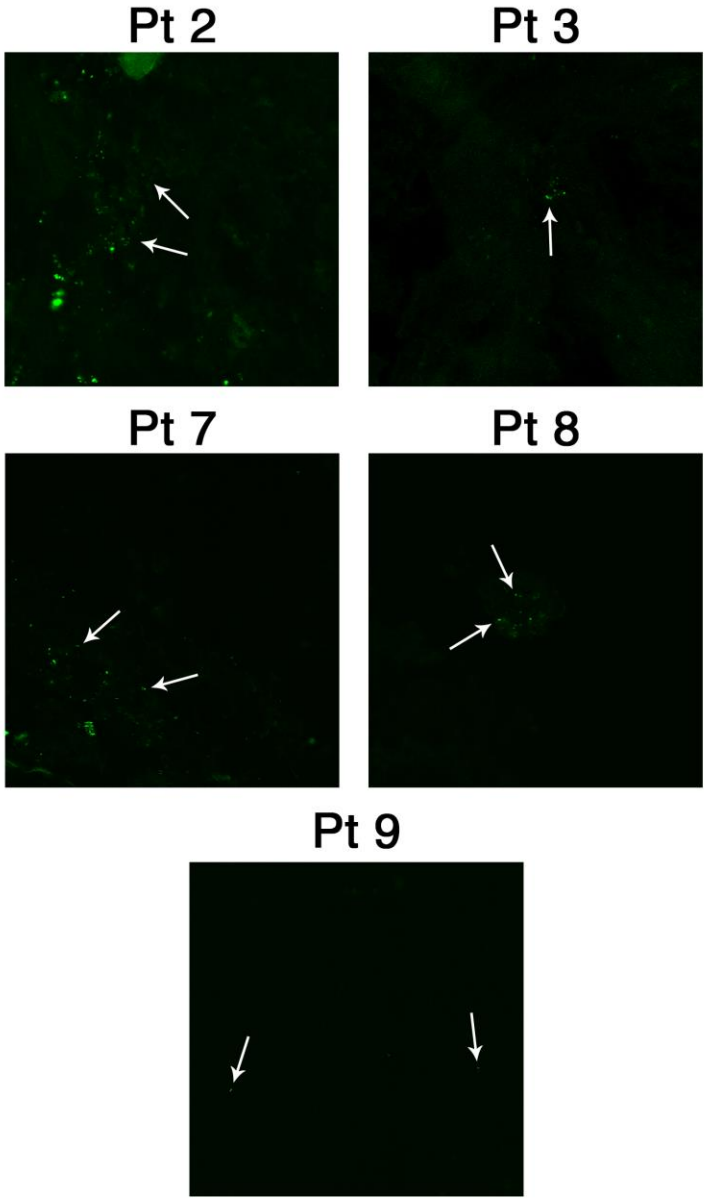

Fig A.3 Positive CPT signal in posttreatment tumor tissues. Posttreatment tumor images are shown for remaining patients. White arrows indicate examples of CPT signal.

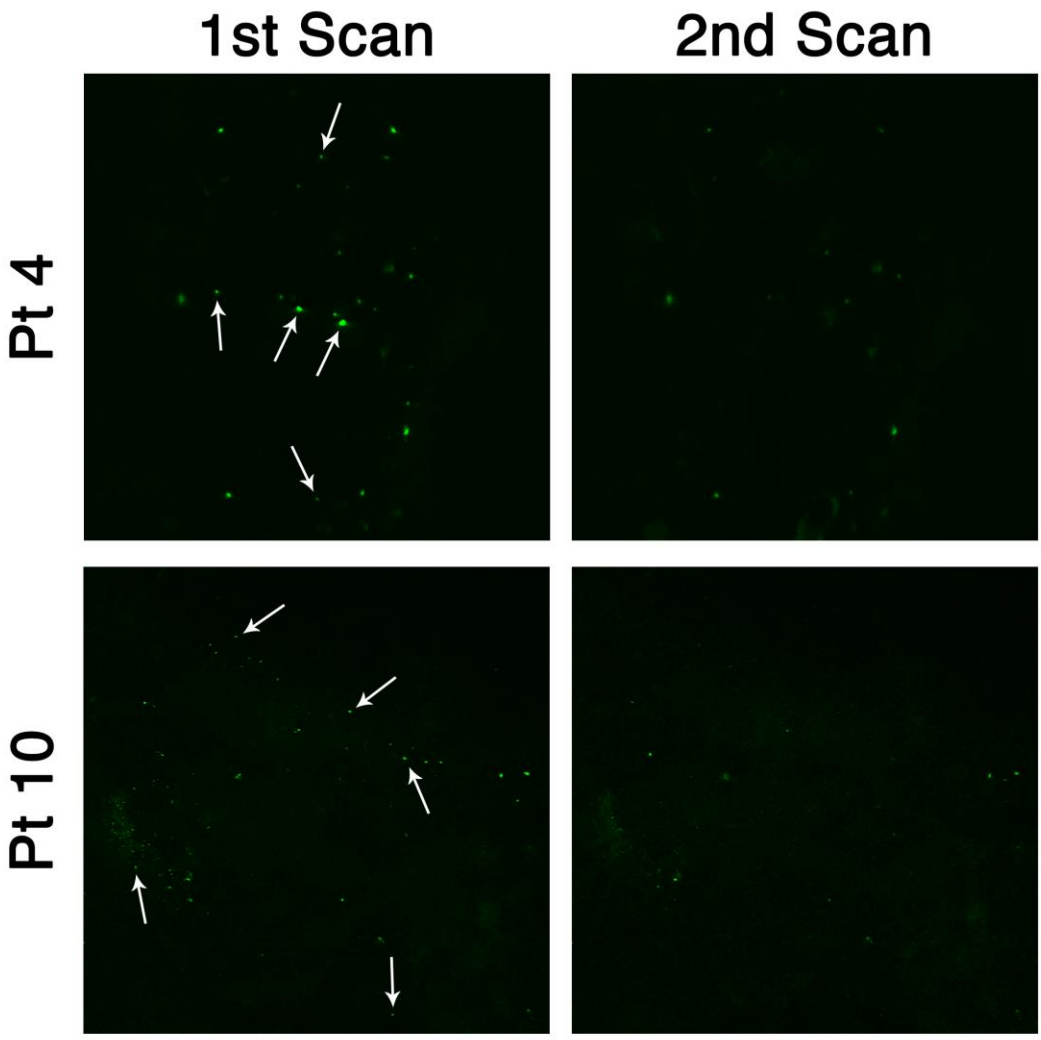

Fig A.4 CPT signal shows significant decrease with sequential laser scans. Points of positive CPT signal in the 1st scan which are absent in a 2nd scan of the same tissue area are indicated by white arrows. The majority of CPT signal is absent upon the 2nd laser scan.

Patient	Tumor Differentiation	Pre-Treatment Non-Neoplastic Tissue	Pre-Treatment Tumor Tissue	Post-Treatment Non-Neoplastic Tissue	Post-Treatment Tumor Tissue
2	Poor	0	0	0	++
3	Well	0	0	0	++*
4	Moderate to poor	0	0	0	+++*
5	Moderate	0	0	0	++*
6	Poor	0	0	0	++*
7	Poor	0	0	0	++
8	Moderate	0	0	+	++*
9	Moderate to poor	0	0	0	++
10	Poor	0	0	0	++

Table A.1 Summary of biopsy investigation results for each patient. Tumor quality was determined using standard histological techniques. CPT signal in the tissue sample was graded the following ways: (0) indicates no CPT signal was observed in the tissue; (+) indicates potential CPT signal was observed in the tissue, but did not meet both requirements used to determine true CPT signal [(1) observed signal was punctate and patchy in distribution and (2) signal rapidly diminished upon repeated confocal laser scans]; (++) definitive CPT signal was observed but only in a minority of images acquired; (+++) definitive signal was observed in the majority of images acquired. Tissues marked by an (*) indicate CPT signal co-localization with PEG stain was observed. Patient 1 was not included in the analysis because no tumor tissue was identified in the biopsy samples both pre and post-CRLX101 treatment.

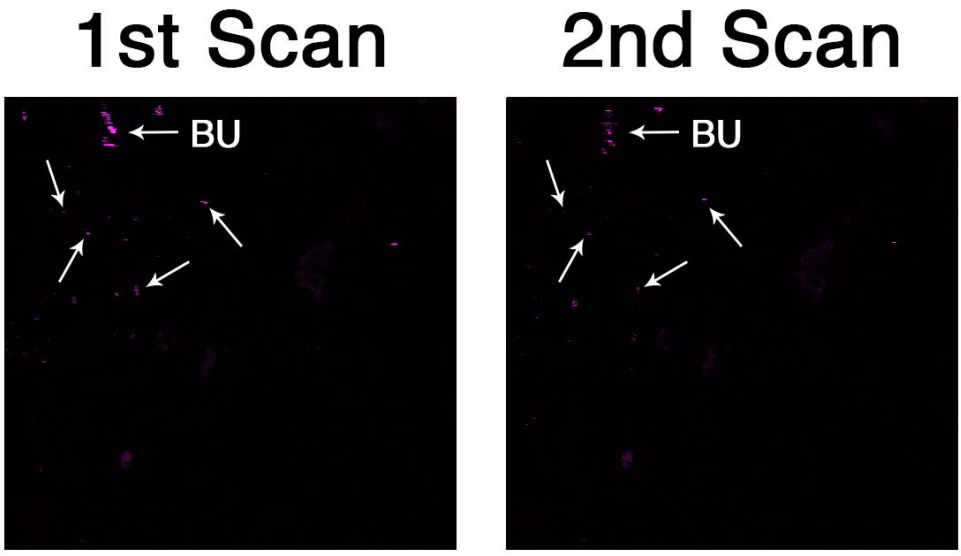

Fig A.5 Potential positive CPT signal (purple dots) in patient 8 posttreatment non-neoplastic tissue. Areas of potential CPT signal that did not diminish upon multiple confocal laser scans are indicated with white arrows. A bubble within the tissue section identified with a brightfield image is indicated with the BU label. The overall decrease in CPT signal in this tissue area was not as pronounced as that observed in the posttreatment tumor tissues (Fig. S2) so this tissue was not determined to contain definitive CPT signal.

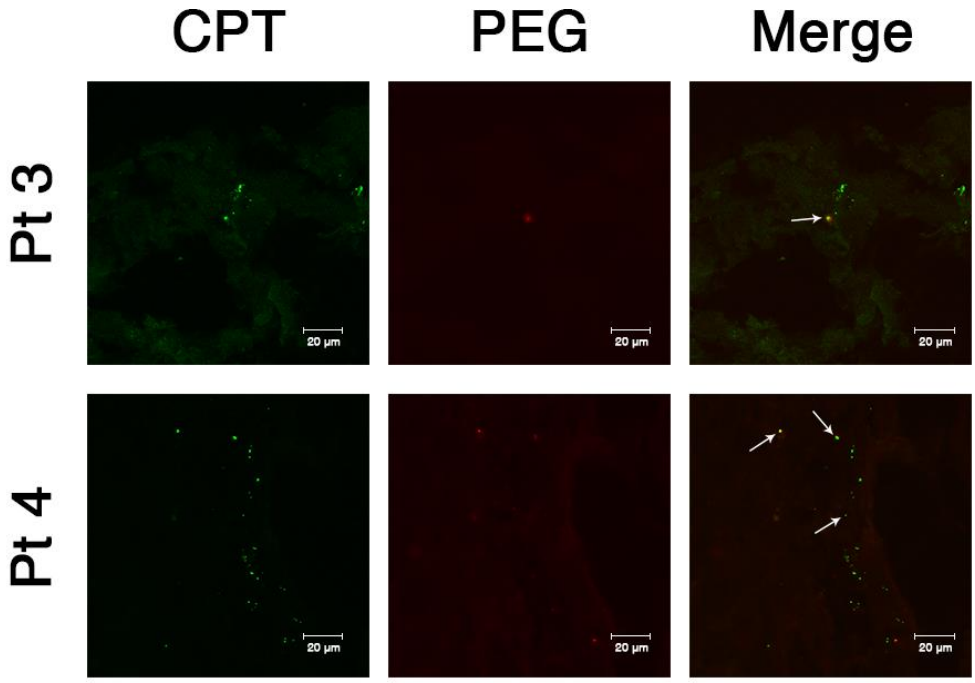

Fig A.6 CPT-PEG co-localization. Tissue samples were stained with an anti-PEG antibody to identify the polymer component of CRLX101. Evidence of co-localized CPT signal (bright green dots) and PEG stain (red dots) were observed in 5 of 9 patients. White arrows indicate points of stain co-localization.

A.3.3 Pharmacodynamics investigation of CRLX101 in human gastric tumors

To confirm the pharmacokinetic observations, a pharmacodynamics study was performed. A haematoxylin and eosin (H&E) stain was performed first to verify the quality of existing tumors and surrounding, uninvolved tissue (Fig A.7). The CA IX antibody stain showed high intracellular expression in pre-treated tumor samples, whereas the post-treatment samples revealed much less staining, suggesting a decrease in HIF-1□, a transcription factor upstream of CA IX (9). The Topo-I stain showed reduced staining from pre-treatment to post-treatment samples (Fig A.8). This result suggests CPT released from the nanoparticle, bound Topo-I, and triggered its degradation.

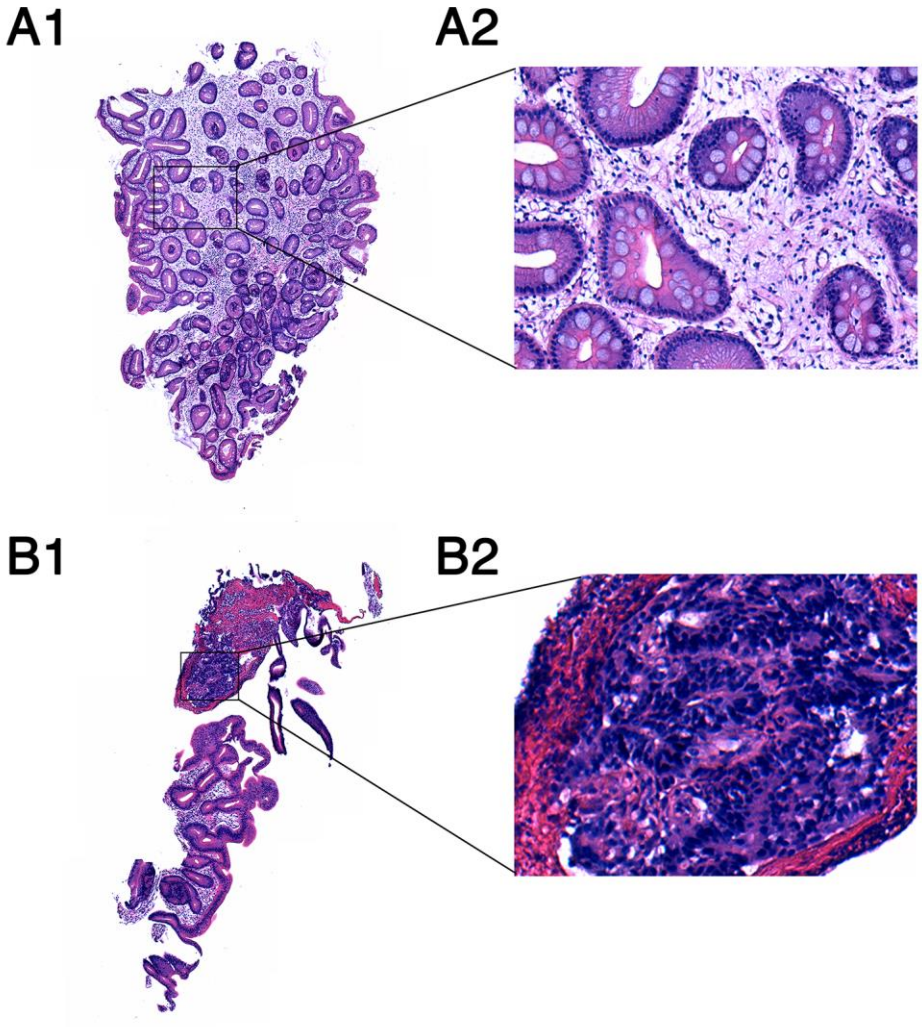
A1
A2
B1
B2

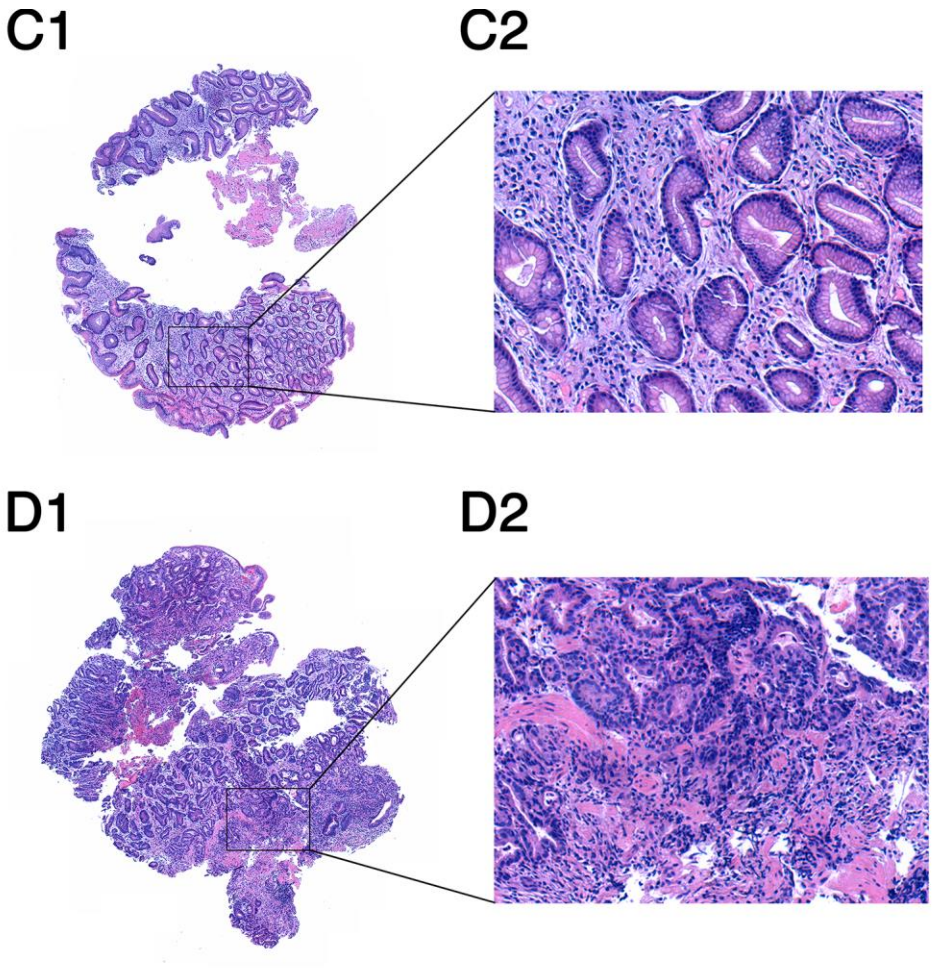

Fig A.7 H&E stain of biopsy series from a single patient. Sections of entire tissue biopsy for pre-treatment non-neoplastic (A1), pretreatment tumor (B1), posttreatment non-neoplastic (C1), and posttreatment tumor (D1) tissues are shown. The image in the right column (X-2) contains a high-magnification image of the area indicated by the box overlaying the corresponding full tissue section.

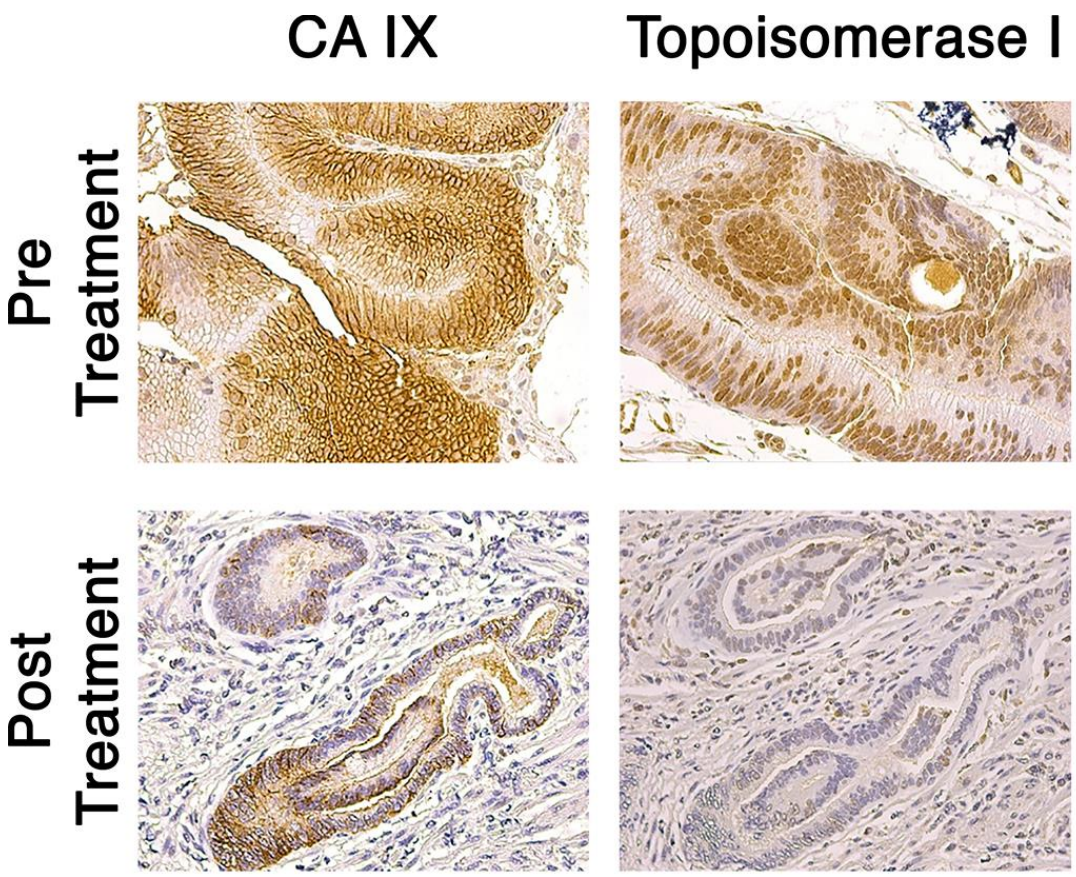

Fig A.8 Pharmacodynamics investigation of tumor biomarkers. Tumor tissues of six patients were stained for two different tumor biomarkers (CA IX and Topo-I) before and after treatment with CRLX101. The results shown here are indicative of the trend observed in the six individual tissue series.

A.4 Discussion

The ability of intact nanoparticles to extravasate and deposit within tumor tissue is fundamental to their therapeutic activity and selectivity. This mechanism of tumor deposition, known as the EPR effect, has only ever been demonstrated directly in animal models, specifically in xenograft tumors in mice that, in general, do not faithfully represent the true architecture of human tumors. There is considerable debate in the literature surrounding the existence of this phenomenon in human tumors. Because most nanoparticle therapeutics systems have been designed from the optimization of delivery to xenografted

human tumors in mice, it is important to show that similar mechanisms of deposition take place in human tumors.

Here, we demonstrate through matched sets of pre- and post-nanoparticle dosing biopsies of tumor and adjacent, non-neoplastic tissue evidence of intact nanoparticle deposition in human tumors after intravenous administration. All nine tumor-bearing patients showed evidence of CPT in the post-treatment tumor tissue. Furthermore, no definitive CPT signal was observed in adjacent, non-neoplastic tissue. Interestingly, the signal observed within the human tumors appeared to be solely due to drug within the tumor parenchyma. If drug were retained within the microvasculature following tissue fixation and processing, we would expect to see some signal in the normal tissue, but this was not observed. Due to poorly preserved tissue architecture of the fresh-frozen biopsy samples following processing, identification of drug signal within different tumor compartments (e.g. intracellular vs. interstitial) was not possible. An understanding of how uniformly and deeply CRLX101 diffuses throughout the tumor and how this affects free drug concentration within the tumor is critical to maximizing CRLX101 efficacy.

Although there was detectable CPT signal in the post-treatment tumors, it was significantly lower than what we have previously experienced in mouse xenografts (Fig A.2). CRLX101 first enters mouse model xenografts within six hours of IV administration and slowly diffuses away from blood vessels and deeper into tumors over several days (5). Therefore, the quantity of CPT present in the patient samples 24 hours after treatment may strongly depend on location of the biopsy relative to vasculature. The biopsies were acquired randomly from a patient's primary tumor and measured only ~3mm^3, which is just a fraction of the total tumor volume. In contrast, it is possible to isolate entire xenografts and readily identify vasculature and areas of high drug signal. Human tumors also express a high degree of heterogeneity (10,11). In gastric cancer patients, the tumor microvascular density can significantly vary depending on the extent of invasion to surrounding tissues as well as gross tumor morphology (12). Factors that influence vascular density and heterogeneity within human tumors may affect the magnitude and reproducibility of the EPR effect in humans.

To investigate whether intact nanoparticles were present within the human tumors, an antibody against the PEG component of CRLX101 was used (Fig A.6). In 5 of 9 patients,

CPT signal co-localized with the PEG stain was observed, suggesting that at least some drug is still retained within intact nanoparticles in these tissues. In vitro investigation of CPT release from CRLX101 has shown only 30% of loaded CPT released from the nanoparticle at neutral pH after 24 hours with that value dropping to 10% at the tumor microenvironment pH (pH 6.5-6.9) (13). These kinetics suggest a significant portion of the loaded CPT should be retained within the nanoparticle core when the post-treatment biopsies were acquired. Experiments using PET with radiolabeled CRLX101 in mice have shown increasing, selective accumulation of the nanoparticle within tumors over the first 24 hours after an initial dose (8). A similar result was found using MRI where CRLX101 showed increasing apparent diffusion coefficient over the first seven days after dosing in tumor-bearing mice (14). Both these in vivo results indicate intact nanoparticles are likely accumulating within the human tumors over the first 24 to 48 hours. The lack of co-localized CRLX101 polymer-CPT signal in 4 of the 9 patients may be explained by poor sensitivity of the anti-PEG antibody stain used. Several PEG mAb's were investigated and all showed significantly decreased affinity to the CRLX101 polymer component after exposure to tissue fixation agents. This likely limited the ability to detect the CRLX101 polymer within the fixed tissue sections. Combined with the scarcity of positive CPT signal in most tumor biopsies, this factor may have caused false negative co-localization results for the four patients. It is also possible that these patients experienced less overall nanoparticle deposition into the tumor due to tumor characteristics that are unfavorable—compared to the six positive patients—to nanoparticle extravasation, reducing potential binding sites for the PEG antibody.

Despite relatively low CPT signal in the human tumor compared to mouse xenograft tissue, investigation of tumor biomarkers showed clear pharmacodynamic effects of the drug within tumors. CA IX expression is driven directly by HIF-1α and can be used to measure HIF-1α activity. The decreased expression of CA IX in the post-treatment tumors is consistent with the inhibitor effect of CRLX101 on HIF-1α expression, which has been previously observed (7,15). CPT has been known to cause rapid degradation of Topo-I through the ubiquitin-proteasome system in tissue culture (16-20). Our result reveals this may also be occurring in vivo as evident by the lower staining of Topo-I in the post-treatment

tumors. This finding would be the first result demonstrating down-regulation of Topo-I by CPT in human tumors collected from clinical trials.

A.5 Conclusions

In summary, we show evidence of the nanoparticle CRLX101 accumulating within gastric tumors in humans but not adjacent, non-neoplastic tissue. This result supports the hypothesis that nanoparticle therapeutics can localize within human solid tumors, and this may occur via the EPR effect. Co-localization of the CPT and PEG components of CRLX101 was observed in several patients, indicating intact nanoparticles are reaching tumors in humans. Though signal observed from the CPT component of CRLX101 was lower than what had been previously observed in xenografts, this decrease might be due to biopsy sampling location and tumor heterogeneity, and in particular, microvascular density. IHC revealed changes in two tumor biomarkers consistent with the biological activity of CPT within tumors.

A.6 Methods

Mice studies: All mice were treated according to the National Institutes of Health Guidelines for Animal Care and Use as approved by the Caltech Institutional Animal Care and Use Committee. Mice were treated with CRLX101 via lateral tail vein injection then euthanized after 24 hours. Their tumors were resected, embedded in optimal cutting temperature compound and frozen for fluorescence microscopy.

Patient enrollment and CRLX101 treatment: Patients with advanced gastric, gastroesophageal junctional, esophageal adenocarcinoma carcinoma, or squamous cell carcinoma, who had progressed on at least one prior line of systemic therapy, were enrolled in a pilot clinical trial to assess preferential uptake of CRLX101 in tumor tissue versus healthy, adjacent tissue (ClinicalTrials.gov identifier: NCT01612546). Patients were discontinued of all systemic therapy at least four weeks prior to receiving CRLX101. Pre-treatment biopsies were acquired by endoscopy 6-21 days before receiving the first IV infusion of 15 mg/m2 CRLX101. The post treatment biopsies were performed between 24 to 48 hours after receiving CRLX101.

Human gastric tissue sample acquisition and preparation: Human gastric tissue samples were obtained from patients enrolled in a CRLX101 pilot trial with consent in accordance with City of Hope Institutional Review Board (IRB) guidelines (City of Hope IRB Protocol 11276). Biopsy specimens used for fluorescence were immediately embedded in optimal cutting temperature media and frozen on dry ice. Biopsies acquired for IHC were immediately placed in 4% paraformaldehyde. All specimens were transferred to the City of Hope Translational Research Laboratory before processing. The clinical trial was sponsored by the City of Hope. CRLX101 was supplied by Cerulean Pharma Inc.

Tissue immunofluorescence: Fresh frozen tissue samples were sectioned, washed briefly in PBS, and fixed for ten minutes with 10% formalin. Slides were blocked for one hour in 5% normal goat serum in PBS and followed by overnight stain at 4°C with an anti-PEG antibody

(1:100 dilution, Abcam ab94764). Slides were then washed and stained for one hour with an Alexa-Fluor 488-conjugated secondary antibody (1:500 dilution, Invitrogen A-21212) and mounted using ProLong Gold antifade reagent. Tissues were imaged with a Zeiss LSM 510 inverted confocal scanning microscope using a Zeiss Plan Neofluar 63x/1.25 oil objective. The excitation wavelength for camptothecin was 710 nm (two-photon laser) and 488 nm for detection of PEG. The corresponding emission filters were 390-465 nm and 565-615 nm, respectively. Images were adjusted to have equivalent mean brightness using the brightness adjustment tool in LSM 5 Image Browser (Leica).

Tumor biomarker immunohistochemistry: Tumor tissues were fixed with 10% formalin and embedded in paraffin. Tissues sections 5μm in thickness were prepared and deparaffinized in xylenes followed by rehydration in graded alcohols. The sections were baked in 0.01 M sodium citrate buffer, pH 6.0, for 15 minutes for antigen retrieval. Endogenous peroxidase was quenched with 3% hydrogen peroxide at room temperature (20–25°C). Primary rabbit Topo-I (Santa Cruz, CA, USA) and rabbit CA IX (Proteintech, Chicago, IL) was applied overnight at 4°C with a final concentration of 1:200 (Topo-1) and 1:2000 (CA IX). The sections were counterstained with hematoxylin, followed by dehydration in graded alcohols and xylenes. Tissue sections were then developed using horseradish peroxidase (HRP) DAB Quanto kit according to the manufacturer's instructions (Thermal Scientific, Fremont, California, USA). Sections containing no primary antibody stain were processed simultaneously and used as negative controls while samples known to strongly express Topo-I and CA IX served as positive controls. Photomicrographs were taken on Leica microscope equipped with a CCD camera (Leica Microsystems, Wetzlar, Germany).

A.7 References

1. Davis ME, Chen Z, Shin DM (2008) Nanoparticle therapeutics: an emerging treatment modality for cancer. *Nat Rev Drug Discov* 7(9):771-782.
2. Harrington KJ *et al.* (2001) Effective Targeting of Solid Tumors in Patients with Locally Advanced Cancers by Radiolabeled Pegylated Liposomes. *Clin Cancer Res* 7:243-254.
3. Koukourakis MI *et al.* (1999) Liposomal Doxorubicin and Conventionally Fractionated Radiotherapy in the Treatment of Locally Advanced Non-Small-Cell Lung Cancer and Head and Neck Cancer. *Clin Oncol* 17:3512-3521.
4. Davis ME *et al.* (2010) Evidence of RNAi in humans from systemically administered siRNA via targeted nanoparticles. *Nature* 464:1067–1070.
5. Eliasof S. *et al.* (2013) Correlating preclinical animal studies and human clinical trials of a multifunctional, polymeric nanoparticle. *Proc Natl Acad Sci USA* 110:15127–15132.
6. Weiss GJ, Chao J, Neidhart JD, Ramanathan RK, Bassett D, Neidhart JA, *et al*. (2013) First-in-human phase 1/2a trial of CRLX101, a cyclodextrin-containing polymer-camptothecin nanopharmaceutical in patients with advanced solid tumor malignancies. *Investigational New Drugs* 31(4):986–1000.
7. Pham E, Birrer MJ, Eliasof S, Garmey EG, Lazarus D, Lee CR, *et al*. (2015) Translational impact of nanoparticle-drug conjugate CRLX101 with or without bevacizumab in advanced ovarian cancer. *Clin Cancer Res* 21(4):808–818.
8. Schluep T, *et al.* (2009) Pharmacokinetics and tumor dynamics of the nanoparticle IT-101 from PET imaging and tumor histological measurements. *Proc Natl Acad Sci USA* 106(27):11394–11399.
9. Kaluz S, Kaluzová, M, Liao S-Y, Lerman M, Stanbridge EJ (2009) Transcriptional control of the tumor- and hypoxia-marker carbonic anhydrase 9: A one transcription factor (HIF-1) show? *BBA Rev Can* 1795(2):162–172.

10. Maeda H (2015). Toward a full understanding of the EPR effect in primary and metastatic tumors as well as issues related to its heterogeneity. *Adv Drug Deliv Rev* 91:3–6.
11. McGranahan N, Swanton C (2015) Biological and Therapeutic Impact of Intratumor Heterogeneity in Cancer Evolution. *Cancer Cell* 27(1):15–26.
12. Araya M, Terashima M, Takagane A, Abe K, Nishizuka S, Yonezawa H, *et al*. (1997). Microvessel count predicts metastasis and prognosis in patients with gastric cancer. *J Surg Oncol* 65(4):232–236.
13. Cheng J, Khin KT, Jensen GS, Liu A, Davis ME (2003) Synthesis of Linear, β-Cyclodextrin-Based Polymers and Their Camptothecin Conjugates. *Bioconjugate Chem* 14(5):1007–1017.
14. Ng TSC, Wert D, Sohi H, Procissi D, Colcher D, Raubitschek AA, Jacobs RE (2013) Serial Diffusion MRI to Monitor and Model Treatment Response of the Targeted Nanotherapy CRLX101. *Clin Cancer Res* 19(9):2518–2527.
15. Gaur S, Wang Y, Kretzner L, Chen L, Yen T, Wu X, *et al*. (2014) Pharmacodynamic and pharmacogenomic study of the nanoparticle conjugate of camptothecin CRLX101 for the treatment of cancer. *Nanomed Nanotech Biol Med* 10(7):1477–1486.
16. Desai SD, Liu LF, Vazquez-Abad D, D'Arpa P (1997) Ubiquitin-dependent destruction of topoisomerase I is stimulated by the antitumor drug camptothecin. *J Biol Chem* 272(39):24159–24164.
17. Fu Q, Kim SW, Chen HX, Grill S, Cheng YC (1999) Degradation of topoisomerase I induced by topoisomerase I inhibitors is dependent on inhibitor structure but independent of cell death. *Mol Pharmac* 55(4):677–683.
18. Lin C-P, Ban Y, Lyu YL, Liu LF (2009) Proteasome-dependent Processing of Topoisomerase I-DNA Adducts into DNA Double Strand Breaks at Arrested Replication Forks. *J Biol Chem* 284(41):28084–28092.
19. Zhang H-F, Tomida A, Koshimizu R, Ogiso Y, Lei S, Tsuruo T (2004) Cullin 3 promotes proteasomal degradation of the topoisomerase I-DNA covalent complex. *Cancer Res* 64(3):1114–1121.

20. Desai SD, Zhang H, Rodriguez-Bauman A, Yang JM, Wu X, Gounder MK, *et al*. (2003) Transcription-Dependent Degradation of Topoisomerase I-DNA Covalent Complexes. *Mol Cell Biol* 23(7):2341–2350.